UNIVERSIDAD DE LAS PALMAS DE GRAN CANARIA

Doctoral Thesis

From large scale to mesoscale dynamics in the Cape Verde Frontal Zone

---

Author:

Nadia BURGOA GREGORIO

Supervisors:

Dr. Francisco José MACHÍN JIMÉNEZ

Dr. Ángel RODRÍGUEZ SANTANA

Programa de Doctorado en Oceanografía y Cambio Global

Departamento de Física

April 27, 2022

Cover image: Salinity field at 200 m depth on July 23, 2017 of GLORYS12V1 model. Extracted from My Ocean property of Copernicus Marine Service (https://myocean.marine.copernicus.eu/)

Dª SANTIAGO MANUEL HERNÁNDEZ LEÓN COORDINADOR/A DEL PROGRAMA DE DOCTORADO EN OCEANOGRAFÍA Y CAMBIO GLOBAL DE LA UNIVERSIDAD DE LAS PALMAS DE GRAN CANARIA

INFORMA,

De que la Comisión Académica del Programa de Doctorado, tomó el acuerdo de dar el consentimiento para su tramitación, a la tesis doctoral titulada *"From large scale to mesoscale dynamics in the Cape Verde Frontal Zone"* presentada por la doctoranda **Dª Nadia Burgoa Gregorio**, dirigida por el **Doctor Ángel Rodríguez Santa** y codirigida por el **Doctor Francisco José Machín Jiiménez**.

Y para que así conste, y a efectos de lo previsto en el Artº 11 del Reglamento de Estudios de Doctorado (BOULPGC 04/03/2019) de la Universidad de Las Palmas de Gran Canaria, firmo la presente en Las Palmas de Gran Canaria,

This thesis proposal has been carried out at the OFYGA research group in the Physics Department of the University of Las Palmas de Gran Canaria. It has been financed by the Research State Agency and the Ministry of Economy, Industry and Competitiveness of Spain through a FPI pre-doctoral training grant in the frame of the research project entitled "Carbon fluxes in a Coastal Upwelling System - Cape Blanc, NW Africa" (FLUXES, ref: CTM2015-69392-C3-3-R) within the Spanish National Research Program and the European Regional Development Fund (MINECO/FEDER). During this thesis, the author has actively participated in the two oceanographic cruises linked to the project, has engaged in two research stays in the Physics Department of the Centro de Investigación Científica y de Educación Superior de Ensenada in Baja California (Mexico) and has participated in five international symposiums.

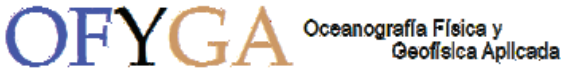

Itsasoan urak handi dire,
murgildu nahi dutenentzat.

Xabier Lete

Nire amaren oroimenez

Summary

The main goal of this research work, contextualized within Physical Oceanography but also with some multidisciplinary nature, is to complete the ideas that have been established throughout history around the Cape Verde Frontal Zone, CVFZ. Nestled within the highly productive coastal upwelling off Northwest (NW) Africa, the CVFZ is located off the coast of Cape Blanc, in the convergence zone of the Subtropical and Tropical gyres of the North Atlantic where the central waters transported by both gyres, NACW and SACW, form a thermohaline front practically compensated in density and with abundant associated mesoscale structure. Based on in situ measurements carried out during the two cruises of the COCA project and two other cruises of the FLUXES project, the characterization of the CVFZ deepens in order to achieve a better understanding of the physical components that govern its dynamics, from the basin scale, in which the circulation patterns are described north and south of Cape Blanc influenced by the unresolved mesoscale, up to the mesoscale and submesoscale, in which the main thermohaline structures detected above and below 100 m and the associated frontal dynamics are detailed, including the secondary ageostrophic circulation with its respective horizontal and vertical components. In addition, this research work describes the distribution and behavior of the different water masses detected at different levels, as well as, other associated biochemical variables, such as inorganic nutrients, dissolved oxygen and dissolved organic carbon, addressing the uncertainties in the balances of the large-scale biochemical fluxes in the CVFZ.

Contents

Part I

Chapter 1

General introduction

1.1 Scales and interactions

The natural processes that occur in the oceans cover a wide range of scales of time, from fractions of second to hundreds of decades, and of space, from the global to the smallest scales of dissipation (Fig. 1.1). This classification is adequate in physical terms, but what happens with the scales of biochemical processes? What are they governed by? The distributions of biochemical properties are affected by, on the one hand, the scales of the biochemical processes themselves and on the other hand, by the physical processes. That is why, it is very necessary to pay attention to the physical and biochemical process' scale ranges in order to make an excellent design of the sampling and a precise analysis, and therefore, obtain realistic results and important conclusions about the complex interactions between the physical and biochemical processes.

1.1.1 Physical processes

The stratification of the ocean, i.e., that the density increases with depth or the Brunt–Väisälä frequency (N) is positive, contributes to the predominance of the horizontal scales over the vertical ones at the basin level (Cushman-Roisin and Beckers, 2011). That is, when we talk about the large-scale oceanic circulation, in general, we refer to the water masses' horizontal movements through the currents. However, some exceptions in which the water masses driven by can also move vertically, such as the areas of convergence and/or divergence (Colling, 2001). On smaller scales, such as mesoscale or submesoscale, upward and downward movements are also very important in dinamically active structures (McGillicuddy et al., 1998; Rodriguez et al., 2001; Mahadevan and Tandon, 2006).

A practical way to dynamically classify the scales of oceanographic processes is with the Rossby number, R_o, and/or Rossby radius of deformation, R_d. Depending on its value, the first one provides the information about the scale of the process, i.e., if it is in mesoscale ($R_o < 1$) or submesoscale ($R_o \geq 1$). When $R_o < 1$, the geostrophic adjustment in the horizontal and the hydrostatic equilibrium in the vertical minimize vertical mixing processes. On the other hand, when $R_o \geq 1$, the momentum transference and mixing processes in the vertical, due to the shear, and the ageostrophy become significant. It is also important to analyze the R_d value to know what it is the size of the scale of the geostrophic adjustment and

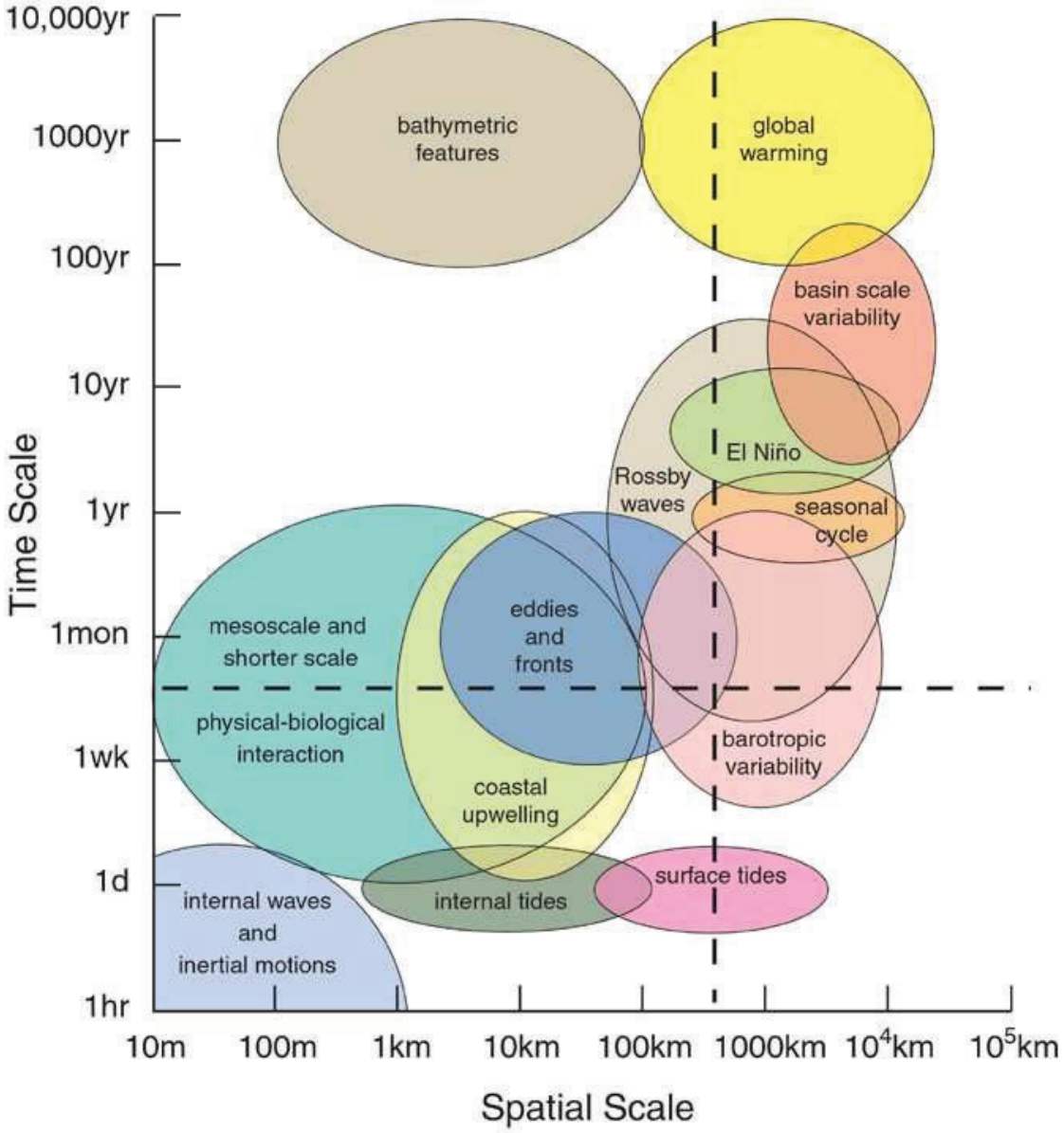

Figure 1.1: Time and space scales of physical oceanographic phenomena extracted from Chelton (October 2001).

distinguish the submesoscale from the mesoscale. On the finest scales, from the submesoscale to the mixing and tubulence processes, in which already significant vertical movements are, the energy dissipation cascade comes into play. In these last cases, it is essential to analyze the Richardson gradient number (Ri) to know if the turbulence generated by the vertical shear dominates, or not, over the static stability represented by N^2.

1.1.2 Biochemical processes

Classifying the kinetic and dynamic processes of the biochemical variables according to their scales is a difficult task to perform because: the parameters and their distributions interact with each other; the mechanisms and velocities of biochemical reactions are conditioned by the physical characteristics of the marine environment; and the biochemical processes are forced mainly by physical processes.

For example, the dissolved oxygen (O_2) concentration can be altered by biological processes, such as remineralization and photosynthesis, and physical processes, such as ventilation and circulation (Shaffer, 1996; Matear and Hirst, 2003). But the concentration of O_2 can also be altered by changes in the temperature of the water mass itself as it would happen if it were heated that it would lead to a decrease in its solubility (Matear and Hirst, 2003).

Another example is the variability of available inorganic nutrients (INs) that support photosynthetic activity in the photic layer. INs are mainly generated by remineralization of organic matter in poorly ventilated subsurface waters where they have long residence times (Williams and Follows, 2003). Their movements towards shallower layers are conditioned by the predominant physical process. While the stratification, that can be generated by the heating of the water column, would act as a barrier and reduce the entry of nutrients to the photic layer, some processes forced by the wind can cause upwelling of cold waters loaded with nutrients on the coasts and/or vertical mixing on smaller scales that breaks the water layers and distributes the nutrients in the water column (Pelegrí, Marrero-Díaz, and Ratsimandresy, 2006).

The organic matter mostly found in dissolved form in the ocean and with the dissolved organic carbon (DOC) as the most abundant element of all that compose it, is classified according to its reaction velocity as: refractory, labile and semi-labile (Álvarez-Salgado and Arístegui, 2015). The refractory organic matter remains in the oceans from decades to thousand years without being used by any organisms (Hansell, 2013). The labile organic matter is produced and processed within the same water parcel (Álvarez-Salgado and Arístegui, 2015). And the semi-labile organic matter is horizontally or vertically transported to be processed away from where it was produced (Hansell et al., 2009).

In general, the supply of biochemical properties associated with a specific water mass can be carried out by lateral or vertical transport, from regional to the smallest scales. The horizontal advective processes are usually related to regional patterns while the vertical mixing processes are more linked to the mesoscale and smaller scales. Therefore, the study of the variability that acts on one or another spatial and temporal scale mainly depends on the type of the sampling carried out.

1.2 Vertical velocities in submesoscale and mesoscale of frontal dynamic

Many measurements explain and argue how the different water masses move horizontally in the ocean. However, the processes that generate vertical movements of water are still great unknowns to science, despite these ascendent and descendent movements transcendently impact on heat and fresh water exchanges, oxygen ventilation, biological productivity and carbon export, between the surface and the interior ocean. In fact, improving the observation and understanding of all the physical processes involved in vertical movements and their impacts on a climatic scale is one of the main challenges faced by physical oceanography.

Specifically, the frontal regions are highly dynamically active zones in the oceans, related to frequent density's and (or) other physical variables's fronts in over a wide range of scales and with important cross-frontal fluxes (Bower and Rossby, 1989; Pastor et al., 2008), significant mixing processes (Klein and Siedler, 1995; Martínez-Marrero et al., 2008) and ascendent and descendent water vertical movements that facilitate the supply of nutrients and give place to high phytoplankton productivity (Lévy, 2003; Nagai, Tandon, and Rudnick, 2006; McGillicuddy Jr, 2016; Ruiz et al., 2019).

Currently, the knowledge about the frontal dynamic, which focuses on the meso- and submesoscales, begins to grow little by little because the complexity and difficulty that involves its analysis, multiple processes interacting at a wide range of spatial and temporal scales, and the high observational efforts that requires to sample the spatial and temporal scales involved in their dynamics (Pallàs-Sanz, Johnston, and Rudnick, 2010b; McGillicuddy Jr, 2016). While the dynamic of surface fronts, specifically of those detected in density, generates great interest and begins to be known due to the key functions that performs (McWilliams, 2021), such as extract the available potential energy from horizontal density gradients and facilitate the transfer of kinetic energy to small-scale mixing and dissipation (D'asaro et al., 2011), or, transport materials vertically by their secondary circulations and concentrate buoyant materials along surface convergence lines (Mahadevan, 2016); the deepest oceanic fronts' abundance and their associated dynamic is still unknown.

On the other hand, making direct measurements of vertical velocity (w) at meso- and submesoscale spatiotemporal resolutions is very difficult because its magnitude is below the noise level of any existing current meter for the typical time scales over which they vary (Pietri et al., 2021). Therefore, over time, different methodologies have been developed to indirectly estimate the vertical velocity w (Bower and Rossby, 1989; Giordani, Caniaux, and Prieur, 2005; LaCasce and Mahadevan, 2006; Horii et al., 2011; Yu et al., 2019). In general, the most commonly used method for inferring w is the so-called Omega equation (Hoskins, Draghici, and Davies, 1978) which combines two lines of arguments (Hoskins, 1982):

- Regions of gradient intensification are produced by a turbulent flow stirring an heterogeneous surface buoyancy field. Specifically, the confluence and shear, that frequently encounter in mesoscale turbulent conditions, promote the frontal intensification.

- Frontal intensification, in which horizontal gradients in density are enhanced while the vertical velocity shear is being reduced, disrupts the thermal wind balance. This leads to the development of secondary ageostrophic circulations that try to fight againts the thermal imbalance by shear restoration and slumping isopycnes. In general, at the air-sea interface, the upper boundary condition $w \approx 0$ limits the efficiency of ageostrophic circulations so frontal intensification can generally proceed further and yield intense vertical velocities. In contrast, this process is very efficient at preventing frontal intensification in the ocean interior where the vertical velocities away from the surface are usually weak.

Overall, the adiabatic Quasi-Geostrophic (Hoskins, Draghici, and Davies, 1978) and generalized Omega equations (Viúdez, Tintoré, and Haney, 1996) are the most widely used forms to reconstruct oceanic vertical velocity from high-resolution 3-D synoptic oceanographic observations (Pietri et al., 2021). Since the 1990s, numerous investigations of vertical velocity estimates based on the Omega equation have been carried out, most frequently in the context of mesoscale- and submesoscale- resolving observational efforts (Tintoré et al., 1991; Giordani and Planton, 2000; Mahadevan and Tandon, 2006; Ruiz et al., 2009; Barceló-Llull et al., 2017b; Estrada-Allis et al., 2019; Buongiorno Nardelli, 2020). One of many examples is that work made by Pallàs-Sanz, Johnston, and Rudnick (2010b) in which the vertical velocities diagnosis is shown from the diabatic version of the generalized Omega equation that includes vertical mixing, in a shallow front of the California Current.

1.3 Location and employed datasets

The studies carried out in this thesis are located off the northwestern African coasts (Fig. 1.2) in a great scientific and economic relevance area of one of the major eastern boundary upwelling (eco)systems in the world (Pelegrí and Benazzouz, 2015a). The domain that spans from 17.5°N, just north of the Cape Verde Islands, to 26°N, just south of the Canary Islands, is mainly under the influence of the coastal upwelling, the eastern boundary currents, and important mesoscale activity. In spite of the northern and southern of the domain are connected by a current's system, the scheme of the predominant dynamics is different north and south of Cape Blanc, located around 21°N (Pelegrí and Peña-Izquierdo, 2015; Pelegrí and Benazzouz, 2015a; Pelegrí et al., 2017).

The physical processes, that affect the biochemical distribution of the entire study area, are analyzed thanks to multidisciplinary in situ data acquired during the great observational effort cruises of COCA (Coastal-Ocean Carbon Exchange in the Canary Region, REN2000-U471-CO2-02-MAR) and FLUXES (Carbon Fluxes in a Coastal Upwelling System - Cape Blanc- NW Africa, CTM2015-69392-C3-3-R) projects.

The two cruises of COCA, carried out in September-October, 2002, and, May-June, 2003, had a similar station distribution that was optimal to study the ocean circulation and transports of water masses, INs and *DOC* within the enclosed area formed with the three oceanographic transects and the coast of western Sahara, from the south of Canary Islands to Cape Blanc and, from the African coast to 26°W. This study was repeatedly conducted in fall and spring, separated by a

period of six months, approximately.

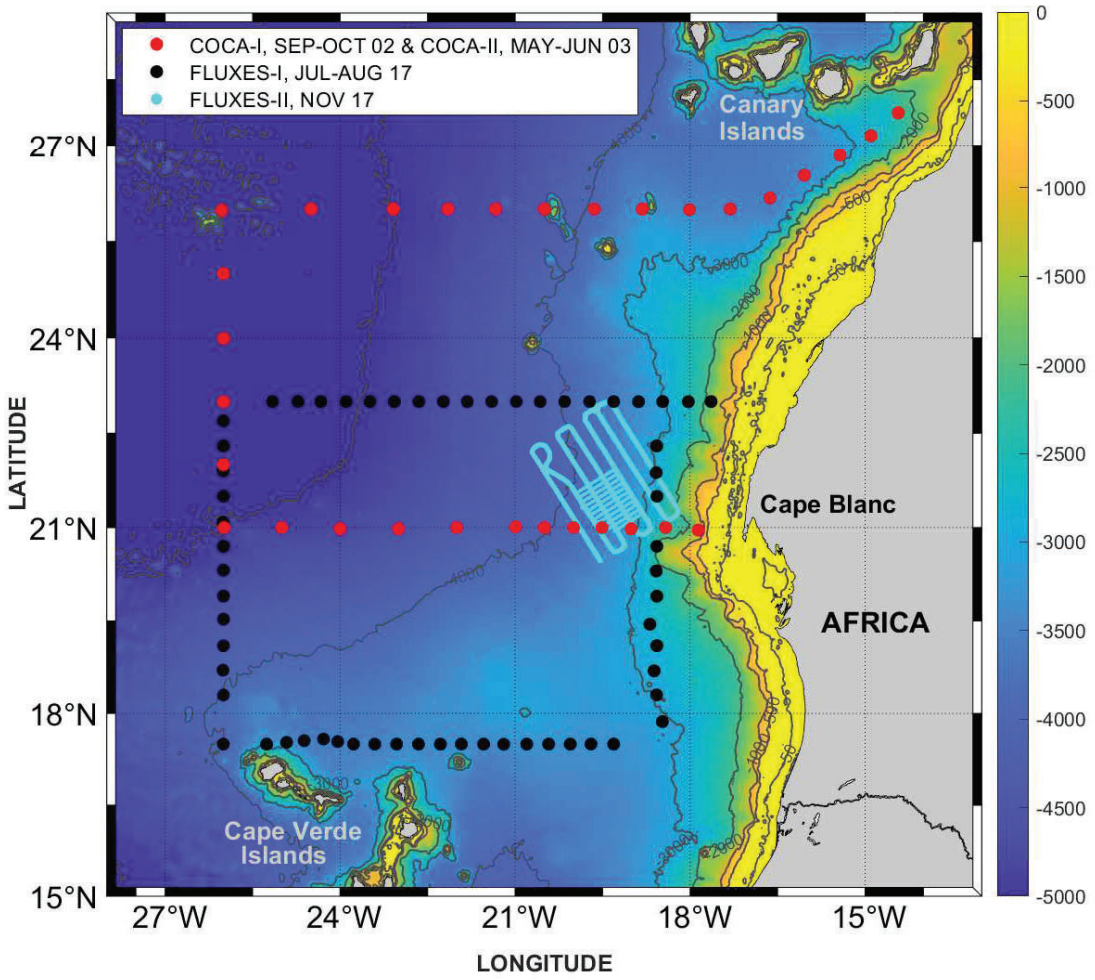

Figure 1.2: Studied region with both COCA, FLUXES-I and FLUXES-II cruises' oceanographic stations represented in red, black and cyan colors. The Smith–Sandwell bathymetry V19.1 (Smith and Sandwell, 1997) is employed.

The design of the two cruises of FLUXES conducted in 2017 was determined by the spatio-temporal scales of the processes to be sampled. The summer cruise (FLUXES-I), carried out in July-August, had a closed box distribution that spanned from the north of Cape Blanc to the north of Cape Verde Islands, in latitude, and from 18.6 to 26°W, in longitude. This distribution made possible to study again the ocean circulation and transports associated with the sampled physical and biochemical variables among which were included the concentration of organic matter and its elemental (C:N:P) or molecular composition. In the second cruise (FLUXES-II) carried out in November, the area sampled off the coast of Cape Blanc was much smaller, barely of 3° x 3°. However, the horizontal and vertical spatial resolutions achieved were much higher than in the summer cruise, due to employment of the Seasoar. In this case, these resolutions made possible to get to study the mesoscale and submesoscale dynamic and structures, undetectable in the previous cruises.

1.4 Hydrography and ocean circulation

1.4.1 Water masses

The predominant water masses located in the studied area are: Surface Water (SW), North Atlantic Central Water (NACW), South Atlantic Central Water (SACW), Antartic Intermediate Water (AAIW), Mediterranean Water (MW) and North Atlantic Deep Water (NADW) (Zenk, Klein, and Schroder, 1991; Martínez-Marrero et al., 2008; Peña-Izquierdo et al., 2015; Pelegrí et al., 2017).

The SW is considered as the transition water between the atmosphere and deep ocean, placed from the surface to some meters under the base of mixed layer. SW, which is the water mass with the highest energy and variability of the entire water column, groups the most homogeneous water of the mixed layer and the upper thermocline water with high gradients of temperature, salinity and density. Below the SW, the NACW and SACW coexist. These water masses formed in the central regions of the North and South Atlantic subtropical gyres are detected by a nearly linear relationship between their temperatures and salinities in a TS-diagram. Additionally, they are clearly different because the SACW is relatively colder, fresher, richer in INs and poorer in O_2 than the NACW at any given density level (Tomczak, 1981; Pastor et al., 2008; Pastor et al., 2012; Peña-Izquierdo et al., 2015). Some of the works carried out, pose different varieties of both water masses, such as the Western and Eastern NACW (WNACW and ENACW) and the Eastern SACW (ESACW), that reflected different formation regions (Emery and Meincke, 1986; Poole and Tomczak, 1999). On the other hand, the most recent studies (Pastor et al., 2012; Peña-Izquierdo et al., 2015), subdivide the central waters into two zones: an upper layer (upper central waters, $\sigma_\theta < 26.8$) and a lower layer (lower central waters, $26.8 < \sigma_\theta$) where the predominance of NACW and SACW is determined according to their predefined characteristics and the paths followed by the waters from their origin to the CVFZ.

Under the central waters at intermediate levels (between 700 m to 1600 m), it is located the AAIW that is easily identified by low salinities and temperatures (Zenk, Klein, and Schroder, 1991; Machín and Pelegrí, 2009). It is also characterized by maximum values of INs and moderately low O_2. Below it, in some specific cases, small isolated lens-shaped patches of MW called " meddies " (McDowell and Rossby, 1978) have been detected, which are saltier and warmer than the AAIW. Despite the mixing processes suffered throughout their long paths, the intermediate waters detected in the studied area, have differentiated values of salinity and temperature that tend towards the values of their formation, in the TS diagrams (Pastor, Vélez-Belchí, and Hernández-Guerra, 2015). The NADW is located below the MW and has been mainly formed as mixture of different water masses (Van Aken, 2000). Specifically, the shallowest NADW, defined as the upper NADW, is identified by its high salinity values due to mixing with MW (Hernández-Guerra et al., 2005).

1.4.2 Eastern boundary currents

The eastern margin boundary currents of the studied area are held by the North Atlantic Subtropical and Tropical gyres (NASG and NATG) which bring the sur-

face and upper thermocline waters, NACW and SACW, from the interior ocean to the African coast where it recirculates thanks to a system of along-slope currents (Fig. 1.3). In the anticyclonic NASG, the Azores Current (AC) feeds the Canary Current (CC) that flows southward (Klein and Siedler, 1989; Hernández-Guerra et al., 2005). Specifically, between the Canary Islands and Cape Blanc, the trade wind blows all year long generating permanent upwelling on the coasts of Western Sahara (Benazzouz et al., 2014a; Benazzouz et al., 2014b). Associated to the coastal upwelling, a near-slope jet, considered as the eastern branch of the CC or the Canary Upwelling Current (CUC) (Pelegrí et al., 2005; Pelegrí, Marrero-Díaz, and Ratsimandresey, 2006), conditioned by the mesoscale structures with which it interacts along its path (Mason et al., 2011), also flows southward. In the cyclonic NATG, the North Equatorial Counter Current (NECC) becomes the Cape Verde Current (CVC) that flows anticlockwise around the Guinea Dome (GD) and feeds the Mauritanian Current (MC) that moves northward at the Mauritanian slope (Peña-Izquierdo et al., 2015; Pelegrí et al., 2017). These two gyres converge into the Cape Verde Frontal Zone (CVFZ) where the southward and northward currents meet, making the flow turn westward and discharging water to the interior ocean, as the North Equatorial Current (NEC) (Hernández-Guerra et al., 2005; Pastor et al., 2008). Although most of the water is diverted offshore, it is also possible that a small fraction of the CUC may follow south in winter, when there is a narrow band of shallow upwelling between the Cape Verde Peninsula (around 14.5°N) and Cape Blanc (Pelegrí and Benazzouz, 2015a).

In addition, the Poleward Under Current (PUC) is extended at least between the Cape Verde Peninsula and Canary Islands (Barton, 1989) below the shallowest along-slope currents, and sometimes coexisting with them. This slope current flows northward at a variable depth in function of the season, bathymetry and predominant dynamic processes. Off Senegal and Mauritania, PUC flows at surface, mingling with MC, during summer and fall, and, at subsurface during winter and spring (Peña-Izquierdo et al., 2012; Pelegrí et al., 2017). In fact, south of Cape Blanc, the seasonality is very marked due to the alternation of trade winds (that blow during boreal winter) and periods of relaxation (Benazzouz et al., 2014a; Benazzouz et al., 2014b), and, the movements of the Intertropical Convergence Zone (ITCZ, which has a further north position in summer). Both dynamical processes directly affect the circulation's patterns north and south of the CVFZ (Lázaro et al., 2005; Castellanos et al., 2015). On the other hand, there are studies that detect PUC at greater depths, even carrying AAIW northward beyond the Canary Islands (Mittelstaedt, 1983; Machín and Pelegrí, 2009; Vélez-Belchí et al., 2021).

1.4.3 Main mesoscale structures external to the CVFZ

When the upwelling process is generated due to the trade winds, permanently between Canary Island and Cape Blanc and commonly during winter south of Cape Blanc (Fig. 1.3), a Coastal Upwelling Front (CUF) is produced separating the upwelled subsurface cold and denser waters on the seashore side and the offshore stratified waters, that develops and behaves differently north and south of Cape Blanc (Benazzouz et al., 2014b). In the subtropical gyre (north of the cape), the upwelling is characterized by a large-scale wind-driven connection affecting typically 200-250 m deep, while in the tropical gyre (south of the cape), the upwelling

is shallower responding fast to coastal winds and affecting the upper 50-100 m of the water column (Benazzouz et al., 2014b; Pelegrí and Benazzouz, 2015a; Pelegrí et al., 2017).

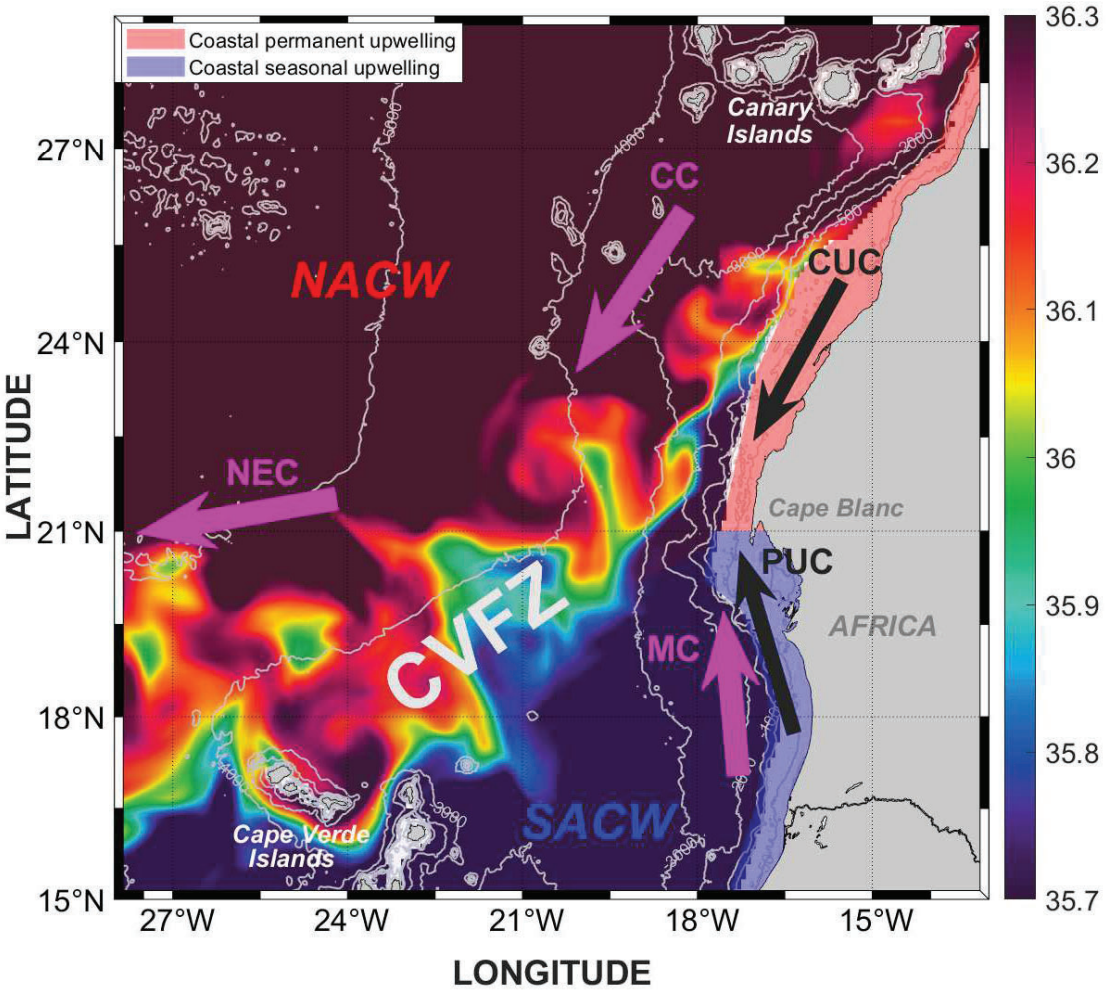

Figure 1.3: Monthly mean salinity of November 2017 at 156 m, extracted from GLOBAL_REANALYSIS_PHY_001_031 (https://doi.org/10.48670/moi-00024). The green color indicates the position of the isohaline of 36 at this depth, used to identify the Cape Verde Frontal Zone (CVFZ). North Atlantic and South Atlantic Central waters' acronyms, NACW and SACW, indicate both water masses' locations. There are also represented the two upwelling regions and the circulation pattern showing the main currents: Canary Upwelling Current (CUC), Canary Current (CC), North Equatorial Current (NEC), Mauritania Current (MC) and Poleward Undercurrent (PUC).

North of Cape Blanc, isolated eddies might also be found created from the interaction between the Canary Island and CC (Sangrà et al., 2009; Barceló-Llull et al., 2017a), as well as upwelling filaments which form from the coastal upwelling due to instabilities of coastal jet (CUC) that could also interact with the isolated eddies (Meunier et al., 2012; Ruiz et al., 2014). Both mesoscale structures may play a main role in the physical and biochemical fluxes balances of the stratified areas of the NASG and NATG having a great impact on the locally and regionally

modulation and distribution of physical and biogechemical properties (Mahadevan and Archer, 2000; Bonino et al., 2021).

Besides, all kind of mesoscale (and submesoscale) activity associated with the CVFZ (Barton, 1987; Meunier et al., 2012; Hosegood et al., 2017; Appen et al., 2020) is commonly found which will be treated independently in the next section as the main subject of study of this thesis.

1.5 CVFZ

The confluence area between the NASG and NATG, that approximately extends from Cape Verde Islands to Cape Blanc (17°N - 21°N), moving north during fall and south during spring (Pastor et al., 2008), and that constitutes an open-ocean diffused frontier between the NACW and SACW off the northwest Africa EBUS, started to be explored in the seventies and eighties (Hughes and Barton, 1974; Mittelstaedt, Pillsbury, and Smith, 1975; Barton, Huyer, and Smith, 1977; Voituriez and Chuchla, 1978; Tomczak, 1981; Barton, 1987; Stramma and Siedler, 1988; Barton, 1989). In particular, Zenk, Klein, and Schroder (1991) introduced the Cape Verde Frontal Zone (CVFZ, Fig. 1.3) term to appoint this highly dynamic area where the cyclonic near-surface currents of the tropical gyre and the anticyclonic near-surface currents of the subtropical gyre converge, making SACW and NACW collide and exchange salt, heat and other properties such as INs and O_2, through a wide range of physical processes.

The CVFZ, that is distinguished by a persistent frontal activity, the currents convergence mainly along the Mauritanian continental slope (Peña-Izquierdo et al., 2012; Peña-Izquierdo et al., 2015; Burgoa et al., 2021), and an offshore water discharge that has maximum values during summer and fall and exports among others INs (Pastor et al., 2008; Pelegrí and Peña-Izquierdo, 2015), also acts as a source of lateral mixing with mesoscale, submesoscale and other scale features.

The thermohaline front between NACW and SACW, described by maximum horizontal gradients in salinity and temperature, but not in density, and dominated by interleaving processes with double-diffusive intrusions (Barton, 1987; Klein and Tomczak, 1994; Klein and Siedler, 1995; Pérez-Rodríguez, Pelegrí, and Marrero-Díaz, 2001; Martínez-Marrero et al., 2008), stands out among other structures of different scales which favor the horizontal mixing between both central waters. Barton (1987), who was the first to describe this front, considered it as a density-compesated front as a result of the compesated effects of the salinities and temperatures of both waters on the density field that generate a stable stratification and a relatively weak along-front geostrophic current. Subsequently, Zenk, Klein, and Schroder (1991) would be responsible to define the NACW-SACW front as the Central Water Boundary, with the simple criterion of the intersection of the 36.0 isohaline at 150 m depth. However, the high number of meso and submesoscale structures that interact each other in the CVFZ, such as the meanders, eddies and intrusions associated to this front (Barton, 1987), make really complex the studies of the physical processes involved in its formation and evolution. Similarly, it occurs with other mesoscale and submesoscale structures generated from instabilities of different origins in the CVFZ, that have scarcely been studied with in-situ data, remote sensing measurements (Lázaro et al., 2005; Appen et al., 2020) and/or

high-resolution models (Onken and Klein, 1991; Erasmi, Siedler, and Onken, 1998; Dilmahamod et al., 2021), such as the upwelling filaments that generate off Cape Blanc, expand into the ocean and interact with eddies (Gabric et al., 1993; Meunier et al., 2012). In fact, there are not many works that describe and argue the existing interactions between the different mesoscale and submesoscale structures associated to the NACW-SACW front and the coastal upwelling front, as for example, it would be the study about the complex circulation pattern generated as a result of the interaction between both fronts. However, the importance of advective processes around, and associated to, the NACW-SACW front has already been demonstrated with ADCP measurements (Martínez-Marrero et al., 2008).

On the other hand, the mixing processes' studies suggest that double diffusion influences the vertical balance of salt and heat in the boundary zone between NACW and SACW (Klein and Siedler, 1995) and that a competition between double diffusion and vertical shear instabilities exist in this water column (Martínez-Marrero et al., 2008).

1.6 Biochemical features

The distributions of INs, O_2 and DOC are differentiated in the following three regions: the southeastern extension of the NASG, the northeastern extension of the NATG and the upwelling region along the latitudinal coastal band off northwest Africa. In terms of primary productivity, the northwest African upwelling region is the most seasonally and spatially variable among the major Eastern Boundary Upwelling Systems (EBUS) (Carr and Kearns, 2003; Auger et al., 2016). It is characterized by a combination of areas of permanent and very seasonal upwelling processes that generate high primary production that depends on the right winds and nutritive quality of the upwelled waters. In contrast, the interior of both gyres are oligotrophic (especially the NASG with low nutrients contents at subsurface levels) and high stratification zones, except near their boundaries where lateral inputs from the northwest African upwelling region occur intermittently given by upwelling filaments, mesoscale eddies and the interactions between them (García-Muñoz et al., 2004; Ruiz et al., 2014; Lovecchio et al., 2017; Bonino et al., 2021). In addition to these lateral sources with important influence in biological processes, other possible injections could be also given from the subsurface levels favored by the vertical movements of isolated mesoscale structures, such as eddies generated south of the Canary Islands, that are efficient breaking the stratification (McGillicuddy et al., 1998).

The proportions of the labile and semi-labile fractions of organic matter in the northwest Africa EBUS are higher than the proportions normally found in the oceans, in a global scale (Álvarez-Salgado and Arístegui, 2015). Two-thirds of the DOC caught and exported by the filaments and eddies (Gabric et al., 1993; García-Muñoz et al., 2004; García-Muñoz et al., 2005; Álvarez-Salgado et al., 2007; Sangrà et al., 2009; Lovecchio et al., 2017) and presented in the upwelled waters, is old, while, the rest of DOC, produced during the phytoplankton primary production triggered by the entry of upwelled INs, is recent and fresh (Álvarez-Salgado and Arístegui, 2015). That is to say, about 33% of the dissolved organic matter exports into the oligotrophic adjacent ocean from the productive shelf waters is

bioavailable, a proportion much higher than the global estimate of $< 1\%$, previously mentioned by Hansell (2013) (Álvarez-Salgado and Arístegui, 2015).

In general, the concentrations of INs and O_2 vary both vertically and horizontally. In the subsurface layers, the organic matter produced on the surface is remineralized along the water path modifying the concentrations of INs and O_2. In addition, these concentrations will also change depending on the hydrodynamic processes which affect and the rate of water supply, which already contains INs, O_2 and organic matter. Specifically in the studied area, marked latitudinal gradients are observed due to the differences in INs and O_2 contents between the young NACW, with a relative short path since its formation that is transported by the NASG and the old SACW, with long residence times carried by the NATG (Pelegrí and Benazzouz, 2015b). On the other hand, south of Cape Blanc within the tropical waters, the Oxygen Minimum Zone of the North Atlantic (Luyten, Pedlosky, and Stommel, 1983; Peña-Izquierdo et al., 2015) is developed where high primary production and slow ventilation of the subsurface waters lead to enhanced remineralization with low O_2 concentration and high levels of INs. Specifically in this area, the nutrient supply shoots up during winter also due to high coastal upwelling and river discharge, brought north by the surface MC (Pastor et al., 2013; Pelegrí and Peña-Izquierdo, 2015).

1.7 Objectives and thesis outline

The general objective of this thesis is to contribute to the knowledge of the CVFZ completing its characterization from basin scale to smaller scales with the COCA and FLUXES projects data.

Although this thesis is focused on the physical processes that influence the CVFZ, biochemistry has also its importance due to the size of the project in which it is framed. Therefore, an attempt will be made to address the biochemical distributions marked by the water masses transports and other involved processes (given special attention to related uncertainties and unbalances).

In particular, this thesis aims to address several specific objectives associated with:

1. Spatial changes of the CVFZ (defined at 150 m by the isohaline of 36) between different seasons. Influence of these changes on circulation patterns and horizontal transport of *DOC* and INs north of the CVFZ at basin scale.
2. Extension of the NACW-SACW front definition to the entire water column where the central waters coexist in the CVFZ. Influence of the NACW-SACW front (with its new definition) on the currents and on the distribution of water masses and their biochemistry.
3. The NACW-SACW front structure at mesoscale and submesoscale levels. Description and analysis of the processes, horizontal and vertical circulation and structures associated to the NACW-SACW front on smaller scales.

These main goals are presented in three central chapters that are compiled as

scientific articles (published and/or in preparation) in part II. In the second chapter, the differences between fall and spring in the circulation patterns and transported properties are analyzed relating them to the position of the NACW-SACW front. In the third chapter, the currents circulation and associated transports are independently analyzed during summer north and south of the NACW-SACW front, expanding its definition up to 650-700 m depth. In the fourth chapter, the NACW-SACW front is detected well marked in salinity and temperature, and slightly compensated in density, between abundant mesoscale and submesoscale activity that is horizontally and vertically described in fall 2017.

Specifically, the details of the scientific articles that appear in this thesis are the following:

Burgoa, N., Machín, F., Marrero-Díaz, A., Rodríguez-Santana, A., Martínez-Marrero, A., Arístegui, J., and Duarte, C. M. , (2020) *Mass, nutrients and dissolved organic carbon (DOC) lateral transports off northwest Africa during fall 2002 and spring 2003*, Ocean Science 16/2

Burgoa, N., Machín, F., Rodríguez-Santana, A., Marrero-Díaz, A., Álvarez-Salgado, X. A., Fernández-Castro, B., Gelado-Caballero, M. D. and Arístegui, J., (2021) *Cape Verde Frontal Zone in summer 2017: lateral transports of mass, dissolved oxygen and inorganic nutrients*, Ocean Science 17/3

Burgoa, N., Rodríguez-Santana, A., Pallàs-Sanz, E., Machín, F., Marrero-Díaz, A., Valencia, L. P., Grisolía, D., Gordo, C. and Martínez-Marrero, A., *Dynamic characterization of submesoscale and mesoscale structures in the Cape Verde Frontal Zone*, In prep.

Asides the mentioned articles, this thesis also includes a first part with an introductory chapter in which a few aspect of the theoretical framework, the state of the art and the cruises' data used in the development of this thesis are presented, and, a final part of general conclusions and future research, as well as, a wide Spanish abstract with the main objectives and conclusions.

Part II:
Scientific papers

Chapter 2

Mass, nutrients and dissolved organic carbon (DOC) lateral transports off northwest Africa during fall 2002 and spring 2003

Burgoa, N., Machín, F., Marrero-Díaz, A., Rodríguez-Santana, A., Martínez-Marrero, A., Arístegui, J., and Duarte, C. M. (2020). Mass, nutrients and dissolved organic carbon (DOC) lateral transports off northwest Africa during fall 2002 and spring 2003. *Ocean Sci.* **16**, 483–511, doi:10.5194/os-16-483-2020

Abstract

The circulation patterns and the impact of lateral export of nutrients and organic matter off NW Africa are examined by applying an inverse model to two hydrographic datasets gathered in fall 2002 and spring 2003. These estimates show significant changes in the circulation patterns at central levels from fall to spring, particularly in the southern boundary of the domain related to zonal shifts of the Cape Verde Frontal Zone. Southward transports at surface and central levels at 26°N are 5.6±1.9 Sv in fall and increase to 6.7±1.6 Sv in spring; westward transports at 26°W are 6.0±1.8 Sv in fall and weaken to 4.0±1.8 Sv in spring. At 21°N a remarkable temporal variability is obtained, with a northward mass transport of 4.4±1.5 Sv in fall and a southward transport of 5.2±1.6 Sv in spring. At intermediate levels important spatiotemporal differences are also observed, and it must be highlighted that a northward net mass transport of 2.0±1.9 Sv is obtained in fall at both the south and north transects. The variability in the circulation patterns is also reflected in lateral transports of inorganic nutrients (SiO_2, NO_3, PO_4) and dissolved organic carbon (DOC). Hence, in fall the area acts as a sink of inorganic nutrients and a source of DOC, while in spring it reverses to a source of inorganic nutrients and a sink of DOC. A comparison between nutrient fluxes from both in situ observations and numerical modeling output is finally addressed.

2.1 Introduction

The North Atlantic Subtropical Gyre (NASG) is one of the most important components in the thermohaline circulation. It presents a well-known intensification

in its western margin, the Gulf Stream, with maximum velocities up to 2 m s^{-1} (Halkin, Rossby, and Rossby, 1985). The currents observed in this western margin of the gyre occupy a small horizontal extension compared to that of the currents in the eastern side, resulting in an asymmetric gyre ((Stramma, 1984; Tomczak and Godfrey, 2003)). The low intensity of the currents at the eastern boundary made them very little studied until the 1970s, when CINECA (Cooperative Investigations of the Northern Part of the Eastern Central Atlantic) program focused on the productive African upwelling system (Ekman, 1923; Hughes and Barton, 1974; Tomczak, 1979; Hempel, 1982). Käse and Siedler (1982) found strikingly intense currents south of the Azores connected to the Gulf Stream and suggested that part of the recirculation of the NASG occurs southward in the vicinity of the African coast. Later on, several surveys based on both in situ and remote sensing observations contributed to defining the general characteristics for the average flow of the region (Käse and Siedler, 1982; Stramma, 1984; Käse et al., 1986; Stramma and Siedler, 1988; Mittelstaedt, 1991; Zenk, Klein, and Schroder, 1991; Fiekas et al., 1992; Hernández-Guerra et al., 1993).

Most of the eastward flow from the Gulf Stream is confined to a band between the Azores and Madeira islands, recirculating southward through the Canary Islands and north of Cape Verde to become a southwestward flow (Stramma, 1984). This current system is composed by the Azores Current (AC), the Canary Current (CC), the Canary Upwelling Current (CUC), the North Equatorial Current (NEC) and the Poleward Undercurrent (PUC). The AC divides into several branches defining the boundary current system off northwest Africa. It first feeds the Iberian Current (Haynes, Barton, and Pilling, 1993), while a second significant branch enters the Mediterranean Sea (Candela, 2001). Most of the AC recirculates southward, splitting into the main CC across the Canarian archipelago and the secondary CUC (Pelegrí et al., 2005; Pelegrí, Marrero-Díaz, and Ratsimandresy, 2006). These currents extend southward, developing the Cape Verde Frontal Zone (CVFZ), a density-compensated front with North Atlantic Central Water at its northern side and South Atlantic Central Water at its southern one (Zenk, Klein, and Schroder, 1991; Martínez-Marrero et al., 2008). Finally, the PUC is located below the CUC, flowing northward on the continental slope (Barton, 1989; Machín and Pelegrí, 2009; Machín et al., 2010; Pelegrí and Peña-Izquierdo, 2015).

Mesoscale activity constitutes a second main feature in the area of interest, which might be even more energetic than the average flow itself (Sangrà et al., 2009). Three mesoscale domains may be defined: the Canary Eddy Corridor (CEC, (Sangrà et al., 2009)), the CVFZ and the upwelling front. The CEC is located downstream of the Canary Islands where the interaction between the southward flow and the archipelago generates long-lived eddies (Arístegui et al., 1994; Barton et al., 1998; Sangrà et al., 2007; Sangrà et al., 2009; Ruiz et al., 2014; Barceló-Llull et al., 2017a). The second mesoscale domain is the CVFZ, where several meanders and eddies produce strong interleaving between the water masses involved (Pérez-Rodríguez, Pelegrí, and Marrero-Díaz, 2001; Martínez-Marrero et al., 2008). In this domain, the CC and the CUC separate from the African coast, fueling the NEC and giving rise to a shadow zone featured by poorly ventilated waters (Luyten, Pedlosky, and Stommel, 1983). The third area is the front arising between the coastal upwelled waters and the stratified interior waters, defining the Eastern

Boundary Upwelling System (EBUS) in the northwest African region (Mittelstaedt, 1983; Pastor et al., 2008; Arístegui et al., 2009). This EBUS is actually located off the African slope from the Gulf of Cádiz until Cape Blanc-Cape Verde in summer-winter with high mesoscale variability in the form of both filaments and eddies (Hagen, 2001; Sangrà et al., 2009; Ruiz et al., 2014). The upwelling process raises nutrient-rich waters to the euphotic layer, developing a high-primary- production latitudinal band off northwest Africa known as the Coastal Transition Zone (CTZ) (Barton et al., 1998; Pelegrí, Marrero-Díaz, and Ratsimandresy, 2006). These mesoscale features play an essential role as a lateral source of organic matter towards the oligotrophic waters of the NASG (Barton et al., 1998; García-Muñoz et al., 2004; García-Muñoz et al., 2005; Pelegrí, Marrero-Díaz, and Ratsimandresy, 2006; Álvarez-Salgado et al., 2007; Sangrà et al., 2009).

The distribution of inorganic nutrients and organic matter in the ocean responds to a combined effect of physical and biogeochemical processes. Within the euphotic zone, primary production is solely limited by the availability of inorganic nutrients (INs) (Copin-Montegut and Copin-Montegut, 1983; Falkowski, Barber, and Smetacek, 1998). Below the euphotic zone respiration exceeds primary production. As a result, the organic matter produced at the sea surface is remineralized in the subsurface layers, and hence the concentration of INs increases from the interplay between the local rate of remineralization and the rate of water supply (Azam, 1998; Del Giorgio and Duarte, 2002; Pelegrí, Marrero-Díaz, and Ratsimandresy, 2006; Pelegrí and Benazzouz, 2015b).

In order to study the impact of lateral transports on the distributions of biogeochemical variables, the first step to follow is to analyze the dynamic of the area with an inverse box model. This method provides a velocity field consistent with both mass and property conservation within a closed volume and with the thermal wind equation (Wunsch, 1996). Several authors have already described the circulation patterns of the NASG by applying an inverse model (Ganachaud and Wunsch, 2002; Ganachaud, 2003a; Ganachaud, 2003b; Hernández-Guerra et al., 2005; Machín, Hernández-Guerra, and Pelegrí, 2006; Pérez-Hernández et al., 2013; Hernández-Guerra et al., 2017). Moreover, some recent papers addressing lateral advective transports of biogeochemical variables have shed light on this topic in the EBUS off NW Africa (Álvarez and Álvarez-Salgado, 2009; Alonso-González et al., 2009; Santana-Falcón et al., 2017; Fernández-Castro, Mouriño-Carballido, and Álvarez-Salgado, 2018).

To sum up, the main goal of this paper is to present an in situ hydrographic database and to estimate lateral mass as well as IN and *DOC* transports during fall and spring seasons south of the Canary Islands in the context of a highly variable environment featured by the Canary Eddy Corridor, the upwelling off northwest Africa and the CVFZ. The remainder of this paper is organized as follows: the dataset is presented in Sect. 2; the seasonal distribution of the water masses and their properties is displayed in Sect. 3; the technical details of the inverse box model are covered in Sect. 4; and the resulting velocity field and the corresponding mass, nutrient and organic matter transports are presented in Sect. 5. Section 6 is devoted to the discussion, with some conclusions in Sect. 7.

2.2 Dataset

The COCA-I and COCA-II cruises were carried out in fall (10 September to 1 October 2002) and spring (21 May to 7 June 2003), respectively, aboard the BIO *Hesperides* as part of the research project Coastal-Ocean Carbon Exchange in the Canary Region (Hernández-León et al., 2019). The location of conductivity-temperature-depth (CTD), inorganic nutrient (IN) and dissolved organic carbon (DOC) stations in COCA-I and COCA-II defines a closed box along three transects (Fig. 2.1). The northern transect (N) spans from station 1 to 32 at 26°N (the section from stations 1 to 11 is tilted some 30° with respect to the east). The western transect (W) is located at 26°W from station 32 to 42. Finally, the southern zonal transect (S) at 21°N runs from station 42 to 63 (COCA-I) or 66 (COCA-II) over the continental slope (Tab. 2.1). The distance between neighbouring CTD stations was some 50 km except for the stations over the continental slope where this distance was shortened. Adjacent DOC and IN stations were separated by a variable distance, with the shortest distance being about 50 km at stations closer to the coast.

CTD data were collected from the sea surface down to 2000 m of depth with a vertical resolution of 2 dbar. In situ temperature was calibrated with 45 readings performed with a reversible digital thermometer, while salinity was calibrated by analyzing 60 water samples with the Portasal salinometer. The residuals have an average value of 0.00013±0.00400 °C and 0.0005±0.005 in salinity.

DOC was measured with a total organic carbon (TOC) analyzer (Shimadzu TOC-5000), assuming that almost all TOC was in dissolved form. Water samples (10 mL) were dispensed directly into glass ampoules, previously combusted at 500 °C during 12 h; 50 μL of H_3PO_4 was immediately added to the sample, sealed and stored at 4 °C until analyzed. Before the analysis, samples were sparged with CO_2-free air for several minutes to remove inorganic carbon. TOC concentrations were determined from standard curves (30 to 200 μM) of potassium hydrogen phthalate produced every day (Thomas, Cauwet, and Minster, 1995). To check accuracy and precision, reference material from Jonathan H. Sharp laboratory (University of Delaware) was analyzed daily. DOC distribution up to 2000 m of depth presented a more representative coverage in fall than in spring (Fig. 2.2, green dots), despite the number of stations being higher in spring than in fall (Fig. 2.1, black circles; Tab. 2.1).

The three inorganic nutrients sampled were silicates (SiO_2), nitrates plus nitrites (NO_x), and phosphates (PO_4). These samples were frozen until measured with a Bran+Luebe AA3 autoanalyzer following the standard methodology established by Hansen and Koroleff (1999). Nutrient data covered up to 2000 m, while in fall they concentrated in the shallowest layers ($<$ 200 m, Fig. 2.2, pink crosses).

Wind data were selected from the QuikSCAT database made available by CERSAT (Centre ERS d'Archivage et de Traitement, http://www.ifremer.fr/cersat/). These wind fields were averaged weekly with a spatial resolution of 0.5° (shown in Fig. 2.1 with half of the original spatial resolution). The Smith-Sandwell database with 1 min horizontal resolution was used as the source of bathymetry data (Smith and Sandwell, 1997).

Freshwater flux data were estimated from the rates of evaporation and precipitation extracted from the Surface Marine Data 1994 of Da Silva (http://iridl.ldeo.

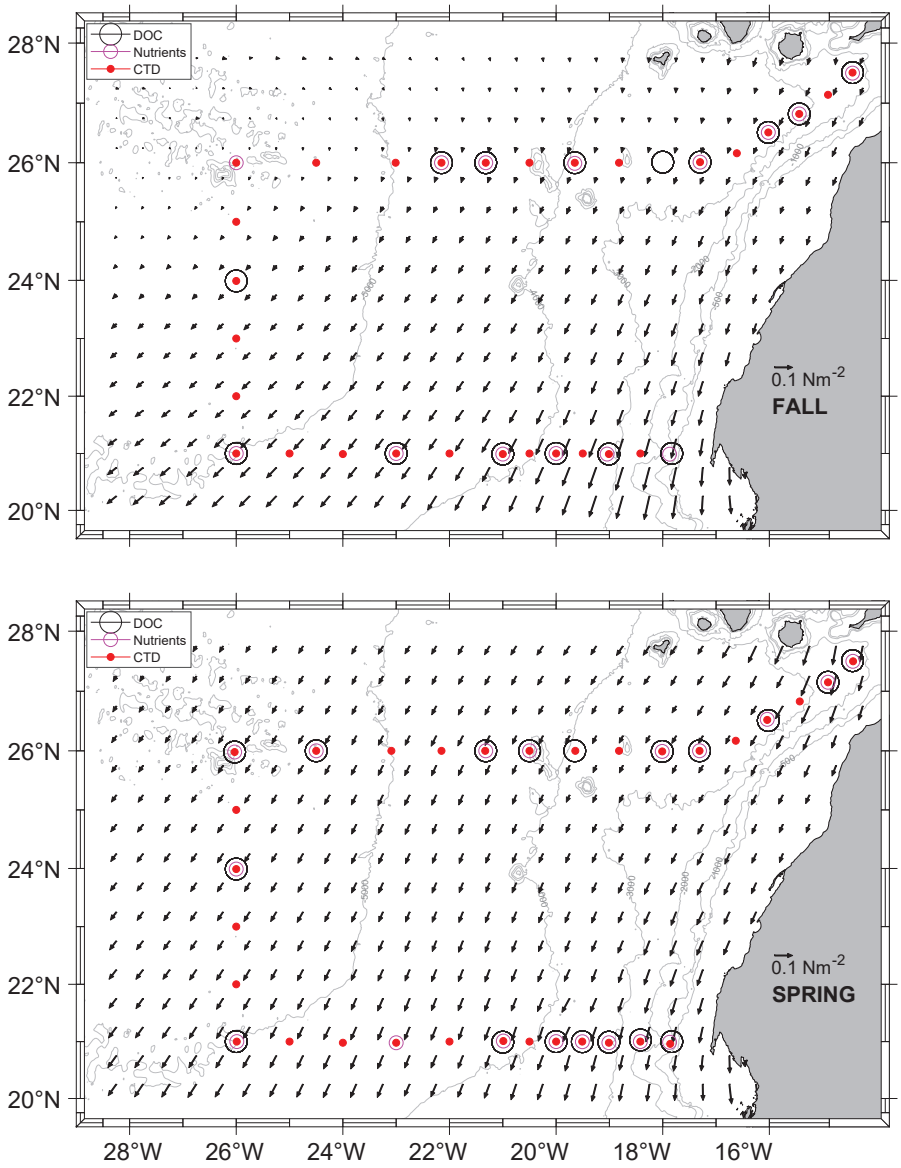

Figure 2.1: Hydrological (red dots), inorganic nutrient (pink circles) and *DOC* (black circles) sampling stations during the COCA-I (top) and COCA-II (bottom) cruises. Time-averaged wind stress during each cruise is also represented with the inset arrow denoting the scale (shown with half of the original spatial resolution).

Table 2.1: Summary of the number and type of measurements at stations per transect and season.

SEASON [Cruise]	**Type of measurement**	**Number of stations**			
		North	**West**	**South**	**Total**
FALL [COCA-I]	**CTD**	14	6	11	29
	IN	8	2	6	14
	DOC	8	2	6	15
SPRING [COCA-II]	**CTD**	15	6	12	31
	IN	9	3	8	18
	DOC	10	3	7	18

columbia.edu/SOURCES/.DASILVA/.SMD94/). The climatological mean depths of the neutral density field for the years 2002 and 2003 were calculated from the climatological temperature and salinity extracted from the World Ocean Atlas 2013, WOA13 (Locarnini et al., 2013; Zweng et al., 2013).

GLORYS (GLOBAL_REANALYSIS_PHY_001_025 product) issued by Copernicus Marine Environment Monitoring Service, CMEMS (Garric and Parent, 2018) was used as a primary source of dynamic variables. Its horizontal resolution is 1/12° with 50 standard depths. Hydrological data from GLORYS were also employed to diagnose the average oceanographic conditions during each cruise. This product assimilates field observations in real time.

The SEALEVEL_GLO_PHY_L4_REP_OBSERVATIONS_008_047 product provided surface geostrophic currents estimated from sea level anomalies. These data capture the mesoscale structures and are helpful to validate the near-surface geostrophic field estimated from the inverse model.

GLORYS-BIO (GLOBAL_REANALYSIS_BIO_001_029 product) produced daily mean 3D biogeochemical fields with the same resolution as GLORYS. This reanalysis forces the biogeochemical model with the nutrient initial conditions from WOA13. IN concentrations from GLORYS-BIO (SiO_2, NO_3, and PO_4) were used to assess nutrient transports by the model (in Sect. 5).

The data treatment, the graphical representations and the inverse model are coded in MATLAB (MATLAB, 2018). The vertical sections are produced using the 'nearest' 2D interpolations, a method also employed in the estimates of the IN and *DOC* transports. Ocean Data View using the DIVA gridding method is employed to produce *DOC* concentration charts (Schlitzer, Reiner, 2019).

2.3 Hydrography and water masses

Neutral density $\gamma_n = \gamma_n(\theta, S, p)$ is used as the density reference variable, with the isoneutrals representing the surfaces where the values of γ_n are constant (Jackett and McDougall, 1997). The γ_n vertical sections contain the surface (SW), central (CW), intermediate (IW) and deep water (DW) masses according to Macdonald (1998) for the North Atlantic at 24°N, represented with white dashed lines at 26.44, 27.38 and 27.82 kg m^{-3} (Fig. 2.2). The x-axis direction is selected according to the path followed by the vessel during both cruises, starting in the northeast and finishing in the southeast of the domain. The N-W and W-S corners are indicated with two vertical grey dashed lines at stations 32 and 42, respectively.

The $\Theta - S_A$ diagrams exhibit four regions delimited by potential density anomaly contours of 26.39, 27.30 and 27.72 kg m^{-3}, equivalent to the isoneutrals that separate the main water masses (Fig. 2.3). These three isoneutrals are approximately at 132-123, 672-700 and 1294-1305 m of depth (Fig. 2.2). The water masses sampled during both cruises are North Atlantic Central Water (NACW), South Atlantic Central Water (SACW), Antarctic Intermediate Water (AAIW), Mediterranean Water (MW), and North Atlantic Deep Water (NADW) (Emery and Meincke, 1986; Macdonald, 1998; Emery, 2008). Their main hydrological characteristics are summarized in Table 2.2. Below the mixing layer and above 700 m ($26.44 < \gamma_n < 27.38$ kg m^{-3}), NACW and SACW are the dominant water masses. SACW is featured by a higher amount of nutrients, and it is 1-2 °C colder

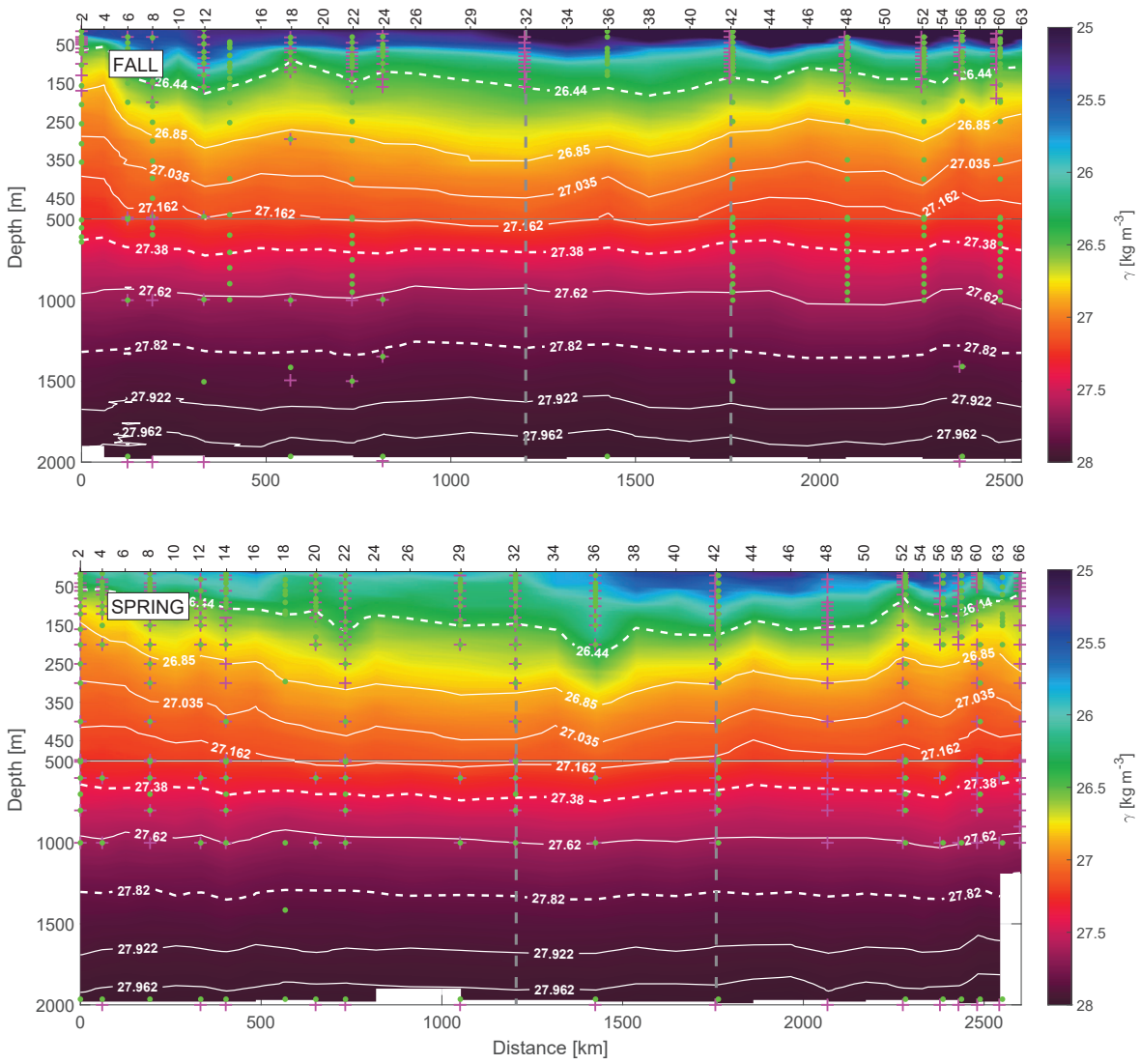

Figure 2.2: The γ_n vertical sections during fall (top) and spring (bottom) cruises. White dashed isoneutrals limit the different water type layers. The direction chosen for the representation of the transects is the course of the vessel. Distance is calculated with respect to the first station (2). The section is divided into three transects: the northern transect from east to west (from station 2 to 32), the western transect from north to south (from station 32 to 42) and the southern transect from west to east (from stations 42 to 63-66). The three transects are separated by two vertical grey dashed lines located at stations 32 and 42. The sampling points of INs and *DOC* used in this work are also represented by pink crosses and green dots, respectively.

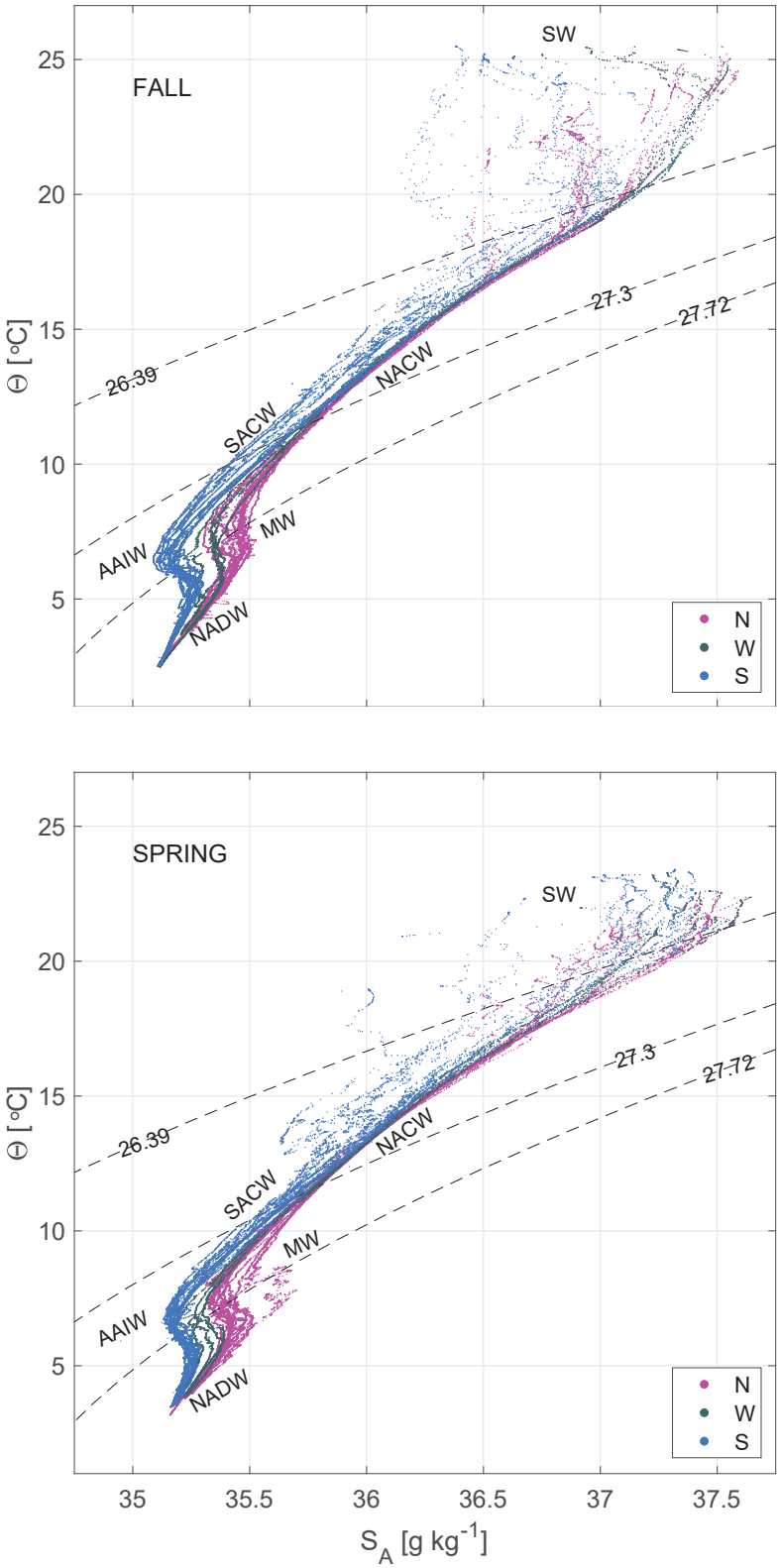

Figure 2.3: $\Theta - S_A$ diagrams of hydrological measurements during the fall (top) and spring (bottom) cruises. The different water masses at the north (N, magenta dots), west (W, dark grey dots) and south (S, blue dots) transects are SW, NACW, SACW, AAIW, MW and NADW. Potential density anomaly contours equivalent to the 26.44, 27.38 and 27.82 kg m^{-3} isoneutrals delimit the surface, central, intermediate and deep water levels.

and 0.1-0.4 fresher than NACW (Fig. 2.3 and Tab. 2.2). Below, from 700 up to 1300 m ($27.38 < \gamma_n < 27.82$ kg m^{-3}), the intermediate waters AAIW and MW are the dominant water masses (Hernández-Guerra et al., 2017). MW is a relatively warm and salty water mass, while AAIW is colder and fresher (Tab. 2.2). Finally, below 1300 m ($\gamma_n > 27.82$ kg m^{-3}) the predominant water mass is NADW, with in situ temperature and salinity values lower than 5.7 °C and 35.14 (Tab. 2.2).

A description of the temporal variability of the water masses is also given with observations from the $\Theta - S_A$ diagrams (Fig. 2.3). The distribution of water masses is quite similar for both cruises. There is a higher temperature variability at surface waters during fall, with maximum values 2-3 °C higher than in spring. During spring, the variability observed at central waters is associated to larger fluctuations in salinity affecting the whole water column. At DW there is a higher contribution of NADW in the whole domain during fall. Finally, the surface layer is thicker in fall than in spring in all the sections made with respect to γ_n.

These temporal differences may also be described transect to transect. The northern transect (Fig. 2.2, stations 2 to 32; Fig. 2.3, margenta dots) is occupied by NACW, AAIW, MW and NADW in both seasons. At intermediate levels, a higher contribution of MW is observed in spring, while a slightly higher contribution of AAIW is obtained in fall. The western transect (Fig. 2.2, stations 32 to 42; Fig. 2.3, dark grey dots) has a similar distribution as the northern one, with a lower variability in the upper layers and a smaller influence of MW. In the southern transect (Fig. 2.2, stations 42 to 63-66; Fig. 2.3, blue dots), the highest spatiotemporal variability is observed. This variability at the surface and central levels is associated with the position of the CVFZ and, in turn, with the mesoscale and submesoscale structures associated with the front. The CVFZ is located where the isohaline of 36, or equivalently $S_A = 36.15$ g kg^{-1}, intersects the 150 m isobath (Zenk, Klein, and Schroder, 1991) (Fig. 2.4). CVFZ is found in the southern transect in its westernmost position in fall, at stations 46-48. Hence, SACW with relatively low S_A is observed above the upper limit of CW east of the CVFZ location (Fig. 2.4). In spring, the CVFZ shifts to a position closer to the African coast at station 52, with a water incursion of higher-salinity NACW centered at station 58 (Figs. 2.4 and 2.5). At intermediate levels, MW is registered at the northern transect, while in the southern one the predominant water mass is AAIW. Regarding the seasonal variability, the contribution of MW in the northern transect is higher in spring, while the contribution of AAIW in the southern transect is higher in fall.

Although the INs have been extracted from the model and the distributions of Θ, S_A and γ_n have been obtained from the hydrographic observations, there is a good agreement between the structures described by both datasets. The in situ concentrations of SiO_2, NO_X and PO_4 up to 250 m depth (black dots in Fig. 2.6) are represented together with the time-averaged concentrations of SiO_2, NO_3 and PO_4 up to 2000 m of depth selected from GLORYS-BIO. In this way the IN outputs from the model are compared with in situ observations since their concentration in both cases presents an acceptable match, with the exception of NO_X and PO_4 concentrations at the S transect. On the other hand, the IN model outputs look like INs from historical in situ databases (not shown here).

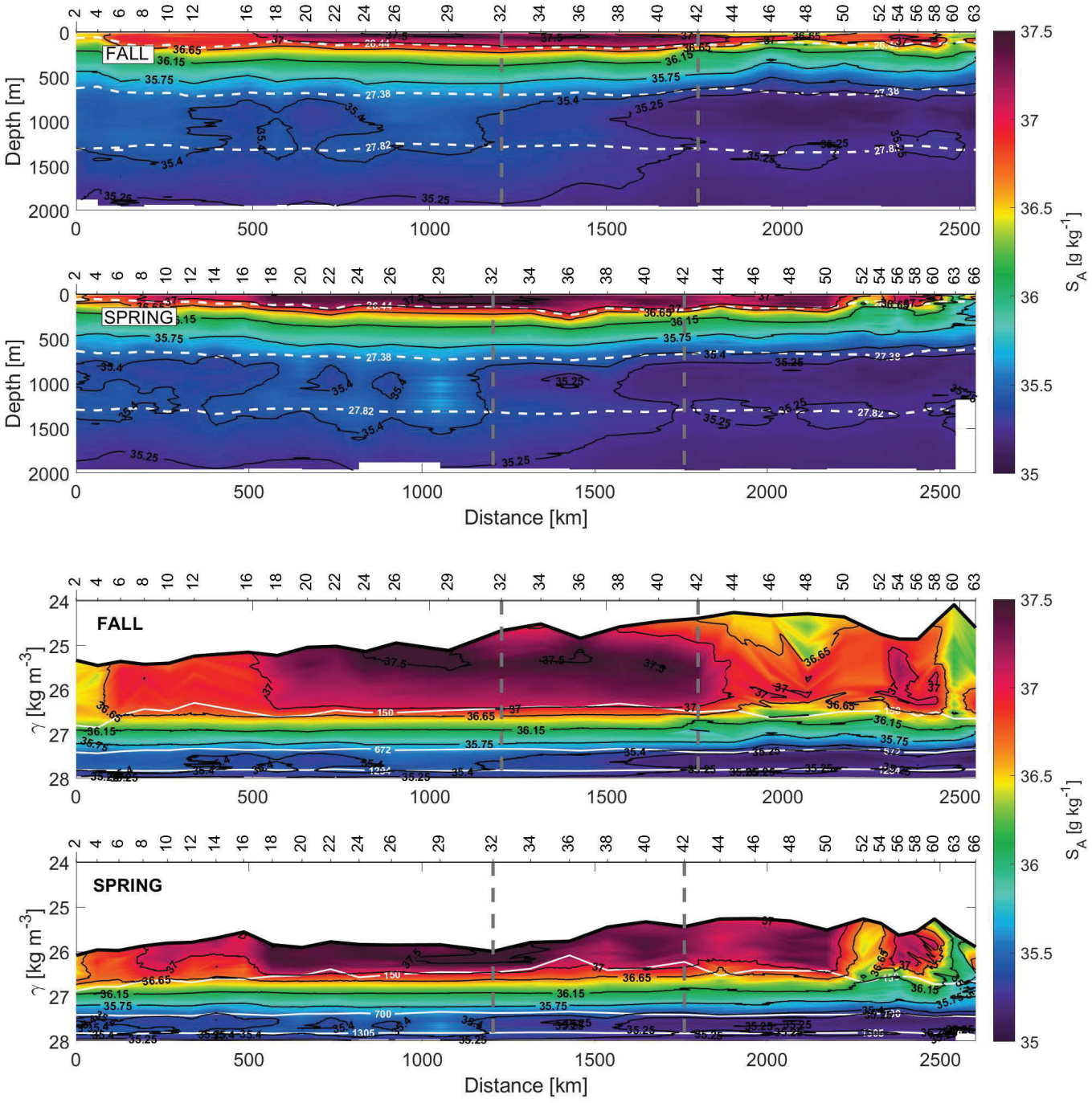

Figure 2.4: Sections of absolute salinity (S_A) with respect to depth (top) and γ_n (bottom) during fall and spring. In the depth section (top), the isoneutrals that delimit the transports at the surface, central, intermediate and deep water are represented by white dashed contours. In the γ_n section (bottom), the depths of 150, 672-700 and 1294-1305 m are also shown.

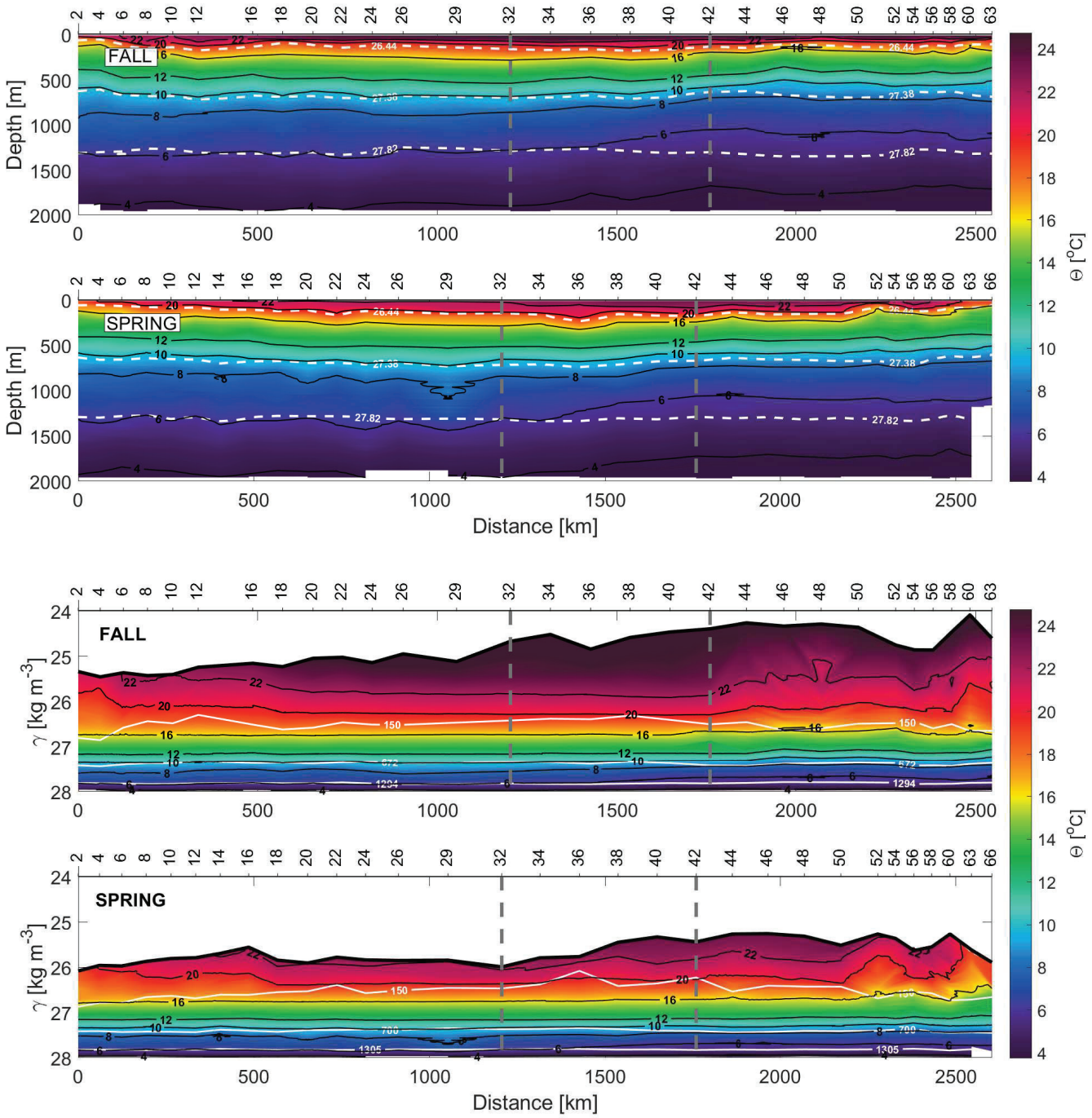

Figure 2.5: Sections of conservative temperature (Θ) with respect to depth (top) and γ_n (bottom) during fall and spring. In the depth section (top), the isoneutrals that delimit the transports at the surface, central, intermediate and deep water in the water column are represented by white dashed contours. In the γ_n section (bottom), the depths of 150, 672-700 and 1294-1305 m are indicated.

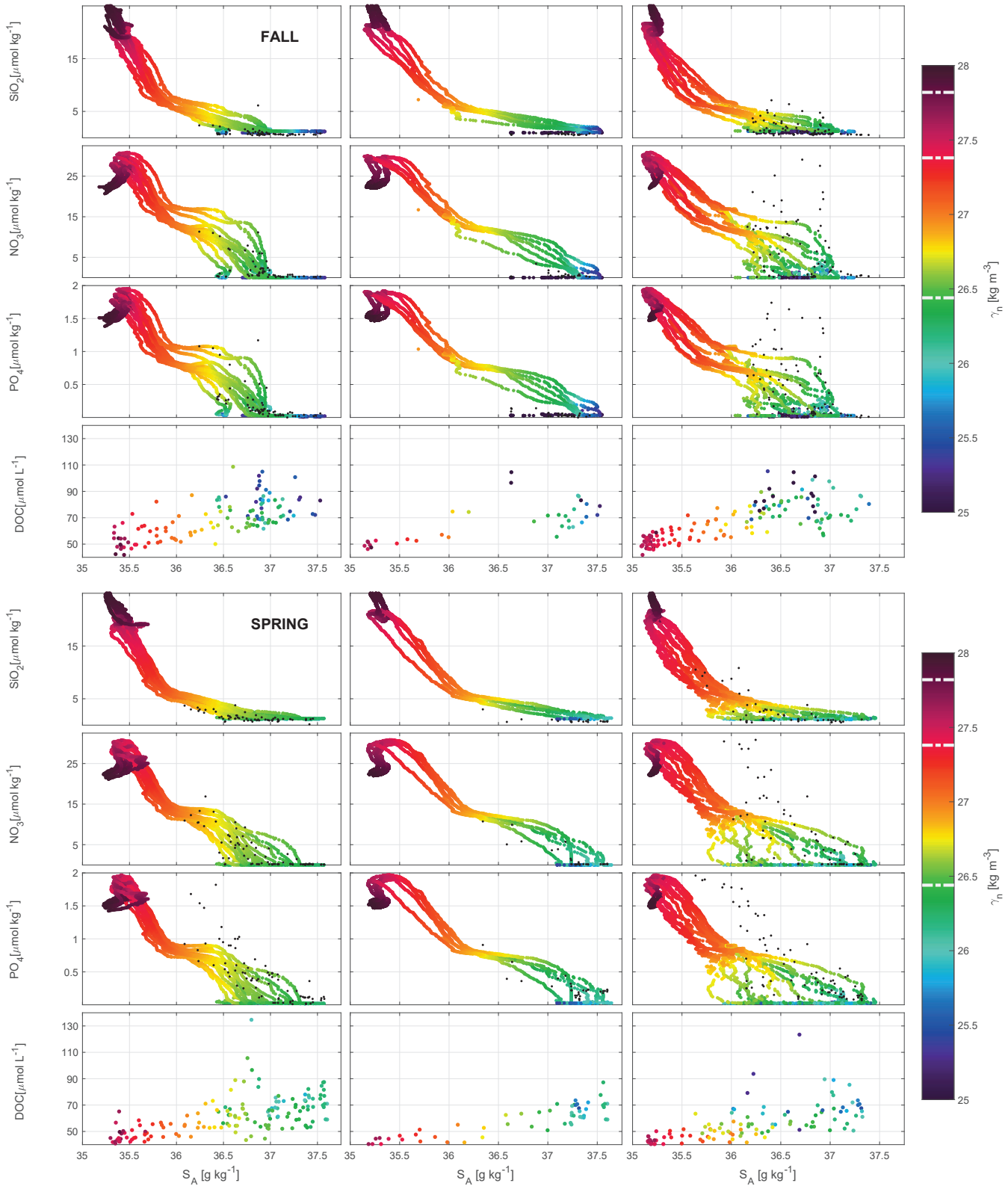

Figure 2.6: Scatter plots for SiO_2, NO_3 and PO_4 nutrients (μmol kg^{-1}; extracted from GLORYS-BIO), as well as for DOC (observational data in μmol L^{-1}) with respect to S_A and γ_n at the north (left), west (middle) and south transects (right) in fall (top) and spring (bottom). The isoneutrals 26.44, 27.38 and 27.82 kg m^{-3} that limit the waters layers are indicated with white dashed lines in the color bar. The measured IN concentrations (μmol kg^{-1}) for SiO_2, NO_X and PO_4 until 250 m of depth are included as black dots.

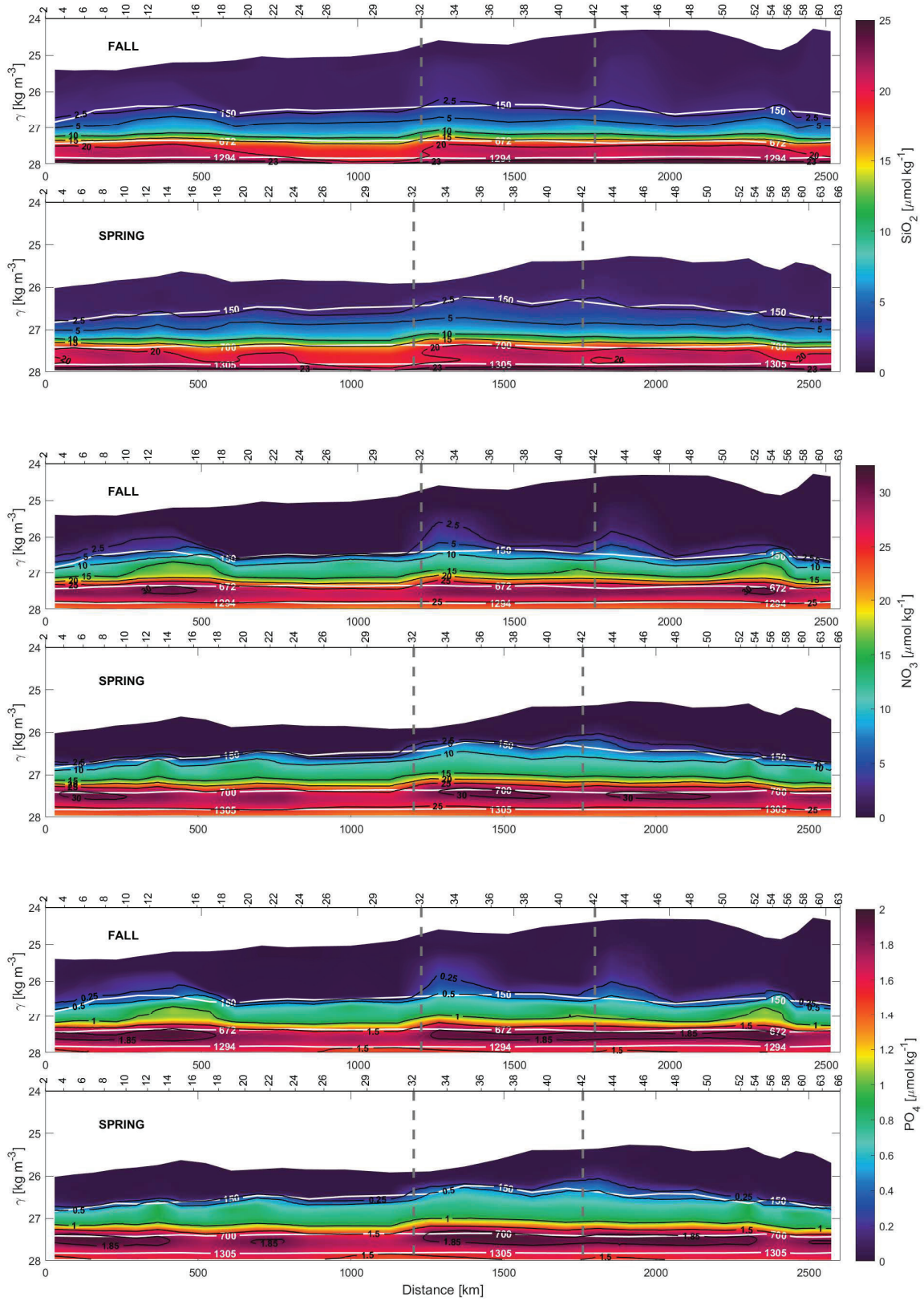

Figure 2.7: Sections for SiO_2 (top), NO_3 (middle) and PO_4 (bottom) concentrations with respect to γ_n during fall (top) and spring (bottom) extracted from GLORYS-BIO. The white isolines are as in the γ_n sections in Figs. 2.4 and 2.5.

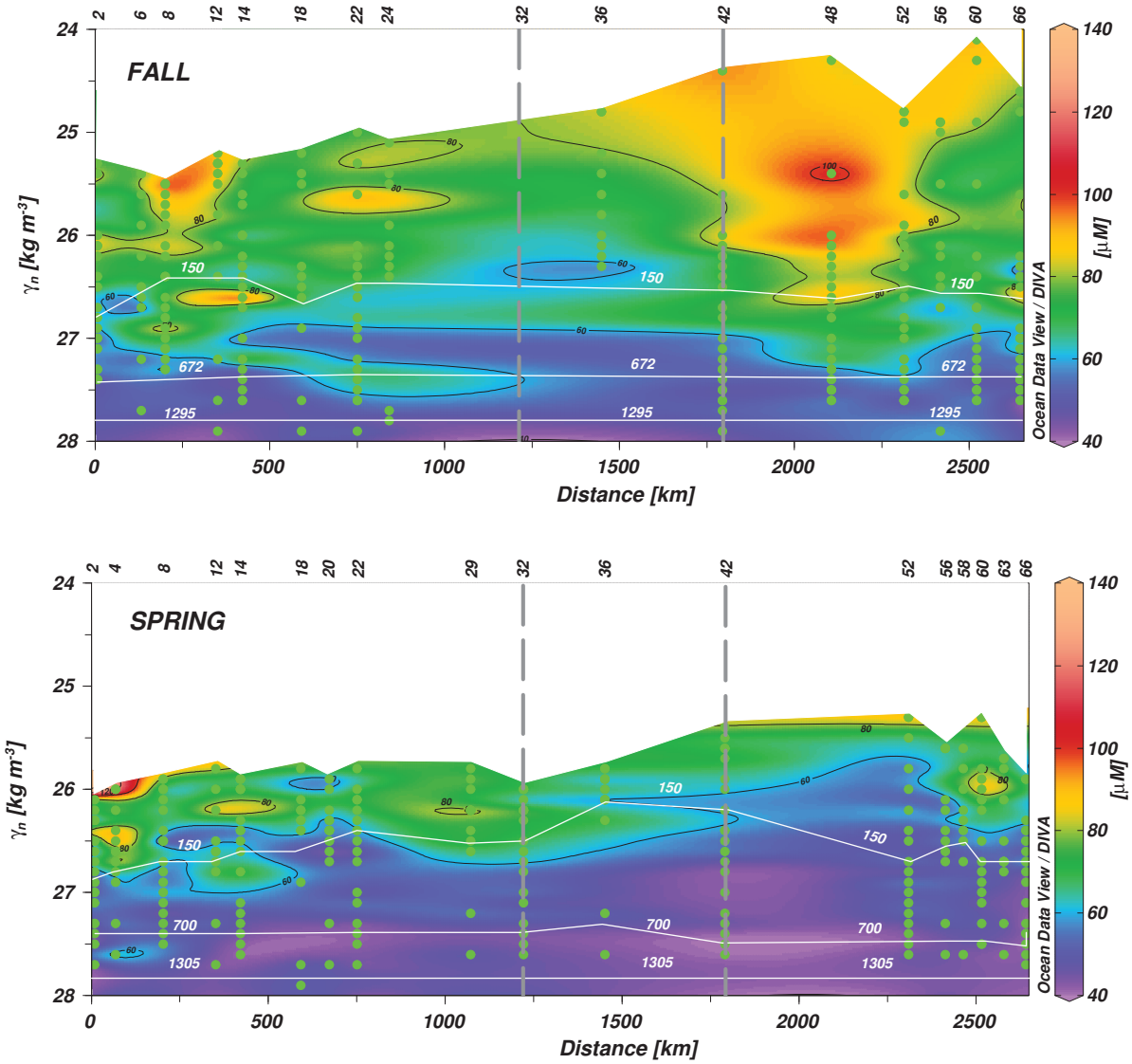

Figure 2.8: Sections of *DOC* concentration with respect to γ_n during the fall (top) and spring (bottom) cruises with the white isolines as in the γ_n sections in Figs. 2.4 and 2.5.

At central levels, high IN concentrations have been sampled near the continental slope in both the northern (stations 10 to 18) and southern (50 to 56) transects in fall. The values observed are 1-5 μmol kg^{-1} for NO_3 and 0.1-0.4 μmol kg^{-1} for PO_4, which are higher values than those recorded in spring at similar places (Fig. 2.7). This might be related to long-lived mesoscale eddies or instabilities related to the CVFZ (Zenk, Klein, and Schroder, 1991; Sangrà et al., 2009). IN concentrations are notably high at intermediate and deep levels compared to those at central levels (Fig. 2.6) and have the same order of magnitude as those documented before in the domain (Pérez et al., 2001; Pérez-Hernández et al., 2013). The distributions of SiO_2, NO_3 and PO_4 are similar during both cruises, and their concentrations increase with depth as a result of the remineralization of organic matter (Fig. 2.7). The area where the least nutrients are found at depth throughout the domain is the northwest corner of the box (stations 24 to 32). With respect to the IN seasonal variability at intermediate depths, the three concentrations do not present large differences between the values measured in fall and spring (Figs. 2.7 and 2.3). In both seasons the concentrations of SiO_2, NO_3 and PO_4 are 4-6, 2-6 and 0.2-0.4 μmol kg^{-1} higher in AAIW than in MW (Tab. 2.2). The NADW is characterized by a moderate increase in SiO_2 and a slight decrease in NO_3 and PO_4 with respect to the values documented here at intermediate levels. In both seasons, the maximum concentration of SiO_2 is 28-29 μmol kg^{-1}. Nevertheless, specifically in spring, the maximum concentrations of NO_3 and PO_4, 28 and 1.8-1.9 μmol kg^{-1}, are lower than those recorded at intermediate levels, providing a similar vertical variability as that reported by Machín, Hernández-Guerra, and Pelegrí (2006) (Tab. 2.2).

DOC concentrations are higher and more widely distributed in the water column in fall than in spring, when the *DOC* maximum values are more confined to surface and central waters (Figs. 2.8 and 2.6, Tab. 2.2). This fact is especially significant in the southern transect occupied by SACW (Fig. 2.6). SACW presents maximum concentrations of *DOC* 35-40 μmol L^{-1} lower than those found for NACW (Tab. 2.2). This difference is more pronounced in spring (Tab. 2.2). In addition, the fall *DOC* observations present a larger variability in central waters, as previously seen for INs. Lower *DOC* concentrations are observed for stations sampled in the western transect, while the highest concentrations are recorded in the stations next to the African slope with values above 100 μmol L^{-1} (Fig. 2.8). On the other hand, the high concentrations of *DOC* recorded at intermediate waters in the northern transect during both cruises are noteworthy (Figs. 2.8 and 2.6).

Table 2.2: Summary of water levels (CW, IW, and DW) with their isoneutral limits and their water masses properties for both seasons from the sea surface to 2000 m. The properties extracted from observations are in situ temperature (T), potential temperature (θ), conservative temperature (Θ), practical salinity (S_P), absolute salinity (S_A), and dissolved organic carbon (DOC). The INs extracted from GLORYS-BIO are silicates (SiO_2), nitrates (NO_3) and phosphates (PO_4).

WATER LEVELS		**CW**				**IW**				**DW**	
γ_n [kg m^{-3}]		**MIN.**		**MAX.**		**MIN.**		**MAX.**		**MIN.**	**MAX.**
		26.44		**27.38**		**27.38**		**27.82**		**27.82**	**27.962**
WATER MASSES		**NACW**		**SACW**		**MW**		**AAIW**		**NADW**	
PROPERTIES	**SEASON**	**MIN.**	**MAX.**	**MIN.**	**MAX.**	**MIN.**	**MAX.**	**MIN.**	**MAX.**	**MIN.**	**MAX.**
T [°C]	FALL	9.12	19.13	8.22	17.18	6.03	10.02	5.25	9.12	3.63	5.66
	SPRING	5.90	19.76	8.35	17.14	6.01	10.04	5.16	9.41	3.63	5.57
θ [°C]	FALL	9.04	19.11	8.14	17.16	5.90	9.94	5.13	9.05	3.46	5.53
	SPRING	5.77	19.74	8.27	17.13	5.88	9.96	5.06	9.34	3.47	5.45
Θ [°C]	FALL	9.03	19.05	8.13	17.12	5.89	9.92	5.12	9.03	3.46	5.53
	SPRING	5.77	19.67	8.26	17.09	5.88	9.94	5.05	9.32	3.47	5.44
S_P	FALL	35.23	36.83	35.04	36.19	35.13	35.44	34.92	35.24	34.99	35.13
	SPRING	33.85	37.06	35.07	36.16	34.55	35.53	34.96	35.30	34.99	35.12
S_A [g kg^{-1}]	FALL	35.40	37.00	35.21	36.36	35.30	35.61	35.09	35.40	35.16	35.30
	SPRING	34.02	37.23	35.24	36.33	34.72	35.70	35.13	35.47	35.16	35.30
SiO_2 [μmol kg^{-1}]	FALL	1.24	18.46	6.39	22.14	13.23	21.73	17.50	25.78	18.94	28.44
	SPRING	1.22	21.99	6.99	23.95	13.97	21.99	17.97	28.06	19.04	28.73
NO_3 [μmol kg^{-1}]	FALL	0.00	30.27	22.03	36.15	23.13	30.92	25.82	36.36	20.55	28.26
	SPRING	0.00	30.36	25.21	36.75	23.78	31.18	25.70	36.81	21.06	27.97
PO_4 [μmol kg^{-1}]	FALL	0.03	1.90	1.46	2.29	1.43	1.98	1.69	2.33	1.37	1.85
	SPRING	0.03	1.90	1.69	2.36	1.49	1.98	1.69	2.39	1.42	1.83
DOC [μM]	FALL	47.85	108.65	49.05	74.13	46.25	66.09	41.83	59.30	41.82	58.72
	SPRING	41.66	105.62	40.86	63.45	40.44	65.15	40.44	50.17	40.44	50.81

2.4 The inverse model

An inverse box model is applied to the hydrographic data from the two COCA cruises to provide the absolute velocity field across the three sections (Wunsch, 1978). This method has been widely applied in different areas of the Atlantic Ocean as an efficient method to obtain absolute geostrophic flows (Martel and Wunsch, 1993; Paillet and Mercier, 1997; Ganachaud, 2003b; Machín, Hernández-Guerra, and Pelegrí, 2006; Pérez-Hernández et al., 2013; Hernández-Guerra et al., 2017; Fu, Karstensen, and Brandt, 2018). Assuming geostrophy and the conservation of mass and other properties in the ocean bounded by the African coast and the hydrological sections, the velocity fields are obtained, allowing for an adjustment of freshwater flux and Ekman transports.

2.4.1 Selection of layers

The closed ocean where the inverse model is applied is divided into nine layers by means of the neutral densities defined by Macdonald (1998) and modified by Ganachaud (2003b) for the North Atlantic Ocean. This distribution is then slightly modified to include two layers instead of one between 26.85 and 27.162 kg m^{-3} by adding the isoneutral 27.035 kg m^{-3}, as others authors have done previously at this side of the NASG (Comas-Rodríguez et al., 2011; Pérez-Hernández et al., 2013). The locations of the isoneutrals are represented in Figure 2.2. The upper five layers group the surface and central waters, and the first layer until the isoneutral 26.44 kg m^{-3} is related to surface waters, while the four remaining layers between 26.44 kg m^{-3} and 27.38 kg m^{-3} are central waters. The intermediate waters are found in the next two layers between 27.38 and 27.82 kg m^{-3}, while the deepest two layers below 27.82 kg m^{-3} contain the upper deep waters.

2.4.2 The system of equations

The inverse box model takes into account mass conservation per layer and also in the whole water column. The salinity is actually introduced as a salinity anomaly, which is also conservative within individual layers and in the whole water column (Ganachaud, 2003a). On the other hand, heat is introduced as a heat anomaly in the two deepest layers wherein it is also considered conservative. The salinity and heat are added as anomalies to improve the conditioning of the inverse model and get a higher rank in the system of equations by reducing the linear dependency between equations (Ganachaud, 2003a).

Therefore, the model is composed of a set of 22 equations (10 for mass conservation, 10 for salt anomaly conservation and 2 for heat anomaly conservation). Those equations are solved for 32 and 34 unknowns, comprised of 28/30 reference level velocities in fall-spring, 3 unknowns for the Ekman transport adjustments (one unknown per section), and 1 unknown for the freshwater flux. The resulting system is undetermined and a Gauss-Markov estimator is used to select a solution by adding a priori information. This a priori information consists of the uncertainties for both the unknowns (R_{xx}) and the noise of the equations (R_{nn}).

Uncertainties of unknowns (R_{xx})

The geostrophic velocity field is calculated in the central position between two consecutive stations. The isoneutral selected as the reference level is the deepest common γ_n for all the stations, 27.962 kg m^{-3} (Fig. 2.2). Initially, the reference level is considered as a motionless level at which the geostrophic velocity is taken as null before applying the inversion. The variance of the velocity in the reference level at each location is used as a measure of the a priori information. These variances are calculated with an annual mean velocity extracted from the daily velocity provided by GLORYS. These velocities are interpolated to the reference-level depth. This reference-level depth is estimated from the climatological mean depth of 27.962 kg m^{-3} extracted from WOA13. The stations closer to the coast in the northern and southern transects have the highest variability in the velocity field. Machín, Hernández-Guerra, and Pelegrí (2006) provide a comprehensive sensitivity analysis of the solution with respect to the a priori information in a domain just north of the one documented here. They conclude that the final mass imbalance is quite independent of both the reference level considered and also of the a priori uncertainties in the reference-level velocities.

The initial Ekman transports are estimated from the wind stress for both cruises. The uncertainty associated with these Ekman transports is related to the error in their measurements and the variability of the wind stress. A 50% uncertainty is assigned to the initial estimate of Ekman transports. The initial freshwater flux is a climatological mean of 0.0171 Sv, which is also assigned an uncertainty of 50 % as reported in similar approaches (Ganachaud, 1999; Hernández-Guerra et al., 2005; Machín, Hernández-Guerra, and Pelegrí, 2006).

Both the Ekman transports and freshwater flux with their uncertainties are added to the model in the conservation equations corresponding to the shallowest layer of the mass transport and salt anomaly, as well as to the conservation equations of total mass transport and total salt anomaly.

Uncertainties in the noise of equations (R_{nn})

The noise of each equation depends on the density field, the layer thickness and the uncertainties of the unknowns (Ganachaud, 1999; Ganachaud, 2003a; Machín, Hernández-Guerra, and Pelegrí, 2006). In fact, Ganachaud (2003a) established that the largest source of uncertainty in conservation equations arises from the deviation of the baroclinic mass transport from their mean value at the time of the cruise. Thus, an analysis of the annual variability in the velocity field for the nine layers is performed. The velocity variability is examined in the mean depth between two successive isoneutral surfaces whose climatological mean depths are defined by WOA13. This variability is included in the inverse model as the a priori uncertainty or the noise of equations in terms of variances of mass, salt anomaly and heat anomaly transports. The velocity variance from the annual mean velocity for each layer is estimated with GLORYS and transformed into transport values by multiplying the density and the vertical area of the section involved. These a priori transport uncertainties are presented in Table 2.3. Furthermore, the uncertainty assigned to the conservation equation in the total mass is the sum of the uncertainties from the rest of the nine conservative mass equations.

Table 2.3: A priori noise of equations corresponding to the SW, CW, IW and DW levels at which the different water masses are transported.

WATER LEVELS	UNCERTAINTIES (Sv^2)
SW and CW	$(1.6 - 4.7)^2$
IW	$(6.3 - 9.3)^2$
DW	$(4.0 - 7.9)^2$

The equations for salt and heat anomaly conservation depend on both the uncertainty of the mass transport and the variance of these properties (Ganachaud, 1999). In these cases, the a priori noise of each equation will not depend strictly on the water mass but on the layer considered, as shown in the following equation (Ganachaud, 1999; Machín, 2003):

$$R_{nn}(Cq) = a * var(C_q) * R_{nn}(mass(q)) \tag{2.1}$$

where $R_{nn}(Cq)$ is the uncertainty in the anomaly equation of the property (salt or heat anomaly); $var(C_q)$ is the variance of this property; a is a weighting factor of 4 in the heat anomaly, 1000 in the salt anomaly and 10^6 in the total salt anomaly; and q is a given equation corresponding to a given layer.

As documented north of the Canary Islands, dianeutral velocities are of the order of 10^{-8} m s^{-1}, while dianeutral diffusion coefficients are of the order of 10^{-6} m^2s^{-1} (Machín, Hernández-Guerra, and Pelegrí, 2006). The model results are much less affected by these values than by the reference velocities: a mean dianeutral velocity of 10^8 m s^{-1} would contribute with only 0.01 Sv, a value much less than the lateral transports obtained from the inverse model. On the other hand, the inverse model provides information only from the box boundaries and cannot be used to infer any detailed spatial distribution of dianeutral fluxes within the box. Hence, mass transports between the layers due to dianeutral transfers are considered to be negligible compared to other sources of lateral transports and are not included in the inversion.

2.5 Results

2.5.1 Velocity fields and mass transports

Figure 2.9 shows the reference-level velocities obtained after the inversion. The variance of these velocities is also estimated by the model. The uncertainties are much higher than the values themselves and around ± (0.5-1) cm s^{-1}. During fall all nonzero values are positive, while in spring they are negative. This difference is important mainly in the western and southern transects where the module of the velocity increases, reaching values of 0.3 and -0.16 cm s^{-1} in fall and spring, respectively. Furthermore, the estimated reference level velocity values in the northern transect in spring are too small, $O(10^{-4} - 10^{-5})$, while they take positive and significant values between 0.13 and 0.25 cm s^{-1} in some locations of this transect in fall.

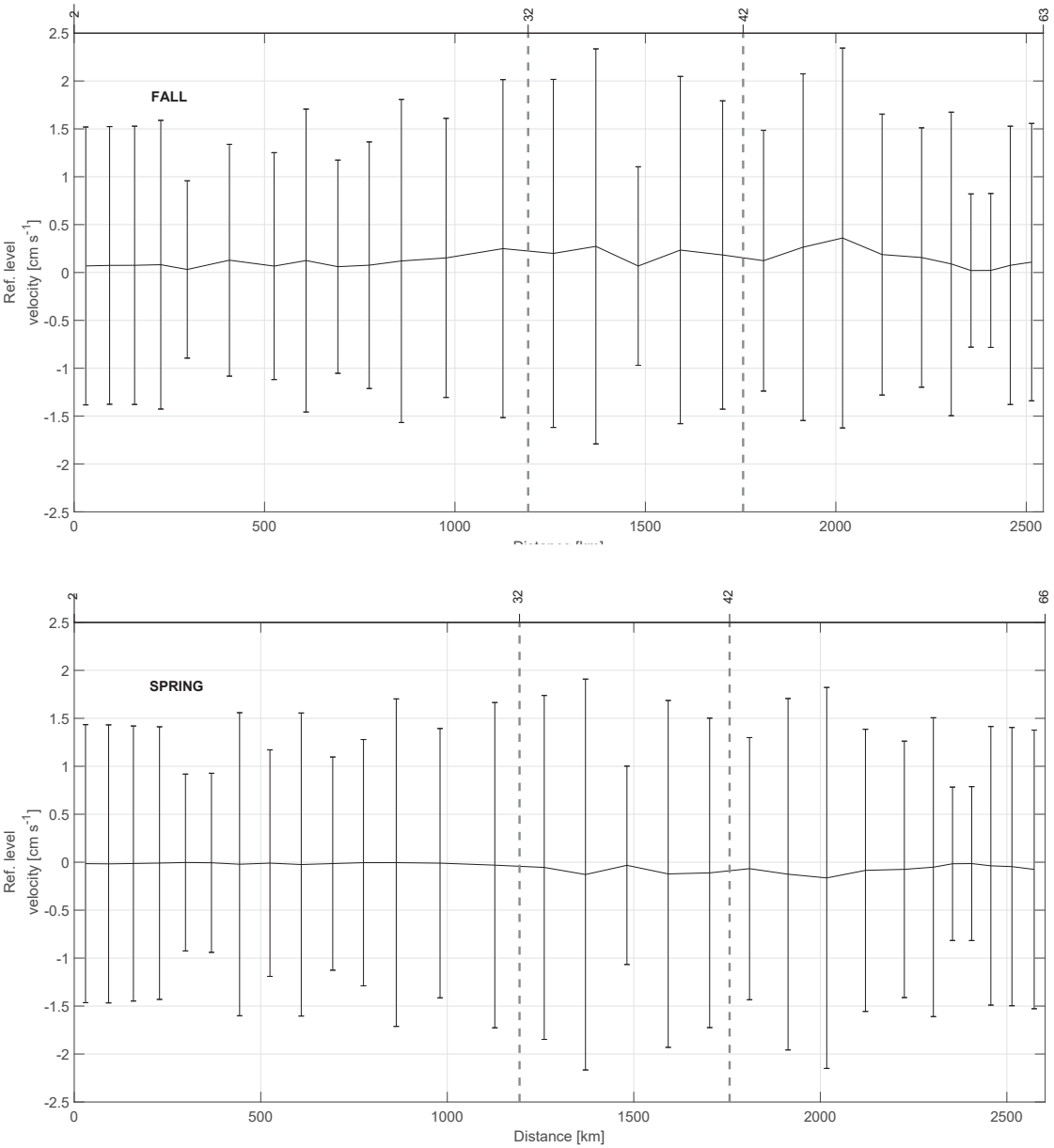

Figure 2.9: Reference-level velocity at 27.962 kg m^{-3} and its standard deviation estimated by the inverse model during fall (top) and spring (bottom). The direction chosen for the representation is the same as in Fig. 2.2. The signs of the velocity are according to the geographical criterion, i.e., the velocities are positive-negative toward north-south, in the northern and southern transects, and they are positive-negative toward east-west in the western transect.

Once the geostrophic velocities at the reference level are estimated, they are integrated into the entire water column to obtain the absolute geostrophic velocities (Fig. 2.10). These results are validated by comparison with the surface geostrophic velocity and the sea level anomaly, SLA, derived from altimetry during the time period that each cruise was performed (Fig. 2.11). To do this, the average fields of SLA and geostrophic velocity at the sea surface are calculated during each cruise and shown as a synoptic result during both surveys. Furthermore, the mass transports at the shallowest layer (red bars in Fig. 2.11) are superimposed with the aim of comparing these transports with the average velocity field from altimetry. Remarkable mesoscale activity can be identified in both the absolute geostrophic velocity sections (Fig. 2.10) and the temporal average of SLA and the geostrophic velocity (Fig. 2.11). In this last case, the position of the structures at the SLA field is somewhat displaced with respect to their positions in the in situ velocity sections. For instance, an anticyclonic eddy is located between stations 10 and 16 in the N transect in both seasons. This eddy, observed in autumn with high velocities at intermediate layers, weakens in spring. This mesoscale structure could be part of the CEC (Sangrà et al., 2009). Furthermore, it coincides with the position of an anticyclonic eddy previously documented (Barceló-Llull et al., 2017a; Barceló-Llull et al., 2017b; Estrada-Allis et al., 2019).

In fall, two eddies are linked in the S transect, an anticyclonic one between stations 48 and 52 and a cyclonic one between stations 52 and 60, both associated with the CVFZ. In spring, two anticyclonic eddies are observed, one centered at station 36 and the other one at station 56, also associated with CVFZ. In both seasons, mesoscale structures present a large vertical extension (Fig. 2.10). In fall, these structures have higher velocities at IW and DW levels and they also affect a higher extension along each transect. The SLA also shows a high-variability region with more intense structures in fall than in spring (Fig. 2.11).

Mesoscale structures are also visible in the vertical sections of NO_3 and PO_4 in fall, when their concentrations are higher than those observed in spring at similar locations (Fig. 2.7). Furthermore, high concentrations of DOC in fall at CW levels are recorded in the same area where the deep anticyclonic eddy is located, between stations 8 and 18 (Fig. 2.8). In spring, mesoscale structures in the vertical sections of INs and DOC at CW levels are less intense than in fall (Fig. 2.10). Nonetheless, DOC concentrations below the two anticyclonic structures at CW levels in spring are higher than in their surroundings.

The accumulated geostrophic mass transport is integrated to group the variability at different levels, with the first shallowest layer for SW, the next four layers for CW, then two layers for IW and the deepest two layers for DW (Fig. 2.12). The total accumulated geostrophic mass transport, integrated for all the nine layers, is also represented. The horizontal axis has the same direction as the rest of the vertical sections, and the three transects are separated by two vertical dashed grey lines. The Sverdrup (Sv) is used here as equivalent to 10^9 kg s^{-1}. The positive-negative transport values indicate outward-inward transports from-to the box. The accumulated mass transports show a significant horizontal spatial variability, especially marked in the southern transect in accordance with the geostrophic velocity distribution (Fig. 2.10). The presence of significant mesoscale structures might be one of the sources of the total imbalances in the accumulated mass transport. In fall,

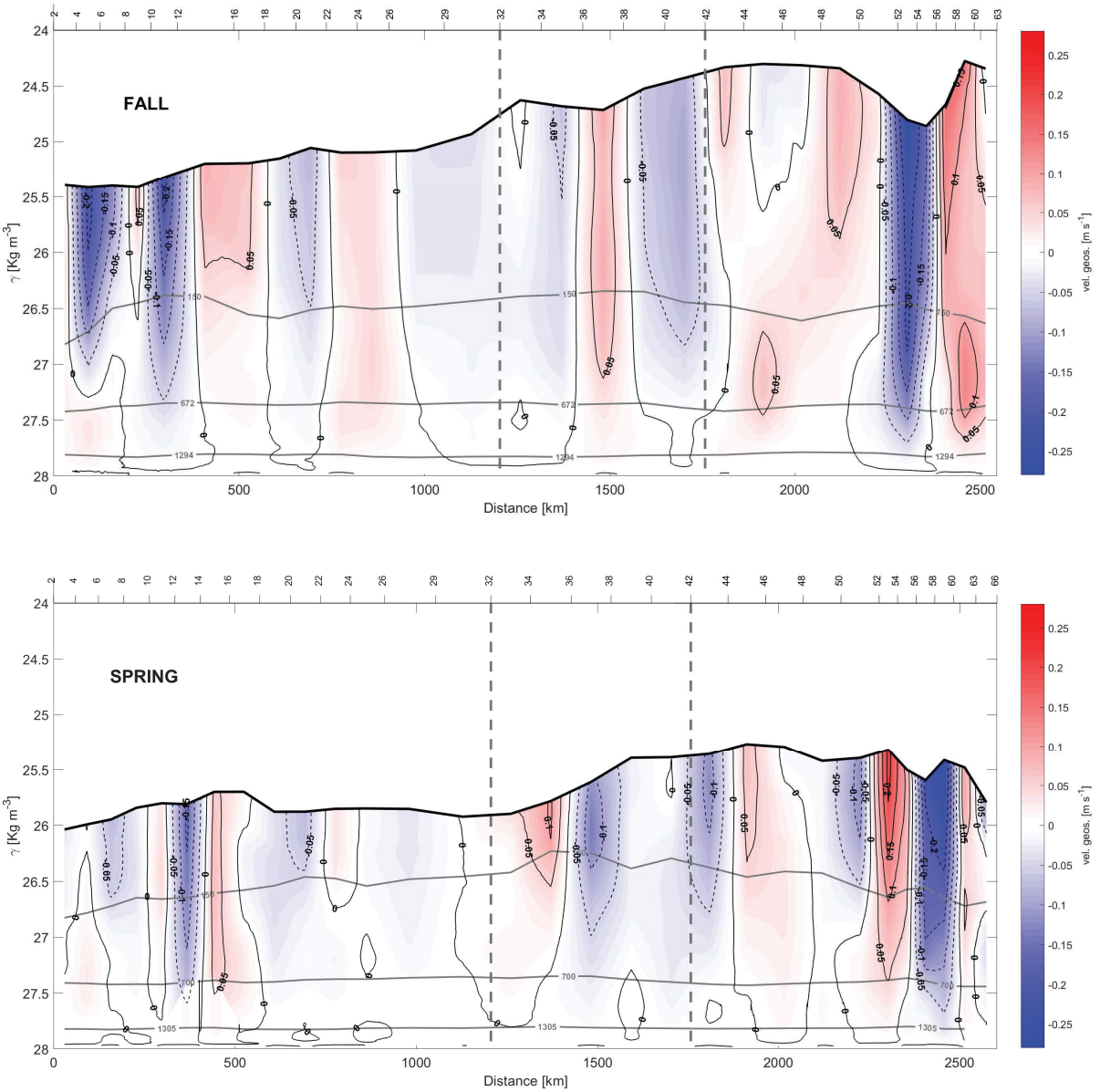

Figure 2.10: Sections of the absolute geostrophic velocity with respect to γ_n during fall (top) and spring (bottom). The horizontal axis has the same direction as Fig. 2.2 and the criterion of the velocity signs is as in Fig. 2.9. The depths 150, 672/700 and 1294/1305 m are highlighted by grey isolines as in the γ_n sections of Figs. 2.4 and 2.5.

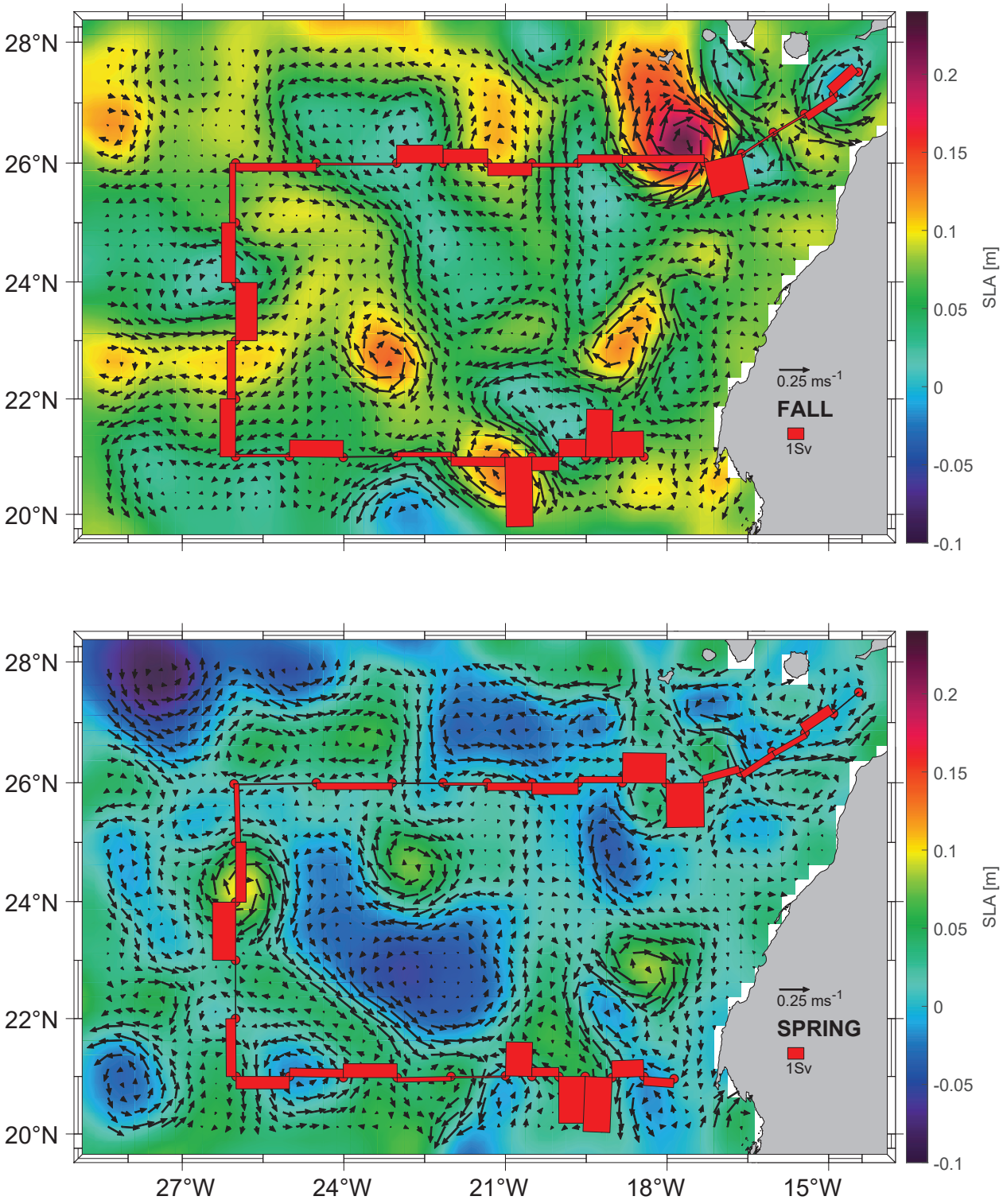

Figure 2.11: Average derived geostrophic velocity and SLA during fall (top) in the course of the fist cruise and spring (bottom) in the course of the second cruise, extracted from AVISO+. The red bars represent the mass transports in the shallowest layer as estimated by the inverse model.

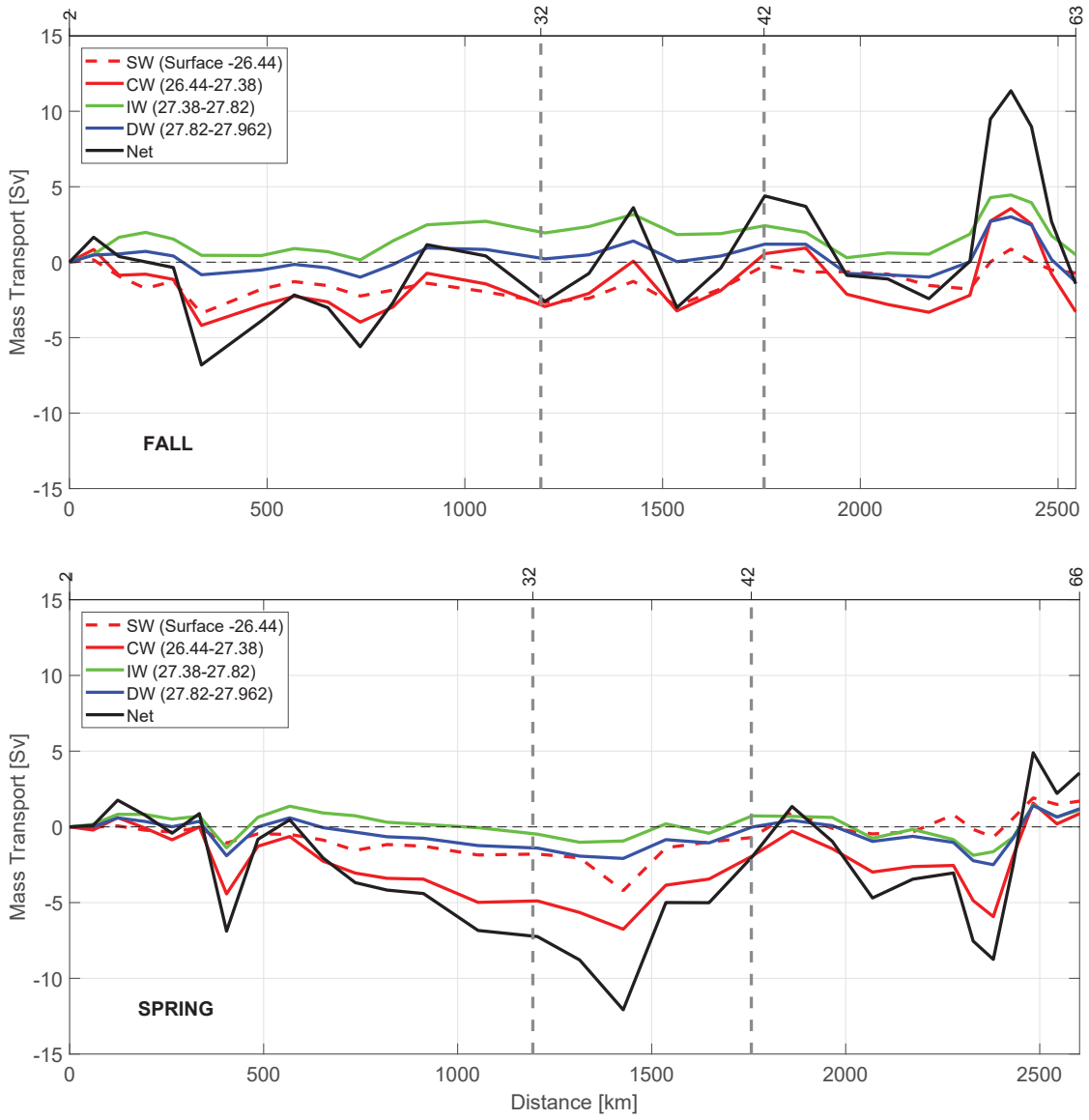

Figure 2.12: Accumulated mass transport along the fall (top) and spring (bottom) cruises at surface waters (SW, in red and dashed line), central waters (CW, in red line), intermediate waters (IW, in green line) and deep waters (DW, in blue line). The accumulated mass transport integrated for all the nine layers is also represented. The horizontal axis has the same direction as Fig. 2.2. Negative/positive values of transports along the three transects indicate inward/outward transports of box delimited by the three transects and the African coast.

the total imbalance is -1.43 Sv, and in spring it is 3.55 Sv (Tab. 2.4).

Table 2.4: Mass transports with their errors (Sv) for SW, CW, IW, and DW across the north, west, and south transects for both seasons. Positive-negative values indicate outward-inward transports. The last row is the integrated transport for the entire water column in each transect, while the fourth column summarizes the imbalances in mass transport for both seasons.

WATER LEVELS	SEASON	NORTH	WEST	SOUTH	IMBALANCE
SW	**Fall**	-2.67 ± 0.60	2.46 ± 0.66	-0.50 ± 0.45	-0.71 ± 1.00
	Spring	-1.80 ± 0.49	1.09 ± 0.69	2.40 ± 0.53	1.70 ± 0.99
CW	**Fall**	-2.94 ± 1.26	3.50 ± 1.09	-3.85 ± 1.03	-3.29 ± 1.95
	Spring	-4.89 ± 1.14	2.96 ± 1.06	2.80 ± 1.02	0.87 ± 1.86
IW	**Fall**	1.94 ± 1.85	0.48 ± 1.71	-1.93 ± 1.69	0.49 ± 3.03
	Spring	-0.48 ± 1.65	1.21 ± 1.68	0.39 ± 1.73	1.1 ± 2.92
DW	**Fall**	0.73 ± 1.71	0.32 ± 1.56	0.19 ± 1.37	1.24 ± 2.69
	Spring	-0.04 ± 1.54	0.09 ± 1.53	0.00 ± 1.42	0.05 ± 2.59
TOTAL	**Fall**	-2.59 ± 2.88	6.99 ± 2.64	-5.82 ± 2.45	-1.43 ± 4.61
	Spring	-7.24 ± 2.57	5.27 ± 2.60	5.53 ± 2.52	3.55 ± 4.44

On the other hand, the geostrophic mass transport can be integrated per layer and transect together with the total imbalance inside the box and the total mass transport uncertainty per layer (the black line and horizontal black bars in Fig. 2.13). Table 2.4 compiles these transports integrated for the different water levels, which are also represented geographically in Figure 2.14. More than 65% of the mass transport is given at SW and CW levels (Tab. 2.4). In fall, these water masses mostly move into the box across the northern and southern transects, with transports of -5.61 ± 1.86 Sv and -4.35 ± 1.48 Sv, respectively; the mass leaves the box by flowing westward with a value of 5.96 ± 1.75 Sv. In spring, water masses also move into the box mostly through the northern transect with -6.69 ± 1.63 Sv, but they leave along the western and southern transects with transports of 4.05 ± 1.75 Sv and 5.20 ± 1.55 Sv, respectively. It is remarkable how the inward transport in fall across the southern transect is reversed to a net outward flow in spring at the southern transect (Fig. 2.13).

The position of CVFZ in both seasons could partly explain the seasonal variability in the mass transports at central levels (Fig. 2.15). In fall, the CVFZ is located further from the African coast, so SACW is present at almost all stations of the south transect. This location of the CVFZ prevents a latitudinal mass transport from north to south. However, in spring the CVFZ is closer to the African slope, allowing for an important mass transport from north to south.

Between 5 and 30% of the mass transport is given in intermediate levels (Tab. 2.4). In fall, the intermediate water transport is directed northward in the southern transect with -1.93 ± 1.69 Sv, and it leaves the box with 1.94 ± 1.85 Sv and 0.48 ± 1.71 Sv across the northern and western transects, respectively. During spring, this transport weakens and changes its direction in the northern and southern transects with transports of -0.48 ± 1.65 Sv and 0.39 ± 1.73 Sv, respectively, increasing its westward transport to 1.21 ± 1.68 Sv.

The mass transport in deep water layers barely exceeds 3% (Tab. 2.4). An exception is the 8% given in the northern transect during fall where the estimated

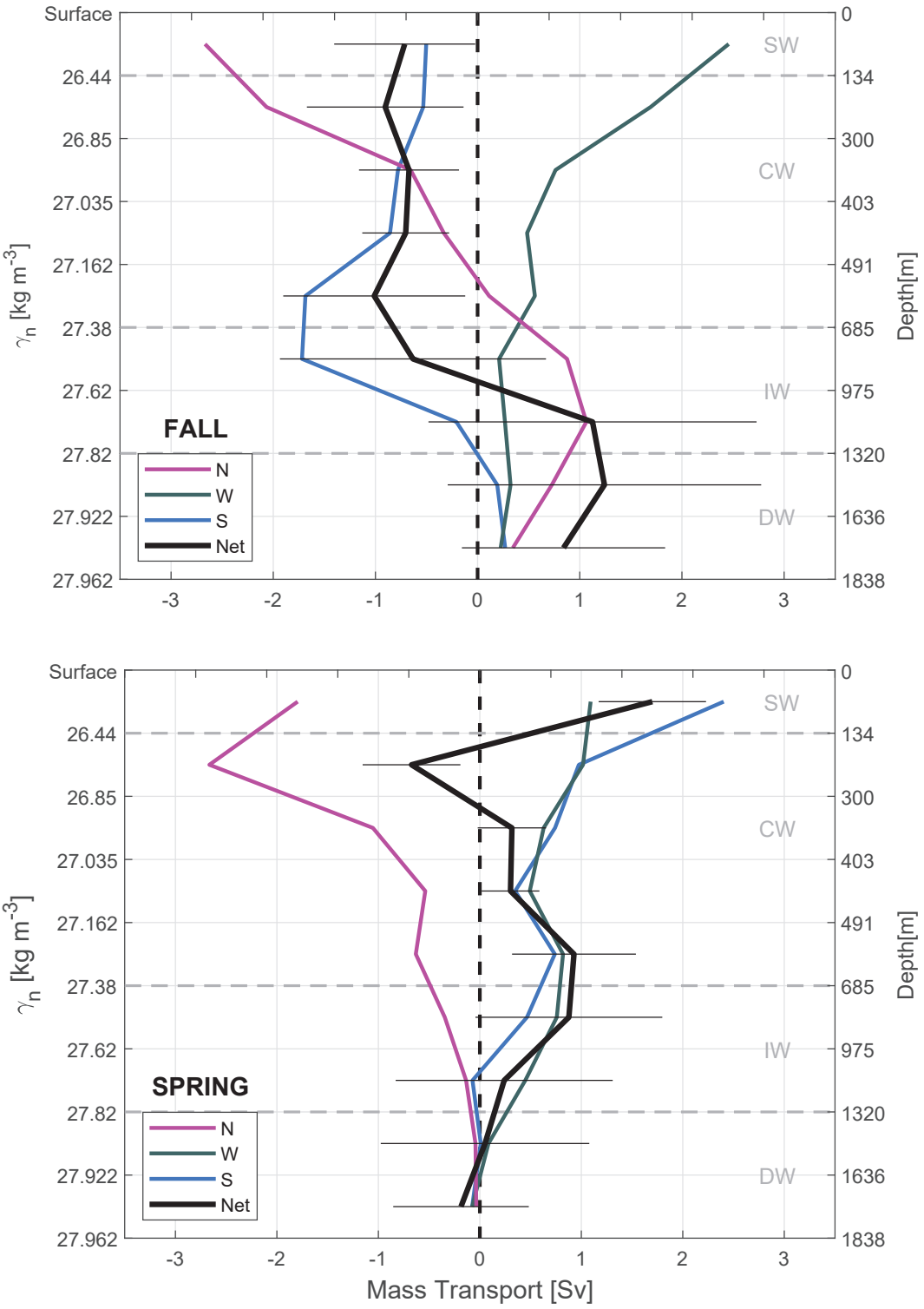

Figure 2.13: Accumulated mass transports per transect at the north (N, magenta line), west (W, dark grey line) and south (S, blue line) transects during fall (top) and spring (bottom). See Tab. 2.2 for the γ_n values bounding every water layer. Negative-positive values indicate inward-outward transports as in Fig. 2.12. Mass conservation in the whole domain is shown by the black line. The horizontal bars represent the uncertainties estimated by the model.

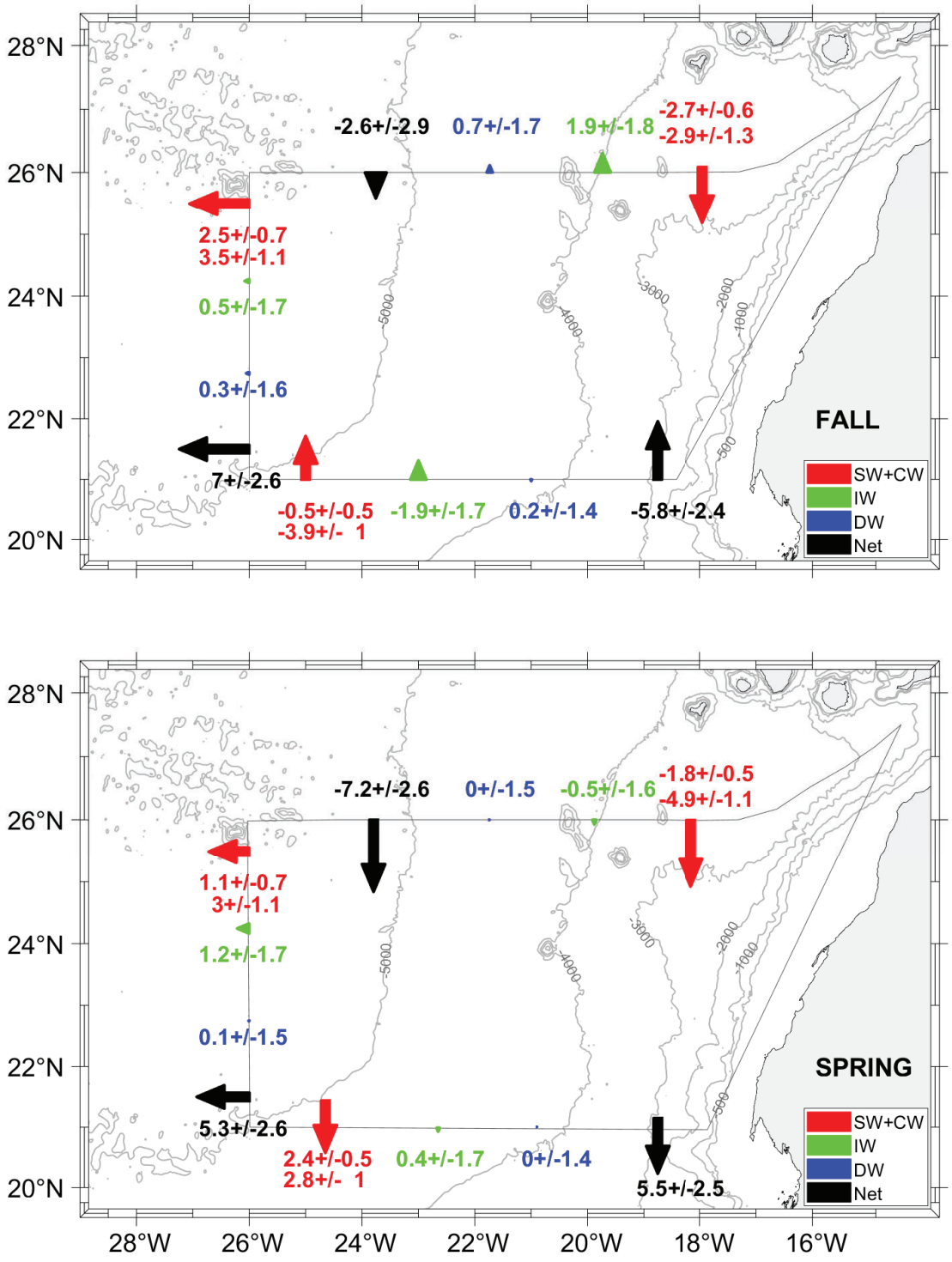

Figure 2.14: Mass transports with their errors (Sv) at the surface and central waters (SW+CW, red arrow), intermediate waters (IW, green arrow) and deep waters (DW, blue arrow) across every transect during fall (top) and spring (bottom). Negative-positive values indicate inward-outward transports as in Fig. 2.12. The arrows in each transect are located at positions that optimize their visibility, representing the integrated transports along each transect. The values of transports at SW (dark red) are given next to the integrated values of transports at CW levels (in red).

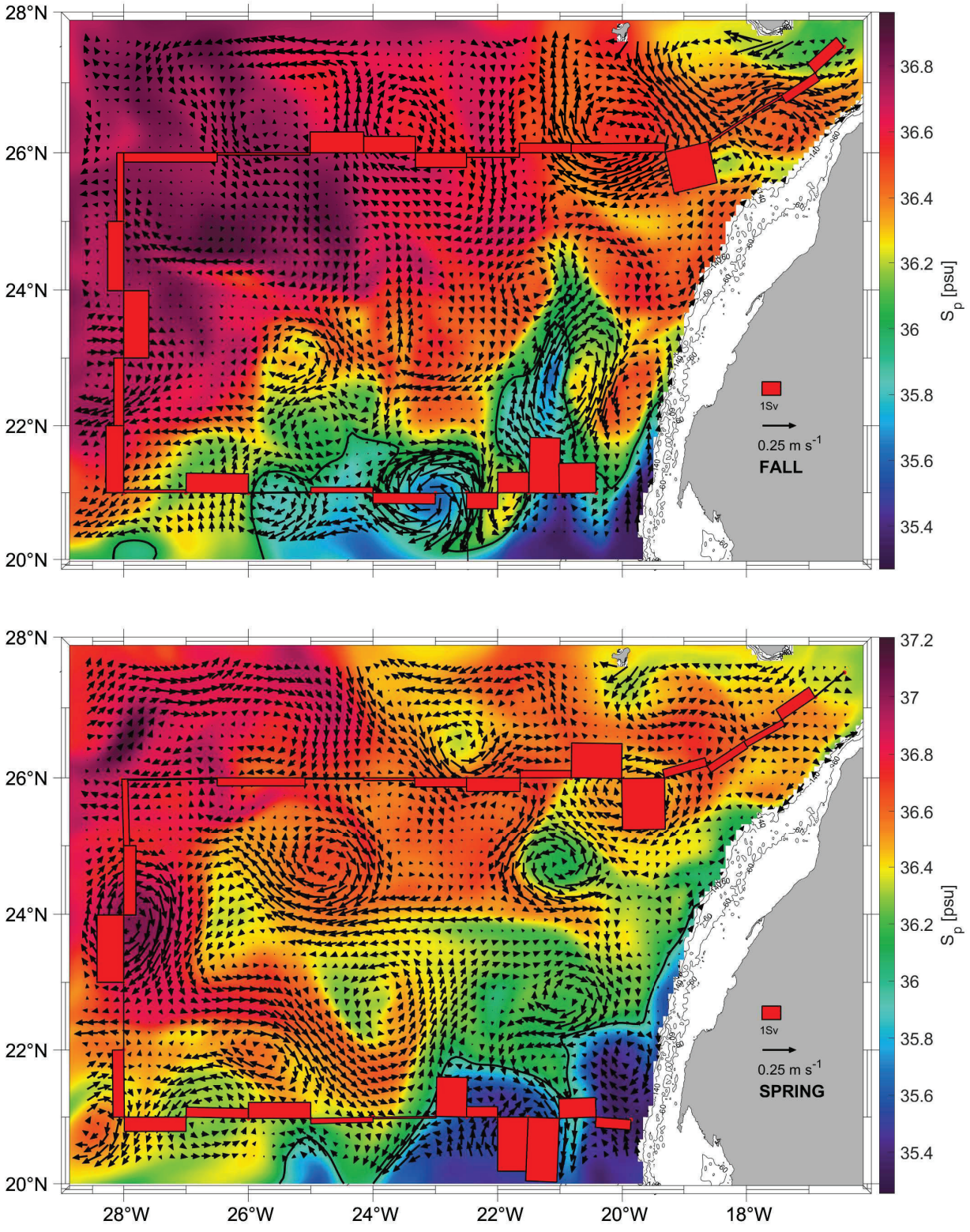

Figure 2.15: Mean salinity and mean geostrophic velocity at 156 m extracted from GLORYS during fall (top) and spring (bottom). The black line indicates the position of the isohaline of 36 at this depth, used to identify the CVFZ. The red bars represent mass transports in the shallowest layer as estimated by the inverse model.

transport is 0.73 ± 1.71 Sv. During both cruises the transport at deep levels was nearly balanced.

2.5.2 Nutrient and *DOC* transports

DOC and IN transports are obtained by multiplying their concentration by mass transports. *DOC*, INs and geostrophic velocities are obtained at different locations, so they need to be interpolated to a common grid. In the case of *DOC*, the velocities are horizontally interpolated to the locations where the concentrations of *DOC* are taken, and, in a second step, the concentrations of *DOC* are linearly interpolated to the depths of the geostrophic velocities. On the other hand, the in situ measurements of INs are scarce at IW and DW where their concentrations become higher. Therefore, instead of using the observational data, the average outputs of GLORYS-BIO are used to estimate the IN transports. SiO_2, NO_3, and PO_4 mean concentrations are interpolated to the grid nodes for which the geostrophic velocities are estimated by the inverse model.

DOC transports are obtained by subtracting a refractory concentration of 40 μmol L^{-1} from the measured *DOC* (e.g., Santana-Falcón et al., 2017). This is done because the refractory fraction renewal is thousands of years, a period much longer than the time required in the processes we are focused on (Hansell, 2002). On the other hand, it should be emphasized that *DOC* transports may be underestimated due to the scarcity of available measurements.

The IN transport values are presented in the text always ordered as SiO_2, NO_3 and PO_4 (Figs. 2.16 and 2.17). Tables 2.5, 2.6 and 2.7 summarize those transports integrated per water level and transect. The errors are relative to the mass transport errors and are calculated as the standard deviations of IN transports. The *DOC* transport estimates per layer and transect are also shown in Figure 2.17 and summarized per water level and transect with their relative error (calculated as in the IN transports) in Table 2.8. In order to be able to compare our transport values of INs and *DOC* with those reported by other authors, equivalent units are employed for IN (kmol s^{-1}) and *DOC* transports ($\times 10^8$ molC day^{-1}).

INs enter the domain both from north and south at CW in fall. At the northern transect the transports are relatively low, while at the southern one transports double the amount coming from north, with -0.41 ± 0.11, -0.78 ± 0.21 and -0.05 ± 0.01 kmol s^{-1}. In spring, instead, the IN transports change their direction in the southern transect and only enter from the north, with values double those during fall, -0.40 ± 0.09, -0.90 ± 0.21, -0.06 ± 0.01 kmol s^{-1}. On the other hand, IN transports at CW layers are overall westward with low values in fall, while in spring IN transports are southward and westward.

At IW levels, during fall the IN transports are inward through the southern transect, with -0.27 ± 0.24, -0.36 ± 0.32, and -0.02 ± 0.02 kmol s^{-1}, and to a lesser extent through the western transect. Outward transports are observed through the northern transect with 0.23 ± 0.22, 0.30 ± 0.28 and 0.02 ± 0.02 kmol s^{-1}. In spring, the INs enter weakly through the northern transect and leave the box, crossing the western and southern transects with significant values of 0.19 ± 0.27 and 0.12 ± 0.55 kmol s^{-1} for SiO_2; 0.25 ± 0.35 and 0.17 ± 0.75 kmol s^{-1} for NO_3; and 0.02 ± 0.02 and 0.01 ± 0.05 kmol s^{-1} for PO_4. In summary, while in fall the main IN transports are in the south to north direction, in spring they are mainly

Table 2.5: SiO_2 transports and their errors (kmol s^{-1}) for CW, IW, and DW for the north, west and south transects. Positive-negative values indicate outward-inward transports. The last row is the integrated transport in the entire water column in each transect, and the last column represents the net transport for this variable inside the box.

WATER LEVELS	SEASON	NORTH	WEST	SOUTH	IMBALANCE
SW	**Fall**	-0.06 ± 0.01	0.06 ± 0.02	0.02 ± 0.02	0.02 ± 0.02
	Spring	-0.06 ± 0.02	0.04 ± 0.02	0.06 ± 0.01	0.04 ± 0.02
CW	**Fall**	-0.14 ± 0.06	0.21 ± 0.06	-0.41 ± 0.11	-0.34 ± 0.20
	Spring	-0.40 ± 0.09	0.45 ± 0.16	0.23 ± 0.08	0.28 ± 0.61
IW	**Fall**	0.23 ± 0.22	-0.13 ± 0.45	-0.27 ± 0.24	-0.17 ± 1.07
	Spring	-0.04 ± 0.15	0.19 ± 0.27	0.12 ± 0.55	0.28 ± 0.72
DW	**Fall**	0.13 ± 0.31	-0.11 ± 0.52	-0.14 ± 1.00	-0.12 ± 0.25
	Spring	-0.01 ± 0.51	0.06 ± 1.15	0.08 ± 13.38	0.13 ± 6.79
TOTAL	**Fall**	0.16 ± 0.17	0.03 ± 0.01	-0.80 ± 0.34	-0.61 ± 1.97
	Spring	-0.51 ± 0.18	0.75 ± 0.37	0.49 ± 0.22	0.73 ± 0.91

Table 2.6: NO_3 transports and their errors (kmol s^{-1}) for CW, IW, and DW for the north, west and south transects. Positive-negative values indicate outward-inward transports. The last row is the integrated transport in the entire water column in each transect, and the last column represents the net transport of this variable inside the box.

WATER LEVELS	SEASON	NORTH	WEST	SOUTH	IMBALANCE
SW	**Fall**	-0.05 ± 0.01	0.13 ± 0.04	0.17 ± 0.15	0.25 ± 0.35
	Spring	-0.03 ± 0.01	0.12 ± 0.07	0.07 ± 0.02	0.16 ± 0.09
CW	**Fall**	-0.36 ± 0.15	0.47 ± 0.15	-0.78 ± 0.21	-0.67 ± 0.40
	Spring	-0.90 ± 0.21	0.91 ± 0.33	0.56 ± 0.20	0.57 ± 1.22
IW	**Fall**	0.30 ± 0.28	-0.16 ± 0.57	-0.36 ± 0.32	-0.23 ± 1.39
	Spring	-0.06 ± 0.20	0.25 ± 0.35	0.17 ± 0.75	0.36 ± 0.94
DW	**Fall**	0.13 ± 0.30	-0.10 ± 0.48	-0.13 ± 0.91	-0.10 ± 0.21
	Spring	-0.01 ± 0.52	0.06 ± 1.05	0.08 ± 12.63	0.12 ± 6.26
TOTAL	**Fall**	0.02 ± 0.02	0.35 ± 0.13	-1.11 ± 0.47	-0.74 ± 2.40
	Spring	-1.01 ± 0.36	1.34 ± 0.66	0.88 ± 0.40	1.21 ± 1.51

Table 2.7: PO_4 transports and their errors (kmol s^{-1}) for CW, IW, and DW for the north, west and south transects. Positive-negative values indicate outward-inward transports. The last row is the integrated transport in the entire water column in each transect, and the last column represents the net transport of this variable inside the box.

WATER LEVELS	SEASON	NORTH	WEST	SOUTH	IMBALANCE
SW	**Fall**	-0.00 ± 0.00	0.01 ± 0.00	0.01 ± 0.01	0.02 ± 0.02
	Spring	-0.00 ± 0.00	0.01 ± 0.01	0.01 ± 0.00	0.01 ± 0.01
CW	**Fall**	-0.02 ± 0.01	0.03 ± 0.01	-0.05 ± 0.01	-0.04 ± 0.02
	Spring	-0.06 ± 0.01	0.06 ± 0.02	0.04 ± 0.01	0.04 ± 0.08
IW	**Fall**	0.02 ± 0.02	-0.01 ± 0.04	-0.02 ± 0.02	-0.01 ± 0.09
	Spring	-0.00 ± 0.01	0.02 ± 0.02	0.01 ± 0.05	0.02 ± 0.06
DW	**Fall**	0.01 ± 0.02	-0.01 ± 0.03	-0.01 ± 0.06	-0.01 ± 0.01
	Spring	-0.00 ± 0.04	0.00 ± 0.07	0.01 ± 0.85	0.01 ± 0.42
TOTAL	**Fall**	0.00 ± 0.00	0.02 ± 0.01	-0.07 ± 0.03	-0.05 ± 0.15
	Spring	-0.06 ± 0.02	0.08 ± 0.04	0.06 ± 0.03	0.08 ± 0.10

southwestward like the mass transport behaviour at these levels during this season (Tab. 2.4).

Finally, at DW during both seasons, the net transports of the three nutrients are similar to those at IW but with smaller values due to the low velocities at these depths, despite their high nutrient concentrations (Figs. 2.16 and 2.17). Furthermore, the relative error in these layers is always larger than the IN transport values.

In spring, *DOC* transports at SW and CW levels are the same order of magnitude and 1 order of magnitude higher than those at IW levels. In turn, these transports at IW levels are 1 order of magnitude higher than those at DW levels during this season. In contrast, during fall at the northern transect *DOC* transports have the same magnitude in SW, CW and IW, and they are 1 order of magnitude smaller than those at CW levels during spring (Tab. 2.8). In this season, *DOC* transports at SW and CW in the western transect have unrealistically small values likely related to the low number of measurements made in this transect during fall. *DOC* transports through the northern transect could also be somewhat underestimated for the same reason. However, at the southern transect during fall, the result is of the same order of magnitude as in spring.

In spring, *DOC* transports behave in a similar way in the entire water column. At SW and CW levels, $-2.33 \pm 0.57 \times 10^8$ molC day^{-1} enters through the northern transect, $0.89 \pm 0.25 \times 10^8$ molC day^{-1} of which leaves the box through the southern transect, approximately half of it through the western transect. During fall, there is an important outward *DOC* transport at SW, CW and IW levels, specially southward through the southern transect at SW and CW levels, with a total of $1.48 \pm 0.66 \times 10^8$ molC day^{-1} (Tab. 2.8).

Two opposite trends can be observed when both cruises are compared. In fall the IN net transports are -0.34 ± 0.20, -0.67 ± 0.40 and -0.04 ± 0.02 kmol s^{-1} at CW levels; -0.17 ± 1.07, -0.23 ± 1.39 and -0.01 ± 0.09 kmol s^{-1} at IW levels, and -0.12 ± 0.25, -0.10 ± 0.21 and -0.01 ± 0.01 kmol s^{-1} at DW levels. The amount of nutrients entering the box is larger than those leaving the box, with

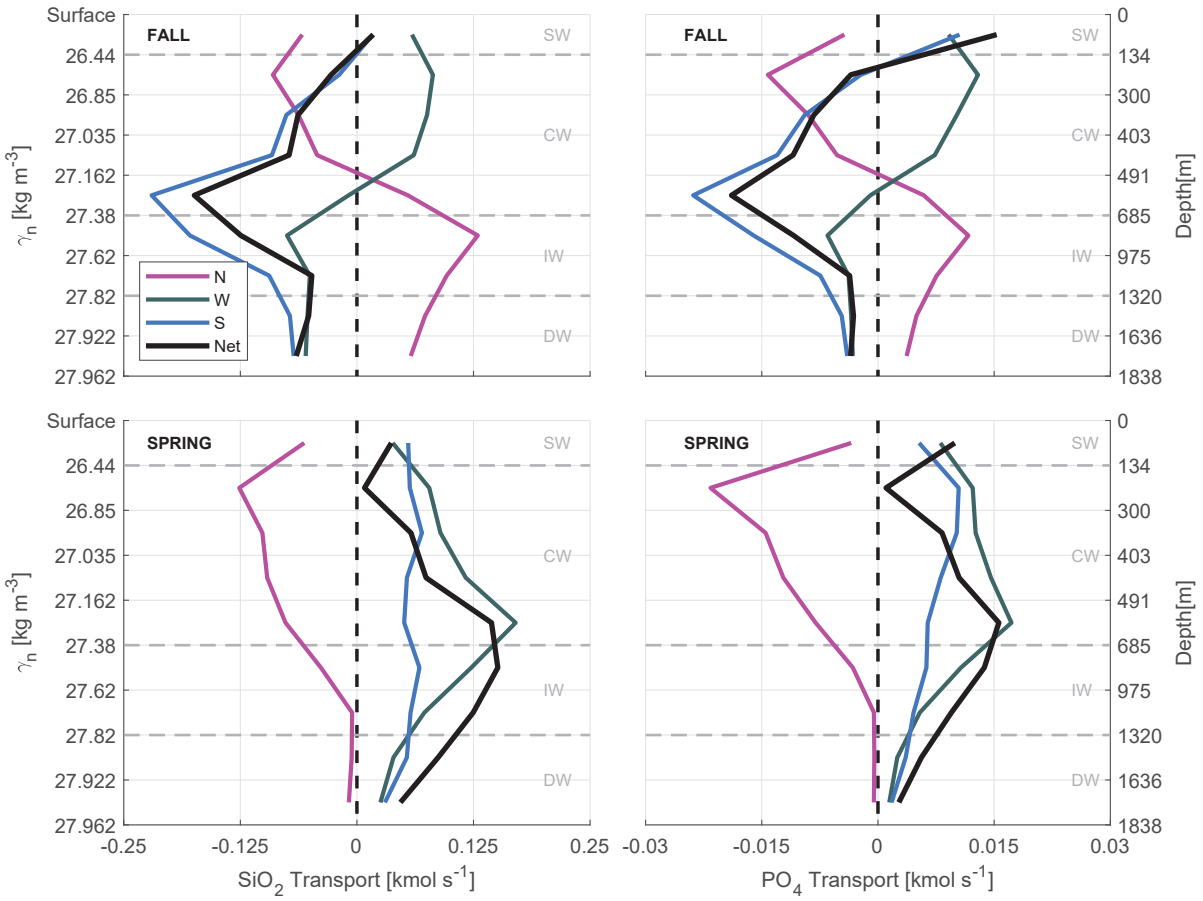

Figure 2.16: Accumulated SiO_2 and PO_4 transports (kmol s^{-1}) at transects in the north (N, magenta line), west (W, dark grey line) and south (S, blue line) during fall (top) and spring (bottom). See Tab. 2.2 for the γ_n values bounding every water layer. Negative-positive values indicate inward-outward transports as in Fig. 2.12. The net transport in the whole box is shown by the black line.

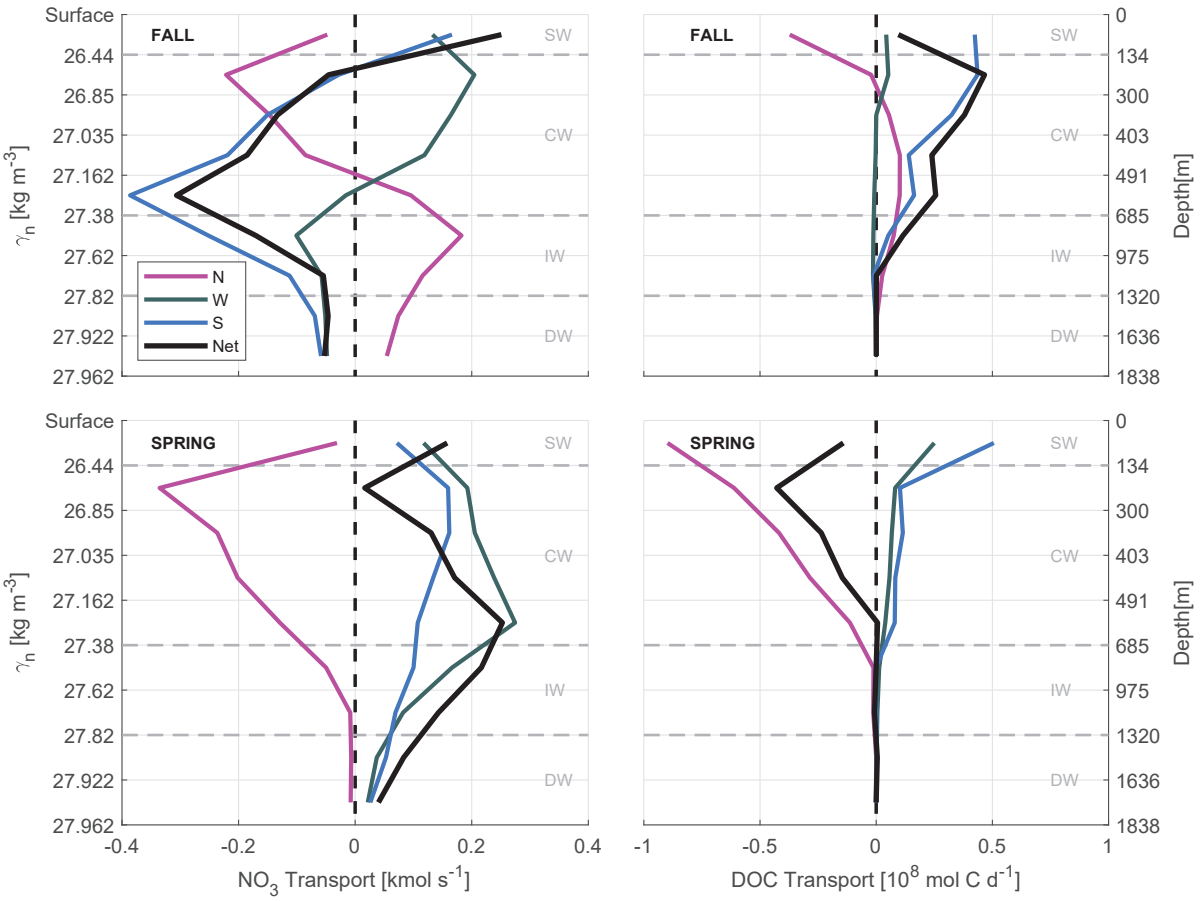

Figure 2.17: Accumulated NO_3 transports (kmol s^{-1}) and accumulated DOC transports (10^8molC day^{-1}) at transects in the north (N, magenta line), west (W, dark grey line) and south (S, blue line) during fall (top) and spring (bottom). See Tab. 2.2 for the γ_n values bounding every water layer. Negative-positive values indicate inward-outward transports as in Fig. 2.12. The net transport in the whole box is shown by the black line.

the exception of the shallowest level at which the INs leave the box (Tabs. 2.5, 2.6 and 2.7 and Figs. 2.16 and 2.17). On the other hand, the net *DOC* transports are outward for SW, CW and IW levels with $0.10 \pm 0.13 \times 10^8$ molC day^{-1} at SW level, $1.34 \pm 0.80 \times 10^8$ molC day^{-1} at CW levels and $0.12 \pm 0.72 \times 10^8$ molC day^{-1} at IW (Tab. 2.8 and Fig. 2.17).

In contrast, during spring a net outward transport is obtained for the three INs with 0.28 ± 0.61, 0.57 ± 1.22 and 0.04 ± 0.08 kmol s^{-1} at CW, 0.28 ± 0.72, 0.36 ± 0.94 and 0.02 ± 0.06 kmol s^{-1} at IW, and 0.13 ± 6.79, 0.12 ± 6.26 and 0.01 ± 0.42 kmol s^{-1} at DW (Tabs. 2.5, 2.6 and 2.7, and Figs. 2.16 and 2.17). The *DOC* net transports are inward with $-0.14 \pm 0.08 \times 10^8$ molC day^{-1} at SW level; $-0.80 \pm 1.72 \times 10^8$ molC day^{-1} at CW levels; and $-0.01 \pm 0.02 \times 10^8$ molC day^{-1} at IW levels (Tab. 2.8 and Fig. 2.17).

Table 2.8: *DOC* transports and their errors (10^8 molC day^{-1}) for CW, IW, and DW for the north, west and south transects. Positive-negative values indicate outward-inward transports. The last row is the integrated transport in the entire water column in each transect, and the last column represents the net transport for this variable inside the box. These values are transports of non-refractory DOC, which is obtained by subtracting an amount of 40 μmol L^{-1} from the measured *DOC*.

WATER LEVELS	SEASON	NORTH	WEST	SOUTH	IMBALANCE
SW	**Fall**	-0.37 ± 0.08	0.04 ± 0.01	0.42 ± 0.38	0.10 ± 0.13
	Spring	-0.90 ± 0.24	0.25 ± 0.16	0.51 ± 0.11	-0.14 ± 0.08
CW	**Fall**	0.24 ± 0.10	0.04 ± 0.01	1.06 ± 0.28	1.34 ± 0.80
	Spring	-1.43 ± 0.33	0.25 ± 0.09	0.38 ± 0.14	-0.80 ± 1.72
IW	**Fall**	0.10 ± 0.10	-0.03 ± 0.09	0.04 ± 0.04	0.12 ± 0.72
	Spring	-0.02 ± 0.08	0.02 ± 0.02	-0.00 ± 0.00	-0.01 ± 0.02
DW	**Fall**	0.00 ± 0.01	-0.00 ± 0.02	-0.00 ± 0.00	0.00 ± 0.00
	Spring	-0.00 ± 0.06	0.00 ± 0.04	0.00 ± 0.58	0.00 ± 0.23
TOTAL	**Fall**	-0.03 ± 0.03	0.06 ± 0.02	1.53 ± 0.64	1.55 ± 5.01
	Spring	-2.35 ± 0.84	0.52 ± 0.25	0.89 ± 0.40	-0.95 ± 1.19

2.6 Discussion

The circulation patterns in the studied area of the Canary Basin change significantly, showing a temporal variability from fall to spring. The differences between the two seasons are reflected in the estimated mass transports for both cruises (Figs. 2.13 and 2.14 and Tab. 2.4).

Trade Winds are intense all year long between the Canary Islands and Cape Blanc (26° N to 21° N), and they generate a quasi-permanent upwelling in this region north of Cape Blanc. In contrast, the developed EBUS intensity and its off-shore development change from fall to spring (Benazzouz et al., 2014b). At the beginning of spring there is a strong heating that generates a sharp water stratification, particularly in the interior ocean of the NASG, and a very intense upwelling that makes the EBUS strongly develop far off-shore. In early fall, the EBUS weakens and becomes a shallower front that approaches towards the coast (Pelegrí and Benazzouz, 2015a). In fact, the variability related to its location and

intensity may be the reason that the estimated mass transports in the north-south direction are distributed between levels of central waters and intermediate waters in fall and that in spring these mass transports parallel to the coast are confined to the shallowest layers at central waters. On the other hand, these changes in the EBUS and the water stratification may also be related to the westward mass transports, which in fall are accentuated and confined to the levels of SW and CW, as a shallow Ekman transport, while in spring the lateral westward transport is distributed from the sea surface down to IW levels (Tab. 2.4 and Fig. 2.13).

SW transports through the N and W transects show similar patterns, but in fall they are significantly more intense than in spring. In addition, CW level transports through these two transects also show similar patterns, with low variability between the two seasons. The largest differences are observed in the estimated transports through the S transect, which change from fall to spring; the transport is northward during fall and southward during spring. This observed variability in the transports in SW and CW levels in the southern part of the domain is likely related to the seasonal changes in the position of the CVFZ, which is in turn related to the seasonal changes in the North Atlantic Tropical Gyre (NATG), south of the domain (Pelegrí et al., 2017). The fact that the Intertropical Convergence Zone moves southward in winter and northward in summer affects the circulation patterns south and north of Cape Blanc (Lázaro et al., 2005; Stramma et al., 2008; Peña-Izquierdo et al., 2012). While in fall the CVFZ crosses the S transect in its westernmost position, in spring it moves closer to the African coast. The output of the GLORYS model matches the observations during both seasons (Fig. 2.15). In addition, the dynamics described by the geostrophic field of GLORYS also agree with the velocity field and the mass transports at CW levels estimated by the inverse model in the S transect for both seasons.

GLORYS velocity outputs also reproduce mesoscale and submesoscale features associated with the CVFZ (Pérez-Rodríguez, Pelegrí, and Marrero-Díaz, 2001; Martínez-Marrero et al., 2008), which are observed directly in the S transect of the velocity sections (Fig. 2.10) and in the accumulative mass transport (black line in Fig. 2.13). Specifically during fall, the reported eddies significantly boost transport at the SW and CW levels from south to north. All these results at CW levels are consistent with the late summer and fall growth of the Mauritania Current and of the PUC, as well as with the decrease in the NATG currents and the weakening of the Guinea Dome in winter and spring (Siedler et al., 1992; Lázaro et al., 2005; Peña-Izquierdo et al., 2012; Pelegrí and Peña-Izquierdo, 2015; Pelegrí and Benazzouz, 2015a). The estimated transports at IW also show seasonal changes between fall and spring. This region is featured by a late summer northward progression of AAIW observed in fall and by a weak southward flow of MW in spring (Machín et al., 2010). The northward significant mass transports observed in fall at the north and south transects is consistent with the northward spreading documented for AAIW (Machín and Pelegrí, 2009; Machín et al., 2010).

In general, the estimated transport of the three INs shows similar patterns, marked by the mass transport variability during both seasons. The level with the highest transport for all the nutrients in both seasons is the deepest CW layer. This is quite in agreement with the local maximum of remineralization found for all tracers in the upper intermediate layer by Fernández-Castro, Mouriño-Carballido,

and Álvarez-Salgado (2018).

CW levels are featured by a relatively high biological production and therefore a nutrient deficit, as well as by large geostrophic velocities. During fall the amount of INs that enters the box through N and S transects is larger than the IN quantity that leaves the box through the W transect. In spring, on the other hand, the amount of INs transported outward through the W and S transects is larger than the INs that enter from the north.

At IW levels the concentrations of INs are high and stable, related to the dominant remineralization process. During spring, the spatial distribution of the three IN transports are the same as at CW levels, with smaller values. In this season the transports of INs are directed westward through the W transect towards the oligotrophic open ocean. In fall, the IN transports at IW levels have a behaviour different than at CW levels, which is the main transport in the south-north direction.

The most significant differences between the *DOC* transports in fall and spring are obtained in the first and second shallowest layers in which there are high lateral velocities and the euphotic layer. During fall, the *DOC* quantity that enters by the north transect is a third of the amount that leaves the region by the south. In the spring, however, the large amount of *DOC* that enters the domain from the north is double the quantity that leaves it by the S transect, while a quarter leaves by the western transect.

In spring, when the stratification is less marked, the most significant and deepest transports of INs are observed toward the open ocean in central and intermediate water levels. However, in fall, when the water column is more stratified and the upwelling process is the main physical forcing for nutrient supply at CW levels (Pastor et al., 2013), the IN transports toward oligotrophic interior ocean are less than in spring. In fact, while in the western transect during spring the IN transports increase with depth to their maximum values at the deepest central layer, in fall the opposite occurs, since the westward IN transports decrease with depth until canceling at the last central layer; these transports reverse towards the coast at the two intermediate layers (green line in Figs. 2.16 and 2.17).

On the other hand, *DOC* transports are deeper and more intensified toward the open ocean during spring than in fall. Nonetheless, in fall there is an important and deeper transport of IN in a direction parallel to the coast. In fact, at IW *DOC* concentrations accumulate next to the African coast in the upwelling region. Furthermore, inside the upwelling region at the N and S transects in fall, the two observed mesoscale anticyclonic eddies could enhance this process.

The variability in the intensity of the stratification, the strength of upwelling, and the position of the boundary between the upwelling and the oligotrophic interior ocean, together with important mesoscale and submesocale structures, control the nutrients availability at CW and IW waters. It is also deduced from *DOC* transport estimates that the upwelling drives the changes in the size of the high-production domain and, equivalently, the position for the eastern boundary of the oligotrophic region in this area (Pastor et al., 2013).

The estimated transports of INs and *DOC* tell us that in fall there is a pronounced import of INs into the domain (with the exception of the SW layer) and a moderate export of *DOC*, especially at CW and IW levels. On the other hand,

during spring there is a pronounced export of INs from the domain at CW and IW levels and a slight import of *DOC* at the shallowest CW levels and at the SW layer.

The observations used so far provide nutrient fluxes during two cruises performed only in two seasons of the years 2002 and 2003. Thus, the full seasonal variability cannot be addressed with in situ observations from those years. Instead, in this section the seasonal variability is analyzed based on numerical modeling outputs to depict the context in which the in situ nutrient fluxes are evaluated. To do so, the time span that contains both cruises of the COCA project from 1 July 2002 to 30 June 2003 is analysed with a climatological approach: summer comprises the months from July to September, fall from October to December, winter from January to March and finally spring from April to June.

The analyses are performed at three different key points located in each transect during both cruises (Fig. 2.18). The northern point is located between stations 18 and 20, the western one between stations 36 and 38, and the southern point between stations 50 and 52. These locations are chosen as the most representative points of each transect. Nutrient profiles at each transect are analyzed for both seasons, and the key points are selected for which the three nutrients profiles are consistent with their average distribution. In the case of northern and southern transects, the key points are located at the intermediate point between the upwelling area and the oligotrophic open ocean, where the nutrient concentrations remain fairly stable among seasons. At the western transect, the middle position is considered to be the representative point since all nutrients profiles are markedly homogeneous along this transect, and, in addition, nutrient concentrations are rather constant from fall to spring (middle column in Fig. 2.6).

The biogeochemical model is combined with the physical model to obtain the seasonal nutrient fluxes at the three key points (Fig. 2.18). Overall, nutrient fluxes are negligible at the surface, where nutrients are depleted as a result of photosynthetic activity. On the other hand, nutrient fluxes usually present their largest values in the depth range from 500 m to 1000 m, as a combination of relatively large currents and nutrient concentrations. Nutrient fluxes at the northern point present a somewhat complex vertical structure, with opposite patterns above and below approximately 600 m of depth. Above 600 m of depth, nutrient fluxes are northward in fall, while they are southward in the rest of the seasons. Below that depth, nutrient fluxes are southward in fall, while they are northward for the remaining seasons. Once the nutrient fluxes from in situ observations are considered, some differences arise from both datasets. On the one hand, during spring both results indicate a southward nutrient flux above 500 m, while below that depth nutrient fluxes are southward for the in situ observations and northward for the numerical results. On the other hand, in fall the nutrient fluxes are southward in the entire water column for the in situ observations, while for the numerical results they are northward in the upper 500 m of depth and southward in the remaining water column. In any case, the intensities in the nutrient fluxes from in situ data and from numerical modeling outputs are quite similar.

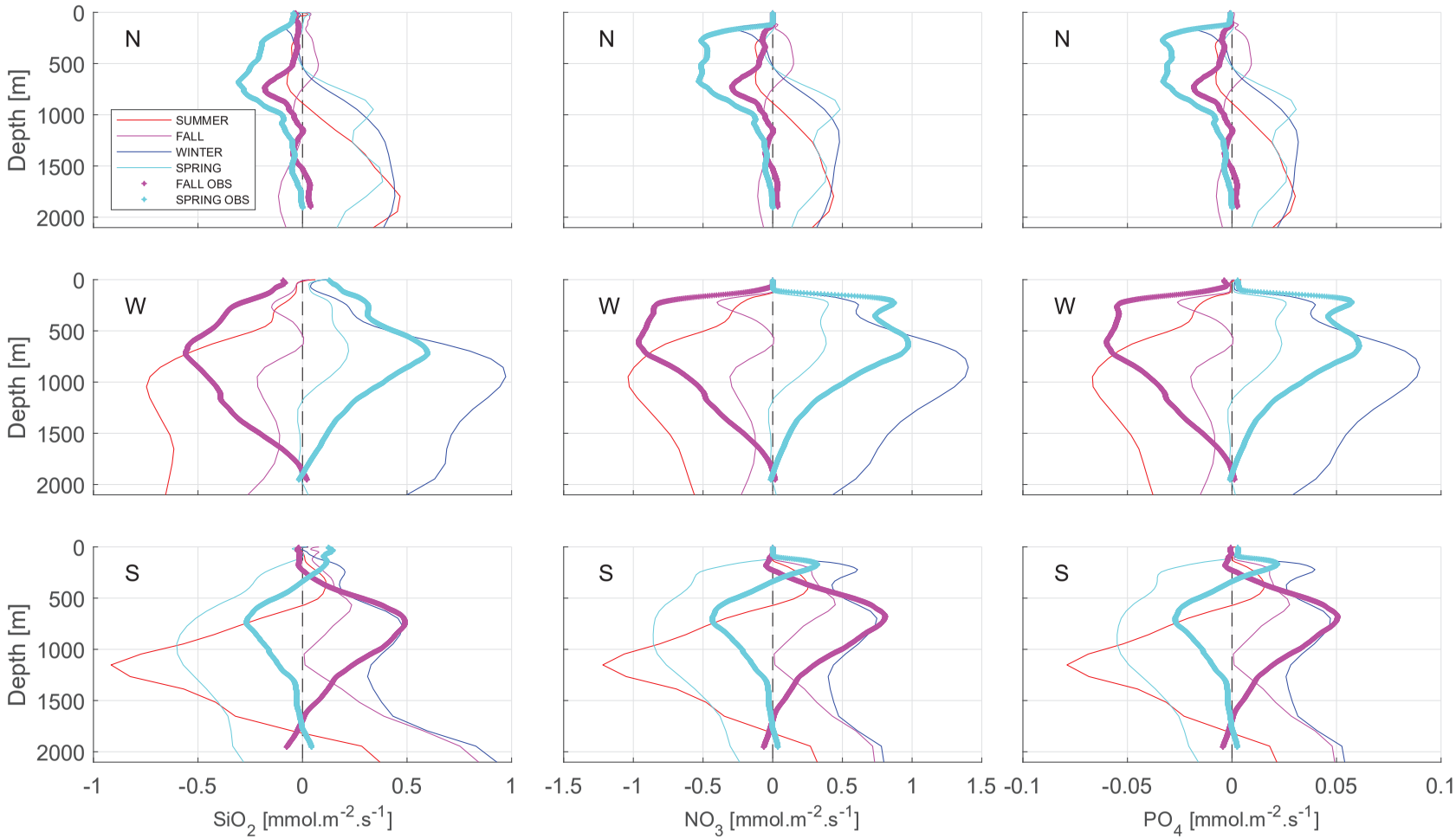

Figure 2.18: Numerical modeling of seasonal SiO_2 (left), NO_3 (center) and PO_4 (right) fluxes ($m$mol m^{-2} s^{-1}) at the three key points (N:in north transect, top; W: in west transect, center; and S: in south transect, down). The following are represented: summer, from July to September, by the thin red line; fall, from October to December, by the thin magenta line; winter, from January to March, by the thin blue line; and spring, from April to June, by the thin cyan line. The three nutrients fluxes observed in situ in fall (magenta) and spring (cyan) are also plotted with thicker dotted lines.

At both the western and southern points, the fluxes present a much simpler vertical structure. At the western point, nutrient fluxes in the whole water column are westward in winter and spring, while they are eastward in summer and fall. Maximum nutrient fluxes are obtained for winter and summer seasons, while minimum values are estimated for the spring and fall seasons. Nutrient fluxes estimated from in situ observations present the same direction as those estimated by the numerical model in both seasons, though somehow the in situ results duplicate the numerical values. At the southern point, nutrient fluxes are southward in fall and winter, while they are mainly northward in spring and summer. The southward nutrient flux modeled in summer in the upper 500 m of depth might be noteworthy. Nutrient fluxes from the in situ observations largely coincide with the numerical results, particularly in their directions below 300 m of depth. In this case, the intensity from the numerical result is double that from the in situ observation in spring, while roughly the opposite occurs in fall.

2.7 Conclusions

An inverse box model has been applied in the eastern North Atlantic to estimate mass, nutrient and organic matter transports during spring and fall. The currents estimated are largely affected by mesoscale features related to the Canary Eddy Corridor and to the Cape Verde Frontal Zone. The net mass transport at SW+CW levels coincides in both seasons in the N transect with a southward flow of 5.61 ± 1.86 Sv in fall that increases in spring to 6.69 ± 1.63 Sv. In the W transect the net westward mass transport at the SW+CW levels weakens from a value of 5.96 ± 1.75 Sv in fall to 4.05 ± 1.75 Sv in spring. The most remarkable change in the net mass transport at SW+CW layers occurs in the southern transect where in fall the net mass transport is northward with a value of 4.35 ± 1.48 Sv, while in spring it is southward with a value of 5.20 ± 1.55 Sv.

At IW layers, the net transport in the south-north direction is intense and northward in fall at 1.94 ± 1.85 Sv, while it weakens and reverses southward in spring to 0.48 ± 1.65 Sv. In the W transect, the net westward mass transport at IW layers is less intense in fall at 0.48 ± 1.71 Sv, than in spring at 1.21 ± 1.68 Sv. Finally, the net mass transport at DW levels is small compared to the other water levels, with the exception of the 0.73 ± 1.71 Sv estimated in the N transect during fall.

This geographical distribution of the mass transports is consistent with a south-westward flow mainly fed by the Canary Current. On the other hand, the temporal variability of mass transports in the southern section is likely related to a zonal shift of the CVFZ, which might be located in its westernmost position in fall, bolstering the presence of waters from the South Atlantic in the domain considered. At intermediate levels the significant northward transport observed at both the north and south transects during fall must be highlighted.

With regard to the IN and DOC net transports, in fall the domain works as a nutrient sink, with a total IN net import of 0.61 ± 1.97, 0.74 ± 2.40 and 0.05 ± 0.15 kmol s^{-1} for SiO_2, NO_3 and PO_4, respectively, while in spring it works as a source of nutrients, with a total nutrient net export of 0.73 ± 0.91, 1.21 ± 1.51 and 0.08 ± 0.1 kmol s^{-1}. It is also observed that the net DOC outward transport

is 1.55 ± 5.01 $\times 10^8$ molC day^{-1} in fall when the domain acts as a source of DOC, while the net inward value of 0.95 ± 1.19 $\times 10^8$ molC day^{-1} describes it as a DOC sink in spring.

With respect to the lateral transports of both INs and DOC to the open ocean through the W transect, during spring there is a continuous westward IN transport of 0.75 ± 0.37, 1.34 ± 0.66 and 0.08 ± 0.04 kmol s^{-1} of SiO_2, NO_3 and PO_4, respectively, in the entire water column. These transports coincide with an important westward transport of DOC of 0.52 ± 0.25 $\times 10^8$ molC day^{-1}, mainly at SW and CW levels. In fall, these transports weaken at CW and reverse at IW, which means that the net westward transport of INs is smaller than in spring, with values of 0.03 ± 0.01, 0.35 ± 0.13 and 0.02 ± 0.01 kmol s^{-1} for SiO_2, NO_3 and PO_4. Westward transports of DOC during fall are lower than in spring, with only 0.06 ± 0.02 $\times 10^8$ molC day^{-1}.

Overall, nutrient fluxes estimated with in situ observations compare well with those estimated from numerical modeling outputs. The main differences in their directions are obtained in the northern section, while the differences in the western and southern sections are mainly related to their intensity.

It is still necessary to continue building an understanding of physical and biogeochemical processes and the interactions between the productive EBUS and the interior ocean in its vicinity, especially in dynamically complex regions such as this area where the EBUS interacts with both the CVFZ and mesoscale features. Larger and more robust hydrological and biogeochemical databases would help to achieve this goal.

Chapter 3

Cape Verde Frontal Zone in summer 2017: lateral transports of mass, dissolved oxygen and inorganic nutrients

Burgoa, N., Machín, F., Rodríguez-Santana, A., Marrero-Díaz, A., Álvarez-Salgado, X. A., Fernández-Castro, B., Gelado-Caballero, M. D. and Arístegui, J. (2021). Cape Verde Frontal Zone in summer 2017: lateral transports of mass, dissolved oxygen and inorganic nutrients. *Ocean Sci.* **17**, 769–788, doi:10.5194/os-17-769-2021

Abstract

The circulation patterns in the confluence of the North Atlantic subtropical and tropical gyres delimited by the Cape Verde Front (CVF) were examined during a field cruise in summer 2017. We collected hydrographic data, dissolved oxygen (O_2) and inorganic nutrients along the perimeter of a closed box embracing the Cape Verde Frontal Zone (CVFZ). The detailed spatial (horizontal and vertical) distribution of water masses, O_2 and inorganic nutrients in the CVF was analyzed, allowing for the independent estimation of the transports of these properties in the subtropical and tropical domains down to 2000 m. Overall, at surface and central levels, a net westward transport of 3.76 Sv was observed, whereas at intermediate levels, a net 3 Sv transport northward was obtained. We observed O_2 and inorganic nutrients imbalances in the domain consistent with O_2 consumption and inorganic nutrient production by organic matter remineralization, resulting in a net transport of inorganic nutrients to the ocean interior by the circulation patterns.

3.1 Introduction

The Cape Verde Basin (CVB) is located on the eastern boundary of the North Atlantic Ocean, at the meeting point of the subtropical and tropical domains. This area is influenced by the North Atlantic subtropical gyre, (NASG; Stramma and Siedler, 1988), the North Atlantic tropical gyre (NATG; Siedler et al., 1992) and the upwelling region off northwestern (NW) Africa (Ekman, 1923; Tomczak, 1979; Hughes and Barton, 1974; Hempel, 1982). In the central waters level (from 100 to 650-700 m depth) within this domain, the Cape Verde Frontal Zone (CVFZ)

extents from Cape Blanc to Cabo Verde (Cape Verde) islands as a northeast-southwest boundary between subtropical and tropical waters (Zenk, Klein, and Schroder, 1991). In addition, the coastal upwelling front (CUF) along the Mauritanian coast, until Cape Blanc (Cape Verde) in summer (winter), separates stratified oceanic waters and more homogeneous slope waters in the CVB (Benazzouz et al., 2014a; Benazzouz et al., 2014b; Pelegrí and Benazzouz, 2015a). These two frontal systems also act as a dynamic source of mesoscale and submesoscale variability related to interleaving mixing processes and filaments associated with the CUF (Pérez-Rodríguez, Pelegrí, and Marrero-Díaz, 2001; Martínez-Marrero et al., 2008; Capet et al., 2008; Thomas, 2008; Meunier et al., 2012; Hosegood et al., 2017).

The northern side of the CVFZ is mainly occupied by an ensemble of subtropical waters, generically denominated as Eastern North Atlantic Central Water (ENACW), which flows southward transported by the Canary Current (CC). Once the CC approaches the CVFZ, it turns offshore as the North Equatorial Current (NEC, Stramma, 1984), giving rise to a shadow zone of poorly ventilated waters (Luyten, Pedlosky, and Stommel, 1983). Additionally, long-lived eddies generated downstream of the Canary Islands (Sangrà et al., 2009; Barceló-Llull et al., 2017a) significantly contribute to the westward circulation within the CVB (Sangrà et al., 2009). Between the Canary Islands and Cape Blanc, the steady trade winds force a permanent upwelling (Benazzouz et al., 2014a), which in turn triggers an intense southward coastal jet, the Canary Upwelling Current (CUC; Pelegrí et al., 2005; Pelegrí, Marrero-Díaz, and Ratsimandresy, 2006). Below the CUC and over the continental slope, the Poleward Undercurrent (PUC) flows northward with remarkable intensity (Barton, 1989; Machín and Pelegrí, 2009; Machín et al., 2010).

The South Atlantic Central Water (SACW) is the main water mass on the southern side of the CVFZ. The SACW is formed in the subtropical South Atlantic, and it largely modifies its thermohaline features along its complex path northward to the CVB (Peña-Izquierdo et al., 2015). The northern branch of the North Equatorial Countercurrent becomes the Cape Verde Current (CVC) at the African Slope, carrying the SACW (Peña-Izquierdo et al., 2015; Pelegrí et al., 2017). The CVC flows anticlockwise around the Guinea Dome (GD) to the southern part of the CVFZ (Peña-Izquierdo et al., 2015; Pelegrí et al., 2017). A seasonal pattern has been documented, whereby the GD intensifies in summer as a result of the northward penetration of the Intertropical Converge Zone (ITCZ) (Siedler et al., 1992; Castellanos et al., 2015). In addition, the northward flow along the African coast also intensifies in summer due to the relaxation of the trade winds south of Cape Blanc, so the Mauritanian Current (MC) and the PUC increase their northward progression to just south of Cape Blanc (Siedler et al., 1992; Lázaro et al., 2005).

The meeting of southward-flowing CC/CUC with northward-flowing PUC/MC leads to a confluence at the CVFZ, which fosters the offshore export of mass and seawater properties, with its maximum strength in summer (Pastor et al., 2008). Subtropical and tropical waters exported along the CVFZ exhibit distinct physical-chemical properties. The ENACW is a relatively young, salty and warm water mass with low nutrient and high oxygen concentrations. The SACW is an older water mass that is fresher and colder than the ENACW, and it is largely modified while traveling through tropical regions; hence, the SACW at the CVFZ

is a nutrient-rich and oxygen-poor water mass (Tomczak, 1981; Zenk, Klein, and Schroder, 1991; Pastor et al., 2008; Martínez-Marrero et al., 2008; Pastor et al., 2012; Peña-Izquierdo et al., 2015). The CVF drives nutrient-rich SACW into the southeastern edge of the nutrient-poor NASG - a process that boosts an area of high primary productivity offshore, as revealed by the giant filament at Cape Blanc (Gabric et al., 1993; Pastor et al., 2013).

Intermediate levels (∼700-1500 m depth) are essentially occupied by modified Antarctic Intermediate Water (AAIW), a relatively fresh and cold water mass with high inorganic nutrient and low O_2 concentrations. At this latitude, AAIW flows northward at 700-1100 m depth along the eastern margin of both the NASG and NATG (Machín, Hernández-Guerra, and Pelegrí, 2006; Machín and Pelegrí, 2009; Machín et al., 2010).

The distribution of O_2 and inorganic nutrients below the euphotic layer is determined by biogeochemical and physical processes (Pelegrí and Benazzouz, 2015b). The main biogeochemical processes are related to the availability of organic matter, O_2 and inorganic nutrients in the source regions and also to remineralization processes; conversely, the main physical processes are associated with both the vertical link between surface and subsurface waters and with the lateral transports in subsurface waters (Peña-Izquierdo et al., 2015; Pelegrí and Benazzouz, 2015b). As a consequence, the O_2 and inorganic nutrient concentrations may vary depending on the interplay between the local rate of organic matter remineralization and the rate of water supply (Pelegrí and Benazzouz, 2015b). In other words, the different dynamics between subtropical and tropical regions separated by the CVFZ, and between oceanic and upwelling regions separated by the CUF, establish distinct biogeochemical domains with substantial differences in their O_2 and inorganic nutrient patterns at the CVB. Over the last two decades, several authors have focused on the O_2 and inorganic nutrient distribution, considering both the physical properties of water masses and the dynamical processes involved at varying scales (Pelegrí, Marrero-Díaz, and Ratsimandresy, 2006; Machín, Hernández-Guerra, and Pelegrí, 2006; Pastor et al., 2008; Álvarez and Álvarez-Salgado, 2009; Peña-Izquierdo et al., 2012; Pastor et al., 2013; Peña-Izquierdo et al., 2015; Hosegood et al., 2017; Burgoa et al., 2020).

Here, we address the circulation patterns and the physical processes behind the distribution of O_2 and inorganic nutrients at the dynamically complex CVFZ. To achieve this goal, we used field observations obtained during the FLUXES-I cruise and applied an inverse model to estimate the mass transports. Additional methods are applied to asses the water masses' distribution both horizontally and with depth (to extend the classical definition of the CVF) in order to consistently separate the tropical and subtropical sides.

3.2 Data and methodology

3.2.1 The oceanographic cruise

The FLUXES (Carbon Fluxes in a Coastal Upwelling System – Cape Blanc, NW Africa) project included two cruises during 2017 labeled as FLUXES-I and FLUXES-II. The FLUXES-I cruise provided the dataset to conduct the analyzes presented in this paper. It was carried out from 14 July to 8 August 2017 aboard

the R/V *Sarmiento de Gamboa*. A grid of 35 stations was selected to form a closed box (pink dots, Fig. 3.1). At each station, we sampled the water column with a SBE 38 rosette sampler equipped with 24 Niskin bottles of 12 L volume. Temperature, conductivity and oxygen were measured with a vertical resolution of 1 dbar down to at least 2000 m by means of a CTD SBE 911+. The average distance between neighboring CTD (conductivity-temperature-depth) stations was about 84 km. Shallow stations 1 and 29 were discarded from the analysis. The sample grid was split into four transects: the northern transect (N) spanned zonally from station 2 to 12 at 23°N; the western transect (W) was located at 26°W from station 12 to 19; the southern transect (S) at 17.5°N extended from station 19 to 28; the eastern transect (E) closed the box approximately 18.6°W from station 28 to 3.

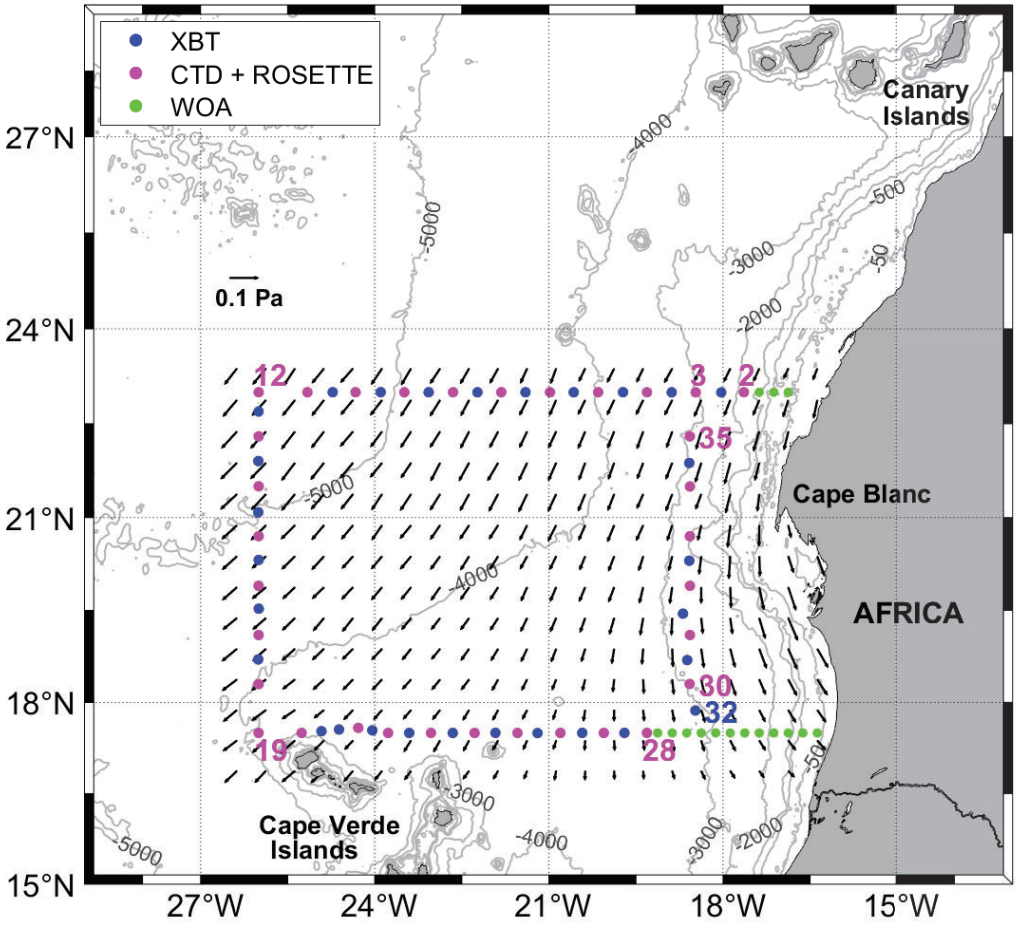

Figure 3.1: CTD rosette sampling stations (pink dots) and XBT sample locations (blue dots) during FLUXES-I cruise. WOA stations are represented by green dots. Time-averaged wind stress during the cruise is also represented, with the inset arrow denoting the scale (shown with half of the original spatial resolution).

A second observational dataset consisted of 39 expendable bathythermograph probes (XBT-T5, Lockheed Martin Sippican, USA) deployed between most CTD stations (blue dots, Fig. 3.1). WinMK21 acquisition software was set up to sample

down to 2000 m - a sampling aided by a reduced boat speed during XBT deployment (5 kn). Some XBTs (12, 19, 30, 31, 38, 39 and 40) were discarded due to malfunction during recording.

Practical salinity (S_P, UNESCO (1985)) was calibrated after analyzing 51 water samples with a Portasal model 8410A salinometer, attaining an accuracy and precision within the values recommended by the World Ocean Circulation Experiment (WOCE). An oxygen sensor SBE 43 was interfaced with the CTD system during the cruise, and these observations were later calibrated with 417 in situ samples, providing a final precision of ± 0.53 μmol kg^{-1}.

Regarding dissolved inorganic nutrients (nitrates, NO_3; phosphates, PO_4; and silicates, SiO_4H_4), 419 water samples were collected in Niskin bottles and transferred to 25 mL polyethylene bottles. These samples were frozen at -20°C before their analysis using a segmented flow Alliance Futura analyzer following the colorimetric methods proposed by Grasshoff, Ehrhardt, and Kremling (1999).

3.2.2 Supplementary datasets

The Ekman transport through the boundaries of the domain was estimated with daily global wind field observations produced with the Advanced SCATterometer (ASCAT) installed on the EUMETSAT METop satellite. This dataset presents a spatial resolution of 0.25° (Bentamy and Fillon, 2012) and is made available by CERSAT (ftp://ftp.ifremer.fr/ifremer/cersat/products/gridded/MWF/L3/ASCAT/Daily/). Freshwater flux was calculated from the average rates of evaporation and precipitation extracted from the Weather Research and Forecasting model (WRF, Powers et al., 2017) and is provided with a spatial resolution of 0.125° and a temporal resolution of 12 h.

The climatological mean depths of the neutral density field during the summer season were evaluated from the climatological temperature and salinity fields extracted from the World Ocean Atlas 2018 (WOA18, Locarnini et al., 2018; Zweng et al., 2018). WOA18 was also used to produce a climatological neutral density field during the summer season to estimate a climatological geostrophic velocity field. Summer WOA18 nodes were used to extend the N and S transects up to the African coast (green dots, Fig. 3.1). Finally, two WOA stations were selected to apply the methodology developed in this paper in order to unveil the vertical location of the CVF (see section 3.2.4, Fig. 3.2).

The SEALEVEL_GLO_PHY_L4_REP_OBSERVATIONS_008_047 product issued by the Copernicus Marine Environment Monitoring Service (CMEMS, http://marine.copernicus.eu) provided the Level 4 Sea Surface Height (SSH) and derived variables as surface geostrophic currents, measured by multi-satellite altimetry observations over the global ocean with a spatial resolution of 0.25°. These data captured the mesoscale structures and were helpful to validate the near-surface geostrophic field produced by the inversion.

GLORYS 12V1 (GLOBAL_REANALYSIS_PHY_001_030) outputs from 25 years, also issued by CMEMS, were used to estimate a summer climatology for the velocity field, temperature and salinity, with a horizontal resolution of 1/12° at 50 standard depths. Specifically, the climatological salinity was used to present the CVF spatial distribution within the domain (see section 3.3.2, Fig. 3.10a).

Data treatments (in situ, operational and modelling), interpolations with Data-Interpolating Variational Analysis (DIVA, Troupin et al., 2012), graphical representations, and the inverse model were coded in MATLAB (MATLAB, 2019). Finally, the Smith–Sandwell bathymetry V19.1 (Smith and Sandwell, 1997) was used in all maps and full-depth vertical sections.

3.2.3 Merged hydrographic dataset

A high-resolution in situ temperature field (T) was produced after merging the CTD and XBT profiles. The remaining variables were interpolated to this same new high-resolution grid to perform additional data treatments.

S_P, O_2, NO_3, PO_4 and SiO_4H_4 were optimally interpolated with DIVA at each transect independently. Before carrying out these interpolations, DIVA was applied to the T suppressing one XBT profile from each transect to validate the method. In fact, the interpolated values had a relative error $< 3.5\%$ in 75% of cases. This allows to set the signal-to-noise ratio (λ) and the horizontal and vertical correlation lengths (L_x and L_y). Hence, the interpolations of the remaining hydrological and biogeochemical variables were carried out with the following parameters: $\lambda = 4$, $L_x = 110 - 135$ km and $L_y = 50$ m. Despite the fact that each variable behaves differently depending on its physical, chemical or biological nature, the correlation scales were considered the same due to the limitation of the sampling resolution. DIVA provided error maps for the gridded fields of each variable which allowed us to check their accuracy and spatial distribution. A total of 75% of the interpolated values of S_P and O_2 had a relative error $\leq 3.5\%$. Due to the lower sampling resolution of NO_3, PO_4 and SiO_4H_4, their interpolated values had higher errors. Between 70% and 75% of the interpolated values had a relative error $\leq 5.7\%$.

Once the interpolations were performed, absolute salinity (S_A, McDougall et al., 2012) and potential and conservative temperatures (θ and Θ, McDougall and Barker, 2011) were calculated (IOC, SCOR, and IAPSO, 2010). In addition, neutral density (γ_n, Jackett and McDougall, 1997) was used as the density variable.

3.2.4 Tracking the Cape Verde Front

One of the main goals of our study was to estimate the lateral fluxes on the tropical and subtropical sides of the Cape Verde Front. For this, we first had to uncover the location of the front - both with respect to depth and along its spatial distribution - within the domain. The classical definition places the CVF where isohaline 36 meets the 150 m isobath. Here, we have developed a method to extend this definition vertically as follows: two climatological profiles from WOA18 representative of the ENACW and SACW consistent with the definitions given by Tomczak, 1981 were selected (Fig. 3.2a). Those selected climatological profiles provide an average relationship between S_P, θ, and depth, which reveals that the traditional definition of the front is based on a salinity value (36) that indeed corresponds to equal contributions (50%) of the ENACW and SACW at 150 m depth. Following the same reasoning of equal contributions, we calculated the climatological salinity that would define the front location at standard depths from 100 to 650 m (Fig. 3.2b).

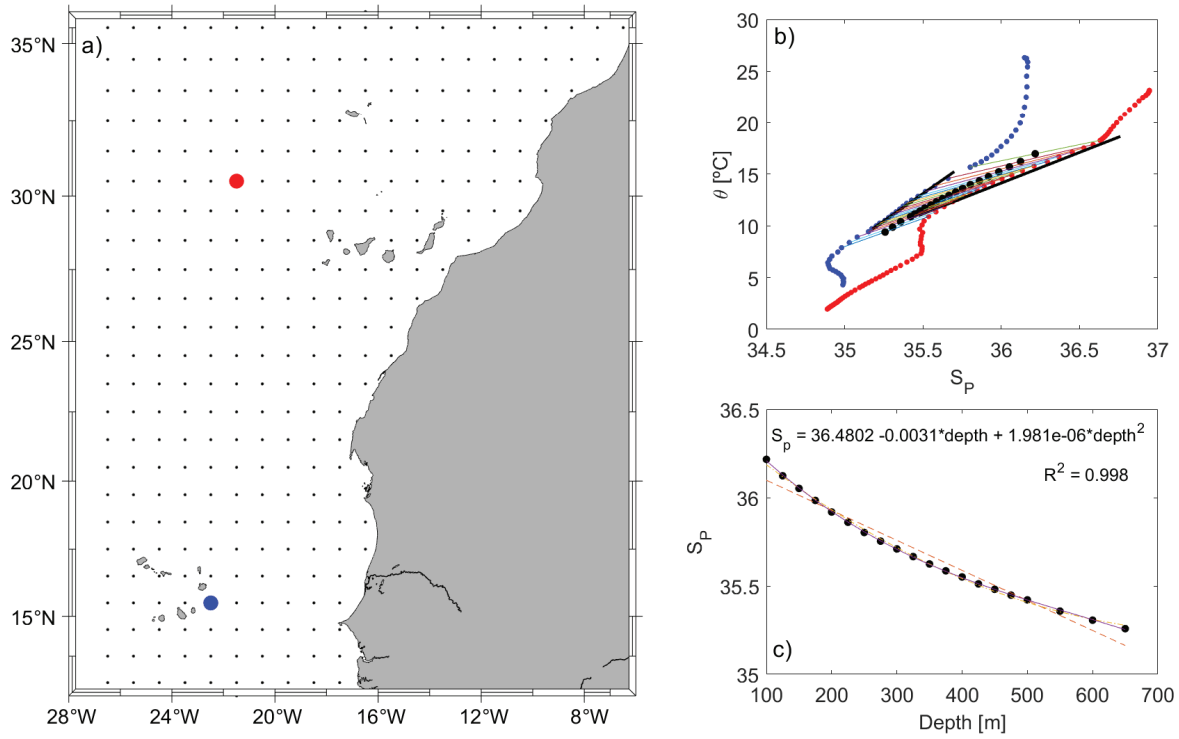

Figure 3.2: a) Map showing the two selected WOA stations in the ENACW (red) and SACW (blue) domains. b) T-S diagram with the average salinity for each depth (in the range from 100 to 650m) shown using black dots between the profiles of the northern and southern WOA stations. Observations at the same depths are connected by a straight line. c) Linear, quadratic and cubic fits for depth versus salinity with the quadratic fit equation.

Finally, three linear, quadratic and cubic relationships between salinity and depth were used to infer the salinity that would define the front location at any given depth. The quadratic relationship was finally chosen due to its tight fit to observations ($R^2 = 0.998$) keeping the polynomial order as low as possible (Fig. 3.2c). Thus, the front location could be uncovered at the depths occupied by the three layers of central waters (CW).

3.2.5 Water masses' distribution

An optimum multiparameter method (OMP, Karstensen and Tomczak, 1998) was used to quantify the contribution to the observations of the following water types: upper and lower North Atlantic Deep Water (UNADW and LNADW, Labrador Sea Water (LSW), Mediterranean Water (MW), AAIW, Subpolar Mode Water (SPMW), SACW at 12°C and 18°C (SACW12 and SACW18), ENACW at 12°C and 15°C (ENACW12 and ENACW15), and Madeira Mode Water (MMW). The hydrographic variables used for the analysis were θ, S_P, SiO_4H_4, and NO ($NO = O_2 + R_N \cdot NO_3^-$, where $R_N = 1.4$ is the stoichiometric ratio of organic matter remineralization; Anderson and Sarmiento, 1994) (Broecker, 1974). The reference values of these variables in the source region of each water type were extracted from the literature (Pérez et al., 2001; Álvarez and Álvarez-Salgado, 2009; Lønborg and Álvarez-Salgado, 2014) and WOA13 (Locarnini et al., 2013; Zweng et al., 2013; Garcia et al., 2014a; Garcia et al., 2014b). A linear system of normalized and weighted equations for θ, S_P, SiO_4H_4, NO and mass conservation was solved to obtain the water type proportions in the observations. Considering the measurement error, the relative conservative nature and the variability in each variable, the weights assigned to the balance of SiO_4H_4, NO, θ and S_P were 1, 2, 10 and 10, respectively. A weight of 100 was imposed on the mass conservation equation assuming the mass was fully conserved. On the other hand, in order to solve this undetermined system of equations, the water types were grouped in a maximum of four according to oceanographic criteria. In this way, the unknowns were reduced from 11 to 5 with the following groups of water types: (1) MW - LSW - UNADW – LNADW, (2) SPMW – AAIW - MW – LSW, (3) SACW12 - ENACW12 - SPMW - AAIW, (4) SACW18 - ENACW15 - SACW12 - ENACW12 and (5) MMW - SACW18 - ENACW15. Surface waters (<100 dbar) were excluded from the analysis due to their nonconservative behavior. This OMP with high determination coefficients ($R^2 > 0.97$) and low standard errors of the residuals of θ, S_P, SiO_4H_4, and NO realistically reproduced the thermohaline and chemical fields during FLUXES-I (Valiente et al., 2022).

3.2.6 Inverse model setup

The lateral geostrophic velocities were calculated at the boundaries of the volume closed by hydrographic stations. Geostrophic velocities were referenced to γ_n=27.82 kg m^{-3} ($\sim$ 1333 m, Fig. 3.3). As an initial guess, the velocities at the reference level were those estimated from the climatological summer mean provided by GLORYS.

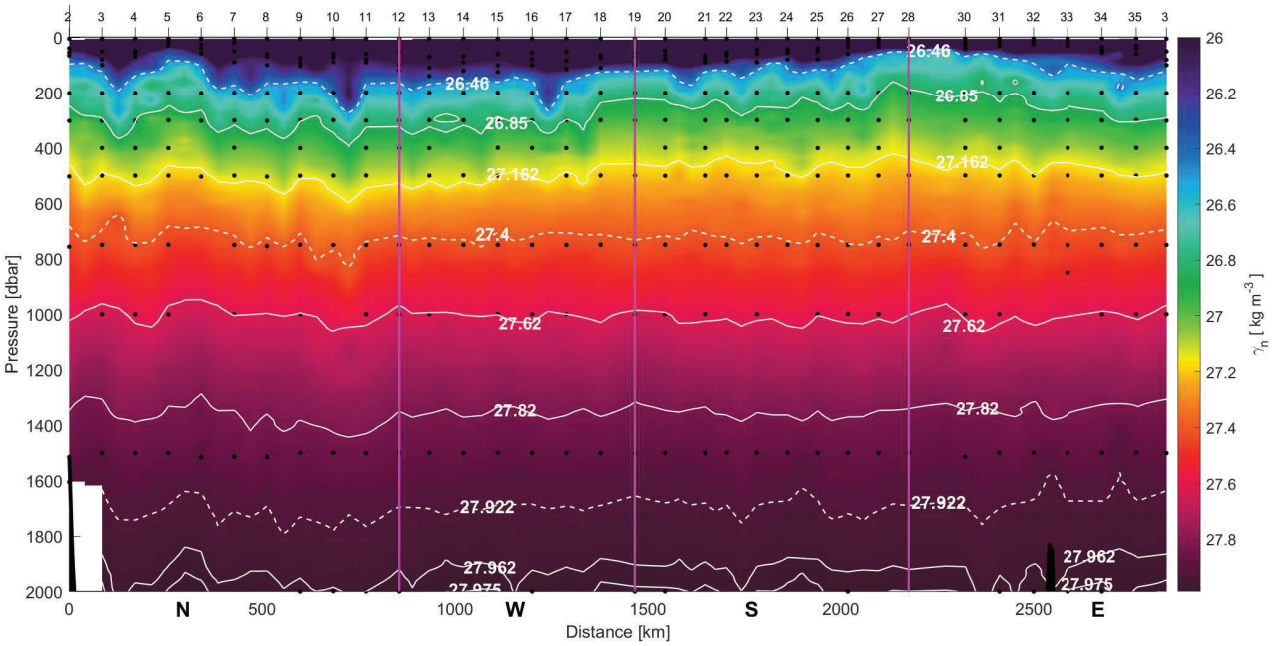

Figure 3.3: γ_n vertical section during the FLUXES-I cruise produced with the CTD-XBT merged dataset. White dashed isoneutrals limit the different water type layers. The direction chosen for the representation of the transects is the course of the vessel. Distance is calculated with respect to the first station (2). The section is divided as follows: transect N from east to west (from station 2 to 12), transect W from north to south (from station 12 to 19), transect S from west to east (from station 19 to 28) and transect E from south to north (from station 28 to 3). The northwestern, southwestern and southeastern corners are indicated by three vertical pink lines at stations 12, 19 and 28, respectively. The sampling points of dissolved oxygen and inorganic nutrients used in this work are represented by black dots.

An inverse box model (Wunsch, 1978) was then applied to estimate a set of unknowns based on the assumption of mass, salt and heat conservation within a closed volume. The unknowns in the system are an adjustment of the initial reference-level velocities, an adjustment of Ekman transports and the freshwater flux. The reference-level velocity field was then used to estimate the absolute water mass transport through each transect of the cruise (Martel and Wunsch, 1993; Paillet and Mercier, 1997; Ganachaud, 2003b; Machín, Hernández-Guerra, and Pelegrí, 2006; Pérez-Hernández et al., 2013; Hernández-Guerra et al., 2017; Fu, Karstensen, and Brandt, 2018; Burgoa et al., 2020).

The cruise was carried out over 25 days - a time lag large enough for the structures to evolve during the sampling. This time lag is not generally an issue that would introduce a relevant bias in the calculations; however, in this case, we have a closed volume composed of four hydrographical legs, so trying to connect the eastern section with the northern one might introduce a large bias in the observations and, consequently, in the geostrophic velocity field. Hence, to avoid any imbalances induced by the temporal evolution of the system, the volume is closed with land instead of with the eastern transect. To do so, WOA18 climatological nodes were used to extend the N and S transects eastward (green dots in Fig. 3.1), where the climatological summer mean of GLORYS was also included at the reference level. Therefore, the geostrophic velocities at the reference level were modified with the inversion in the N, W and S transects, whereas those velocities kept their initial climatological summer mean values from GLORYS in transect E.

The model was made up of eight layers bounded by the free surface and eight isoneutrals (26.46, 26.85, 27.162, 27.40, 27.62, 27.82, 27.922 and 27.962 kg m^{-3}), reproduced essentially from those defined by Ganachaud (2003b) for the North Atlantic Ocean (Fig. 3.3). The inverse model considered mass conservation and salinity anomaly conservation per layer and also over the whole water column (Ganachaud, 2003a). Heat anomaly was introduced only in the deepest layer where it was also considered conservative. Salinity and heat were added as anomalies to improve the conditioning of the model and reduce the linear dependency between equations (Ganachaud, 2003a). Therefore, the inverse model was composed of 19 equations (9 for mass conservation, 9 for salt anomaly conservation and 1 for heat anomaly conservation). Those equations were solved using a Gauss-Markov estimator for 69 unknowns, comprised of 65 reference-level velocity adjustments, 3 unknowns for the Ekman transport adjustments (one per transect) and 1 unknown for the freshwater flux.

It was necessary to provide the uncertainties related to the noise of the equations (R_{nn}) and the unknowns (R_{xx}) a priori in order to solve this undetermined system. R_{nn} and R_{xx} values are compiled in Tab. 3.1. The noise of each equation depends on the layer thickness, the density field and the variability in the velocity field (Ganachaud, 1999; Ganachaud, 2003a; Machín, Hernández-Guerra, and Pelegrí, 2006). Thus, an analysis of the velocity variability was performed in the mean depths of the eight layers. The velocity variance at each layer was estimated from summer months in the 25 years of GLORYS data. These variances were transformed into transport uncertainty values by multiplying by density and the vertical area of the section involved (R_{nn} in Tab. 3.1). The uncertainty assigned to the total mass conservation equation was the sum of the uncertainties from the eight mass

conservation equations. The equations for salt and heat anomaly conservation depend on the uncertainty of the mass transport, on the variance of these properties and, specifically, on the layer considered (Ganachaud, 1999; Machín, 2003). Therefore, the uncertainties for salt and heat anomaly equations were estimated as follows (Ganachaud, 1999; Machín, 2003): $R_{nn}(Cq) = a * var(C_q) * R_{nn}(mass(q))$ where $R_{nn}(Cq)$ was the uncertainty in the anomaly equation of the property (salt or heat anomaly); $var(C_q)$ was the variance of this property; a was a weighting factor (4 in the heat anomaly, 1000 in the salt anomaly and 10^6 in the total salt anomaly); q was a given equation corresponding to a given layer. These variability estimates were then included in the inverse model as the a priori uncertainty of the noise of equations in terms of variances of mass, salt anomaly and heat anomaly transports.

The variance of the velocities in the reference level was used as a measure of the a priori uncertainty for these unknowns. These variances were also calculated from the summer months' velocities provided by GLORYS (R_{xx} in Tab. 3.1).

The initial Ekman transports were estimated from the average wind stress during the days of the cruise. A 50% uncertainty was assigned to the initial estimate of Ekman transports, related to the errors in their measurements and to the variability in the wind stress. An uncertainty of 50% of the initial value of the freshwater flux, which was 0.0935 Sv, was also considered (Ganachaud, 1999; Hernández-Guerra et al., 2005; Machín, Hernández-Guerra, and Pelegrí, 2006). The Ekman transports, the freshwater flux and their uncertainties (R_{xx} in Tab. 3.1) were added to the inverse model in the shallowest layer for mass and salt anomaly as well as in the total mass transport and total salt anomaly transport equations.

Dianeutral transfers between layers were considered to be negligible compared with other sources of lateral transports, so they were not included in the inversion. Furthermore, the inverse model only works with information from the box boundaries and cannot be used to provide any spatial details of dianeutral fluxes for a given interface between layers, just an average value for the whole interface (Burgoa et al., 2020).

The resulting absolute geostrophic velocity field allowed us to calculate transports of O_2 and inorganic nutrients. Those transports were obtained by multiplying their concentration by mass transports, so their concentrations were initially interpolated to the positions where the absolute geostrophic velocities were estimated.

Table 3.1: A priori noise of equations corresponding to the surface water (SW), central water (CW), intermediate water (IW) and deep water (DW) levels and uncertainties of all unknowns of the inverse model.

WATER LEVELS	R_{nn} $[Sv^2]$
SW and CW	$[2.13 - 3.34]^2$
IW	$[2.88 - 3.49]^2$
DW	$[1.70]^2$
UNKNOWNS	R_{xx}
Velocities	$[10^{-4} - 10^{-3}]^2$ $[m\ s^{-1}]^2$
Ekman transports	$[10^{-5} - 10^{-4}]^2$ $[Sv^2]$
Freshwater flux	0.004^2 $[Sv^2]$

3.3 Results

3.3.1 Hydrography and water masses

The main water masses sampled during FLUXES-I were the ENACW (merging the MMW, ENACW15 and ENACW12) and the SACW (SACW18 and SACW12) below the mixing layer and above 700 m; the modified AAIW and MW from 700 up to 1700 m; and North Atlantic Deep Water (the LSW and UNADW) below 1600 m (Zenk, Klein, and Schroder, 1991; Martínez-Marrero et al., 2008; Pastor et al., 2012) (Figs. 3.3, 3.4 and 3.5). $\Theta - S_A$ definitions proposed by Tomczak (1981) for the salty and warm ENACW and the fresh and cold SACW (straight lines in Fig. 3.4) were used to identify CW in all transects: the main water mass sampled in transects N and W was the ENACW ($\sim$ 36.15 g kg^{-1} at 300 m), whereas the SACW was dominant in transect S ($\sim$ 35.65 g kg^{-1} at 300 m). Both the ENACW and SACW were registered along transect E. Water masses were also well defined at intermediate levels, with colder and fresher AAIW over warmer and saltier MW. MW was sampled mainly in transect N and in smaller proportions in the northern part of transects E and W, whereas the AAIW was the main water mass recorded in transects S, E and W (Fig. 3.4).

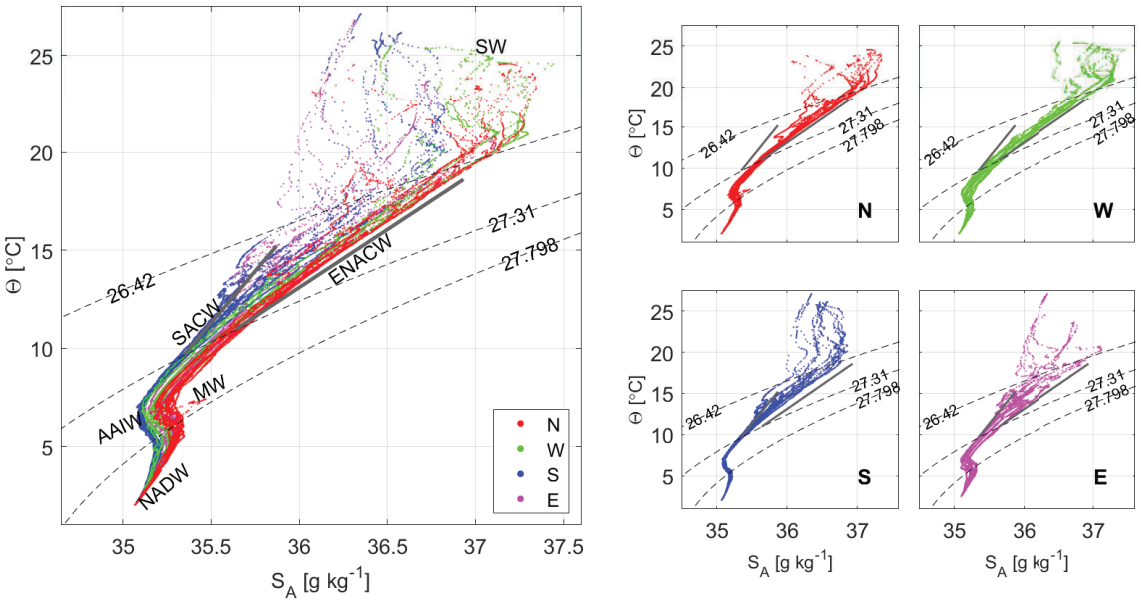

Figure 3.4: $\Theta - S_A$ diagrams during FLUXES-I cruise. The different water masses in the northern (N, red dots), western (W, green dots), southern (S, blue dots) and eastern (E, pink dots) transects for surface waters (SW), North Atlantic Central Water (ENACW), South Atlantic Central Water (SACW), modified Antarctic Intermediate Water (AAIW), Mediterranean Water (MW) and North Atlantic Deep Water (NADW). Potential density anomaly contours (gray dashed lines) equivalent to 26.46, 27.4 and 27.922 kg m^{-3} isoneutrals delimit the surface, central, intermediate and deep water levels. Straight lines represent the $\Theta - S_A$ relationship for ENACW and SACW equivalent to that proposed by Tomczak, 1981.

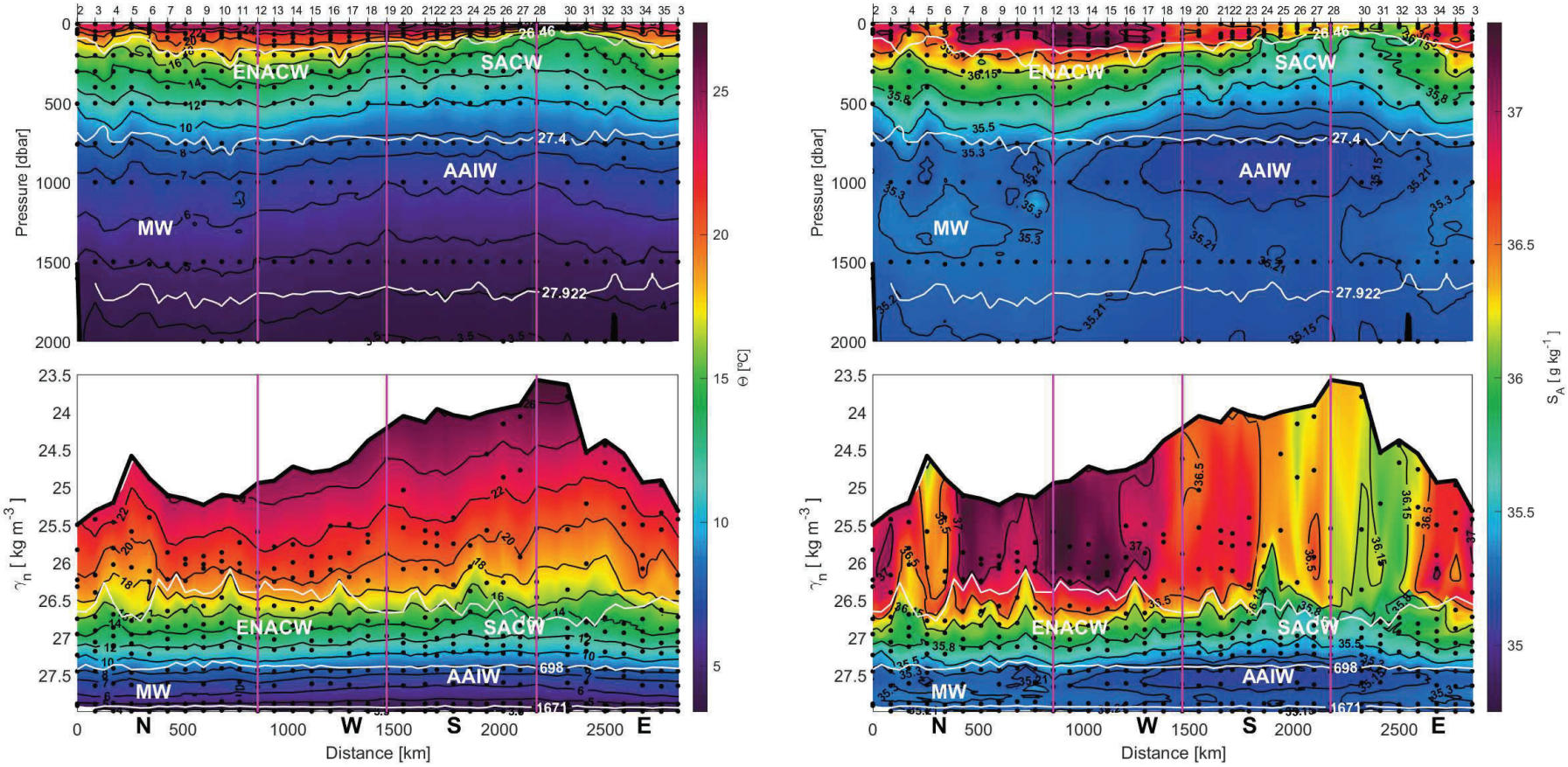

Figure 3.5: Sections of Θ (left) and S_A (right) with respect to depth (upper line) and γ_n (lower line) during the FLUXES-I cruise. The direction chosen for the representation is the same as in Fig. 3.3. The northwestern, southwestern and southeastern corners are indicated by three vertical pink lines at stations 12, 19 and 28, respectively. In depth sections, the isoneutrals that delimit the surface, central, intermediate and deep water are represented by white contours. In γ_n sections, the depths of 150, 698 and 1671 m are also shown. The sampling points for dissolved oxygen and inorganic nutrients used in this work are represented by black dots. Sections are only estimated with the CTD-XBT merged dataset.

Figure 3.3 presents the high resolution γ_n field once the XBTs were considered. The upper four layers transported surface waters (SW, first layer above 26.46 kg m^{-3}) and CW (between 26.46 and 27.40 kg m^{-3}); intermediate waters (IW) flowed along the next three layers between 27.40 and 27.922 kg m^{-3}, whereas deep waters (DW) flowed in the deepest layer below 27.922 kg m^{-3}.

The overall distributions of O_2, NO_3, PO_4 and SiO_4H_4 at CW were highly variable and closely related to the location of the different water masses. In transects N and W, where ENACW was dominant, the O_2 concentrations were higher than in transects S and E where SACW was found, with minimum O_2 values lower than 60 μmol kg^{-1} at 300 m (Fig. 3.6). In contrast, the concentrations of the three inorganic nutrients in these last two transects were higher than in transects N and W at CW levels, with concentrations of around 27-30 μmol kg^{-1} for NO_3, 1.5-1.7 μmol kg^{-1} for PO_4, and 7.5-9.9 μmol kg^{-1} for SiO_4H_4 at 300 m depth (Figs. 3.6 and 3.7).

In IW, the O_2 distribution was quite uniform in all transects, presenting a slight increase with depth. With respect to inorganic nutrients, their concentrations in transect N were lower than in the remaining transects, which were occupied by a larger amount of AAIW. Indeed, the largest NO_3 and PO_4 concentrations were registered as being associated with AAIW at around 1000 m in transects S and E (Figs. 3.6 and 3.7). Finally, in the deepest layer, high concentrations of O_2 and inorganic nutrients were found. Specifically, the highest concentrations of SiO_4H_4 were recorded in this deepest layer.

The hydrological and biogeochemical characteristic of the water masses are summarized in Figs. 3.8 and 3.9, where the relationships between in situ measurements of S_A, O_2, NO_3 and PO_4 are displayed. These property-property distributions might be used to define the characteristic values of the water masses in the domain (Emery, 2001). In CW, inverse tight relationships are obtained for NO_3 and PO_4 with S_A, whereas the relationship is direct and looser for O_2 with S_A. In IW, the relationships between NO_3 and PO_4 with S_A are much less defined, with an 'S'-like pattern. In all cases, the relationships between O_2 and NO_3 or O_2 and PO_4 are rather tight and inverse.

The previous distributions are presented from a large-scale perspective. A second reading on the dataset might be performed, emphasizing the role played by mesoscale structures. For instance, an intrathermocline anticyclonic eddy centered in station 4 was detected in Θ, S_A, O_2, NO_3 and PO_4 (Figs. 3.5, 3.6 and 3.7). On the other side, the CVF was also detected in transects S and E as a sharp transition in all properties (Figs. 3.5, 3.6 and 3.7). In particular, O_2 presented two remarkable minimum values of 60 μmol kg^{-1} between 100 and 150 m when the frontal area was crossed (Fig. 3.6). Just below these O_2 minima, the local maxima of NO_3, PO_4 and SiO_4H_4 were recorded (Figs. 3.6 and 3.7).

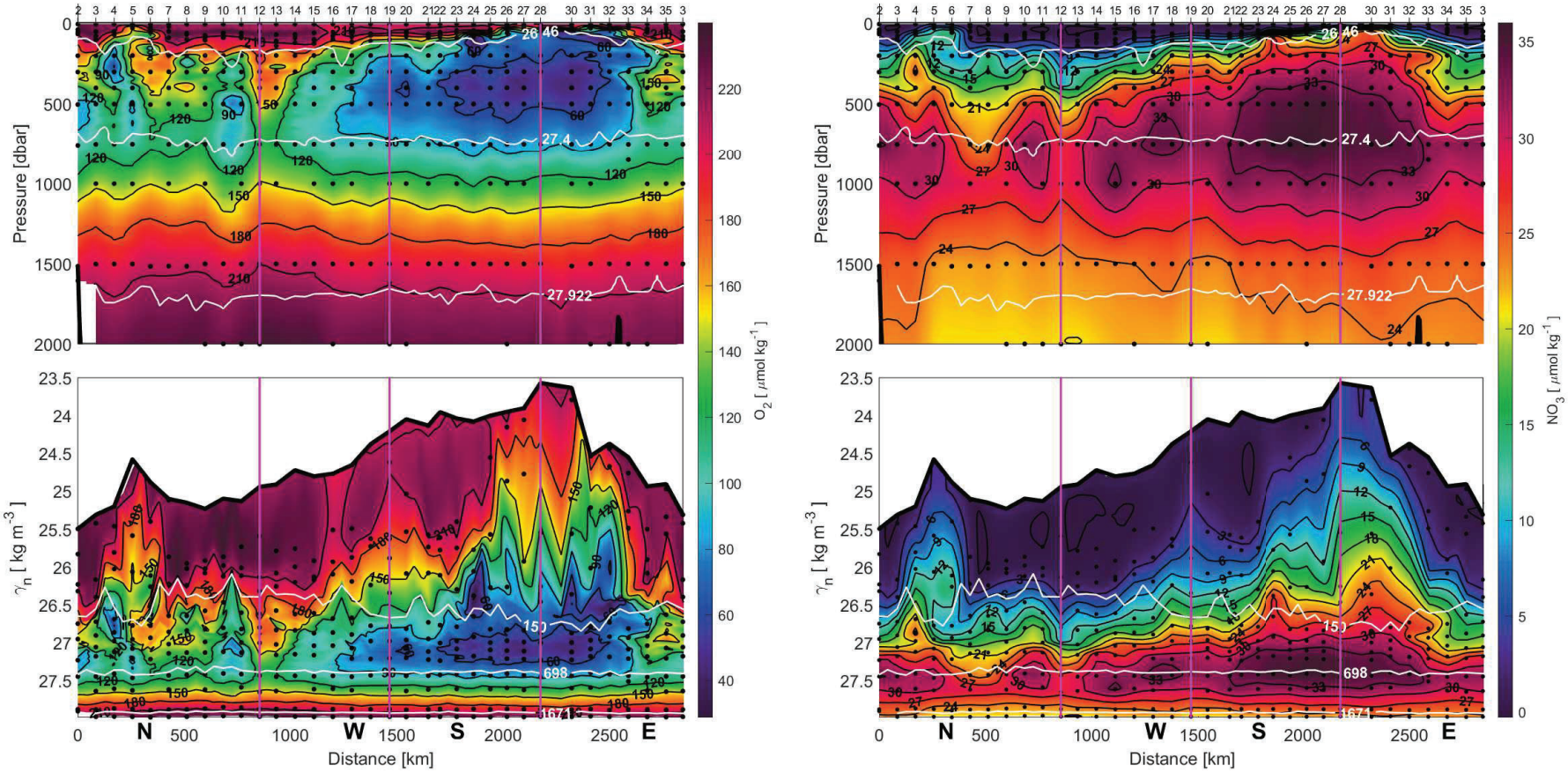

Figure 3.6: Sections of O_2 (left) and NO_3 (right) with respect to depth (upper line) and γ_n (lower line) during the FLUXES-I cruise. The direction chosen for the representation is the same as in Fig. 3.3. The northwestern, southwestern and southeastern corners are indicated by three vertical pink lines at stations 12, 19 and 28, respectively. In depth sections, the isoneutrals that delimit the surface, central, intermediate and deep water are represented by white contours. In γ_n sections, the depths of 150, 698 and 1671 m are also shown. The sampling points of O_2 and NO_3 used in this work are represented by black dots.

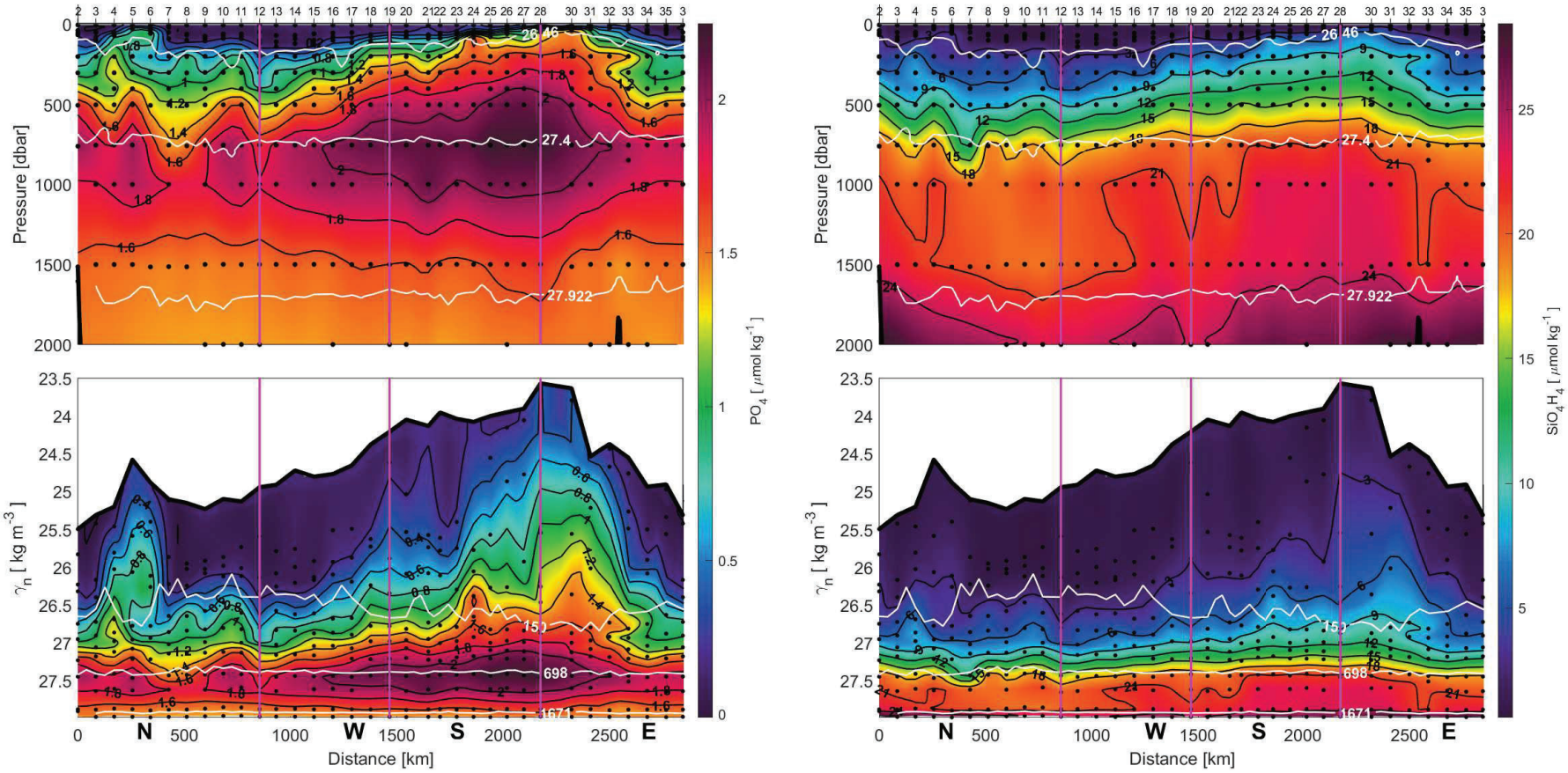

Figure 3.7: Sections of PO_4 (left) and SiO_4H_4 (right) with respect to depth (upper line) and γ_n (lower line) during the FLUXES-I cruise. The direction chosen for the representation is the same as in Fig. 3.3. The northwestern, southwestern and southeastern corners are indicated by three vertical pink lines at stations 12, 19 and 28, respectively. In depth sections, the isoneutrals that delimit the surface, central, intermediate and deep water are represented by white contours. In γ_n sections, the depths of 150, 698 and 1671 m are also shown. The sampling points of PO_4 and SiO_4H_4 used in this work are represented by black dots.

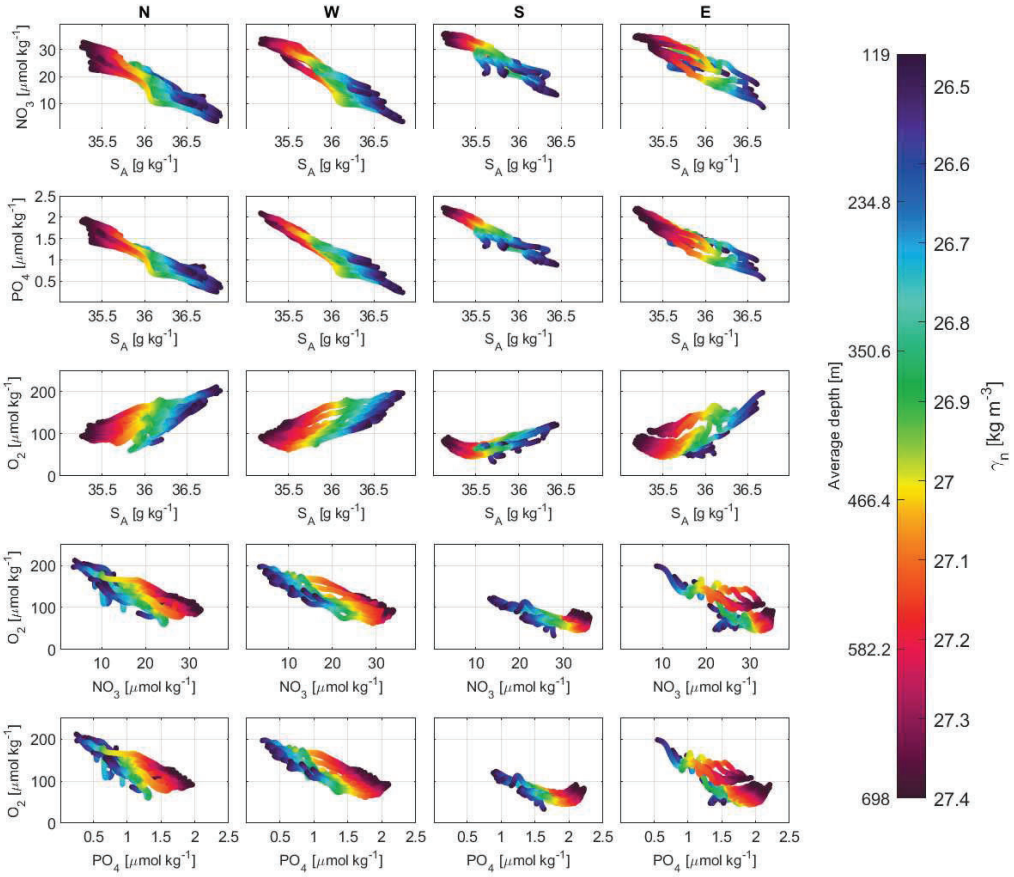

Figure 3.8: Scatterplots of in situ observations of NO_3 (first row), PO_4 (second row) and O_2 (third row) (μmol kg^{-1}) with respect to S_A and γ_n (in colour with an approximate scale of the average depths) in the north (N, first column), west (W, second column), south (S, third column) and east (E, fourth column) transects for CW layers. In fourth and fifth rows, scatterplots of $NO_3 - O_2$ and $PO_4 - O_2$ in four transects for the CW layers are shown.

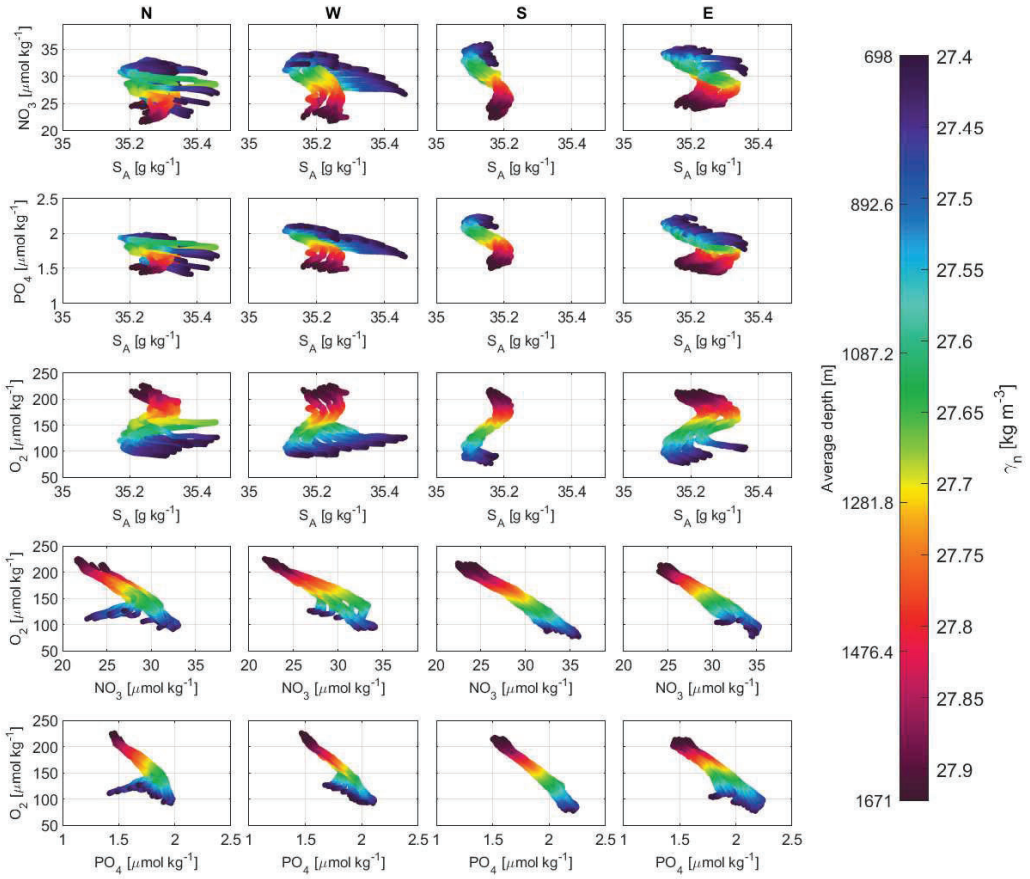

Figure 3.9: Scatterplots of in situ observations ofNO_3 (first row), PO_4 (second row) and O_2 (third row) (μmol kg^{-1}) with respect to S_A and γ_n (in colour with an approximate scale of the average depths) in the north (N, first column), west (W, second column), south (S, third column) and east (E, fourth column) transects for IW layers. In fourth and fifth rows, scatterplots of $NO_3 - O_2$ and $PO_4 - O_2$ in four transects for the IW layers are shown.

3.3.2 Cape Verde Front

The CVF has historically been defined at only one depth, where isohaline 36 (or 36.15 g kg^{-1}, Burgoa et al. (2020)) intersects isobath 150 m (Zenk, Klein, and Schroder, 1991). Following that definition, the CVF could be located during FLUXES-I between stations 23 and 24 in transect S, where $\Delta S_A > 0.70$ g kg^{-1} and $\Delta\Theta > 1.92°$ C were observed between both sides of the front; CVF was also detected between stations 33 and 34 in transect E with lower $\Delta S_A > 0.30$ g kg^{-1} and $\Delta\Theta > 1.10°$ C values (Fig. 3.5).

The method developed in this paper to estimate the vertical location of the front depicted a complex spatial distribution (Fig. 3.10). The CVF is represented by several isohalines associated with specific depths. These isohalines unveil that the front was almost completely vertical in transect E, while in the southwestern corner it presented a notable slope with its surface end located south of its deep end. Hence, the front was oriented from northeast to southwest at near-surface layers, whereas it presented a roughly eastwest orientation at 698 m depth (Fig. 3.10a).

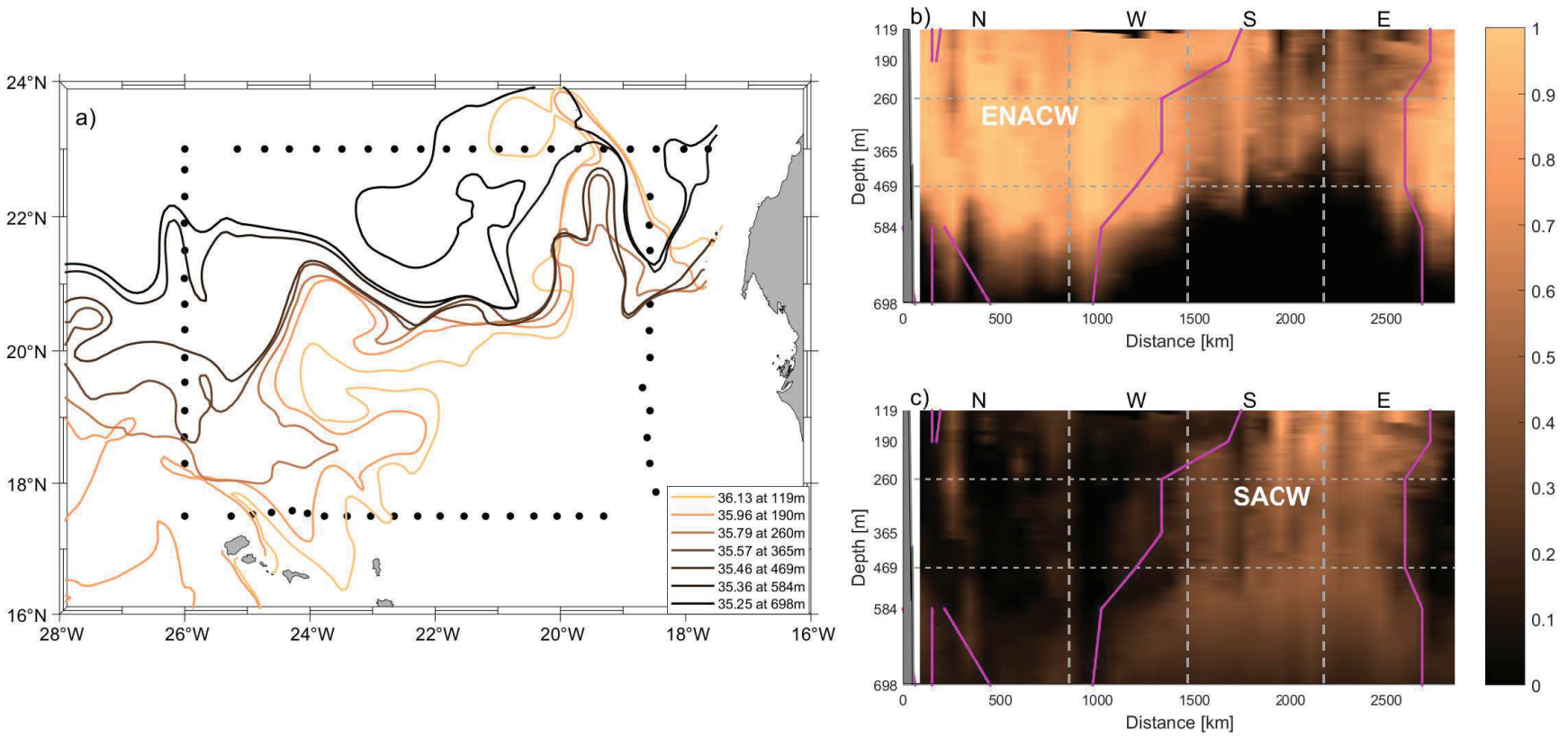

Figure 3.10: a) Location of the front at the 36.07, 35.88, 35.67, 35.43, 35.31, 35.2 and 35.08 isohalines, corresponding to average depths of 119, 190, 260, 365, 469, 584 and 698 m, equivalent to 26.46, 26.63, 26.85, 26.98, 27.162, 27.28 and 27.40 kg m^{-3}, respectively. Vertical sections of the three layers of CW with the percentages of ENACW (b) and SACW (c), and the front location superimposed by pink lines. The direction chosen for the representation is the same as in Fig. 3.3. The northwestern, southwestern and southeastern corners are indicated by three vertical gray dashed lines. Three layers are also separated by two horizontal gray dashed lines.

On the other hand, the CVF location presented with this methodology is indicated along the transects (pink lines), revealing a remarkable match with the distributions of the maximum contributions of ENACW (MMW+ENACW15+ENACW12) and SACW (SACW18+SACW12) estimated with the OMP (Figs. 3.10b and c).

3.3.3 Inverse model solution

The inverse model provided absolute geostrophic velocities for transects N, W and S, extended to the coast with WOA nodes. Mass transports were then evaluated to estimate the mass imbalance within the closed box. Figure 3.11 presents the mass transports accumulated along transects N, W and S, grouped by different water levels (upper panel); the figure also shows the transports integrated per layer and transect (lower panel). Note that positive (negative) values represent outward (inward) transports from (to) the closed box (1 Sv=10^9 kg s^{-1}). The mass transport imbalance in every water level was roughly zero once it was accumulated along the box, indicating that the mass was highly conserved (Fig. 3.11a). An imbalance was observed in the net transport mainly associated with the first and third layers (black line in Fig. 3.11b), likely related to mesoscale structures undersampled during the cruise.

Large transports are obtained in the entire water column. In the two shallowest layers, the mass exchange is basically from north and south to the west, carrying some 3.4 Sv. In the third and fourth layers, transports continued entering from the south, whereas transports reversed in the N and W transects, flowing a total of some 1 Sv. At IW levels, the estimated transports were moderately high and northward, with more than 3 Sv that entered through the W and S transects. At DW levels, the integrated mass transports were around 1 Sv, maintaining the IW levels' scheme.

The results obtained from the inversion are compared with two independent databases: transports from altimetry and transports from the GLORYS numerical model (Fig. 3.12). These transports are calculated by multiplying the velocity at surface by the vertical area covered by the first layer in the inverse model. Accordingly, in the case of the inverse model we have used the accumulated mass transports in the first layer. The overall transport structure is rather similar for all three cases, in particular between the inverse model and the altimetry. GLORYS might not be recovering the mesoscale signal, and its low response to this variability is likely causing it to deviate it from the other two databases. In all cases, the final imbalance is quite similar - about 1.5-2 Sv.

3.3.4 Geostrophic velocity

The previous result is now applied to present the geostrophic velocities along the three transects developed to perform the inverse model. Figure 3.13 displays the absolute velocity field perpendicular to each transect with a geographic criteria (positive velocities are northward and eastward). The absolute velocity field might be described as alternating vertical cells with velocities in the range from -0.25 to 0.25 m s^{-1}; the largest velocities are mainly found in the upper 200-300 m depth.

This velocity field helps to identify several mesoscale features captured during the cruise. Besides the intrathermocline anticyclonic eddy located between stations

3 and 5, another cyclonic eddy was centered between stations 5 and 7, next to the first eddy. Transect N was also crossed by a second anticyclonic eddy between stations 9 and 12. The main mesoscale structures sampled in transect W were a meander between stations 15 and 18 and an intrusion found between stations 18 and 19, which actually entered the box through the southwestern corner. A second part of this intrusion is observed in transect S, where it entered the box between stations 19 and 20 and left between stations 20 and 21. From stations 22 to 26, some additional meandering was observed along transect S. A cyclonic eddy had a notable negative velocity in the middle part of transect S centered at station 27.

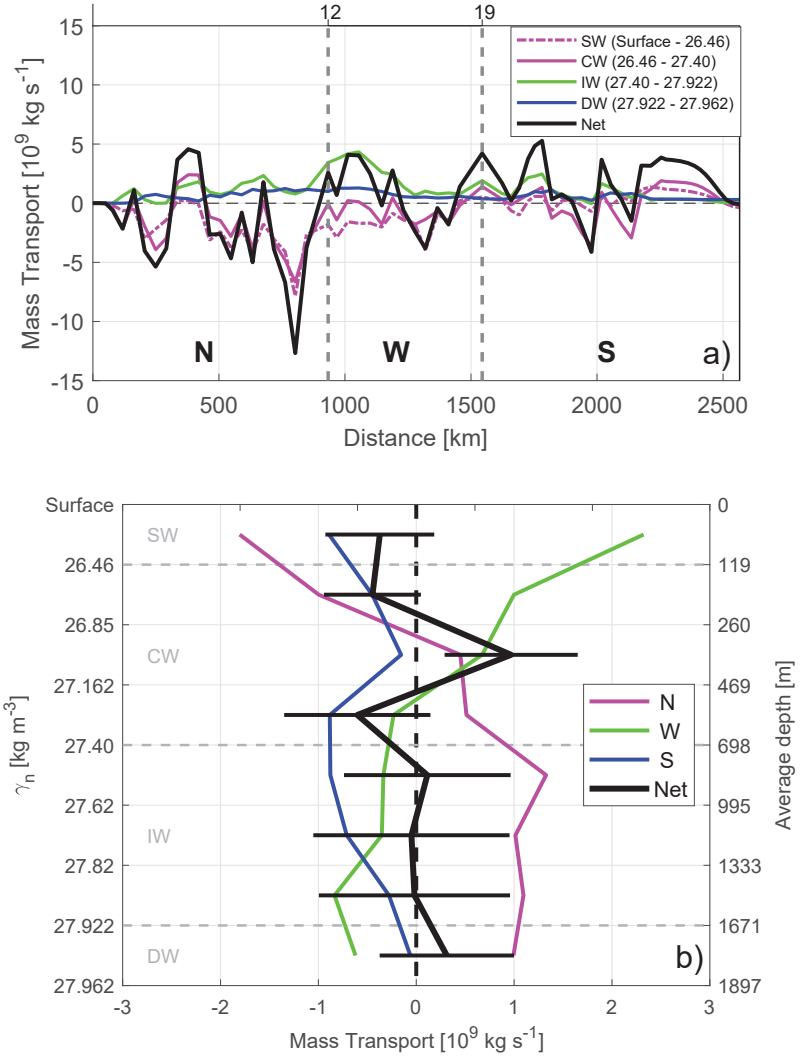

Figure 3.11: a) Accumulated mass transports per SW, CW, IW and DW levels, and b) mass transports integrated per north, west, and south transect, estimated by the inverse model during the FLUXES-I cruise (including WOA stations in transects N and S). Negative (positive) values indicate inward (outward) transports in both plots. Mass conservation in the whole domain close to the coast is shown by the black line. The northwestern and southwestern corners are indicated by vertical dashed lines at stations 12 and 19 in the accumulated mass transports (a). The horizontal bars in each layer represented by the net mass transport are the errors estimated by the inverse model (b).

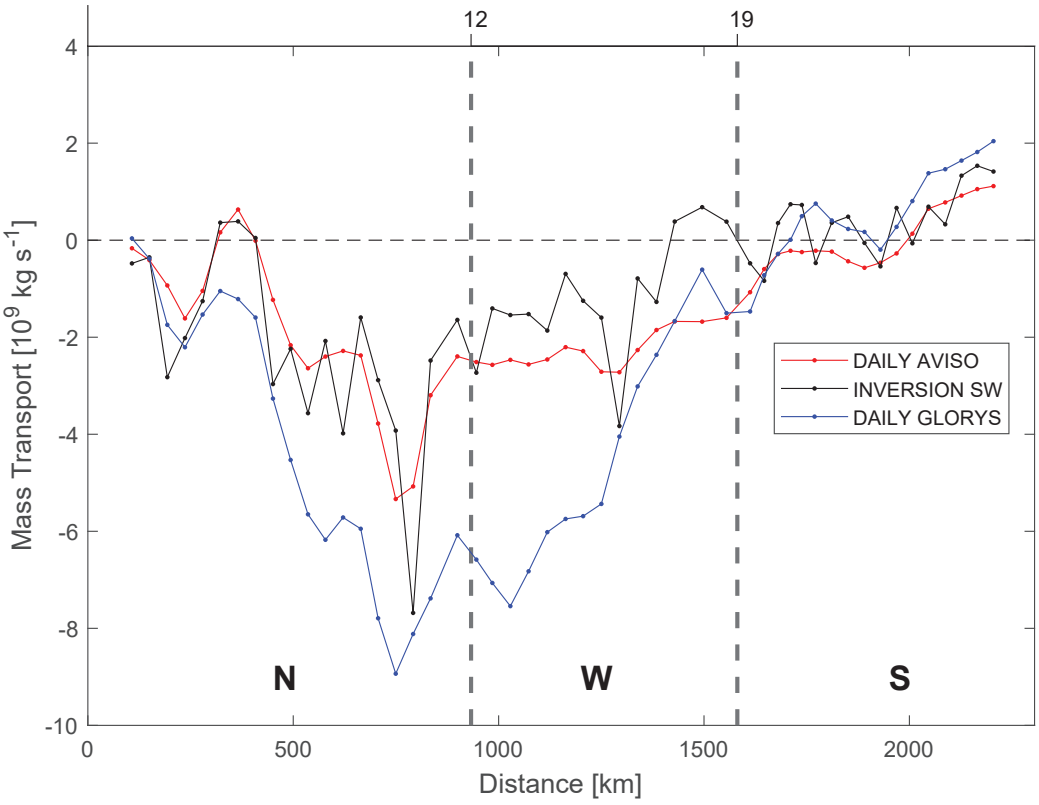

Figure 3.12: Accumulated mass transports in the first layer of SW estimated along the N, W and S transects (without WOA stations) with altimetry-derived geostrophy (red line), inversion (with GLORYS data as reference velocities, black line) and GLORYS field (blue line). Negative (positive) values indicate inward (outward) transports, as in Fig. 3.11. The northwestern and southwestern corners (at stations 12 and 19) are indicated by vertical dashed lines.

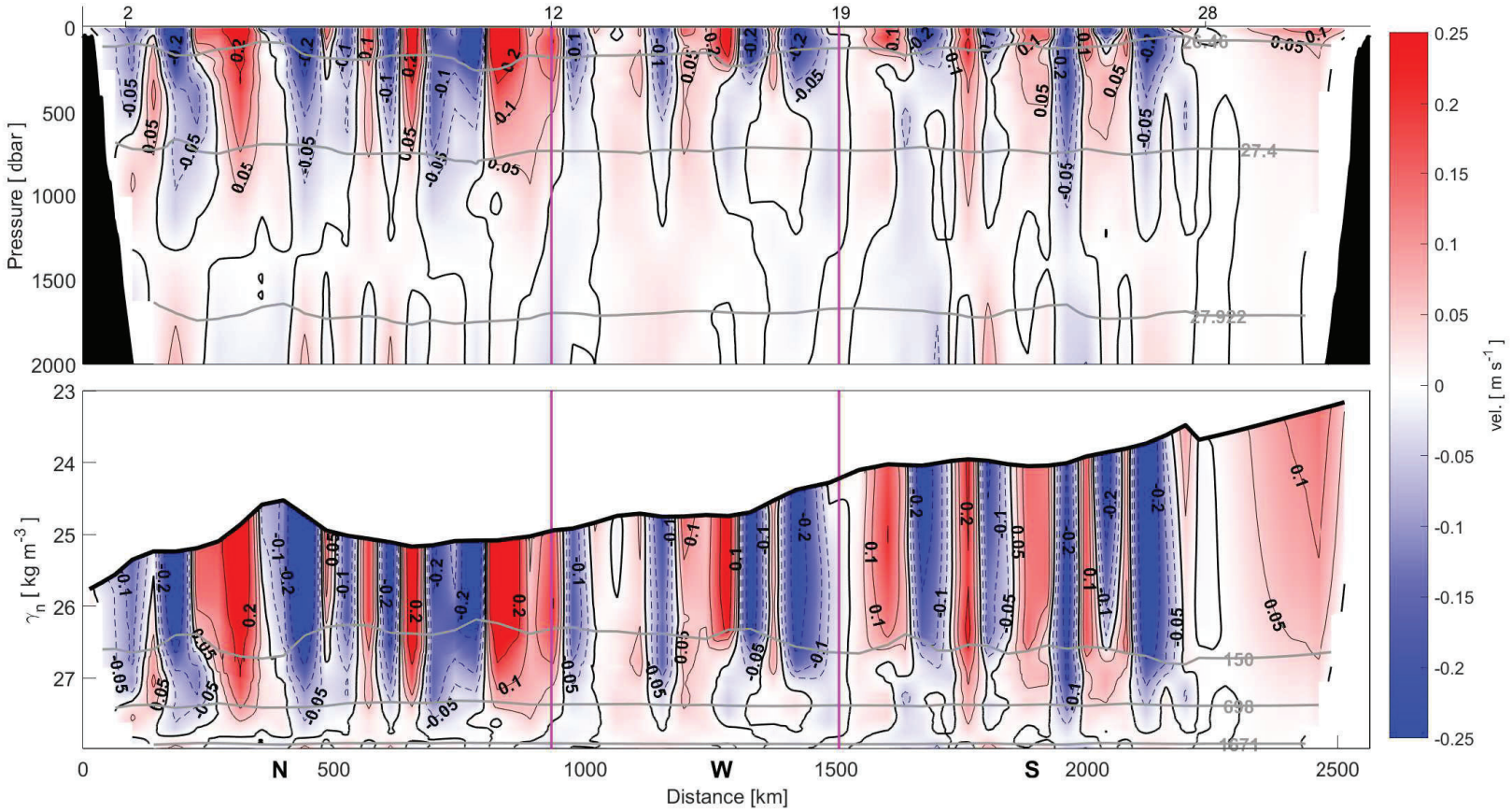

Figure 3.13: Sections of the absolute geostrophic velocity perpendicular to each transect with respect to depth (upper panel) and γ_n (lower panel) during the FLUXES-I cruise (including WOA stations). The velocity sign was selected on geographic criteria (positive sign northward and eastward). The direction chosen for the representation is the same as in Fig. 3.3. The zero contour line is the thick black line. The northwestern and southwestern corners are indicated by vertical pink lines at stations 12 and 19. In depth sections, the isoneutrals that delimit the surface, central, intermediate and deep water are represented by gray contours. In γ_n sections, the depths of 150, 698 and 1671 m are also shown.

3.3.5 Inorganic nutrient and O_2 transports

The transports (integrated per water level and transect) for O_2, NO_3, PO_4 and SiO_4H_4 are presented in Figure 3.14 and compiled in Table 3.2. At IW and DW levels, the transports for all properties are nearly balanced and may be described as a net northward transport with contributions from the western and southern transects.

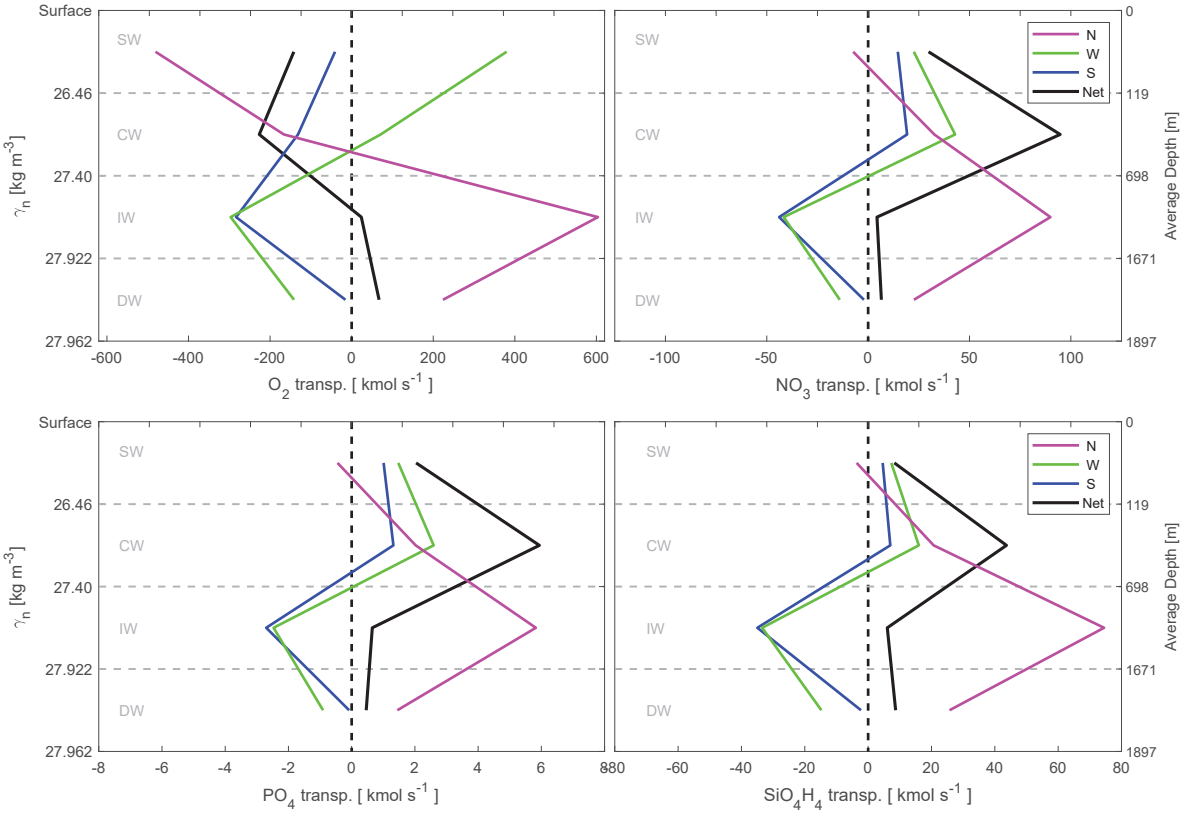

Figure 3.14: O_2, NO_3, PO_4 and SiO_4H_4 transports (in kmol s^{-1}) integrated per water-type level (SW, CW, IW and DW) in the north (N, pink line), west (W, green line) and south (S, blue line) transects during the FLUXES-I cruise (including WOA stations). The black line represents the net transport of each biochemical variable. See Tab. 3.2 to check the O_2, NO_3, PO_4 and SiO_4H_4 transports' values in each layer per transect. Negative (positive) values indicate inward (outward) transports, as in Fig. 3.11.

However, the transports at SW and CW levels present an imbalanced distribution that can not be fully related to imbalances in the mass transports, as mass transports are nearly balanced at those water levels. Transports present a distribution where O_2 enters the box through transects N and S; a lower amount of O_2 leaves the box through transect W, revealing a net O_2 decay within the box. The highest O_2 transports are obtained at SW levels, as a combined effect of large velocities and high O_2 concentration in the photosynthetic layer in contact with the atmosphere. Finally, the pattern in the transports' distribution is quite the same for NO_3, PO_4 and SiO_4H_4: nutrients leave the domain through transects N, W and S, with a tiny amount entering the box through transect N at the SW

and CW levels. The lowest transports for inorganic nutrients are obtained in the SW layer, as a consequence of nutrient depletion within the photic layer, whereas the highest transports are observed at CW and IW levels. A large imbalance is obtained at CW levels, providing a net nutrient increase within the box at CW levels.

Biogeochemical budgets can be obtained for the entire water column once we have produced the net lateral transports of O_2 and inorganic nutrients (Table 3.2). To do so, we first still need to estimate the O_2 exchange between the sea surface and the atmosphere. We have proceeded as documented by Wanninkhof, 2014, using an average wind speed for the whole domain (U, m s^{-1}) and the Schmidt number (Sc) for O_2 to estimate the gas transfer velocity (k, cmh^{-1}) as $k = 0.251 < U^2 > (Sc/660)^{-0.5}$. We then estimated the average apparent oxygen utilization (AOU); the O_2 transport from the sea surface to the atmosphere is also estimated as $F = -k\overline{AOU}A/1000$, where A is the surface area of the domain (m^2). These calculations provide an O_2 export to the atmosphere of 113.54 kmol s^{-1}. This number indicates that the total O_2 consumption within the box is 163.8 kmol s^{-1}, as the lateral transport integrated for the whole sampled water column was -277.34 kmol s^{-1}. On the other hand, the inorganic nutrient positive balances indicate that the domain is producing inorganic nutrients, likely as a consequence of remineralization below the photic layer; the nutrient import from the atmosphere is considered negligible compared with lateral transports, according to climatological values reported by Fernández-Castro, Mouriño-Carballido, and Álvarez-Salgado (2019). Hence, this domain would be acting as an heterotrophic box, as revealed by the net oxygen consumption, with remineralization of NO_3, PO_4 and SiO_4H_4 below the photic layer.

3.4 Discussion

We have presented the dynamics related to the water masses and their O_2 and inorganic nutrient content in the transition between the eastern NASG and the NATG during summer 2017. The water masses' distribution in the CVFZ during FLUXES-I is consistent with that documented previously (Hernández-Guerra et al., 2005; Pastor et al., 2012; Peña-Izquierdo et al., 2012; Burgoa et al., 2020): a latitudinal change between the ENACW and SACW below the mixing layer and above 700 m was detected from north to south (Pelegrí et al., 2017), while a second latitudinal transition was observed in IW between AAIW and MW from south to north (Zenk, Klein, and Schroder, 1991), with AAIW being the dominant water mass. The characteristic of these water masses are conditioned by their origin and the path followed on their way to the CVB. While transects N and S present well-defined water masses, transects W and E reflect a water masses transition between transects N and S. The large variability registered at the SW and CW levels is related to the CVF position, the proximity of the CUF north of the domain and the meso- and sub-mesoscale structures associated with these two frontal systems, as the upwelling filaments off Cape Blanc (Meunier et al., 2012; Lovecchio, Gruber, and Münnich, 2018; Appen et al., 2020). The ENACW and SACW property distributions presented in Figure 3.8 compare well with those reported by Pastor et al., 2008 and Pelegrí and Benazzouz, 2015b. At IW levels, the variability is mainly

related to the AAIW flowing northward to the Canary Islands basin (Machín and Pelegrí, 2009; Machín et al., 2010). The shadow zone documented by Kawase and Sarmiento, 1985 and the development of an oxygen minimum zone (OMZ) within CW and IW levels was centered in transect S between 100 and 800 m depth with its core around 400 m between isoneutrals 27.1 and 27.3 kg m^{-3} (Karstensen, Stramma, and Visbeck, 2008; Brandt et al., 2015; Thomsen et al., 2019). That distribution matches well with the one provided by Peña-Izquierdo et al., 2015, with high concentrations of NO_3 and PO_4.

A major contribution from this paper is the development of an extended version of the classical methodology applied to locate the CVF. Following the definitions of the SACW and ENACW reported by Tomczak, 1981 and the interpretation of the CVFZ by Zenk, Klein, and Schroder (1991), the front 3-D structure from 150 to 650 m depth has been produced combining in situ and GLORYS data (Fig. 3.10). Fist of all, we would like to highlight the consistency between the results produced from the in situ observations compared to the results from the GLORYS model. The front spatial disposition reveals that the CVF is a complex meandering front with several associated mesoscale features, showing a variable geographical orientation at different depths (Barton, 1987; Martínez-Marrero et al., 2008; Pastor et al., 2008; Pastor et al., 2012). The vertical distribution of the CVF enables the interpretation of the imbalances in lateral transports of mass, O_2 and inorganic nutrients at both sides of the front (Tab. 3.3). The predominance (lack) of SACW (ENACW) in transect S suggests that the CVF may be functioning as a barrier against lateral transports across the front. The CVF also influenced its adjacent waters, as observed, for example, in the minima of O_2 and the maxima of NO_3 and PO_4 sampled just below 150 m in the tropical side of the front, which might be indicating a local remineralization (Fig. 3.6) (Thomsen et al., 2019).

The main limitation in the present analyzes were related to the high relative importance of mesoscale features in the domain. These features modify the thermohaline field with an intensity capable of inducing transports of approximately the same order of magnitude as those related to the large-scale circulation (Volkov, Lee, and Fu, 2008; Zhang, Wang, and Qiu, 2014). On the one hand, if the mesoscale field is undersampled, it might induce large imbalances when quantifying the large-scale transports. On the other hand, the important dynamics associated with the mesoscale might also produce a lack of synopticity when the sampling takes longer than 15-20 days. These two effects might be responsible for the main limitations found in the dataset, as mesoscalar structures were observed in almost all hydrographic sections. In turn, mesoscale structures impact on the physical-chemical variables in the domain, which might become significantly altered (Appen et al., 2020). A second limitation could be the absence of diapycnal transfers in the model. The imbalances diagnosed for the SW and CW would be reduced if a downwelling in the upper 300 m developed as a consequence of the upwelling relaxation during the cruise dates.

Table 3.2: Mass transports and their errors (in Sv) and transports of O_2, NO_3, PO_4 and SiO_4H_4 (in kmol s^{-1}) with their errors relative to mass transport for SW, CW, IW, and DW across northern, western, southern and eastern transects for the FLUXES-I cruise (with WOA stations). Positive (negative) values indicate outward (inward) transports. The total row of each inorganic nutrient or O_2 is its integrated transport throughout the whole water column. The last column is the maladjustment or imbalance of each water level.

TRANSPORT	WATER LEVEL	NORTH	WEST	SOUTH	IMBALANCE
CW [Sv]	SW	-1.80 ± 0.75	2.32 ± 0.79	-0.89 ± 0.59	-0.37 ± 1.24
	CW	-0.03 ± 1.49	1.44 ± 1.62	-1.49 ± 1.73	-0.08 ± 2.80
	IW	3.43 ± 2.54	-1.52 ± 2.73	-1.87 ± 2.55	0.05 ± 4.52
	DW	0.99 ± 0.99	-0.62 ± 1.07	-0.06 ± 1.04	0.31 ± 1.79
	TOTAL	2.59 ± 3.19	1.62 ± 3.44	-4.31 ± 3.31	-0.09 ± 5.74
O_2 [kmol s^{-1}]	SW	-480.79 ± 198.59	379.80 ± 129.89	-40.79 ± 27.09	-141.77 ± 225.46
	CW	-166.13 ± 764.92	71.14 ± 79.95	-131.51 ± 152.72	-226.49 ± 489.00
	IW	603.63 ± 446.28	-296.60 ± 530.85	-283.33 ± 387.17	23.70 ± 794.27
	DW	223.75 ± 222.64	-141.27 ± 244.20	-15.25 ± 263.23	67.23 ± 222.93
	TOTAL	180.46 ± 222.42	13.08 ± 27.77	-470.88 ± 361.33	-277.34 ± 975.37
NO_3 [kmol s^{-1}]	SW	-7.39 ± 3.05	22.54 ± 7.71	14.65 ± 9.73	29.80 ± 47.39
	CW	32.64 ± 150.30	42.88 ± 48.19	19.22 ± 22.32	94.74 ± 204.5
	IW	89.91 ± 66.47	-41.65 ± 74.55	-43.90 ± 60.00	4.36 ± 242.61
	DW	22.56 ± 22.45	-13.97 ± 24.15	-2.06 ± 35.47	6.53 ± 21.70
	TOTAL	137.72 ± 169.74	9.80 ± 20.81	-12.09 ± 9.28	135.43 ± 476.30
PO_4 [kmol s^{-1}]	SW	-0.45 ± 0.18	1.47 ± 0.50	1.01 ± 0.67	2.04 ± 3.24
	CW	2.02 ± 9.32	2.59 ± 2.91	1.32 ± 1.53	5.94 ± 12.82
	IW	5.83 ± 4.31	-2.47 ± 4.42	-2.70 ± 3.69	0.65 ± 36.36
	DW	1.45 ± 1.44	-0.91 ± 1.56	-0.08 ± 1.37	0.46 ± 1.53
	TOTAL	8.85 ± 10.91	0.69 ± 1.47	-0.45 ± 0.35	9.09 ± 31.96
SiO_4H_4 [kmol s^{-1}]	SW	-3.63 ± 1.50	7.30 ± 2.50	4.59 ± 3.05	8.27 ± 13.15
	CW	20.68 ± 95.22	16.00 ± 17.98	7.00 ± 8.13	43.68 ± 94.29
	IW	74.49 ± 55.07	-33.46 ± 59.88	-34.98 ± 47.80	6.05 ± 336.72
	DW	25.70 ± 25.57	-14.76 ± 25.52	-2.26 ± 38.92	8.68 ± 28.71
	TOTAL	117.24 ± 144.50	-24.92 ± 52.92	-25.65 ± 19.68	66.67 ± 234.49

Table 3.3: Total imbalances of mass, O_2, NO_3, PO_4 and SiO_4H_4 transports in the subtropical and tropical areas separated by the CVF at the three CW layers. All imbalances are estimated from the integrated transports from each respective side of the front and considering transports between WOA stations.

TRANSPORT	**SUBTROPICAL IMBALANCE**	**TROPICAL IMBALANCE**
CW [Sv]	0.56 ± 1.47	-0.63 ± 1.68
O_2 [kmol s^{-1}]	-153.12 ± 714.98	-73.38 ± 134.08
NO_3 [kmol s^{-1}]	46.68 ± 133.26	47.07 ± 99.62
PO_4 [kmol s^{-1}]	2.88 ± 11.36	3.05 ± 6.20
SiO_4H_4 [kmol s^{-1}]	23.37 ± 109.32	20.32 ± 44.14

The velocity field has a direct impact on the exchange of O_2 and inorganic nutrients at intermediate and deep water levels. The net balanced northward transport carries some 827 kmol s^{-1} of O_2, 112 kmol s^{-1} of NO_3, 7.3 kmol s^{-1} of PO_4 and 100 kmol s^{-1} of SiO_4H_4. These values are well above the horizontal advection estimated from climatological data reported by Fernández-Castro, Mouriño-Carballido, and Álvarez-Salgado, 2019 at intermediate and deep levels. However, the net horizontal transports presented in both analyses have very small values in intermediate and deep waters.

On the other hand, at surface and central levels the role played by biogeochemical processes also needs to be considered to outline the full picture of the processes forcing the variability in the O_2 and inorganic nutrients transports. A westward imbalanced transport of O_2 is observed at SW and CW levels, with a deficit of some 368 kmol s^{-1} related to the lower O_2 concentration in the outflowing compared with the inflowing waters (Fernández-Castro, Mouriño-Carballido, and Álvarez-Salgado, 2019). With respect to nutrients at these levels, the domain acts as a source, with net outward transports through the three transects of some 125 kmol s^{-1} for NO_3, 8 kmol s^{-1}for PO_4 and 52 kmol s^{-1} for SiO_4H_4. The western section presents the highest outward transports for the three nutrients at SW and CW levels, as in Fernández-Castro, Mouriño-Carballido, and Álvarez-Salgado, 2019; our transports, however, are much larger than the climatological values provided by these authors. The calculations performed for the whole box, where the O_2 export to the atmosphere was considered, somehow define a pattern for the offshore export of inorganic nutrients as a consequence of O_2 consumption followed by nutrient remineralization below the photic layer. In this case, we would not expect the result to fit within the Redfield ratio as we are working with the whole box instead of differentiating between the surface layer (where oxygen production and nutrient consumption dominate) and the layers below (where net oxygen consumption and inorganic nutrients mineralization occurs). To do so, we would need to deal with the surface layer separately and estimate the role played by vertical advection and turbulence; this approach is beyond the scope of this study.

Despite the fact that the eastern section was not part of the inverse model, it still may provide insights into the transports within the domain in a location quite close to the coastal upwelling (Fig. 3.15). Mass transports indicate eastward transport at SW, CW and DW levels, whereas the transports reverse westward

at IW levels. Transports related to O_2 and inorganic nutrients reflect a similar pattern. O_2 transports are close to zero at SW and CW levels, likely as a result of the high relative importance of the OMZ in this eastern section. Nutrients at the SW level present low onshore transports, wheras their transports increase at CW levels. At the IW and DW levels, a straight relationship is also observed for O_2 and inorganic nutrients when compared with the mass transports' pattern. Hence, in this eastern section, it seems that the physical forcing is the dominating factor explaining the variability in the transports.

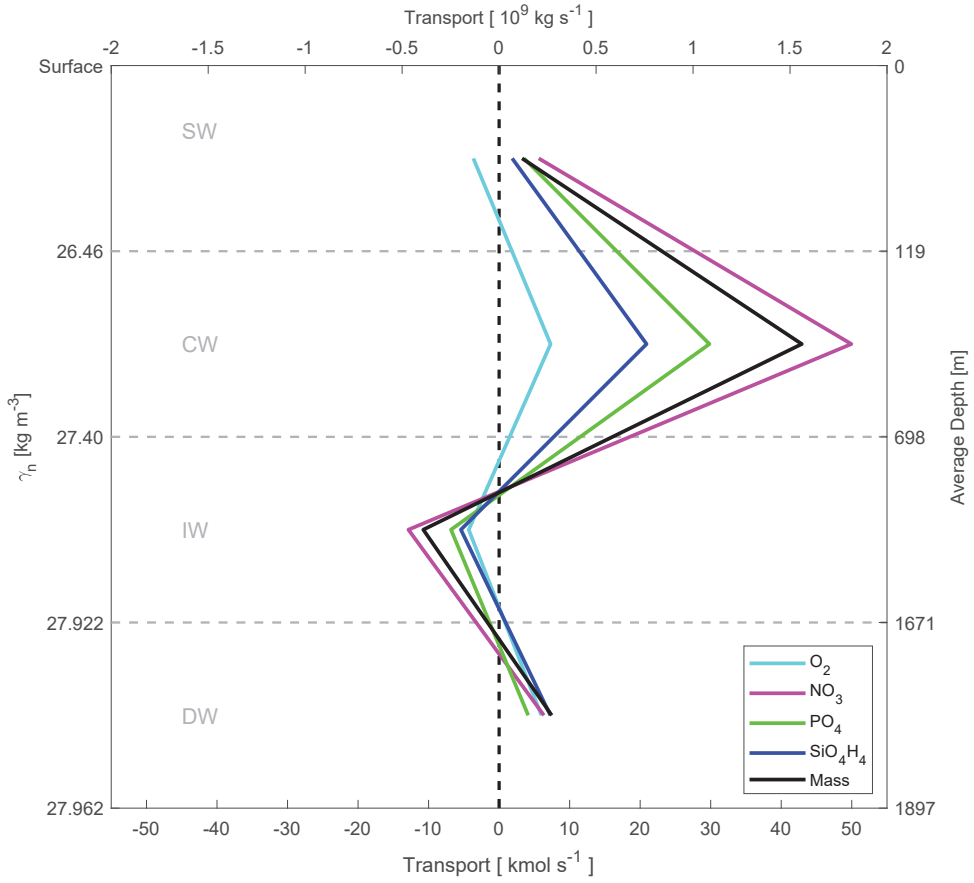

Figure 3.15: Mass (10^9 kg s^{-1}), O_2, NO_3, PO_4 and SiO_4H_4 transports (in kmol s^{-1}) integrated per water-type level (SW, CW, IW and DW) through transect E during the FLUXES-I cruise. Eastward transports were defined as positive. The O_2 (PO_4) transport is represented as being divided (multiplied) by 10.

Finally, the development of a frontal zone provides the opportunity to perform the transports analysis at both sides of the front, in the tropical and subtropical domains within CW levels (Tab. 3.3 and Fig. 3.16). The mass transport imbalance is less than 1 Sv on both sides of the front. The pattern associated with transports is consistent with a southwestward transport on the subtropical side and a westward transport in the tropical domain, consistent with previous authors such as Pastor et al. (2008). Once the O_2 and inorganic nutrient transports are estimated on both sides, their behavior is quite similar, with a net O_2 decay and a net increase of inorganic nutrients. The main difference between both sides is

related to the transports of O_2, which is lower in the tropical side, about a half of the subtropical value, presumably related to the larger extension of the OMZ in this particular area.

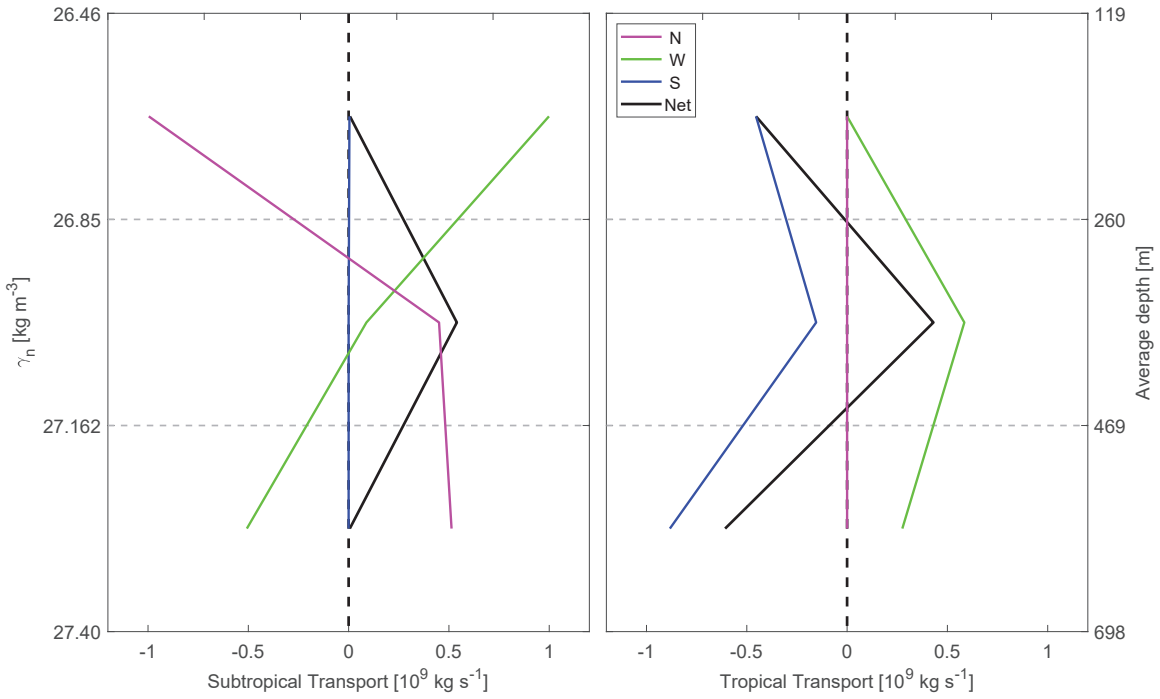

Figure 3.16: Mass transports (10^9 kg s^{-1}) integrated per transect north (N, pink line), west (W, green line) and south (S, blue line) of the subtropical (left) and tropical (right) areas separated by the CVF at the three CW layers (considering transports between WOA stations). The black line represents the net transport. Negative(positive) values indicate inward (outward) transports, as in Fig. 3.11.

3.5 Conclusions

In summary, the circulation in the transition zone between the coastal upwelling and the interior ocean, in the vicinity of the Cape Verde Front, is described as a westward flow at surface and central levels, on both the tropical and subtropical sides of the front, transporting about 3.76 Sv. Below, at intermediate levels, the circulation is markedly northward, carrying about 3 Sv. Mesoscale features constitute a main source of variability in the circulation at these water levels. On the other hand, the Cape Verde Front is featured from 100 to 700 m depth throughout the domain sampled; it presents a large meandering structure with an orientation that varies with depth. Finally, the O_2 and inorganic nutrient transports at central levels are conditioned by biogeochemical processes with a decrease in O_2 and an increase in inorganic nutrients. At intermediate levels, the variability in the O_2 and inorganic nutrient transports are highly conditioned by physical factors. Once the O_2 export to the atmosphere is accounted for, the domain is revealed as an heterotrophic system due to O_2 consumption, with remineralization of inorganic nutrients.

Chapter 4

Dynamic characterization of submesoscale and mesoscale structures in the Cape Verde Frontal Zone

Burgoa, N., Rodríguez-Santana, A., Pallàs-Sanz, E., Machín, F., Marrero-Díaz, A., Valencia, L. P., Grisolía, D., Gordo, C. and Martínez-Marrero, A. Dynamic characterization of submesoscale and mesoscale structures in the Cape Verde Frontal Zone. In prep.

Abstract

The FLUXES-II cruise carried out in November 2017 allows to study the spatio-temporal variability of the Cape Verde Frontal Zone, CVFZ (in which the front develops between the North Atlantic Central Water, NACW, and South Atlantic Central Water, SACW) with two different spatial resolutions and during three successive sampling legs in a total time-period shorter than a month. For the first time, the ageostrophic and geostrophic horizontal fields are estimated from direct current measurements provided by sADCP to describe the horizontal dynamics in the region. The w vertical velocity field estimated by the diabatic Omega equation is shown together with the horizontal dynamics to unveil the processes involved in the development of the mesoscale and submesoscale 3-D thermohaline structures sampled by the towed undulating vehicle with CTD (Seasoar) from the sea surface to 400 m depth in the CVFZ. The structure of the front detected in all the legs allows to deduce that the variability below 100 m depth is less than that located above 100 m where abundant submesoscale thermohaline structure is sampled with the largest horizontal and vertical velocities. However, the mesoscale anticyclonic eddy located in northeast with larger intensities in the first leg and smaller in the last two legs, influences the horizontal advective movements of the water masses and the associated thermohaline structures above and below 100 m depth. The NACW-SACW front displacements influenced by the anticyclonic eddy are described in particular, where the most intense salinity, temperature and density front is simultaneously detected from 70 m to 200 m depth and the geostrophic and ageostrophic horizontal velocities are in opposite direction. Despite the smallest sADCP velocities are measured in the last two legs, the w vertical velocities and the geostrophic and ageostrophic horizontal currents increase when the sampling resolution is higher. Specifically, in the highest resolution leg, an important flow convergence is measured by sADCP associated with a dipole formed by ascending

and descending intense movements at the termohaline front. In general, in all the sampled legs, the best approximation of the vertical velocity is lower than that expected in this highly dynamic and complex zone. This fact may be due on the one side to the w of the total kinematic deformation which is practically canceled by the subtraction between the ageostrophic and geostrophic deformations' w terms that have roughly the same value and with the opposite sign and, on the other side, due to the fact that w terms related to vertical mixing of momentum and buoyancy are especially small.

4.1 Introduction

Submesoscale and/or mesoscale fronts are ocean boundaries often found in areas with strong mesoscale activity (Capet et al., 2008; Pallàs-Sanz, Johnston, and Rudnick, 2010b) and vigorous vertical circulation (Pollard and Regier, 1992; Rudnick, 1996). Depending on the effects that an ocean front has on the density field, the front can be dynamically classified either as a density or as a density-compensated front (Poole and Tomczak, 1999). A density front with geostrophic along-front currents is featured by a maximum horizontal gradient and an associated ageostrophic secondary circulation (ASC) that includes horizontal and vertical velocities to restore geostrophic balance (Hoskins, Draghici, and Davies, 1978; Fedorov, 1986; Pollard and Regier, 1992; Rudnick, 1996; Spall, 1997; Garabato et al., 2001; Capet et al., 2008; Pallàs-Sanz, Johnston, and Rudnick, 2010a; Barceló-Llull et al., 2017b). However, if the front exhibits maximum horizontal gradients in both salinity and temperature but not in density, the front is considered to be a density-compensated, or only thermohaline, front where the effects of the changes in salinity across the front compensate the changes in temperature on the density field (Roden, 1975; Roden, 1980; Roden, 1984). As a consequence, this last kind of fronts is not associated with strong geostrophic flows and the frontal mixing is dominated by double-diffusive interleaving processes (Tippins and Tomczak, 2003; Kuzmina, 2016).

Many authors produced high-resolution in situ data performing exhaustive cruises with substantial observational effort aimed at understanding the fronts' formation, dynamics and persistence. In some of these cases, the undulating SeaSoar (Pollard, 1986) was employed to sample the front's hydrology while the current measurements were gathered with a sADCP (Pollard and Regier, 1992; Barth, Cowles, and Pierce, 2001; Gomis, Ruiz, and Pedder, 2001; Shcherbina et al., 2009; Pallàs-Sanz, Johnston, and Rudnick, 2010a). In the western area of the Mediterranean Sea, hard work has been made comparing in situ, drifters and remote sensing data at meso- and submesoscale levels in the frontal systems of the Alboran Sea (Pascual et al., 2017; Ruiz et al., 2019). However, these high spatial resolution data are incapable to also address the evolution of structures over time. Therefore, the evolution is usually assessed with comprehensive numerical models that would need to validate their outputs with observations (Thomas, Tandon, and Mahadevan, 2008; Soufflet et al., 2016; Aguiar et al., 2020).

Specifically in the Atlantic Ocean, some authors focused on the Azores density front supported by intense in situ observational programmes (Gould, 1985; Rudnick, 1996; Kuzmina, 2000). The Azores front features differ from nearly density-

compensated fronts. Many of the analyses that produced high-resolution in situ datasets are primarily concentrated on the density fronts due to their a priori more relevant dynamics and also to their impact on the chemistry and biology of the waters involved (Mahadevan and Archer, 2000). In fact, only a few analyses about the thermohaline fronts are performed with a high resolution sampling (Ferrari and Rudnick, 2000). An example are those studied carried out in the Argentine basin about deep density-compensated fronts (Roden, 1986; Roden, 1989). Beyond the Atlantic Ocean, the works developed are mostly restricted to the shallowest water column, in particular to the mixed layer, where these fronts are associated with atmospheric forcings (Roden, 1975; Roden, 1977; Chu and Guihua, 2003).

The thermohaline or density-compensated fronts are often found in wide, transitional and relatively time and space stationary regions defined as "frontal zones" (Fedorov, 1986), that present a persistent frontal activity. Moreover, these regions are known to be sites of high productivity (Lima, Olson, and Doney, 2002; McGillicuddy Jr, 2016) and they are important sites for cross-frontal fluxes (Rudnick and Luyten, 1996) and interactions with mixing and entrainment (Dewey and Moum, 1990). The Cape Verde Frontal Zone (CVFZ) is one of them, located in the eastern confluence of North Atlantic Subtropical and Tropical gyres extending from Cape Blanc to Cape Verde Islands (Stramma and Siedler, 1988; Siedler et al., 1992; Zenk, Klein, and Schroder, 1991; Klein and Siedler, 1995; Pérez-Rodríguez, Pelegrí, and Marrero-Díaz, 2001; Martínez-Marrero et al., 2008; Burgoa et al., 2021). This frontal zone is developed when the North and South Atlantic Central Water masses, NACW and SACW, find each other producing a weak or near density-compensated front with a stable stratification induced by their temperature and salinity distributions (Tomczak, 1981; Hagen, 1985; Emery and Meincke, 1986; Zenk, Klein, and Schroder, 1991; Pérez-Rodríguez, Pelegrí, and Marrero-Díaz, 2001; Martínez-Marrero et al., 2008; Meunier et al., 2012; Burgoa et al., 2021). Some works show that the CVFZ is associated with high meso- and submesoscale activity (Meunier et al., 2012; Hosegood et al., 2017; Appen et al., 2020; Burgoa et al., 2021) and relevant mixing processes (Klein and Tomczak, 1994; Klein and Siedler, 1995; Pastor et al., 2008; Martínez-Marrero et al., 2008).

Several authors have reported in situ low-resolution measurements off the coast of Cape Blanc at the convergence zone between NACW and SACW (Zenk, Klein, and Schroder, 1991; Pérez-Rodríguez, Pelegrí, and Marrero-Díaz, 2001; Pastor et al., 2008; Peña-Izquierdo et al., 2012; Burgoa et al., 2020; Burgoa et al., 2021). Some authors document surveys with larger spatial resolution focusing on the smaller scales such as mixing and turbulence (Klein and Siedler, 1995; Martínez-Marrero et al., 2008). However, only a few analyses deal with in situ high resolution measurements that describe and analyze meso- and submesoscale structures associated with the CVFZ (Barton, 1987). One of them was reported by Meunier et al. (2012) who describe in detail the structure and dynamic of the upwelling filaments with data collected during two cruises carried out in 2009; they mainly focused on the development and offshore propagation of the filaments that detach from the upwelling front due to the interaction with the surrounding eddies. Finally, the scarce meso- and submesoscale studies developed in this area have been mostly carried out with remote sensing measurements (Gabric et al., 1993; Lázaro et al., 2005; Appen et al., 2020) and numerical models (Onken and Klein, 1991; Erasmi,

Siedler, and Onken, 1998).

Barton (1987) presented for the first time the meso- and submesoscale structures in detail, with the dataset provided by two high-resolution hydrological transects carried out in 1981 and 1982. Double diffusion in interleaving intrusions was included in his results (Stern, 1960; Turner, 1974; Schmitt, 1994; Shcherbina et al., 2009). In the absence of solid dynamics data (only data from three buoys were analysed), he speculated about the origins of these intrusions; in this regard, he stated that instabilities of the front were possibly pulled out from the front by vertical or horizontal shears and advected by other mesoscale structures. A few years later, Klein and Siedler (1995) analyzed the double diffusion and concluded that this type of mixing considerably influences the vertical balances of salt and heat in the border area of both central water masses. Later on, Martínez-Marrero et al. (2008) described the frontal structure with hydrology and sADCP data and demonstrated the importance of the advection process around the front. They also pointed out the competition between the double diffusion and shear instabilities in the water column of the CVFZ. To conclude that the double diffusion in the form of salt fingers was the predominant process in the frontal area, where significant vertical shear was observed with pure SACW featured by numerous intrusions.

This manuscript intends to fill the gap left after several years without high resolution in situ measurements in the CVFZ. For the first time, the geostrophic and ageostrophic horizontal fields and the w vertical velocities are presented together with the hydrology sampled by the SeaSoar and the dynamics described by the sADCP to unveil the processes involved in the development of the meso- and submesoscale thermohaline structures in the CVFZ. The cruise was organized in three sampling legs carried out in a relatively short time period of 18 days. In this way, the intensity in the associated meso- and submesocale dynamic is captured and also the short-term evolution of the CVFZ.

4.2 Data

4.2.1 Remote sensing data

SEALEVEL_GLO_PHY_L4_REP_OBSERVATIONS_008_047 product of Global Ocean Sea Surface Height was employed to analyze the mesoscale structures and test the near-surface geostrophic field. This database issued by Copernicus Marine Environment Monitoring Service (CMEMS, `http://marine.copernicus.eu`) with a resolution of 0.25° merges multi-satellite altimetry observations and is processed by the SL-TAC multimission altimeter data processing system. The Sea Level Anomaly (SLA) is cross validated, filtered from small scale signals and residual noise, sub-sampled, and gridded by an Optimal Interpolation. The geostrophic velocities are derived from SLA. The Absolute Dynamic Topography (ADT) is computed from the sum of SLA and Mean Dynamic Topography (ADT=SLA+MDT). In addition, the identification of the different oceanographic structures is performed with Sea Surface Temperature provided through the product SST_GLO_SST_L4_REP_OBSERVATIONS_010_024, with a 0.05° resolution at 20 cm depth and distributed by Copernicus Climate Change Service (`http://climate.copernicus.eu`).

4.2.2 *In situ* observations

FLUXES-II cruise was carried out in November 2017 aboard the R/V Sarmiento de Gamboa just over 100 km from the Mauritanian coast near Cape Blanc (Fig. 4.1 and Tab. 4.1). This cruise was conducted along three legs with high-resolution measurements of conductivity, temperature and depth (CTD), and velocity fields up to about 400 m depth.

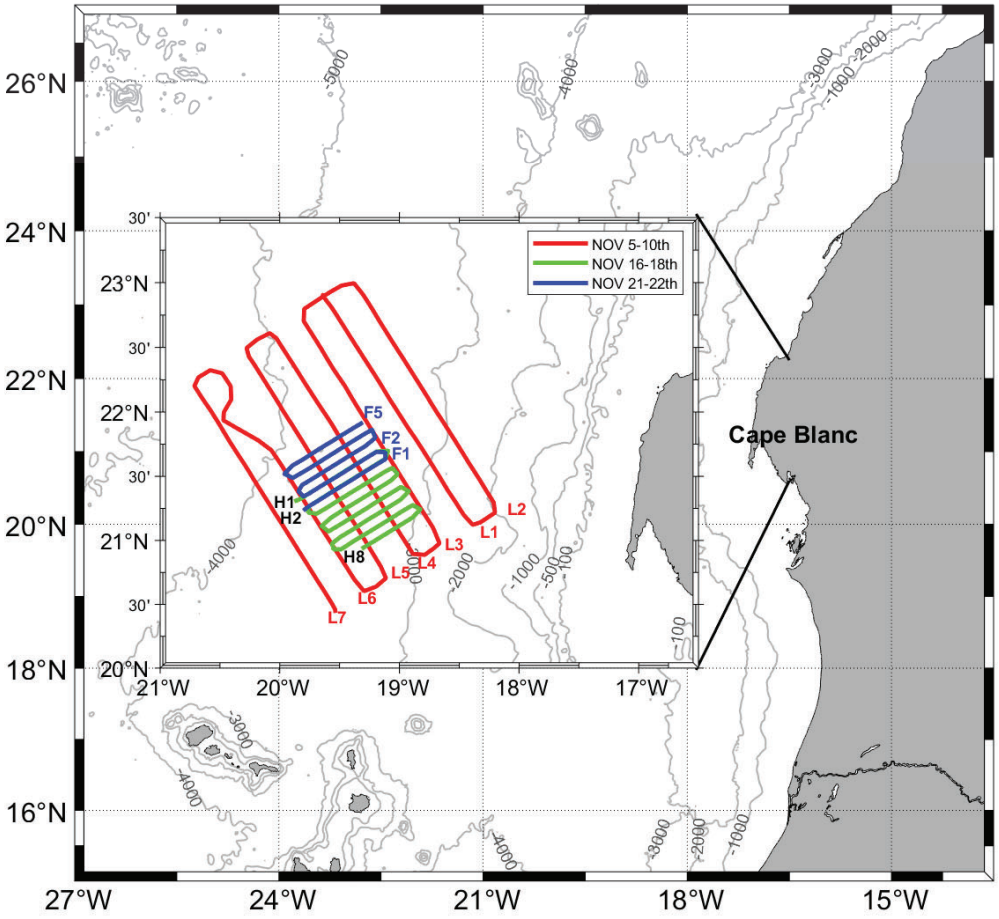

Figure 4.1: FLUXES-II cruise displaying the three SeaSoar sampling legs. Red/green/blue lines represent the ship track during the first/second/third leg (LEG-I/LEG-II/LEG-III) which group transects from L1/H1/F1 to L7/H8/F5. H1 and H2, and, F1 and F2 transects sampled along the same locations.

The hydrographic data and the current velocities were measured with the undulating Seasoar equipped with a SBE911+ CTD and the Ship Acoustic Doppler Current Profiler (sADCP), respectively. A cruise speed of $\sim$ 8 knots for all the legs allowed the SeaSoar to achieve a resolution of $\sim$ 5km along track and an effective vertical resolution of 70-75 cm. The current velocities were measured continuously with a 75 kHz RDI sADCP configured in narrow band mode (or long range). This sADCP provided along track raw data averaged every 5 min from 36 to some 800 m depth.

Table 4.1: Summary of the three sampling legs performed during FLUXES-II cruise with start and end dates, sampling duration, start and end positions, and transect length.

SAMPLING LEG	TRANSECT	START & END DATES (UTC time)	DURATION (hours)	START & END POSITIONS	LENGTH (km)
LEG I MESOSCALE NOV. 5th-10th	L1	11/5 (1:02), 11/5 (17:29)	16.27	22.54N, 19.39W / 21.07N, 18.22W	231.97
	L2	11/5 (20:08), 11/6 (13:41)	17.33	21.15N, 18.11W / 23.01N, 19.23W	227.26
	L3	11/6 (17:24), 11/7 (09:07)	15.83	22.45N, 18.51W / 20.59N, 18.39W	229.82
	L4	11/7 (13:15), 11/8 (04:41)	15.26	20.53N, 18.53W / 22.37N, 20.04W	226.58
	L5	11/8 (6:42), 11/8 (22:02)	15.6	22.28N, 20.18W / 20.43N, 19.06W	228.26
	L6	11/9 (0:16), 11/9 (17:06)	17.19	20.37N, 19.20W / 22.21N, 20.32W	248.71
	L7	11/9 (18:59), 11/10 (10:31)	15.72	22.14N, 20.44W / 20.29N, 19.33W	228.81
LEG II SUBMESOSCALE 1 NOV. 16th-18th	H1	11/16 (21:34), 11/17 (4:03)	6.69	21.17N, 19.54W / 21.44N, 19.08W	91.19
	H2	11/17 (4:52), 11/17 (10:33)	5.81	21.40N, 19.05W / 21.16N, 19.47W	80.89
	H3	11/17 (11:20), 11/17 (16:46)	5.26	21.12N, 19.43W / 21.35N, 19.04W	80.04
	H4	11/17 (17:29), 11/17 (22:47)	5.18	21.30N, 19.01W / 21.08N, 19.40W	76.95
	H5	11/17 (23:34), 11/18 (4:55)	5.21	21.03N, 19.37W / 21.26N, 18.58W	78.85
	H6	11/18 (5:59), 11/18 (10:57)	4.98	21.22N, 18.56W / 20.59N, 19.35W	78.25
	H7	11/18 (11:47), 11/18 (17:11)	5.64	20.55N, 19.32W / 21.18N, 18.52W	76.71
	H8	11/18 (17:53), 11/18 (23:22)	5.69	21.13N, 18.50W / 20.50N, 19.3W	56.95
LEG III SUBMESOSCALE 2 NOV. 21th-22th	F1	11/21 (14:57), 11/21 (21:01)	6.44	21.14N, 19.50W / 21.38N, 19.07W	83.37
	F2	11/21 (21:54), 11/22 (3:10)	5.56	21.43N, 19.10W / 21.20N, 19.49W	76.42
	F3	11/22 (3:58), 11/22 (9:24)	5.66	21.25N, 19.51W / 21.48N, 19.12W	78.48
	F4	11/22 (10:13), 11/22 (15:55)	5.42	21.52N, 19.15W / 21.06N, 19.56W	81.82
	F5	11/22 (16:43), 11/22 (22:12)	5.69	21.33N, 19.59W / 21.56N, 19.17W	80.72

The first leg sampled seven parallel transects orientated from southeast to northwest. These transects were named L1 to L7 and run along more than 200 km, visited from November 5th to 10th and separated an average distance of 27 km from each other. Hence, we name this leg as the 'Mesoscale grid'. The second and third legs were composed by eight (from H1 to H8) and five (from F1 to F5) parallel transects. They were occupied first from the northernmost to the southernmost transect between November 16th and 18th and then from the southernmost to the northernmost transect between November 21th and 22th. In this way, the first and second transects of both last legs were sampled twice in reverse order. On the other hand, the transects during the second and third leg were perpendicular to those during the first leg, presenting a southwest-northeast orientation with more than 75 km long (except the H8) and were separated from each other by an average distance of 9-10 km. Therefore, we name these as the 'Submesoscale grid'.

4.3 Methods

4.3.1 Preliminary data processing

The raw hydrography from the SeaSoar was processed with SBE Data processing version 7.26.7 (`https://www.seabird.com/software/`). This data was filtered every 0.15 s with a low pass filter in pressure. Then, a window filter was applied with a median value every 9 data. Next, the thermal mass of temperature sensor was corrected and then an average was estimated with a bin size of 1 s. Practical Salinity (S_P,(UNESCO, 1985)) derived from conductivity measurements was calibrated with a precision and accuracy within the values recommended by WOCE (World Ocean Circulation Experiment) and it was converted into Absolute Salinity (S_A,(McDougall et al., 2012)). The in situ temperature (T) was transformed into Potential Temperature (θ) and Conservative Temperature (Θ) using the algorithms by McDougall and Barker (2011) for TEOS-10 variables (IOC, SCOR, and IAPSO, 2010). In addition, the potential density anomaly with reference at 0 dbar, $\sigma_0 = \rho(S_A, \Theta, P = 0) - 1000$ (it is also denoted σ_θ in the UNESCO system), was calculated from the algorithms by McDougall et al. (2003) and Roquet et al. (2015).

The sADCP raw data were processed with the Common Oceanographic Data Access System, (CODAS, Firing, 1995) which provided velocity profiles spaced approximately every 10 km along track with a bin size of 16 m. This software fixes and adjusts all associated errors including the heading misalignment (`https://currents.soest.hawaii.edu/docs/adcp_doc/`).

Finally, the mixed-layer depth (MLD) was estimated with the procedure documented by de Boyer Montégut et al., 2004.

4.3.2 2-D DIVA

Data-Interpolating Variational Analysis (DIVA) is an interpolation method for gridding observational data in an optimal way (Troupin et al., 2012) developed by the GeoHydrodynamics and Environment Research group of the University of Liège (GHER,`http://modb.oce.ulg.ac.be/mediawiki/index.php/DIVA`). DIVA uses

a finite-element method to solve elliptic type 2-D differential or variational problems taking into account the distance between interpolated and observational positions, the regularity of the interpolated points and the physical laws. In our case, the DIVA interpolations of hydrographic and dynamic measurements were generated in two consecutive stages in order to achieve a regular 3-D grid: first, each vertical section was interpolated in a vertical 2-D regular grid and then all regular vertical sections were grouped and interpolated producing horizontal sections at selected depths.

Before performing the interpolations, the correlation lengths, L_x and L_y, and the signal-to-noise ratios, λ, were defined for all the hydrographic and dynamic variables Brasseur et al., 1996; Barth et al., 2010. L_x and L_y associated to the spatial scales of each variable were selected by analyzing the autocorrelation matrix between the raw and the interpolated fields. After some testing, the λs were selected in accordance with the correlation scales of each variable and with values near to, or slightly greater than, those reported by other authors (Troupin et al., 2010; Troupin et al., 2012).

Both in the vertical and horizontal sections, the data covariance was fitted with a 2-D Gaussian function (Pallàs-Sanz, Johnston, and Rudnick, 2010a; Barceló-Llull et al., 2017b) instead of applying any other type of fit as Bessel or Kernel functions (Barth et al., 2010; Troupin et al., 2010; Troupin et al., 2012). In the vertical section interpolations, the semi-major axis, L_h, was the horizontal length in kilometers and, the semi-minor axis, L_z, the vertical length in meters. In the horizontal plane interpolations, both L_x and L_y were in units of kilometers alternating the semi-major and semi-minor axes of 2-D Gaussian function from one to another variable.

The errors associated to noise and data coverage were also computed with DIVA interpolations. A mask was applied to interpolation points with errors larger than 18% in vertical and 25% in horizontal sections, associated with domains where real data were missing and therefore an extrapolation had been performed. Regarding the errors of interpolated points within each domain, they were estimated to be less than 12% in more than 70% of the points (Tab. 4.2).

Table 4.2: Percentages of interpolated points with errors less than 12% inside the three sampling domains of FLUXES-II cruise.

SAMPLING LEG	**VARIABLE**	**DEPTH <100 m**	**DEPTH >100 m**
LEG I	S_A, Θ, σ_0	88.03 %	88.17 %
	U, V	85.77 %	85.77 %
LEG II	S_A, Θ, σ_0	86.62 %	87.5 %
	U, V	73.15 %	73.15 %
LEG III	S_A, Θ, σ_0	83.38 %	85.55 %
	U, V	73.14 %	73.14 %

Vertical section interpolation

The vertical interpolations were conditioned by the initial horizontal and vertical resolutions, in particular the values of L_h and L_z for each variable. These res-

olutions were 10 km and 16 m in the velocity fields, and 5 km and 70-75 cm in the hydrographic data. The interpolations of the sADCP components (U,V) were made with the same initial horizontal resolution of 10 km and with a vertical resolution of $\Delta z = 10$ m from the sea surface down to 410, 420 and 430 m depth in the first, second and third legs, successively. In all these interpolations, $\lambda = 5$ and $L_z = 16$ m were the same while $L_h = 15$ km in the first and $L_h = 13$ km in the second and third legs were selected. On the other hand, all regular hydrographic transects had grid size of $\Delta h = 2.5$ km and $\Delta z = 10$ m from the sea surface down to the same maximum depths as in the transects of U and V. The average correlation lengths estimated for $S_A/\Theta/\sigma_0$ were $L_h = 9/168/300$ km and $L_z = 35/20/27$ m respectively. However, these lengths were very large in some cases filtering structures of interest. Therefore, it was decided to reduce the correlation lengths to $L_h = 28/19$ km and $L_z = 16$ m in all the hydrological transects of the mesoscale/submesoscale legs taking $\lambda = 1$.

Horizontal interpolation

After merging the velocities and hydrographic variables of interpolated vertical sections, all data covariances were fitted again. Considering the average distance between the vertical sections during the three legs, the correlation lengths for all the horizontal sections were chosen. $L_x = L_y = 28$ km and $L_x = L_y = 10$ km selected for the mesoscale and submesoscale horizontal sections were in accordance with similar values previously chosen in mesoscale fronts (Rudnick, 1996; Pallàs-Sanz, Johnston, and Rudnick, 2010a). Besides, L_x and L_y values were coherent with sampling resolutions earlier used for the submesocale processes associated with fronts (Pascual et al., 2017), as well as for the upwelling filaments and other submesoscale structures of the Mauritanian Upwelling System (Meunier et al., 2012; Hosegood et al., 2017; Appen et al., 2020).

Horizontal currents and hydrographic data were interpolated into horizontal sections every 10 m depth with two different resolutions that allowed us to check and verify the differences with respect to the actual field. The selected grid sizes were $\Delta x = \Delta y = 7.5$ and 14 km in the mesoscale leg, and $\Delta x = \Delta y = 3.25$ and 6.5 km in the submesoscale domain. In this work, we only show the highest resolution interpolations where the initial resolution increases almost four times, $\Delta x \approx \Delta x_0/4$ and $\Delta y \approx \Delta y_0/4$. In these cases, the density and velocities are somewhat smoothed with respect to the actual values.

On average, $\lambda = 5$ and 10 were chosen for hydrographic horizontal sections at depth$\leq$100 m and depth$\geq$100 m, respectively. In the case of U and V, $\lambda = 10$ was selected for the horizontal sections until 100 m and $\lambda = 20$ for the deepest sections.

4.3.3 Rossby radius of deformation

The Rossby radius of deformation (R_d) defines the length scale in which rotational effects become as important as buoyancy (Gill, 2016). In other words, R_d represents the natural scale of mesoscale processes such as filaments, fronts and eddies in the ocean (Aken, Budeus, and Hähnel, 1995; Sangrà et al., 2005). R_d was

calculated and integrated from 40 to 400 m depth as:

$$R_d = \frac{1}{f}\int_{40}^{400} N(x,y,z)\; dz = \frac{H}{f}\sum_{n=40}^{400} N(x,y,n)$$

where $dz = H = 10$ m was the vertical resolution, $f = 5 \times 10^{-5}$ s^{-1} was the mean Coriolis parameter at the mean latitude of the domain and $N = \sqrt{-g\sigma_z/\bar{\sigma_0}}$ was the square of the Brunt-Väisälä buoyancy frequency at each point where g was gravity, $\bar{\sigma_0}$ was the mean potential density anomaly and subscript z denoted a vertical derivate. The estimated value of R_d for this domain was 40 ± 2 km, close to the values documented by Chelton et al. (1998). This value helps us to roughly estimate in advance the dimensions of the mesoscale structures in the domain and assess how feasible it would be to identify them by remote sensing, as well as by in situ data through the vertical and horizontal sections.

4.3.4 Assessing the geostrophy and ageostrophy horizontal fields

The methodology developed by Rudnick (1996) was employed here to estimate the geostrophic horizontal velocity ($\mathbf{u}_h^g$). This non-linear least-squares problem is based on an adjustment of the total stream function (ψ) to obey the sADCP dynamics (Rudnick, 1996). The geostrophic velocity was estimated by minimizing the sum of the residuals squares between geostrophic and total sADCP velocities and also constrained to be non-divergent. Next, the ageostrophic horizontal velocity ($\mathbf{u}_h^a$) was computed as the difference between the total horizontal velocity measured with the sADCP ($\mathbf{u}_h$) and the geostrophic horizontal velocity $\mathbf{u}_h^g$ estimated by the Rudnick's method: $\mathbf{u}_h^a = \mathbf{u}_h - \mathbf{u}_h^g$.

4.3.5 Diabatic Omega equation

Vertical velocity (w) was estimated following the diabatic Omega equation of Pallàs-Sanz, Johnston, and Rudnick (2010b) which is an extension of the generalized Omega equation from Viúdez, Tintoré, and Haney (1996) that includes vertical mixing as:

$$N^2\nabla_h^2 w + f(f+\zeta)w_{zz} = \underbrace{\underbrace{2\nabla_h\cdot\mathbf{Q}_h}_{S_{DEF}} + \underbrace{f\zeta_{ph}^a\cdot\nabla_h^2\mathbf{u}_h}_{S_{ADV}}}_{ADIABATIC\ \mathbf{Q}-VECTOR\ FORM} + \underbrace{f[\zeta_{ph}\cdot\nabla_h A_v - A_v\zeta_z]_z}_{S_{MOM}} - \underbrace{[\nabla_h^2(K_v\rho_z)]_z}_{S_{BUO}}$$

where N^2 is the Brunt-Väisälä buoyancy frequency, $f = 5 \times 10^{-5}$ s^{-1} is the mean Coriolis parameter and $\zeta = v_x - u_y$ is the vertical relative vorticity where u and v are the zonal and meridional currents and x and y are partial derivates in the eastward and northward directions. The total $\mathbf{Q}$ vector, that may be decomposed into geostrophic $\mathbf{Q}_h^g$ and ageostrophic components $\mathbf{Q}_h^a$, represents the deformation of the horizontal density gradient by the total horizontal velocity field ($\mathbf{Q}_h \equiv \nabla_h\mathbf{u}_h\cdot\nabla_h\rho$), $\zeta_{ph} = \boldsymbol{k}\times\mathbf{u}_h = -v_z\boldsymbol{i} + u_z\boldsymbol{j}$ is the horizontal pseudovorticity vector, that represents the anticlockwise rotation of the vertical shear, and, $\zeta_{ph}^a = \boldsymbol{k}\times\mathbf{u}_h^a = -v_z^a\boldsymbol{i} + u_z^a\boldsymbol{j}$ is the ageostrophic horizontal pseudovorticity vector that can be viewed as the anticlockwise rotation of the thermal wind imbalance (Giordani, Prieur, and

Caniaux, 2006). Vectors $\boldsymbol{i}$,$\boldsymbol{j}$,$\boldsymbol{k}$ are unit vectors in the x, y and z directions and subscript z indicated a vertical derivate. We follow Pallàs-Sanz, Johnston, and Rudnick (2010b) by assuming constant and isotropic vertical mixing of momentum and buoyancy (*Prandtl number* $= Pr = 1 = A_v/K_v$) and by computing the eddy viscosity A_v (or K_v) by using a simplified version of K Profile Parameterization, KPP, where the critical Richardson number, Ri_c, was 0.7 and 50 $\times 10^{-4}$ m^2 s^{-1} was the background deformation viscosity for momentum (Large, McWilliams, and Doney, 1994; Nagai, Tandon, and Rudnick, 2006; Pallàs-Sanz, Johnston, and Rudnick, 2010a).

Diabatic Omega equation's forcing terms located on the right-hand side were: S_{DEF} and S_{ADV} that form the adiabatic $\mathbf{Q}$-vector form where S_{DEF} or the horizontal divergence of $\mathbf{Q}_h$, that is decomposed into its geostrophic and ageostrophic components ($2\nabla_h \cdot \mathbf{Q}_h = 2\nabla_h \cdot \mathbf{Q}_h^g + 2\nabla_h \cdot \mathbf{Q}_h^a$ or $S_{DEF} = S_{DEFG} + S_{DEFA}$), is related to the total deformation field and S_{ADV} denominated as ageostrophic advection is related to the advection of ζ by the ageostrophic vertical shear ($\mathbf{u}_{hz}^a$); and S_{MOM} and S_{MOM} that are related to the vertical mixing due to momentum and buoyancy. For more details of the KPP used or the terms of the diabatic Omega equation we refer to Pallàs-Sanz, Johnston, and Rudnick (2010a) and Pallàs-Sanz, Johnston, and Rudnick (2010b).

In order to carry out a detailed analysis of the vertical velocity sources, the Omega equation was solved independently for each forcing term through an iterative relaxation method with Dirichlet boundary conditions, choosing $w = 0$ at the surface and bottom boundaries (Pallàs-Sanz, Johnston, and Rudnick, 2010b; Barceló-Llull et al., 2017b).

4.4 Results

Next, the results obtained during the FLUXES-II cruise are displayed follows. First, the average surface distributions during each sampling leg are analyzed with the Averaged Absolute Dynamic Topography (ADT) and Averaged Sea Surface Temperature (SST); then, the variability within the water column is presented together with the predominant central water masses in each transect with the in situ profiles of salinity (S_A) and temperature (Θ) and the in situ Θ-S_A diagrams of the mesoscale domain; subsequently, the hydrography and the thermohaline structures sampled along all the transects of the three legs are analyzed in the vertical sections; later, these same structures are analyzed in the horizontal sections, focusing on the shallow and deep structures (at depths above and below 100 m, respectively). Once the hydrographic description is completed, the dynamic analysis is performed, describing the horizontal and vertical velocity fields in each sampling leg.

4.4.1 Remote sensing

The main hydrological and dynamic signatures detected with the remote sensing along the three legs allowed us to depict the evolution of the main sampled structures of the area (Fig. 4.2). Three cyclonic eddies (C1, C2 and C3) and two anticyclonic ones (A1 and A2) were present in the vicinity of the grids during the

samplings, besides the cyclonic meander observed west of the domain that we call "cyclonic intrusion" (CI).

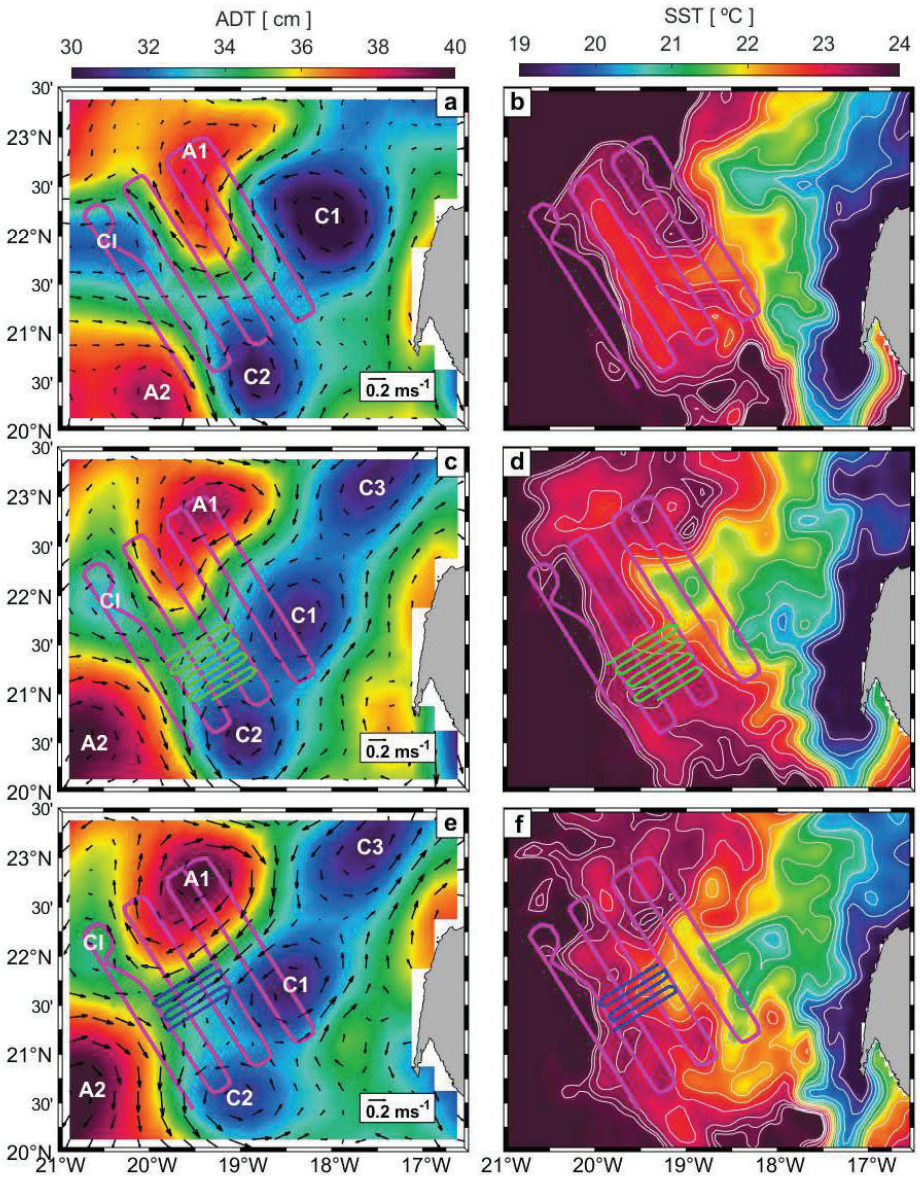

Figure 4.2: Averaged Absolute Dynamic Topography (ADT) with the geostrophic velocity field superimposed (left side) and Averaged Sea Surface Temperature (SST) (right side) during the three sampling legs. The first leg averages (a and b) were made with data from November 5th to 10th; the second one (c and d) with data from 16th to 18th and the third one (e and f) with data from 21st to 22nd.

Between the first and the second legs (Figs. 4.2a and 4.2c), the anticyclonic eddy A1 moved north changing its shape and increasing its intensity. In this period of 6.5 days, the cyclonic eddy C1 got in the sampling domain reducing its intensity while a new cyclonic C3 appeared northwest above C1. Furthermore, the anticyclonic eddy A2 intensified moderately in the second leg, likely weakening the cyclonic intrusion CI on 16th November. By contrast, the southern cyclonic eddy

C2 maintained its location and intensity from the first to the second leg. Later on, 2.5 days passed between the second and third legs in which A1 intensified taking an elliptical shape while C2 shifted slightly southward flattening its shape and weakening; A2 continued intensifying (Figs. 4.2c and4.2e). In all legs the cold water of the upwelling filaments was advected by the jet located between A1 and C1 that entered the sampled domain through the western edge (Figs. 4.2b, 4.2d and 4.2f). While the entrance of the filament occurred from a northernmost area in the first leg (Fig. 4.2b), it entered from a more southern zone to the domain in the second and third legs (Figs. 4.2d and 4.2f).

4.4.2 In situ vertical profiles and $\Theta - S_A$ diagrams

Overall, the variability of the sampled water masses in the entire water column decreased from the easternmost transect L7 to the westernmost transect L2 (Fig. 4.3). This variability was more sharp in salinity than in temperature and it reduced when the depth increased.

Below the MLD (located between 30 and 40 m depth) and the isopycnal $\sigma_0 =$ 25.45 kg m^{-3}, two well differentiated zones were observed during all the samplings with Seasoar. Specifically, the isopycnal $\sigma_0 = 26.48$ kg m^{-3} included in $\Theta - S_A$ diagrams divided the highly variable seasonal thermocline (halocline) waters from another more homogeneous one, where NACW and SACW (Tomczak, 1981) coexist below $\sim$ 100 m (Fig. 4.3). NACW's and SACW's theoretical $\Theta - S_A$ values (Tomczak, 1981) are represented as gray straight lines in $\Theta - S_A$ diagrams, being the SACW on the left side and the NACW on the right one (third row of Fig . 4.3). Together with both central waters theoretical values, their transition (Burgoa et al., 2021) is represented as a black straight line. In fact, this transition or limit between NACW and SACW was described by the equation S_A [g kg^{-1}] =36.6509 - 0.0031 $\times$ depth + 1.98e-6 $\times$ depth^2, equivalent to that documented by Burgoa et al. (2021), that separated the purest SACW/NACW below/above the limit value of S_A estimated for a given depth (black straight line in the S_A vertical profiles of Fig. 4.3).

The transects with the highest abundance of NACW were L2 and L7 (L2 and L7 in first and third row of Fig. 4.3). SACW was always sampled together with NACW except in the westernmost transect, where the presence of SACW was negligible as compared to the abundance of NACW (L7 in Fig. 4.3). The purest, fresh and cold SACW was mainly located in the southernmost part of the transects L2, L3, L4 and L5. Exceptionally, both water masses were clearly differentiated in the easternmost transect, SACW in the south (cold colors in L2 of Fig. 4.3) and NACW in the north (warm colors in L2 of Fig. 4.3). However, the SACW sampled mainly in the central transects (L3, L4 and L5 in Fig. 4.3), was located both to the north, in high latitudes (warm colors), and to the south, in low latitudes (cold colors), of the domain.

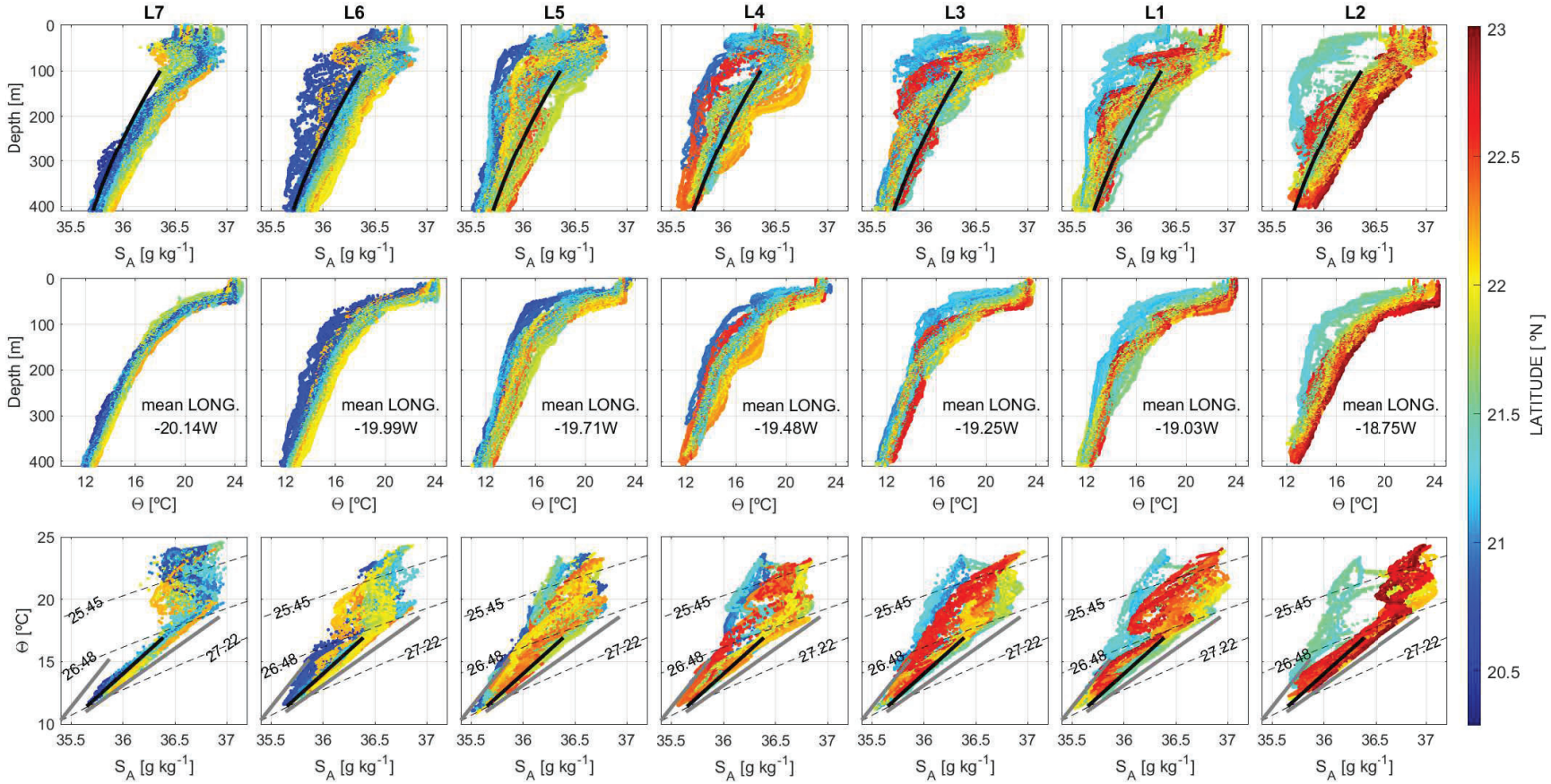

Figure 4.3: In situ data along sampled transects with Seasoar during mesoscale sampling, from the westernmost (L7) to easternmost one (L2): vertical profiles of S_A in g kg^{-1} and Θ in °C (first and second rows) and $\Theta - S_A$ diagrams (third row) with gray straight lines representing the least mixed SACW on the left, and NACW on the right, according to Tomczak (1981). The salinity-depth relationship that differentiated the two water masses is also included in vertical profiles of salinity and the limit between both waters in $\Theta - S_A$ diagrams, both in black lines, developed by Burgoa et al. (2021).

On the other hand, the water masses description between the MLD and 100 m depth, i.e, in the highly variable seasonal thermocline, was very complex. Small water bagging with well-defined physical characteristics were sampled differing significantly from the water ubicated directly below them, an example is observable north of transect L1 (warm colors in L1 of Fig. 4.3). Nonetheless, in other cases the physical characteristics of the water had similarities and continuity from 30-40 m to more than 100 m depth, such as in the southern end of transect L5 where the water characteristics above 100 m were similar to those of SACW (cold colors in L5 of Fig. 4.3).

4.4.3 Hydrographic structures in vertical sections

The high resolution achieved with the SeaSoar allowed to resolve scales shorter than those previously described with the remotely sensed variables. To differentiate submesoscale from mesoscale structures, the deformation radius of 40 km was considered.

Overall, the structures defined mainly in the salinity field above 100 m depth (represented by a thick gray dashed line in all vertical sections of Figs. 4.4, 4.5 and 4.6), were smaller in size and much flatter than the large structures simultaneously described by the salinity and temperature fields below 100 m that covered greater thicknesses in the water column (S_A and Θ in first and second row of Figs. 4.4, 4.5 and 4.6). In the transition between these two zones of the water column and partially occupying both of them, an intrathermocline anticyclonic eddy was detected with a diameter of 30-35 km and a core of S_A=36.75 g kg^{-1}, centered at $\sim$ 160 km of transect L4, from 80 m depth down to more than 200 m (first row of L4 in Fig. 4.4). This non-symmetric structure with respect to the vertical axis (it was flatter on its top than its base) was also described by the isopycnal of σ_0 that specially curved bordering the core below 100 m (third row of L4 in Fig. 4.4). Another two bigger structures also connected the water above and below 100 m depth in the first leg: in the southernmost zone of the domain, a very low salinity (S_A <36 g kg^{-1}) and cold (Θ <16.5°C) water emerged above 100 m reaching to 70 m depth, in a mean distance equal or less than 40 km from the origin in transects L2, L3, L4, L5 and L6; on the other part, in the northern half of the domain; another water with salinity less than 36.3 g kg^{-1} but with no significant signal in temperature was also detected at 70 m depth, beyond 150, 200 and 180 km from the origin in transects L5, L4 and L3 (first row in Fig. 4.4).

On the other hand, the main shallow structure detected in the first leg between the MLD (represented by a thick black line in all vertical sections of Figs. 4.4, 4.5 and 4.6) and 100 m depth was a filament-form intrusion of slightly cold and low salinity (S_A <36.3 g kg^{-1}) core of more than 100 km length sampled between 40 m and 60 m depth in the southernmost part of transect L5 (from approximately 20 to 125 km in the first row of L5 of Fig. 4.4). This intrusion of approximately 20 m thick was also detected in the southernmost part of transect L3 and L4 (in S_A of L3 and L4, Fig. 4.4). The intrusion had the same salinity than in L5 but its length barely reached to 65 km from its origin in transect L4 (first row of L4, Fig. 4.4). In contrast, this intrusion core was thicker ($\approx$25 m) and shorter (<50 km) in transect L3 than in the other two transects but with salinity values smaller than 36.15 g kg^{-1} and attached with the low salinity (S_A <36 g kg^{-1}) and

cold (Θ <16.5°C) emerged water in its base (from the origin in first row of L4, Fig. 4.4).

It should also be mentioned the $\sim$ 30 km length isolated lenses of S_A <36.3 g kg^{-1} sampled above 100 m located in the northernmost boundary (>200 km) of the transects L1 and L6 (first row in L1 and L6, Fig. 4.4). In fact, these two structures were clearly observed in the seasonal thermocline zone of the S_A and Θ vertical profiles of both transects (warm colors in first and second rows of L1 and L6, Fig. 4.3).

In general, the isopycnals located between the MLD and approximately 100 m depth behaved differently to those isopycnals located below 100 m where the SACW and NACW coexist (σ_0 field in the third row of Figs. 4.4, 4.5 and 4.6). In the first leg, the isopycnals located above 26.3-26.48 kg m^{-3} typically slopped up toward north in the southernmost part of transects L1, L3, L4 and L5 (between 30 m and 100 m depth in σ_0 field, Fig. 4.4). In contrast, the slopes of the deep isopycnals did not describe a defined pattern in these transects and at some specific locations they were locally greater than those of shallowest isopycnals (for example at 150 km distance of transect L5 in σ_0 field, Fig. 4.4).

Below 100 m depth, except in the transect L7, abundant structures extended into the water column, alternating cold and fresh water with relatively warmer and more saline water (S_A and Θ in Fig. 4.4). While warm and saline NACW-like (Θ >16.5°C and S_A >36.23 g kg^{-1} at 150 m depth, third row in Fig. 4.3), predominated in transects L6 and L2, colder and fresher water SACW-like (Θ <16.5°C and S_A <36.23 g kg^{-1} at 150 m depth, third row in Fig. 4.3) abounded in transects L1, L3, L4 and L5 (first and second rows in Fig. 4.4). On the other hand, the limits between the different structures described deep fronts in temperature and markedly in salinity: horizontal variations run from 0.27 to 0.36 g kg^{-1} at 150 m depth, after only 12.5-17.5 km, and in some cases extended vertically more than 100 m (for example at 150 km in transect L5 and at 200 km in transect L6 in S_A field, Fig. 4.4). Although these deep fronts were clearly detected in salinity and temperature, they were not so easy to identify with the slopes of the isopycnals (third row, Fig. 4.4).

Some transects of the second (H8 and H4 in Fig. 4.5) and third (F1 and F5 in 4.6) legs perpendicular to the transects L3, L4, L5 and L6 are indicated in Figure 4.4 to analyze the temporal evolution of the structures above and below 100 m.

In the zone between the MLD and 100 m depth, the filament-shaped intrusion of S_A < 36.3 g kg^{-1} sampled along transects L4 and L5 (first row in L4 and L5, Fig. 4.4) was detected in transects H5, H6 and H7 (from second to fourth row in S_A field, Fig. 4.5). While this intrusion continued to have a thickness of 20 m, limited by a more saline water with S_A >36.45 g kg^{-1} at its base, in transect H5 (such as in the first leg transects), this structure had a greater thickness and remained attached with the water that had similar physical characteristics below 100 m, in transect H7 (S_A <36 g kg^{-1} and Θ <16.5°C) and with a water slightly different in transect H6. This connection was detected at a located point close to L5 ($\sim$30 km) in transect H6. In contrast, the connection length was at least 28 km, the distance between transects L4 and L5, in transect H7. The intrusion width measured along these transects varied from a minimum width of 40 km in H4 (second row in S_A field, Fig. 4.5) to a maximum width of more than 60 km in

H6 (fourth row in S_A field, Fig. 4.5). Likewise, it is deduced that the intrusion was advected or extended westward from the first to the second leg: as it was detected in the intersections between transect L6 and transects H5, H6 and H7 during the second leg (from second to fourth row in S_A field, Fig. 4.5) while it was not sampled in transect L6 in the first phase (S_A in L6, Fig.4.4); on the other side, the intrusion exceeded H4 in transect L5 during the first leg (S_A in L5, Fig.4.4) and it was not detected in the intersection between transects H4 and L5 in the second leg (first row in S_A field, Fig. 4.5). Below 100 m depth, warm and saline NACW-like (with Θ >16.5°C and S_A >36.23 g kg^{-1} at 150 m depth) was detected from the origin up to 40 km away and SACW (with Θ <16.5°C and S_A <36.23 g kg^{-1} at 150 m depth) beyond 40 km, in transects H4 and H5 (first and second rows, Fig. 4.5). In contrast, the cooler and fresher SACW-like (Θ <16.5°C and S_A <36.23 g kg^{-1} at 150 m depth) was detected in the west before 60-65 km, and some NACW (Θ >16.5°C and S_A >36.23 g kg^{-1} at 150 m depth) on the eastern part of the two southernmost transects (in H7 and H8, Fig. 4.5). In addition, in transect H8, the characteristics of the water (S_A < 36.15 g kg^{-1} and Θ <16.5°C) remained unchanged from 80 m to more than 100 m depth, approximately in the position where this transect intersected transect L5, at 27-28 km (at S_A in H8, Fig. 4.5). Moreover, a very marked deep front in salinity was also observed at 68-70 km of its origin with horizontal variation of 0.35 g kg^{-1} at 150 m depth along 10 km distance, which was present in the slopes of the isopycnals greater than 26.6 kg m^{-3} that fell eastward (Θ and σ_0 in H8, Fig. 4.5).

During the third leg (Fig. 4.6), below the MLD and above 100 m depth, the well-defined shallow intrusion of low salinity (S_A < 36.3 g kg^{-1}) was not detected in any of the transects. Nevertheless, smaller, abundant and flat structures (isolated or connected to the water in their base) were detected mainly in the salinity field with S_A <36.45 g kg^{-1} and/or S_A >36.45 g kg^{-1} (second column, Fig. 4.6). For example, high alternation of lenses of different sizes defined by salinity were detected along transect F4 (second row and column, Fig. 4.6).

Below 100 m depth, not very marked deep fronts were sampled in salinity and temperature fields (second and third columns, Fig. 4.6) such as the examples described in the two previous legs. However, the cold and fresh SACW-like (Θ <16.5°C and S_A <36.23 g kg^{-1} at 150 m depth) located in the center, between L4 and L5, and the warm and saline NACW-like (Θ >16.5°C and S_A >36.23 g kg^{-1} at 150 m depth) located on the western (<10 km) and eastern (>70 km) edges, generated two fronts between 100 and 200 m depth at different points close to both extremes of transects of last leg (S_A and Θ fields, Fig. 4.6). Specifically, the front located in the easternmost part (>40 km) of the transects was more abrupt (with larger horizontal gradients in salinity and temperature) than the one located further west (S_A and Θ fields, Fig. 4.6).

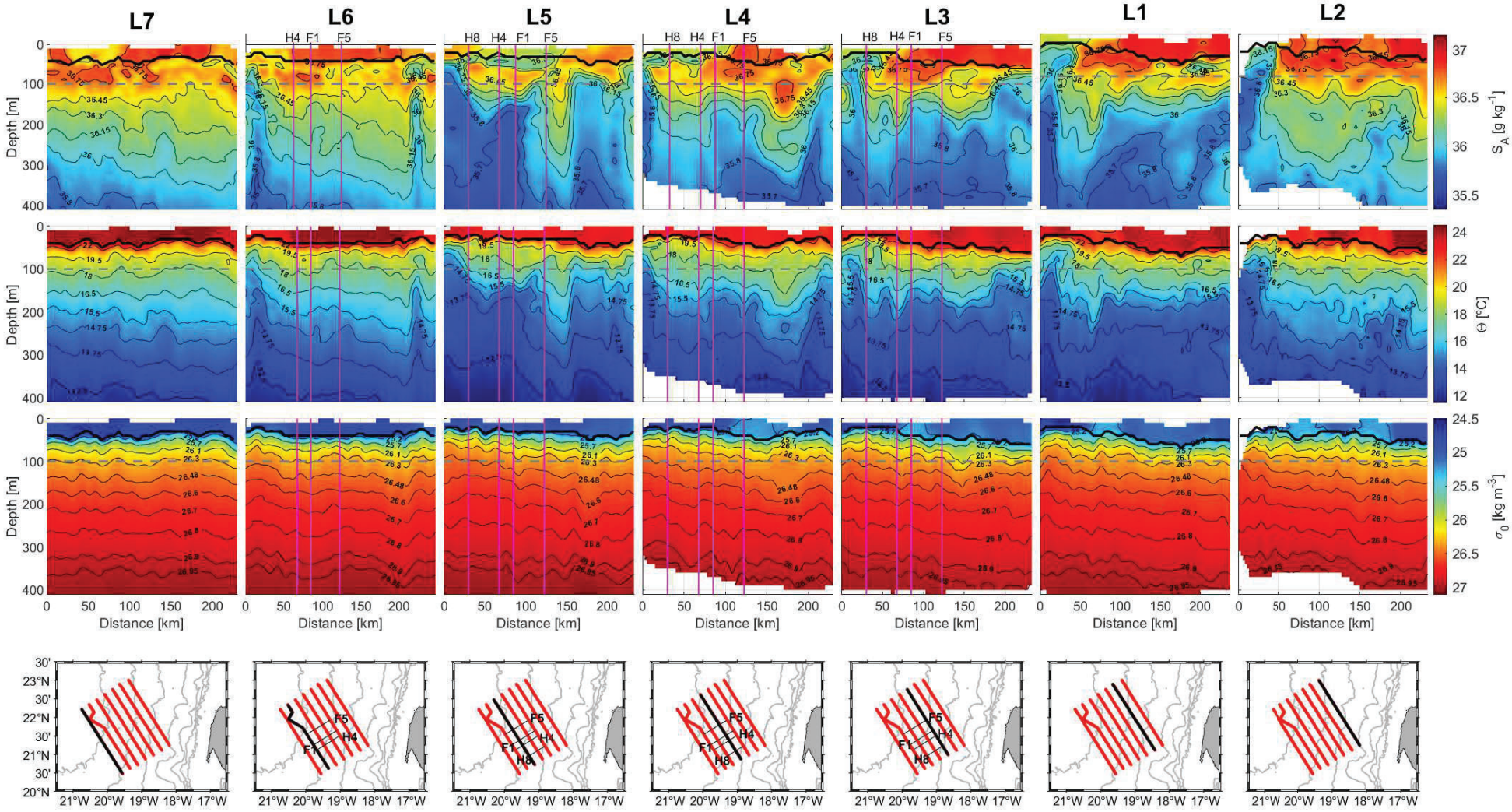

Figure 4.4: Interpolated vertical sections during the mesoscale grid: S_A (g kg^{-1}), Θ (°C) and σ_0 (kg m^{-3}) are presented in the first, second and third rows. The mixed-layer depth (MLD) is represented by a thick black line and the 100 m depth by a thick gray dashed line. The location of each transect is represented as a thick black line in the maps shown at the fourth row. All sections of this first leg have a southeast-northwest orientation, with the origin at the southeast. Transects H8, H4, F1 and F5 of the submesoscale grids I and II, are also represented by pink vertical lines in first, second and third rows and by black lines in the fourth row maps.

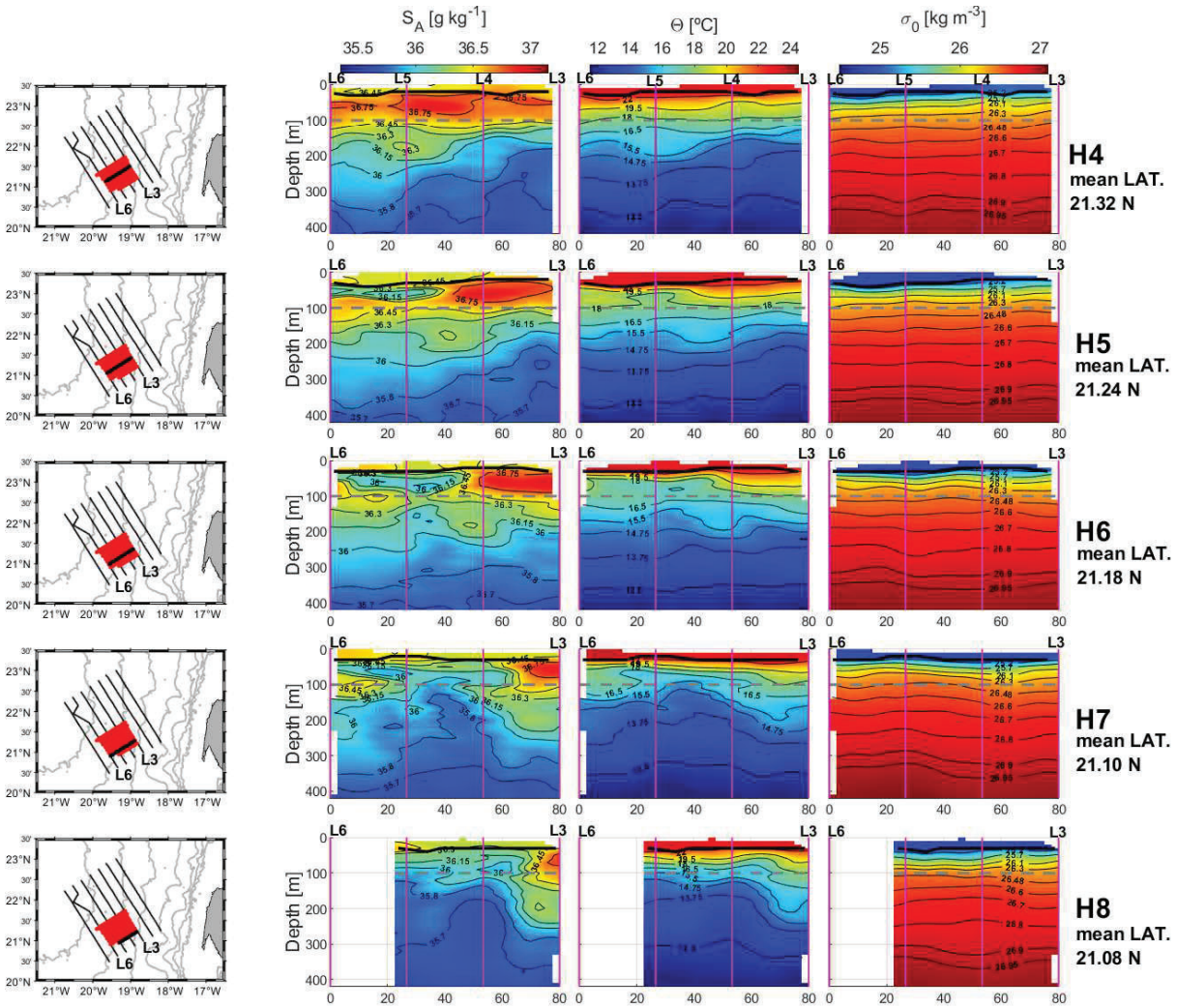

Figure 4.5: Interpolated data along the five southernmost sampled transects, from north to south, of the submesoscale grid I: vertical sections of S_A (g kg^{-1}), Θ (°C) and σ_0 (kg m^{-3}) (in second, third and fourth columns). The mixed-layer depth (MLD) is represented by a thick black line and the 100 m depth by a thick gray dashed line. The location of each transect is represented as a thick black line in the maps shown at the first column. All sections of the second leg have a southwest-northeast orientation, with the origin at the southwest. Transects L3, L4, L5 and L6 of the mesoscale grid are also represented by pink vertical lines in second, third and fourth columns and transects from L1 to L7 by black lines in the first column maps.

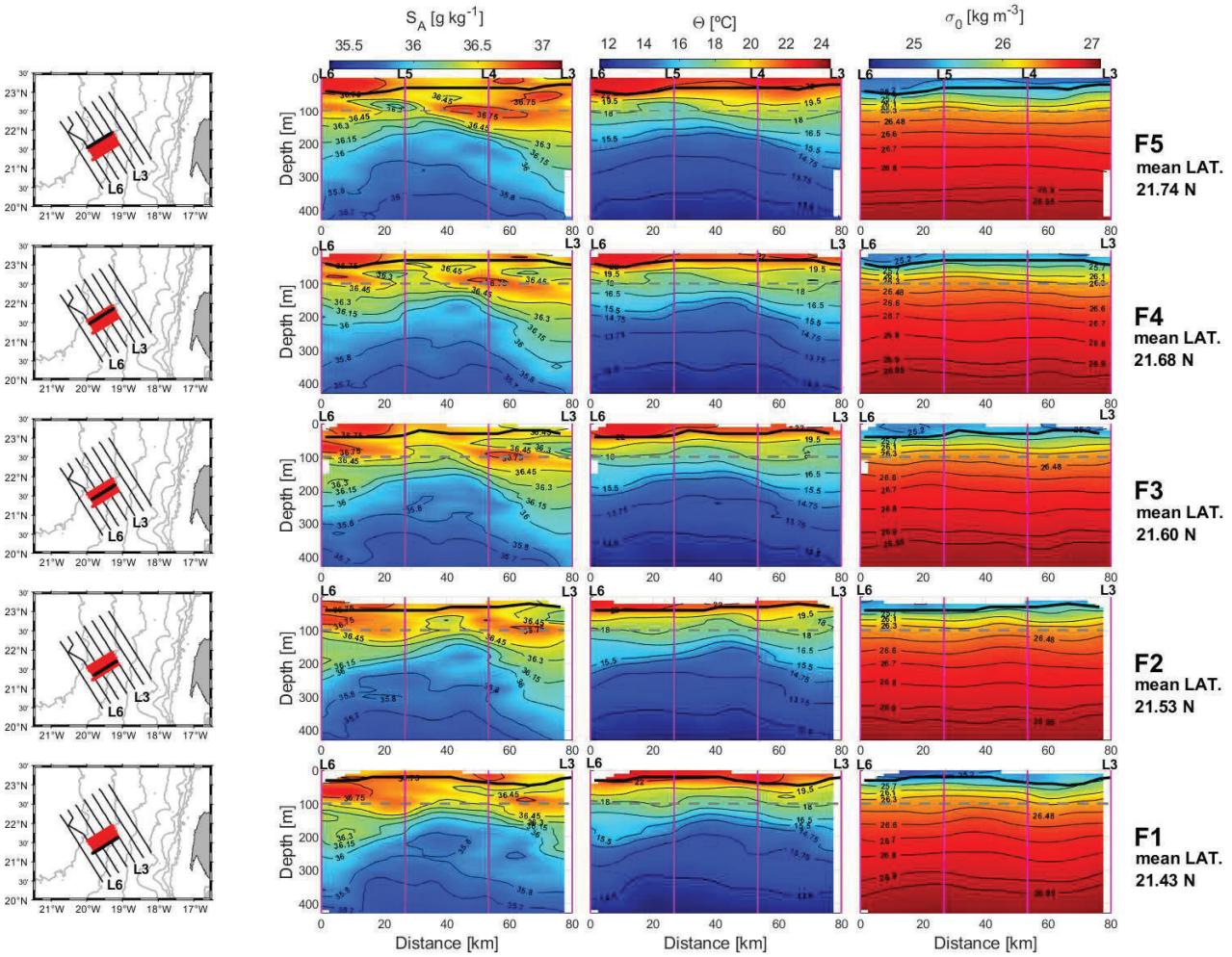

Figure 4.6: Interpolated data along the sampled transects, from north to south, of the submesoscale grid II: vertical sections of S_A (g kg^{-1}), Θ (°C) and σ_0 (kg m^{-3}) (in second, third and fourth columns). The mixed-layer depth (MLD) is represented by a thick black line and the 100 m depth by a thick gray dashed line. The location of each transect is represented as a thick black line in the maps shown at the first column. All sections of the third leg have a southwest-northeast orientation, with the origin at the southwest. Transects L3, L4, L5 and L6 of the mesoscale grid are also represented by pink vertical lines in second, third and fourth columns and transects from L1 to L7 by black lines in the first column maps.

4.4.4 Shallow horizontal sections

Below the MLD and above 100 m (Figs. 4.7, 4.8 and 4.9), the sampled structures were described in detail mainly in the salinity field (S_A) and to a lesser extent in the temperature and potential density anomaly fields (Θ and σ_0). Especially above 40 m, the descriptions of the particular structures were slightly different in the three fields and therefore, it was complicated to relate any structure described by one of them with the "same" structure in the other two fields (first, second and third rows in Figs. 4.7, 4.8 and 4.9). Particularly, this fact was very complex in the mesoscale grid. For example, in the small domain of the northeast corner of the first leg, in transects L2, L1 and L3, and from ∼114 km from the origin of transect L1 to the end of these transects, in which the mixed layer deepened and reached to greater depths (thick black line in L2, L1 and L3, Fig. 4.4), the water was quite homogeneous, warm and not very dense between 10 and 70 m depth. However, small flat structures were described at 70 m depth in S_A field, such as the S_A <36.3 g kg^{-1} lens north of transect L2 (∼200 km), that were not detected at lower or higher depths, either in Θ or σ_0 fields. In contrast, further west, the small structure with values less than 36.3 g kg^{-1} in transect L6 (∼200 km) at 70 m depth was also described in the others two fields with cores of Θ = 18°C and σ_0 =26.1 kg m^{-3} (third column, Fig. 4.7) and with slightly smaller values (S_A <36.5 g kg^{-1}, Θ = 21°C and σ_0 =25.5 kg m^{-3}) at 40 m depth (second column, Fig. 4.7).

On the other hand, in the shallower horizontal sections south of the domain, the long intrusion of filament shape with the subsurface core of salinity smaller than 36.3 g kg^{-1} centered at 40 m depth was also observed extending northward, from practically the origin of almost all transects (except L6 and L7) to more than 60 km and 120 km in transects L4 and L5, respectively (second column, Fig. 4.7). In the water column, this subsurface filament's core occupied a thickness of 20 m, below the MLD and over a saltier water of S_A >36.45 g kg^{-1} located at 70 m depth (first row and third column, Fig. 4.7). In the subsurface filament's upper limit, it was detected in a more limited area and with a smoothed signal of 36.4 g kg^{-1}, slightly observable in the temperature field ($\Theta \approx$ 22°C) and practically undetectable in the potential density anomaly at 10 m depth (first column, Fig. 4.7). At 40 m depth (second column, Fig. 4.7), the physical characteristics of this subsurface filament varied from more saltier and warmer waters in transects L4 y L5 to less saltier and colder waters in transect L3, at a given distance less than 50 km from their origin. Moreover, this subsurface filament's horizontal extension, thickness and physical characteristics were limited by the water that emerged reaching to 70 m depth in the southernmost part of the domain. This very low salinity (S_A <36 g kg^{-1}) and cold (Θ <16.5°C) water detected south of the domain in practically all the transects (with the exception of transect L7) and reaching to 70 m depth (third column, Fig.4.7), had a 140 km width between transects L2 and L6, and occupied a thickness of more than 30 m in the water column, joining similar water above and below 100 m depth (Figs. 4.7 and 4.10). The intrathermocline eddy with a core of S_A=36.75 g kg^{-1}, centered at ∼ 160 km of transect L4 (Fig. 4.4) also connected water located above and below 100 m; however, at 70 m depth it was not observed because its upper limit was located at 80 m (first row and third column, Fig.4.7).

Overall, the variation in the salinity and temperature fields at 40 and 70 m depth

in the first leg, with less saline and colder waters in south, between transects L2 and L6, and more saline and warmer waters in north, mainly between transects L2 and L3, generated that the densest waters were located south and the least dense north of the domain at this range of the water column (last row, Fig. 4.7). However, at constant depth, the gradient or variation of σ_0 along each transect was different. Specifically, in the easternmost transects the variations of σ_0 from the southernmost to the northernmost point was greater than 1 kg m^{-3} at 40 m and 70 m depth, while in the central and westernmost transects this variation was less than 1 kg m^{-3} at these two depths (last row, Fig. 4.7). The exception was the transect L7 in which the characteristics of the saline and warm water did not change from south to north, staying constant along this transect at any constant depth.

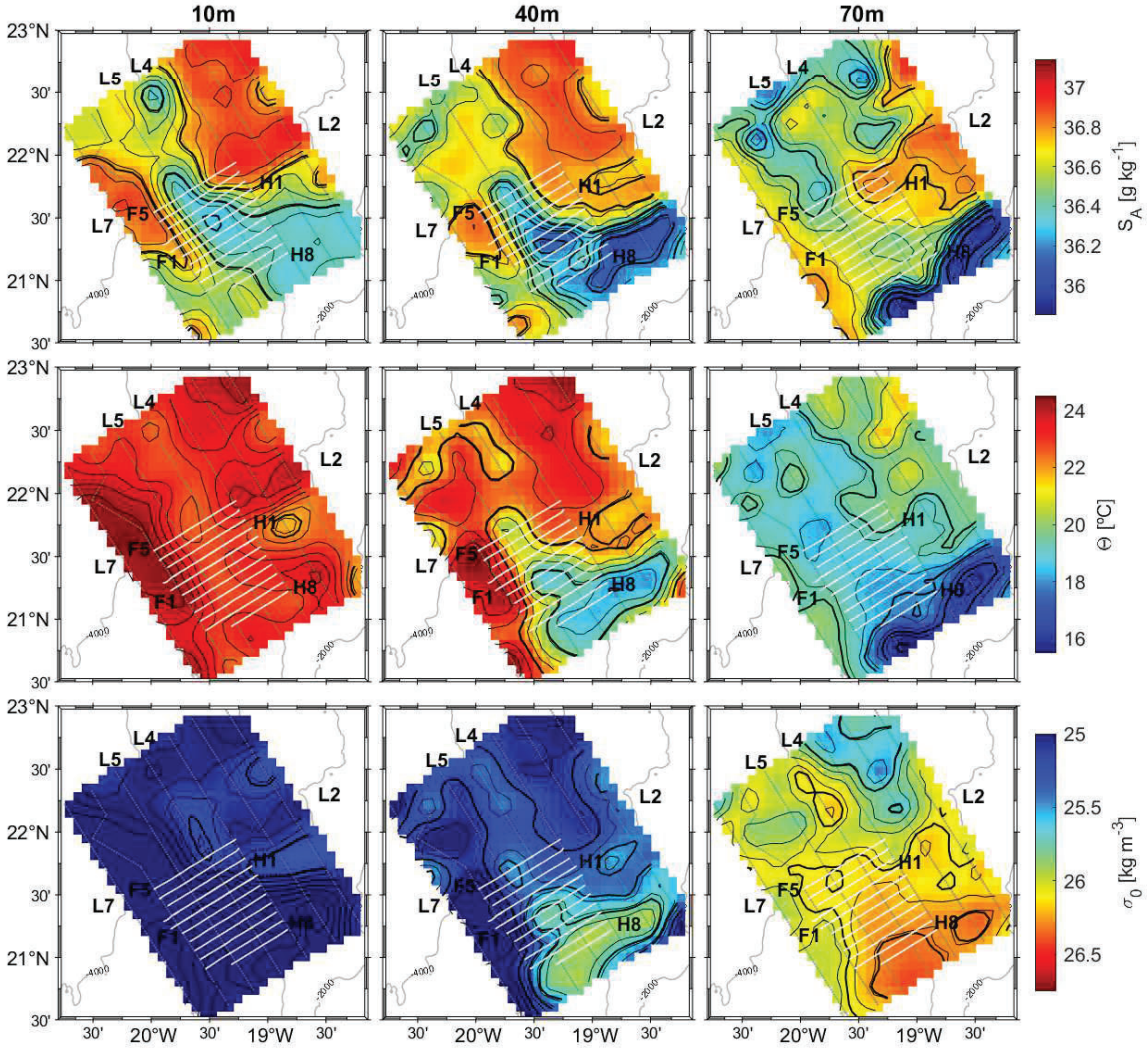

Figure 4.7: Interpolated horizontal sections of S_A (g kg^{-1}), Θ (°C) and σ_0 (kg m^{-3}) (first, second and third rows) during the mesoscale sampling, at 10, 40 and 70 m depth (in first, second and third columns). The sampled transects of this first (L1-L7) leg are represented by small gray dots and the transects of second (H1-H8) and third (F1-F5) legs by white lines.

The structures that were not well-solved or that could hardly be related through their descriptions in the fields of S_A, Θ and σ_0 at 10, 40 and 70 m depth in the mesoscale grid (Fig. 4.7), highlight the importance of submesoscale samplings at the seasonal thermocline zone of the water column of this region (Figs. 4.8 and 4.9). The structures described in the interpolated S_A and Θ fields were easier to relate each other in the second and third leg (Figs. 4.8 and 4.9) than in the first leg, at 40 and 70 m depth. Therefore, they will be considered as thermohaline structures from now on. However, correlating these thermohaline structures with the σ_0 field continued to be tricky in many cases.

In the second leg, the filament-shaped subsurface intrusion with the 20-30 m thick core of S_A <36.3 g kg^{-1} was also sampled centered at 40 m depth, just below the MLD (second column, Fig. 4.8). However, it was located further west than in the previous leg, specifically, between transects H5 and H7 westward of transect L5 and reaching transect L6 (from origin to 27.5 km distance along these transects in S_A of second column, Fig. 4.8). West of transect L5 (>27.5 km), the structure remained constant in salinity field from 40 to 70 m depth. This structure of diagonal shape in which it was concentrated the strongest gradient in salinity, crossed the domain separating less saline waters (S_A <36.3 g kg^{-1}) in the southwest and more saline waters (S_A >36.3 g kg^{-1}) in the northeast (second and third columns, Fig. 4.8). In contrast, at 10 m depth, the salinity signal near the sea surface was more complex and slightly different than that described at 40 and 70 m depth, with very saline waters (S_A >36.65 g kg^{-1}) limited only to the transects H1, H2 and H3, between transects L3 and L5 (S_A in the first, second and third columns, Fig. 4.8). On the other hand, while the temperature field at 70 m depth agreed with the salinity field, with a strong temperature gradient dividing the less saline cold water ($\Theta < 18$°C) in the southwest and the most saline warm water ($\Theta > 18$°C) in the northeast, at 40 m depth, small structures were detected in Θ that slightly varied its field with respect to that described by salinity at this depth (first and second rows in second and third columns, Fig. 4.8). In fact, at this depth, warmer water was concentrated on the diagonal across the domain perpendicularly to the maximum salinity gradient, leaving cooler water to its southwest and northeast (Θ in second column, Fig. 4.8). In general, at 40 and 70 m depth, the σ_0 field crossed the domain with a diagonal of dense water in the same direction of the salinity and temperature maximum gradients, leaving less dense water in the remaining space of the northwest and southeast corners (σ_0, Fig. 4.8).

In the horizontal sections of 10, 40 and 70 m depth of the third leg, the fields described by salinity, temperature and potential density anomaly were more complex than in the previous two legs. In fact, the filament-shaped intrusion with salinity core less than 36.3 g kg^{-1} between 40 and 60-70 m depth was not clearly observed in the last leg's horizontal sections (S_A, Fig. 4.9). Instead, abundant small thermohaline structures that alternated throughout the domain were described simultaneously by salinity, temperature and to a lesser extent by σ_0, mainly at 70 m depth. The structures at 10 m were more extensive than at greater depths with a predominance of less saline (S_A <36.5 g kg^{-1}), cold ($\Theta < 21.75$°C) and dense (σ_0 >25.2 kg m^{-3}) water in the easternmost area, specifically westward of transect L5 (<27.5 km). At 40 m depth, smaller thermohaline structures began to be de-

tected, alternating slightly saline and cold water with more saline and warm water that were clearly differentiated at 70 m depth (first and second rows, Fig. 4.9). This alternation of structures was reflected in the potential density anomaly field (third row, Fig. 4.9).

In summary, there was a continuity between the first and second legs in relation to the common structures analyzed and related in the shallowest horizontal sections.

From the first leg of mesoscale resolution to the second one of submesoscale resolution, certain differences were observed in the slightly modified common structures in size, location, and physical characteristics (S_A, Θ and σ_0) at 10, 40 and 70 m depth. The third leg of submesoscale resolution did not have much continuity with the previous legs due to the structures described by salinity, temperature and potential density anomaly changed completely from the second to the third leg. This made difficult to relate the situation analyzed in the third section between 10 and 70 m depth with those previously described in the first and second legs in this highly variable seasonal thermocline zone.

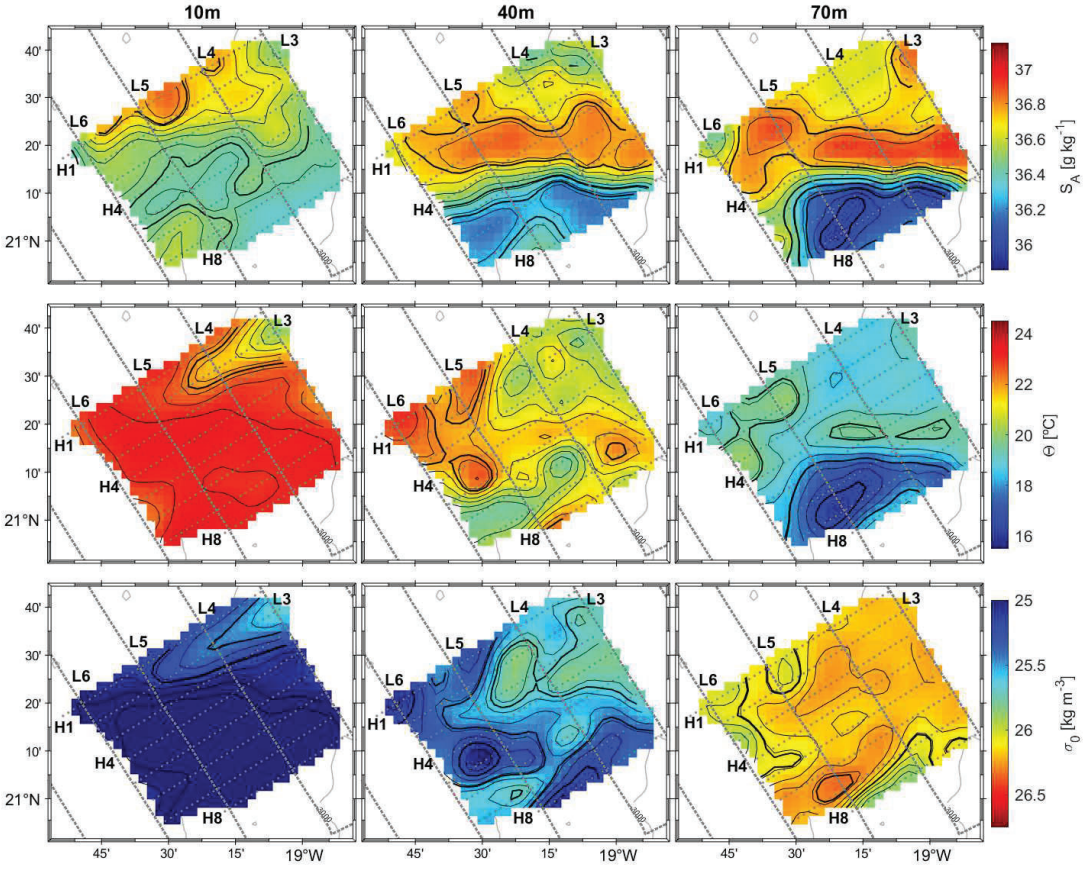

Figure 4.8: Interpolated horizontal sections of S_A (g kg^{-1}), Θ (°C) and σ_0 (kg m^{-3}) (in first, second and third rows) during the submesoscale grid I at 10, 40 and 70 m depth (in first, second and third columns). The sampled transects of first (L3-L6) and second (H1-H8) legs are represented by small gray dots.

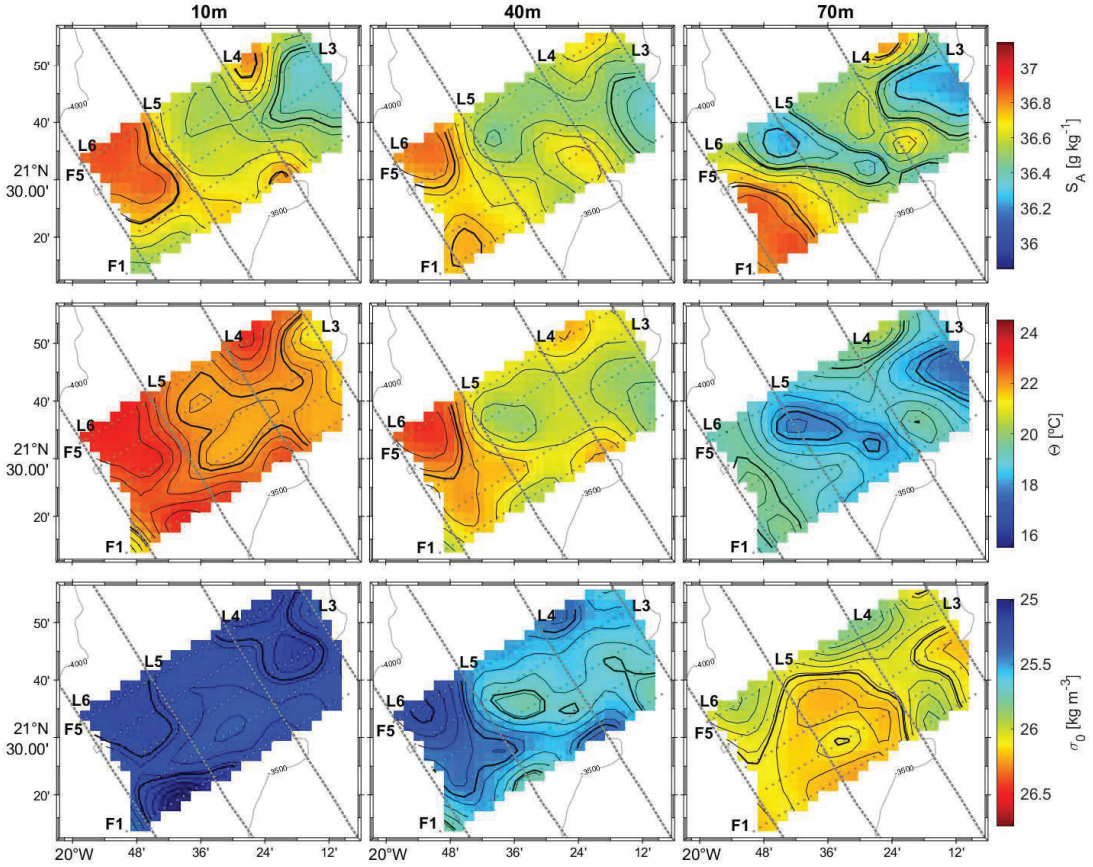

Figure 4.9: Interpolated horizontal sections of S_A (g kg^{-1}), Θ (°C) and σ_0 (kg m^{-3}) (in first, second and third rows) during the submesoscale grid II at 10, 40 and 70 m depth (in first, second and third columns). The sampled transects of first (L3-L6) and third (F1-F5) legs are represented by small gray dots.

4.4.5 Deeper horizontal sections

The variation of the physical properties (S_A, Θ and σ_0) decreased significantly in the deepest horizontal sections (Figs. 4.10, 4.11 and 4.12). This fact was previously analyzed in the vertical profiles and sections of Figures 4.3, 4.4, 4.5 and 4.6. This decreased variability in the physical properties at greater depths a priori could be associated with a different thermohaline structure and the identification of the central water masses located in these depths. However, the structure concordance in the S_A and Θ fields and the definition of the thermohaline front between NACW and SACW available below 100 m (with the limit between these waters defined in salinity with respect to depth) facilitated the analysis and description of the thermohaline structure featured by both central water masses from 100 to 300 m depth. In fact, the front between NACW and SACW determined theoretically by the salinity versus depth equation and represented by the isohalines of 36.36, 36.23 and 35.9 g kg^{-1} at 100, 150 and 300 m depth (pink lines, Figs.4.10, 4.11 and 4.12), respectively, largely coincided with the structure traced by the in situ fields of salinity and temperature and to a lesser extent, the potential density anomaly

in all the legs.

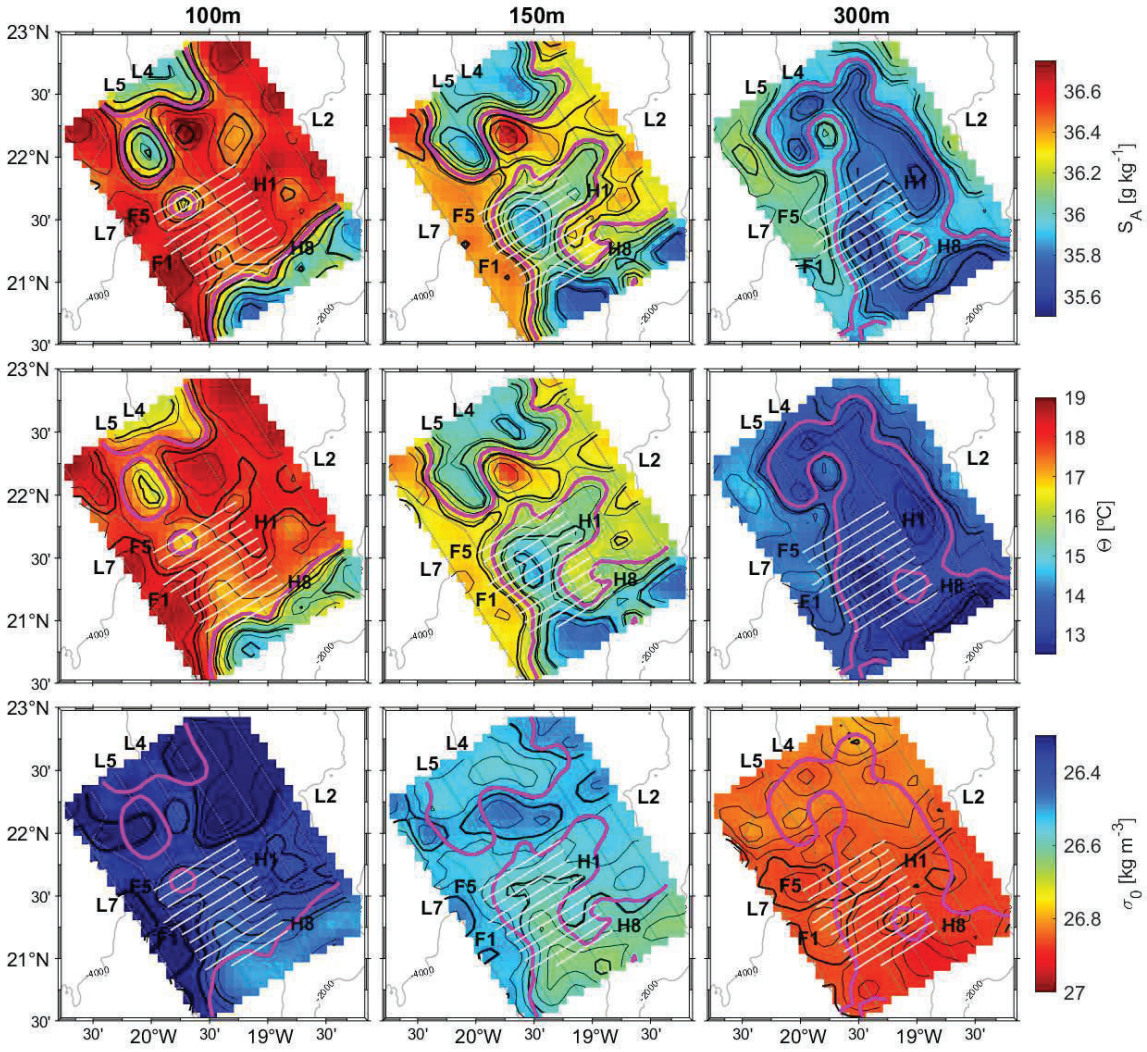

Figure 4.10: Interpolated horizontal sections of S_A (g kg^{-1}), Θ (°C) and σ_0 (kg m^{-3}) (in first, second and third rows) during the mesoscale sampling, at 100, 150 and 300 m depth (in first, second and third columns). The pink lines represent the isohalines of 36.36, 36.23 and 35.9 g kg^{-1}, respectively, that separated NACW and SACW at 100, 150 and 300 m. The sampled transects of this first (L1-L7) leg are represented by small gray dots and the transects of second (H1-H8) and third (F1-F5) legs by white lines.

In the first leg, the NACW-SACW front was crossed more than once in most of the transects except in transect L7. The NACW with salinities and temperatures larger than 36.36 g kg^{-1} and 16.75°C, respectively, dominated the entire domain at 100 m depth (first column, Fig. 4.10). SACW was also detected with salinities and temperatures less than 36.36 g kg^{-1} and 16.75°C in some small areas north and south (between transects L3 and L5 and transects L2 and L6,respectively) of the domain. Likewise, two closed structures with SACW inside them, the first of approximately 40 km of diameter centered at 125 km (between transects F4 and F5) and the second larger and elongated than the first centered at 175 km from

the origin, were detected along transect L5. On the other hand, the 30-35 km diameter intrathermocline eddy with S_A =36.75 g kg^{-1} core centered at 160 km of transect L4 was observed bordered by the SACW of transects L3 and L5. At 150 m depth, SACW kept its physical characteristics fairly constant (S_A <36.23 g kg^{-1} and Θ <16.25°C) expanding horizontally and occupying larger extension than at 100 m (second column, Fig. 4.10). Specifically, SACW extended from south to north reaching to 125 km along transect L5. Similarly, the SACW located north penetrated southward at transects L3 and L5. In contrast, the expansion was not observed in transect L4 due to the intrathermocline eddy found in its path. This structure clearly described in salinity and temperature at 100 m depth was perfectly traced with a core of Θ >18°C of well differentiated NACW inside it at 150 m depth. Both last features produced an intense and shallower front with a vertical extension of more than 100 m between the SACW "tongue" and the NACW trapped within the intrathermocline eddy (between transect L4 and L5 at 160 km from the origin at 100 and 150 m depth, Fig.4.10). At 300 m depth, the differences in salinity and temperature were drastically reduced between both central water masses (third column, Fig. 4.10). However, the predominating water at this depth was SACW, verified through the isohaline 35.9 g kg^{-1}, with salinities lower than this value and temperatures below 13.5°C. In this way, the two tongues of SACW detected in north and south at 100 and 150 m depth joined below the NACW located in the middle of them in the central area of the domain between 100 m and 150 m depth. At deepest horizontal sections, the structure in σ_0 field remained consistent with that described at shallowest depths but with less intense horizontal gradients, i.e., the maximum variations of more than 1 kg m^{-3} recorded at 40 and 70 m depth were reduced to 0.2 and 0.1 kg m^{-3} at 100 and 150 m depth respectively (being practically undetectable at 300 m).

On the other hand, the horizontal sections of the first leg evidenced a strong front in S_A and Θ, that was also marked in σ_0 field, in the transition area between the purest NACW and SACW, detected in transects L7 and L5, respectively, of the southernmost zone (<25 km) of the domain, at 100 and 150 m depth (first and second columns, Fig. 4.10). In this location, the NACW-SACW front was extended vertically more than 100 m depth, featured by a $\Delta S_A \approx 0.60$ g kg^{-1}, $\Delta\Theta \approx 2^\circ$ and $\Delta\sigma_0 \approx 0.12$ kg m^{-3} at 150 m depth.

NACW of S_A >36.36 g kg^{-1} and Θ >16.75°C, also predominated in the second leg at 100 m depth (first column in Fig. 4.11). Moreover, some (dilute) SACW was detected in northeast between transects H1 and H3 and transects L3 and L4, with slightly different characteristics from the purest SACW of S_A <36.36 g kg^{-1} and Θ <16.75°C sampled south of the domain (between H6 and H8). At 150 m depth (second column, Fig. 4.11), both SACW cores covered larger areas maintaining the physical characteristics (S_A <36.23 g kg^{-1} and Θ <16.25°C) of the same water in the previous leg. Specifically, the SACW located north penetrated to the south crossing transect H5 and the southernmost SACW expanded mainly westward reaching to transect L6. In fact, the NACW-SACW front detected at 150 m depth, almost over the intersection between transects H7 and L4 and crossing transect H8 at 65 km, had similar characteristics to that previously sampled in the southernmost zone (<25 km, between transects L5 and L7) of the mesoscale grid (second column, Fig.4.10). Furthermore, the NACW-SACW front was also

detected in σ_0 (third row and second column, Fig. 4.11). At 300 m depth (third column, Fig. 4.11), practically all the mass water sampled was SACW, while NACW (S_A >35.9 g kg^{-1} and Θ >13.5°C) was only detected in a small area (westward) between transects H4 and H7.

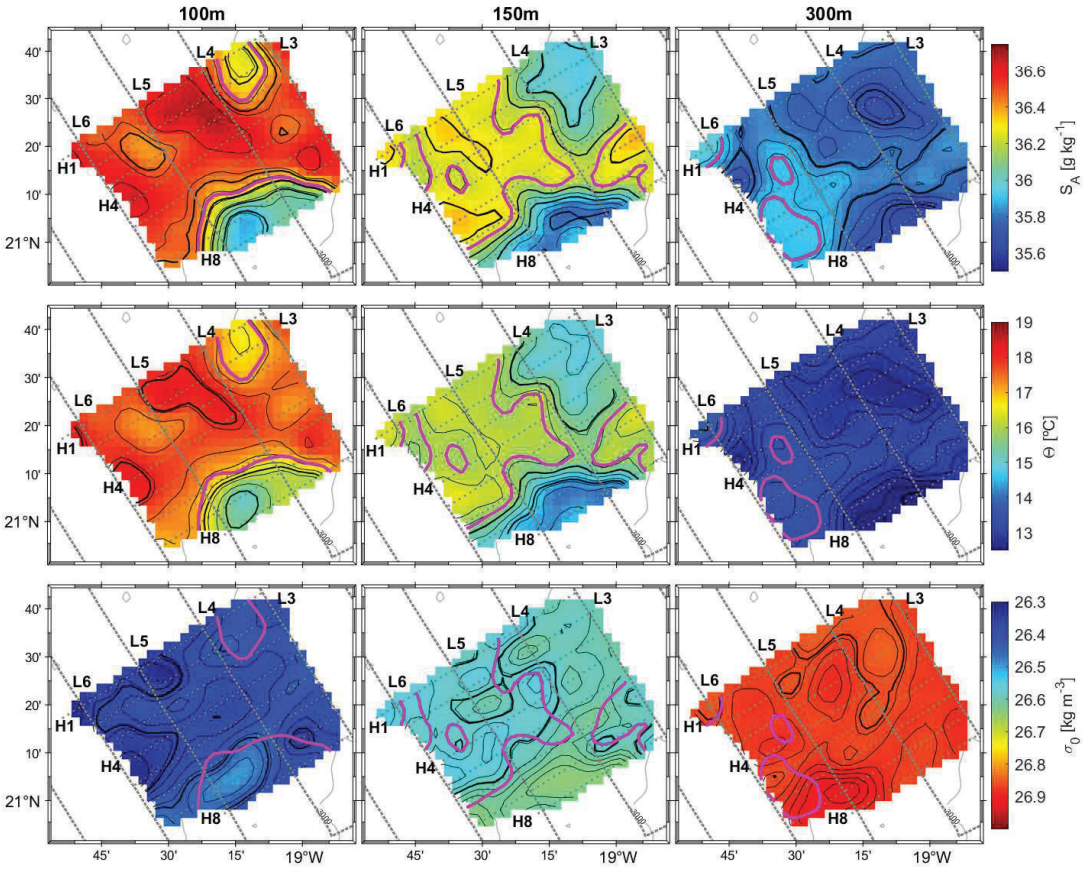

Figure 4.11: Interpolated horizontal sections of S_A (g kg^{-1}), Θ (°C) and σ_0 (kg m^{-3}) (in first, second and third rows) during the submesoscale grid I, at 100, 150 and 300 m depth (in first, second and third columns). The pink lines represent the isohalines of 36.36, 36.23 and 35.9 g kg^{-1}, respectively, that separated NACW and SACW at 100, 150 and 300 m. The sampled transects of first (L3-L6) and second (H1-H8) legs are represented by small gray dots.

The NACW-SACW front was barely appreciated in the last leg at 100 m depth due to NACW predominance at this depth. Its salinity and temperature values, above 36.5 g kg^{-1} and 18 °C, were slightly larger than those sampled in NACW in the two previous legs (first column in Fig. 4.12). The front was only crossed on transects F3 and F5 when two small bags of SACW (S_A <36.36 g kg^{-1} and Θ <16.75°C) were sampled at 40 and 30 km from the origin, respectively (between transects L4 and L5 in first column, Fig. 4.12). However, along each transect (from F1 to F5) the NACW-SACW front was detected twice at 150 m depth due to the slightly altered SACW (S_A ≈36.1 g kg^{-1} and Θ ≈15.5°C) located in the central area (mainly between transects L4 and L5) crossing the entire domain from southeast to northwest, perpendicularly to the sampled direction (second column, Fig. 4.12). At this depth, the NACW located east and west of the SACW and

with characteristics slightly different, was sampled with salinities and temperatures larger than 36.23 g kg^{-1} and 16.25°C. Due to the eastern (>52.5 km) NACW was more differentiated or purest, the eastern NACW-SACW front, almost on transect L4, was more intense than the western one (second column, Fig. 4.12). In contrast, the water sampled westward (<27.5 km) seemed more to the NACW sampled in the two previous legs at the same depth. At 300 m depth (third column, Fig. 4.12), the SACW with salinities and temperatures below 35.9 g kg^{-1} and 13.5°C, predominated in the entire domain. Some NACW (S_A >35.9 g kg^{-1} and Θ >13.5°C) was also sampled in the easternmost zone, between transects L3 and L4, at this depth. On the other hand, the mean values of σ_0 were slightly smaller than those described in the first and second legs at 100, 150 and 300 m depth. However, as in the previous legs, the potential density anomaly field was the most difficult to relate to the NACW-SACW front location at different depths.

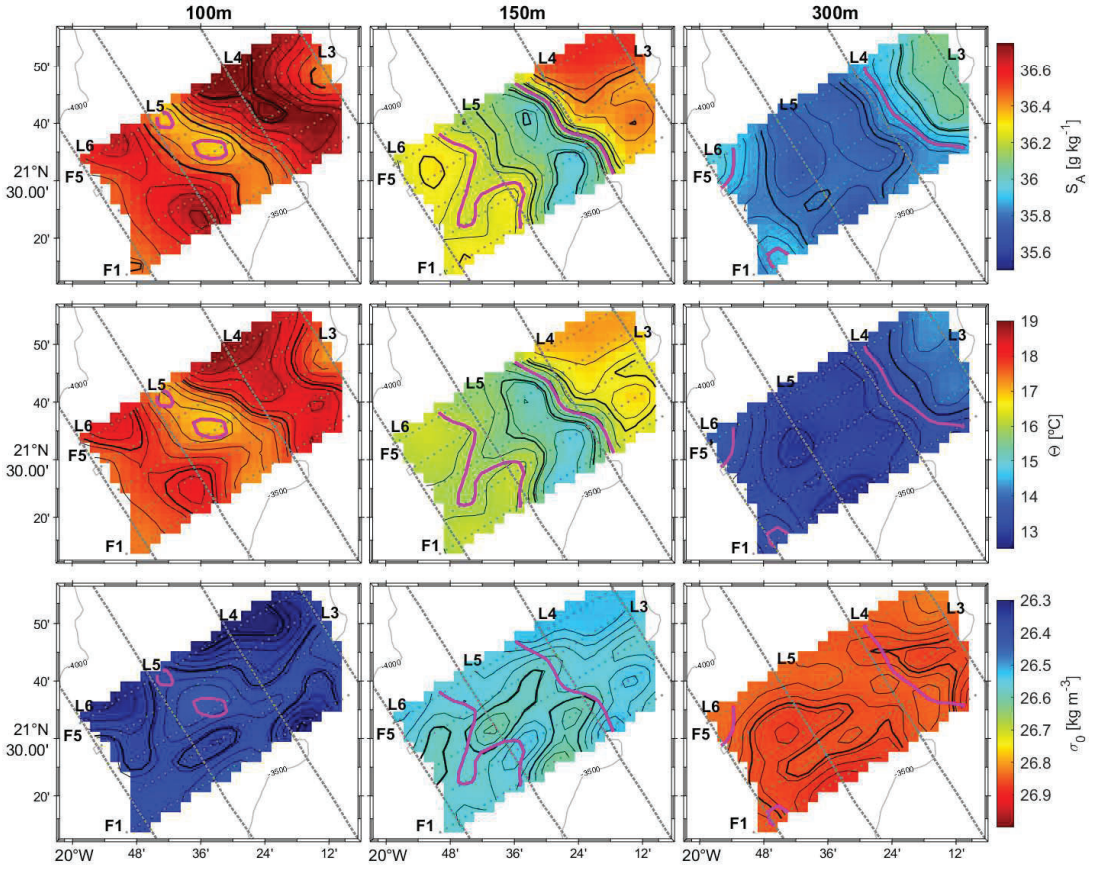

Figure 4.12: Interpolated horizontal sections of S_A (g kg^{-1}), Θ (°C) and σ_0 (kg m^{-3}) (in first, second and third rows) during the submesoscale grid II at 100, 150 and 300 m depth (in first, second and third columns). The pink lines represent the isohalines of 36.36, 36.23 and 35.9 g kg^{-1}, respectively, that separated NACW and SACW at 100, 150 and 300 m. The sampled transects of first (L3-L6) and third (F1-F5) legs are represented by small gray dots.

4.4.6 Horizontal currents

In the three phases, the total velocity sampled by the sADCP and the interpolated one described the same dynamic structure, with practically the same intensities from 40 m to 300 m depth (the interpolated field is shown in the first column of Figs. 4.13, 4.14 and 4.15). Overall during the two submesoscale grids (second and third legs), the sADCP velocities were smaller than those measured during the first mesoscale grid throughout the entire water column (first column, Figs. 4.13, 4.14 and 4.15). Above 100 m depth, these structures were determined by more intense velocities, while, they were gradually reduced below 100 m. Likewise, the estimated geostrophic and ageostrophic fields also presented the highest intensities at 40 m depth (second and third columns, Figs. 4.13, 4.14 and 4.15).

In the first leg, sADCP velocity field showed an anticyclone circulation in the northeast area of the entire water column (first column, Fig. 4.13). Maximum velocities that reached up to 0.3 m s^{-1} at 40 m depth were measured southward in the middle (≈135 km) of transect L2 (with interpolated error less than 5%), and northward in the north (≈160 km) of transect L4 (with interpolated error less than 10%). Furthermore, moderately high westward velocities were measured between 21.25 and 21.75°N in the transects L3 and L4 in the entire water column. This anticyclonic circulation advected the long filament-shaped intrusion with subsurface core of salinity smaller than 36.3 g kg^{-1} at relative-shallow waters centered at 40 m depth in transects L4 and L5 (Fig. 4.4) and extended northward from the origin to more than 60 km and 120 km in transects L4 and L5, respectively (Fig.4.7); it also advected at least part of the SACW of S_A and Θ less than 36.23 g kg^{-1} and 16.25°C, at 150 m depth, from the southeast toward northwest in transects L4 and L5 (Fig.4.10). On the other hand, a current that broke off from the base of the anticyclonic circulation southward in transect L5 (between 35 and 65 km from the origin) had coherence and continuity with the current of 0.25 m s^{-1} observed at 40 m depth and at a distance less than 50 km from the origin in transect L6 (Fig. 4.13). This current was maintained from 40 to 150 m depth. In the same way, further east, at a distance less than 50 km from the origin in transects L1 and L3, another current of at least 0.17 m s^{-1} broke off also from the base of the anticyclonic circulation in south-southwest direction that was observed in the entire water column. In contrast, the sADCP sampled weaker currents south of the anticyclonic circulation (<50 km) in transect L4, with a north-northwest direction, contrary to those sampled in the two transects located next to it.

The geostrophic field also described the northeast anticyclonic circulation sampled by the sADCP but to a lesser extent (second column, Fig. 4.13). This anticyclonic eddy likely corresponds to the A1 structure detected by remote sensing data (Fig. 4.2). While the sADCP revealed it more clearly throughout the water column, the geostrophy clearly described it at 40 and 70 m depth. On the other hand, a geostrophic cyclonic circulation (likely corresponding to the C2 structure in Fig. 4.2) was mainly visible at 40 and 70 m depth (second column, Fig. 4.13) bordering the coldest and least saline water located in the southern boundary of the domain (Fig. 4.7). Finally, it was obtained an intense geostrophic signal between transects L5 and L7 (at more than 180 km from their origin) without a well-defined direction in the northwestern corner of the domain mainly at 40 and 70 m depth which was not visible in the total velocity field of the sADCP with

negligible currents in this area (first and second columns, Fig. 4.13).

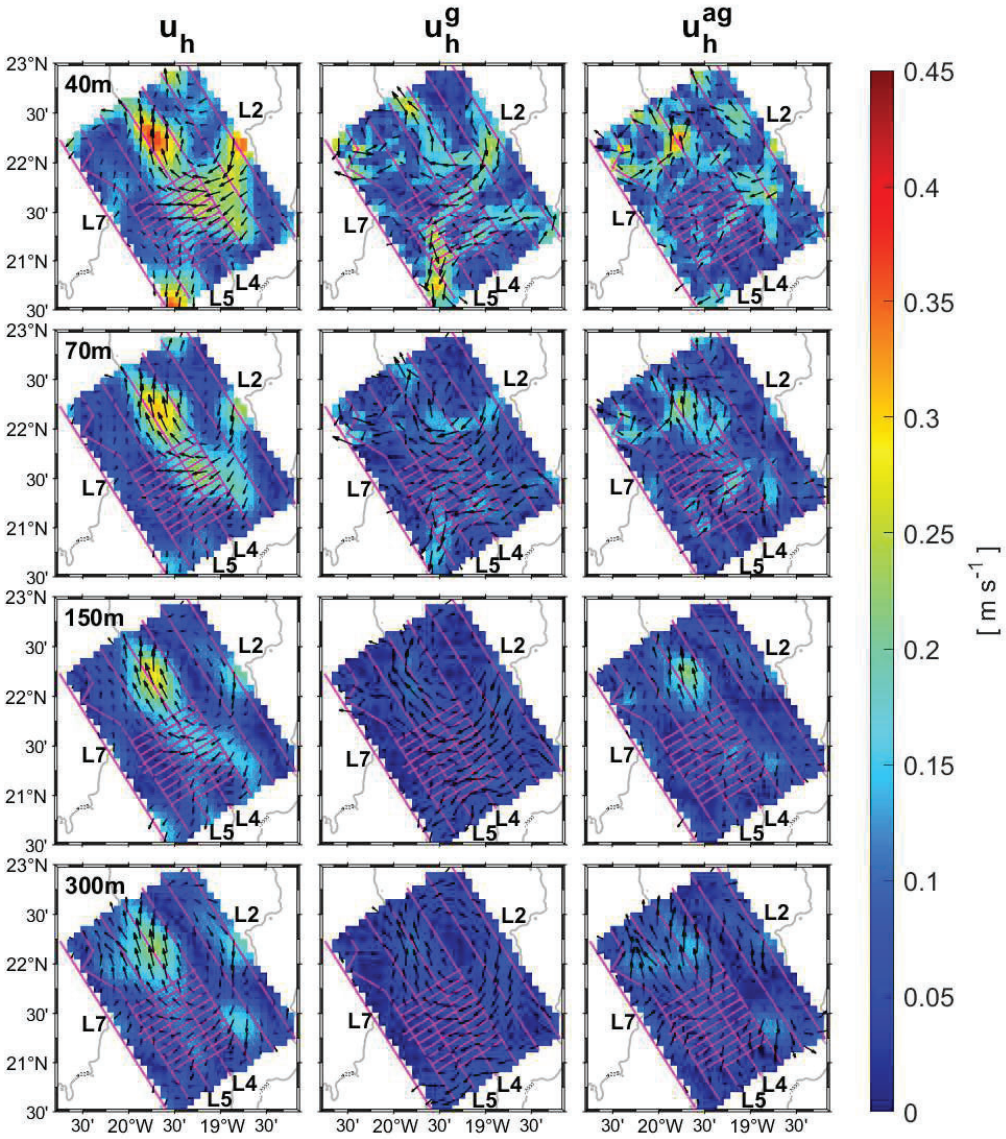

Figure 4.13: Interpolated horizontal sections of the total horizontal velocity field (first column) and the estimated horizontal geostrophic and ageostrophic velocity fields (second and third column, respectively) in units of m s^{-1} at 40, 70, 150 and 300 m depth in the mesoscale grid (first, second, third and fourth rows). The transects of first (L1-L7), second (H1-H8) and third (F1-F5) legs recorded by the ADCP are represented by small pink dots.

The ageostrophic field presented a quite random distribution that had little in common with the consistent signal of the sADCP, especially in the upper 100 m. However, a clear and organized ageostrophic signature was visible in the northern area between transects L3 and L5 at more than 180 km from their origin (third column, Fig. 4.13), where a northward jet was detected in the transition from the NACW (S_A =36.75 g kg^{-1} and Θ >18°C) cored "intrathermocline eddy" and the SACW (S_A <36.23 g kg^{-1} and Θ <16.25°C) "tongue" that extended southward on transect L5 (at 150 m depth in Fig. 4.10). This jet was observed in practically the entire water column down to 300 m depth. Another ageostrophic signal was also observed south-southwestward between transects L1 and L3, at a distance less than 50 km from the origin, between 40 and 300 m depth whose location and intensity were in agreement with the total velocity of the sADCP signal. In fact, the ageostrophic signal was also maintained at depths greater than 150 m in other locations of the domain, such as between transects L1 and L3 at 50 km from the origin where south-southwestward current was observed in the entire water column, coinciding with the behavior of total velocity (first and third columns, Fig. 4.13). This last current could be the secondary horizontal circulation normal to the NACW-SACW front described by Barton, 1987.

In summary, in the first leg, the sADCP field was correctly explained by the geostrophy in the upper levels (mainly from 40 to 70 m depth) but in a poor way below 150 m depth where the ageostrophy agreed with the field described by the sADCP.

Although the second and third leg's sADCP velocities were smaller than those measured in the first mesoscale leg (first column in Figs. 4.14 and 4.15), the geostrophic and ageostrophic fields were more intense with frequent maximum reaching up to 0.30 (more larger in the second leg) at 40 m and 0.20 m s^{-1} at 70 m depth (second and third column in Figs. 4.14 and 4.15). However, the geostrophy and ageostrophy drastically decreased in intensity below 70 m depth in both submesoscale phases. As in the mesoscale grid, the circulation described by the sADCP in these two submesoscale grids was highly explained by the geostrophic current in most of the water column (first and second column in Figs. 4.14 and 4.15). In fact, the total current was "subgeostrophic" due to be smaller than the geostrophy in both cases. Nevertheless, some exceptions in some specific locations were present mainly at the shallowest depths where the total and geostrophic velocities were not be in agreement in intensity or/and direction such as between transects H2 and H3 at 40 km distance from their origin in the submesoscale grid I (Fig. 4.14) or between transects F1 and F2 east of transect L5 in the southwest of the submesoscale grid II (Fig. 4.15). Additionally, in these locations, and in many others (for example, between transects H5 and H7 from the origin to 40 km east, in Fig. 4.14), where the ageostrophic and geostrophic velocities had similar intensities, they had also opposite directions, mainly above 150 m (second and third columns, Figs. 4.14 and 4.15). Moreover, the most intense Θ and σ_0 gradients were located in these same locations or in their surroundings at 40 and 70 m depth (second and third rows, Figs. 4.8 and 4.9). This fact was mainly observed in some locations of the second leg at 40 m depth, for example, on the southern part of the domain with variations of 2.5°C and 0.75 kg m^{-3} in Θ and σ_0 between transects H7 and H8 (second and third rows, Fig. 4.8). On the other hand, while

the ageostrophy did not coincide with the sADCP field at any depth of the second leg, it explained the description given by the sADCP below 150 m depth in some locations of the third leg (third column in Figs. 4.14 and 4.15).

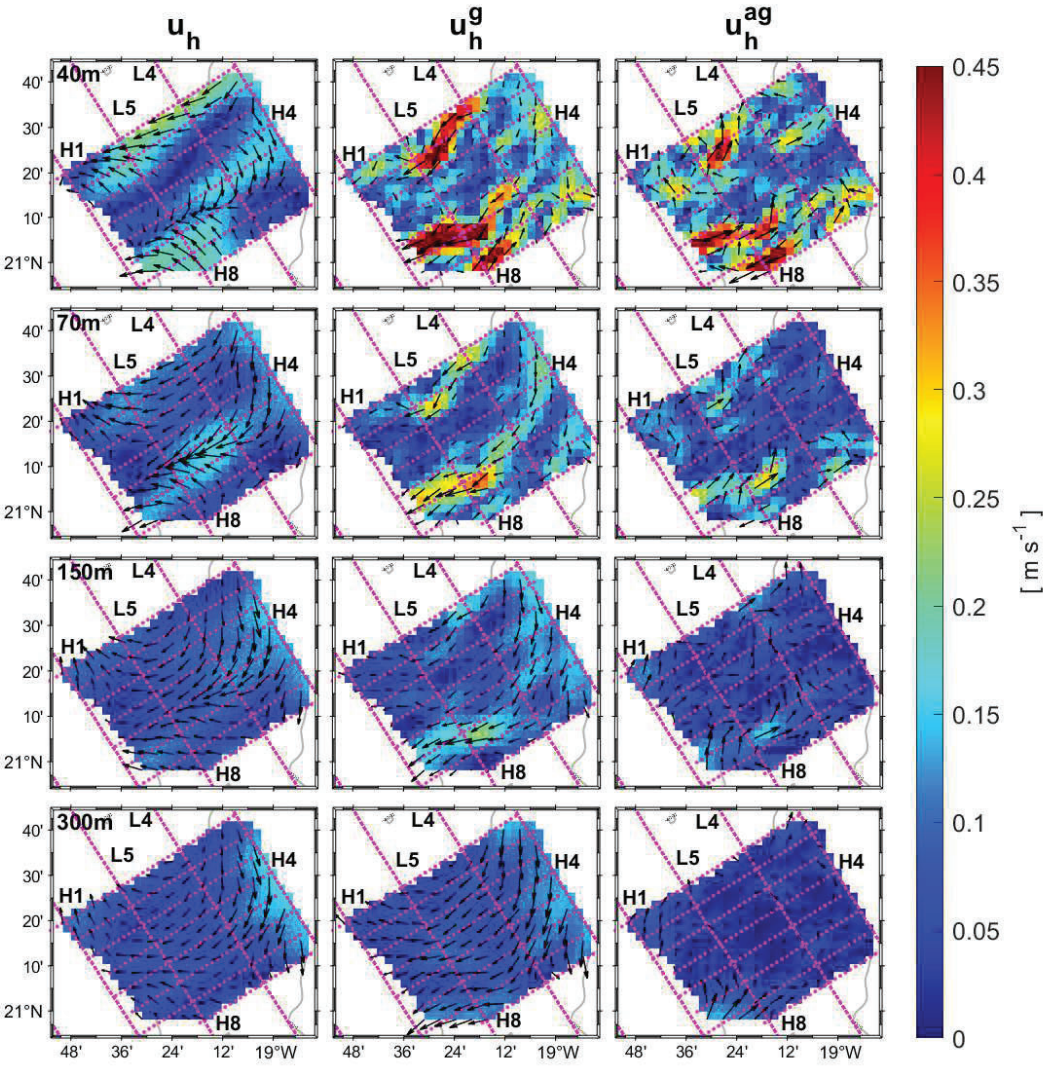

Figure 4.14: Interpolated horizontal sections of the total horizontal velocity field (first column) and the estimated horizontal geostrophic and ageostrophic velocity fields (second and third column, respectively) in units of m s^{-1} at 40, 70, 150 and 300 m depth in the submesoscale grid I (first, second, third and fourth rows). The transects of first (L4 and L5) and second (H1-H8) legs recorded by the ADCP are represented by small pink dots.

During the submesoscale grid I, it is remarkable the flow convergence sampled with the sADCP between H5 and H6, extending southwestward more than 50 km through the entire water column. This convergence detected between the 9 km distance that separated both transects was not sampled before during the cruise (first column, Fig. 4.14). North of the convergence, the anticyclonic circulation described by the sADCP between transects H1 y H5 was in agreement with the dynamics previously described by the current meter in the first mesoscale grid, but slightly more displaced to the northwest in the second leg (Figs. 4.13 and 4.14). This circulation still remained similar in the submesoscale grid II, i.e., tracing a southward flow in the easternmost zone and a northward flow in the westernmost zone of the domain (Fig. 4.15).

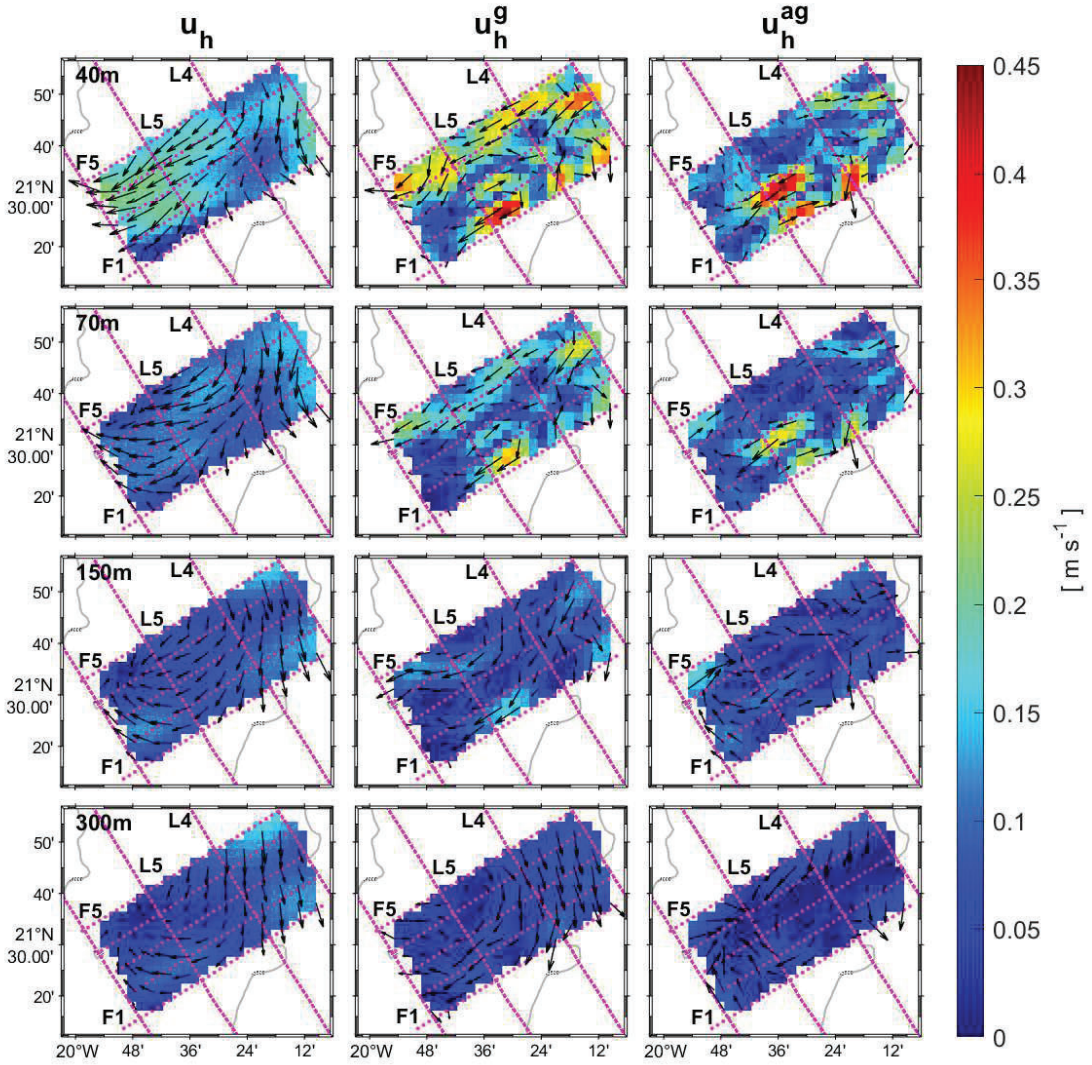

Figure 4.15: Interpolated horizontal sections of the total horizontal velocity field (first column) and the estimated horizontal geostrophic and ageostrophic velocity fields (second and third column, respectively) in units of m s^{-1} at 40, 70, 150 and 300 m depth in the submesoscale grid II (first, second, third and fourth rows). The transects of first (L4 and L5) and third (F1-F5) legs recorded by the ADCP are represented by small pink dots.

4.4.7 Vertical velocities

The importance (weight) of the different sources of estimated vertical velocity (w) in the first (red line), second (green) and third (blue) legs is shown in Figure 4.16.

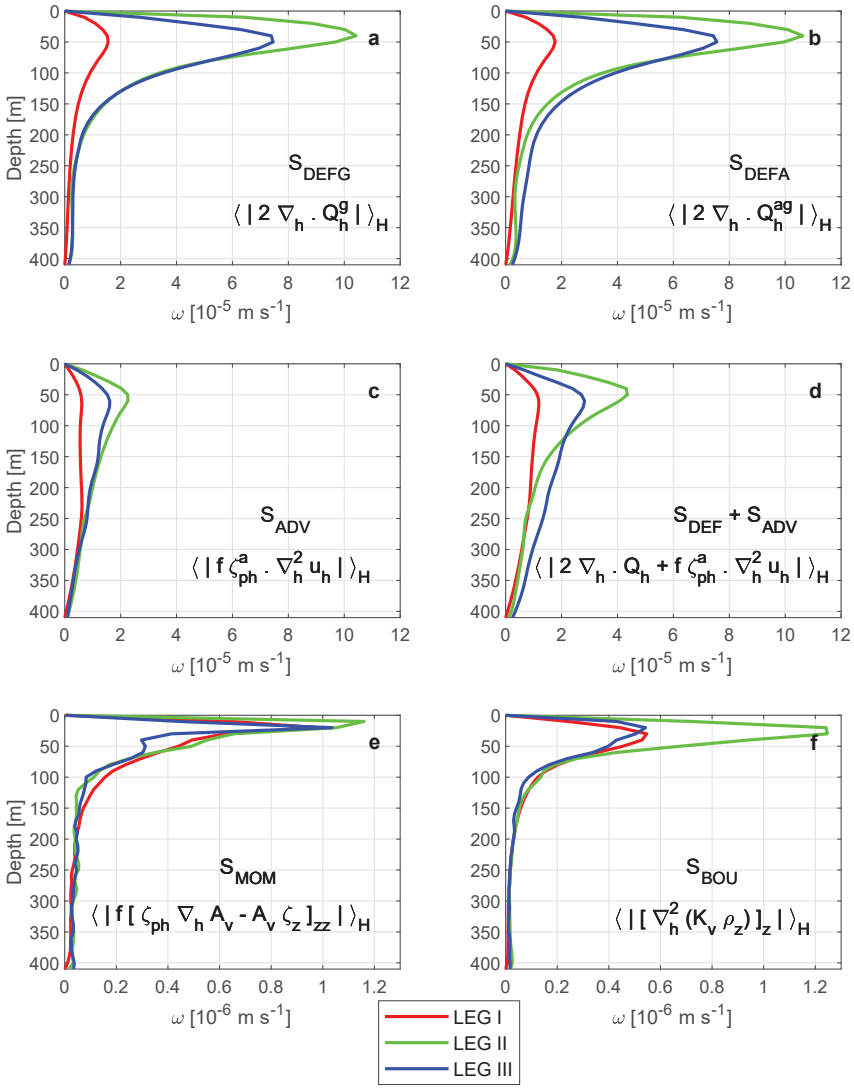

Figure 4.16: Horizontal average of the absolute value of vertical velocity estimated with each forcing term of the diabatic Omega equation, respect to the depth, in LEG-I (red line), LEG-II (green line) and LEG-III (blue line). The individual (S_{DEFG}, S_{DEFA} and S_{ADV}) and the sum ($S_{DEF} + S_{ADV}$) of all the terms of the adiabatic **Q**-vector form are shown in the first four plots (from a to d) and the mixing terms (S_{MOM} and S_{BOU}) in the last two plots (e and f).

In all the legs, the terms of w due to vertical mixing (Figs. 4.16e and 4.16f), were one-or two orders of magnitude smaller than any term of the adiabatic **Q**-vector form (S_{DEFG}, S_{DEFA} and S_{ADV}) throughout the water column. Both mixing terms were maxima above 20-40 m and dropped down drastically below 200 m. The w due to momentum (S_{MOM}) was higher than the buoyancy (S_{BOU}) except in the second leg where S_{BOU} was slightly higher than S_{MOM} (green line, Figs. 4.16e and 4.16f).

In general, the other source terms for w, that form the adiabatic part (Figs. 4.16a, 4.16b and 4.16c), had maxima around 50-70 m decreasing moderately through the water column. Taking into account the terms included in the adiabatic part (S_{DEFG}, S_{DEFA} and S_{ADV}), the w estimated from the ageostrophic deformation (S_{DEFA}) was the largest one, followed by the geostrophic deformation (S_{DEFG}), which was similar or slightly smaller, and by last, the smallest w estimated from the ageostrophic advection (S_{ADV}). It should be emphasized that the total w of the adiabatic **Q**-vector form indicated in Figure 4.16d was smaller than the geostrophic (S_{DEFG}) and ageostrophic (S_{DEFA}) deformations' ws.

All the ws in both submesoscale grids (green and blue lines) were considerably larger than those estimated in the mesoscale grid (red line). In fact, the maximum values of w of the adiabatic **Q**-vector form for LEG-II (green line) and LEG-III (blue line) were more than two times higher than those estimated in LEG-I (red line), at least up to 200 m depth (Fig. 4.16d). Overall, the largest values of w were obtained in LEG-II (green line), followed by the values of LEG-III (blue line) and finally, with the smallest values in LEG-I (red line). However, practically all the w estimated from the geostrophic (S_{DEFG}) and ageostrophic (S_{DEFA}) deformations behaved similarly throughout the water column in all the legs (Figs. 4.16a and 4.16b). In contrast, the w calculated from the ageostrophic advection (S_{ADV}) was slightly different in the first leg where it gained more importance between 50 and 250 m depth (line red, Fig. 4.16c).

Considering the vertical mixing due to momentum (S_{MOM}) and buoyancy (S_{BOU}) were negligible, Figures 4.17, 4.18 and 4.19 show the horizontal sections of the vertical velocity contributions at 40, 70, 150 and 300 m depth in the first, second and third legs, respectively. The distribution of the total vertical velocity associated with the adiabatic part remained constant in practically the entire water column. Small alternating upwelling and downwelling cells associated with ageostrophic and geostrophic deformations (S_{DEFG} and S_{DEFA}) were distributed throughout most of the domain (first and second columns, Figs. 4.17, 4.18 and 4.19). The w associated with the ageostrophic deformation was slightly larger and of opposite sign to vertical velocity due to geostrophic deformation, reducing the w due to total kinematic deformation $2\nabla_h \cdot \mathbf{Q}_h$ in all the legs (fourth column, Figs. 4.17, 4.18 and 4.19). However, the deformation was higher in the last two legs, while the maxima of w due to ageostrophic and geostrophic deformations exceeded the value of $3{\times}10^{-4}$ m s^{-1} at 40 m depth in the submesoscale domains (first and second columns, Figs. 4.18 and 4.19), w barely reached to $1{\times}10^{-4}$ m s^{-1} at the same depth in the mesoscale grid (first and second columns, Fig. 4.17). In fact, the sum of all the vertical velocities due to the terms that formed the adiabatic part (S_{DEFG}, S_{DEFA} and S_{ADV}) was much larger in the two submesoscale grids throughout the water column (fourth column, Figs. 4.17, 4.18 and 4.19). In all the legs, the most intense and important total vertical velocities (with the highest values) of ascent (and/or descent) were described in specific zones where the w due to the ageostrophic deformation (S_{DEFA}, first column) and ageostrophic advection (S_{ADV}, third column) were added (fourth column, Figs. 4.17, 4.18 and 4.19). Moreover, the w direction of the S_{ADV} term coincided with the total w in almost all these areas where the vertical velocity was maximum and upwards.

In the first leg, the ageostrophic and geostrophic alternating cells (first and

second columns, Fig. 4.17) bordered the southernmost SACW (S_A <36.23 g kg^{-1} and Θ <16.25°C) and described the thermohaline NACW-SACW front at 150 m, specifically in the southwestern area between transects L6 and L7, where the most marked density front was sampled (Fig. 4.10) and these cells were especially intense. On the other hand, the small ageostrophic and geostrophic cells also bordered the filament-shaped intrusion with subsurface core of salinity smaller than 36.3 g kg^{-1} centered at 40 m and the very low salinity and cold water (S_A <36 g kg^{-1} and Θ <16.5°C) located to the south at 70 m depth (Fig. 4.7). However, these facts were not reflected in the total vertical velocity (fourth column, Fig. 4.17) that only described a quadrupole with four small cells, two ascending and two descending, in the southernmost area between transects L3 and L4 at 40 and 70 m depth. On the other hand, it should be noted another quadrupole structure described by the total vertical velocity at 40 and 70 m, further north of the domain, just above the location of the small intrathermocline eddy crossed in transect L4 (Figs. 4.4 and 4.10).

Apart from this small-scale variability of the first leg, the best approximation of w, that was estimated by the sum of all the w terms (fourth column, Fig. 4.17), roughly described a vertical velocity dipole, with an upwelling in east and downwelling in west, associated with the large anticyclonic eddy located in the northeast of the domain (first column, Fig. 4.13) and an isolated upwelling cell in southwest with a maxima of $1{\times}10^{-4}$ m s^{-1} at 40 m depth, slightly west of the shallow filament-shaped intrusion of S_A <36.3 g kg^{-1} (Fig. 4.7) and that also described with less intensity at other depths, such as at 150 m, west of the NACW-SACW front (Fig. 4.10).

Small structures were also described in the total w field in the other two legs (the sum of all the w terms due to S_{DEFG}, S_{DEFA} and S_{ADV} in the fourth column of Figs. 4.18 and 4.19). Except for the northeastern corner of LEG-II, the alternating cells of w due to the geostrophic and ageostrophic deformations were distributed throughout the domain in both legs (first and second columns, Figs. 4.18 and 4.19). Additionally, in the southeastern part of the domain of LEG-II, the w due to ageostrophic advection described two alternating positive and negative cells with their cores between transects H6 and H7 that were larger but less intense than the geostrophic and ageostrophic deformations' cells, that extended down to 150 m depth (third column, Fig. 4.18). These two cells with maximum vertical velocities of more than 2×10^{-4} m s^{-1} (at 40 m depth) seem to mark the behavior of the total adiabatic vertical velocity (fourth column, Fig. 4.18) around the zone where the convergence measured by the ADCP was located (between H5 and H6 in first column of Fig. 4.14), with ascending (descending) movements of mostly colder (warmer) and less (more) salty water in west (east) (Figs. 4.8 and 4.11). By contrast, the ageostrophic advection did not define any significant cells in LEG-III (third column, Fig. 4.19).

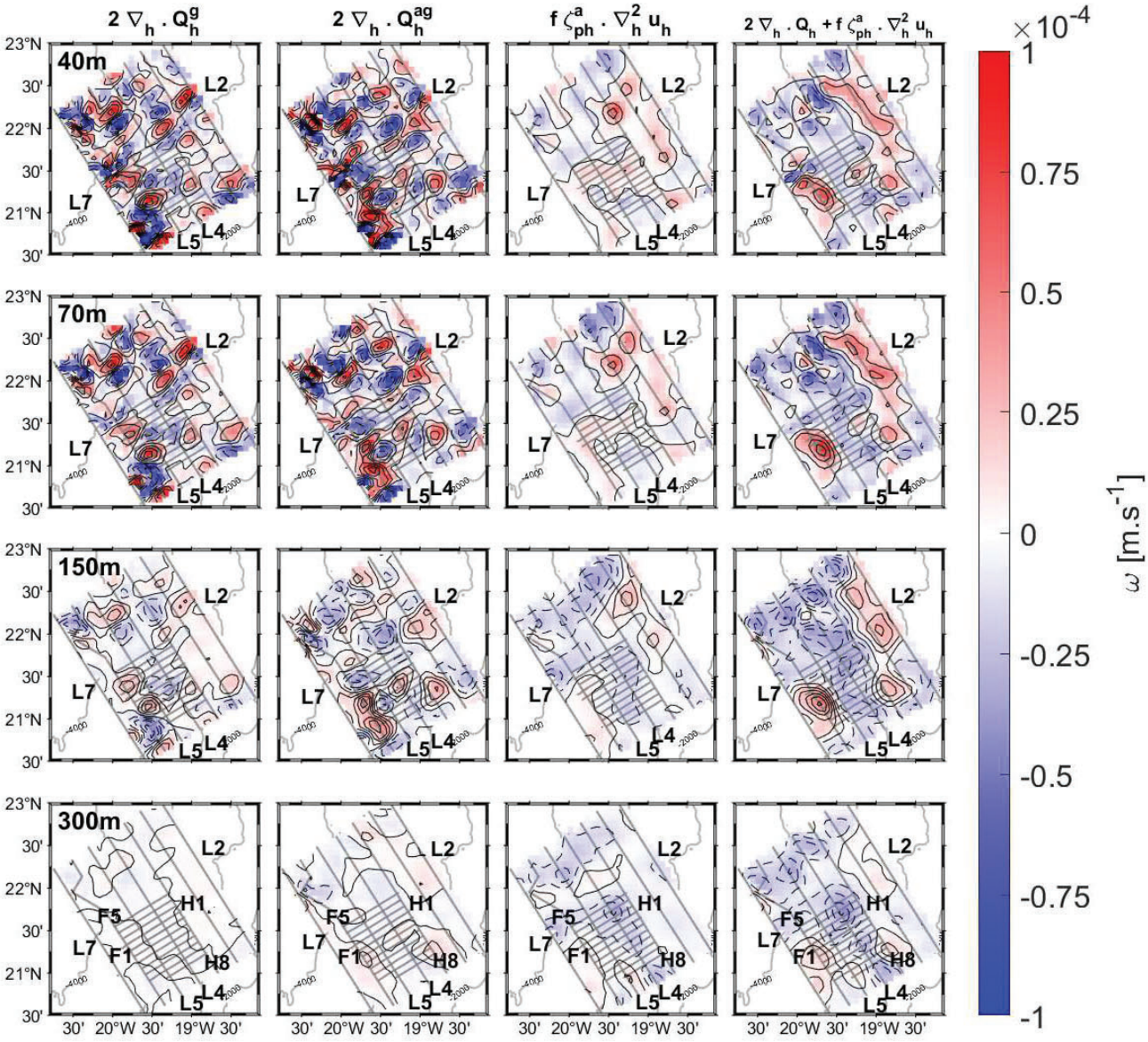

Figure 4.17: Vertical velocity (w) estimated with each individual forcing term (S_{DEFG} in first, S_{DEFA} in second and S_{ADV} in third columns) and the sum of all of them (fourth column) of the adiabatic **Q**-vector form Omega equation at 40, 70, 150 and 300 m depth (first, second, third and fourth rows) in the mesoscale grid. The sampled transects in the first (L1-L7), second (H1-H8) and third (F1-F5) legs are represented by small gray dots.

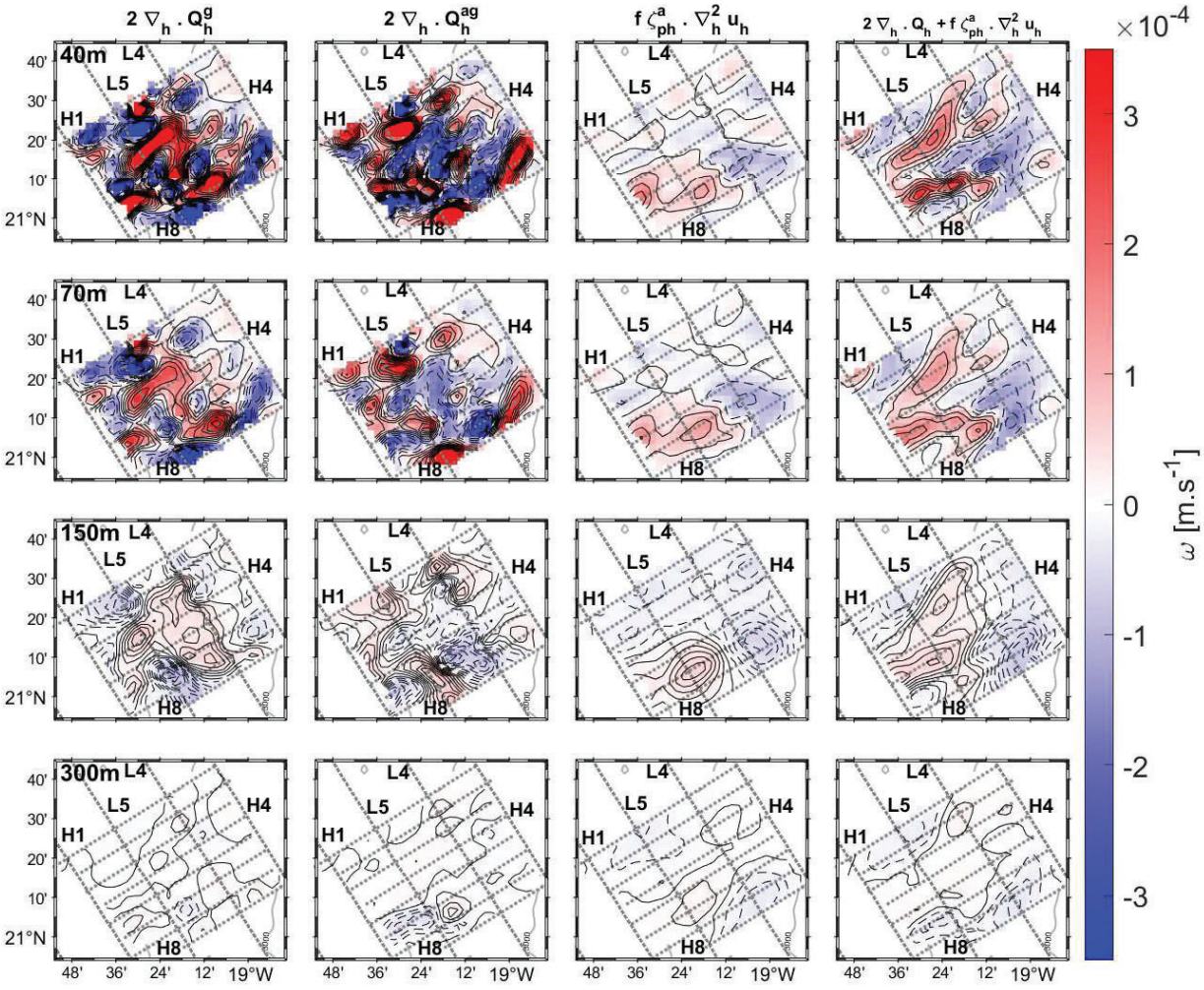

Figure 4.18: Vertical velocity (w) estimated with each individual forcing term (S_{DEFG} in first, S_{DEFA} in second and S_{ADV} in third columns) and the sum of all of them (fourth column) of the adiabatic **Q**-vector form Omega equation at 40, 70, 150 and 300 m depth (first, second, third and fourth rows) in the submesoscale grid I. The sampled transects in the first (L4 and L5) and second (H1-H8) legs are represented by small gray dots.

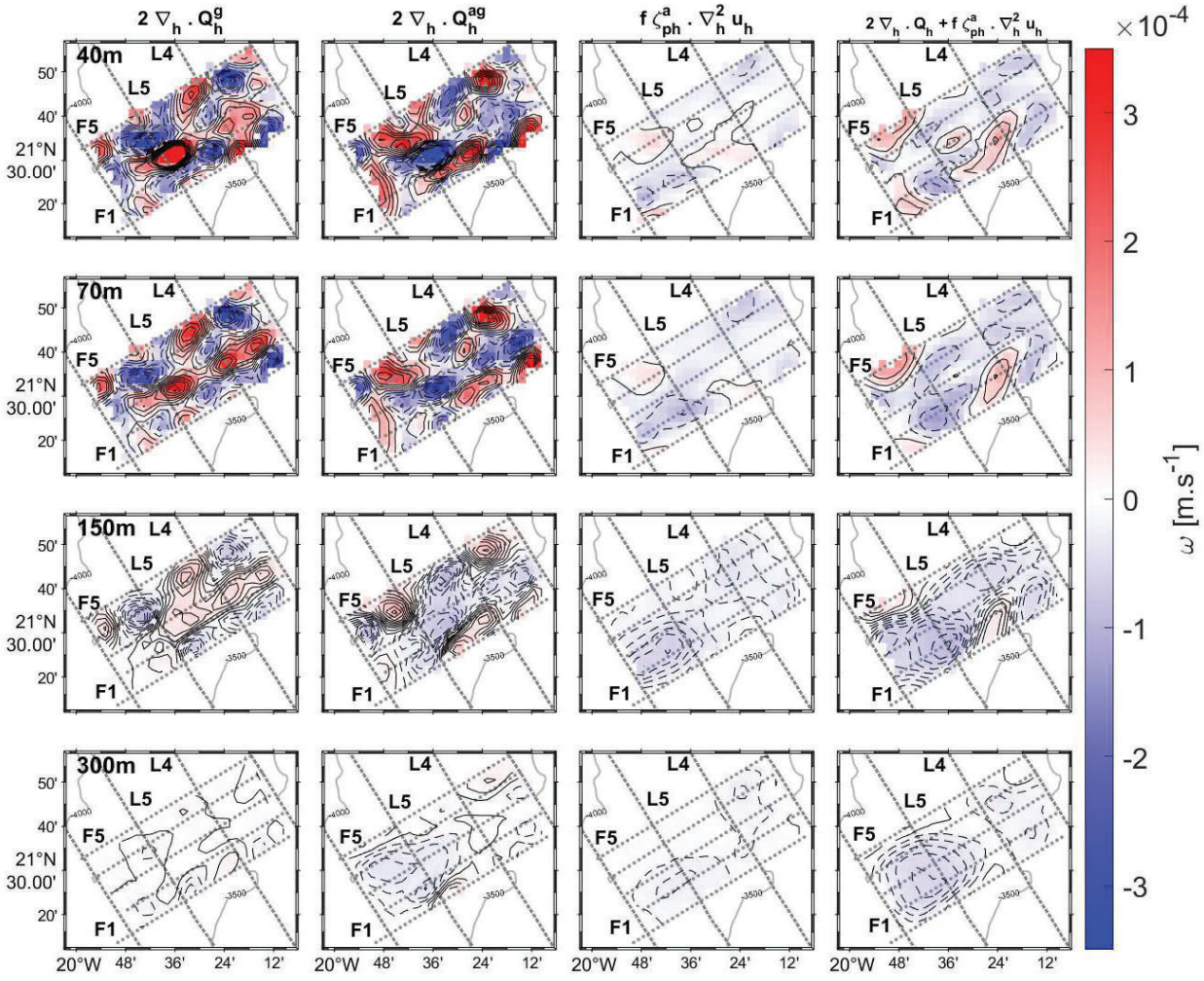

Figure 4.19: Vertical velocity (w) estimated with each individual forcing term (S_{DEFG} in first, S_{DEFA} in second and S_{ADV} in third columns) and the sum of all of them (fourth column) of the adiabatic **Q**-vector form Omega equation at 40, 70, 150 and 300 m depth (first, second, third and fourth rows) in the submesoscale grid II. The sampled transects in the first (L4 and L5) and third (F1-F5) legs are represented by small gray dots.

The total w mainly described an upwelling in the northwest and a downwelling in the southeast of the submesoscale I grid and a downwelling in almost all the submesoscale II grid, in agreement to a great extent with the direction of the total w estimated in same locations of the first mesoscale leg (fourth column, Figs. 4.17, 4.18 and 4.19). Regarding the w magnitude, it is reiterated that the intensity of the total w was greater throughout the water column in both submesoscale grids than in the mesoscale grid.

4.5 Discussion and conclusions

For first time, the evolution of 3-D thermohaline structures associated with the CVFZ is addressed producing a high spatial resolution data set comprised of twenty

hydrological and sADCP transects carried out during 18 days of November 2017. Initially, mesoscale grid was sampled with a minimum spatial resolution of $\sim$ 27 km between the transects. Six days later, a second submesoscale grid sampling was performed with a resolution of $\sim$ 9 km between the transects, in a smaller domain within the mesoscale grid. Finally, a second submesoscale grid was performed with an identical spatial resolution as the previous one in an area located slightly further north also within the mesoscale grid. The two submesoscale grids share two of their transects that were therefore sampled twice.

The water column may be separated in four domains according to the behavior of meso- and submesoscale structures: first, the shallowest zone within the mix layer waters, above 30-40 m depth; second, the seasonal thermocline zone from 30-40 m to 100 m; third, the upper central waters between 100 and 300 m; and finally, the deeper central waters below 300 m depth. This last domain is featured by a homogeneous zone with few spatial and temporal variability between the water mass properties and by the smallest horizontal and vertical velocities. In contrast, the second zone below the MLD and above 100 m exhibits a high variability and intense horizontal and vertical velocities. In particular, a filament-shaped intrusion with subsurface core of salinity smaller than 36.3 g kg^{-1} centered at 40 m depth and a very low salinity and cold water (S_A <36 g kg^{-1} and Θ <16.5°C) located to the south at 70 m depth are remarkable common structures in the first two legs that are not detected in the third leg. Lastly, the water column between 100 and 300 m presents a moderately high variability with relative high velocities. Within this zone, the NACW-SACW thermohaline front is detected with different forms below 100 m depth in all the legs. In some specific locations, such as in the southern area between L6 and L7 in the first leg and between H7 and H8 in the second leg, the thermohaline front vertically extends to more than 200 m depth with its main characteristics clearly represented at 150 m: the warm and salty NACW is separated by abundant strongly marked isotherms and isohalines, and some much less marked isopycnals, from the cold and fresh SACW (Barton, 1987; Zenk, Klein, and Schroder, 1991). Moreover, in these same locations, despite the NACW-SACW front is not defined a priori at shallow depths, it seems to extend up to 70 m in the first two legs. This fact can be explained due to the continuity in physical characteristics that remains constant between 70 and 100 m depth and that simultaneously define the very low saline and cold water at 70 m and the SACW found at 100 m depth in LEG-I and LEG-II.

The mesoscale structures present a spatial distribution closely related to the dynamic unveiled by the sADCP and to a lesser extent by the geostrophic field, that is also in line with the situation described by remote sensing (except in the LEG-III). The dynamic situation may be described by the anticyclonic eddy (A1) in the north and the cyclonic circulation (C2) in the south, both in geostrophic balance, and the locations of the shallow filament-shaped intrusion of small salinity under the MLD, of the very low salinity and cold water (of similar characteristics of SACW) at 70 m depth and of the SACW (and therefore, of the NACW-SACW front) at 100 and 150 m depth, in LEG-I and LEG-II. These waters of well-defined characteristics located on the edge of the anticyclonic eddy are advected and entrained around the latter (Meunier et al., 2012) in the first leg. The filament-shaped intrusion could detached from the interaction between the very low salinity and cold

water "similar" to SACW located to the south at 70 m depth and the northeastern anticyclonic eddy (Barton, 1987). In the second leg, the weakening of the anticyclonic eddy (A1) that moved northward from the first to the second leg could enable a westward shift of the shallow filament-shaped intrusion, reaching to transect L6, in which it had not been previously detected at 40 m depth, and a slight northward movement of the SACW and the NACW-SACW front (relative to their previous positions in the first leg) at 100 m. At 150 m depth, the NACW-SACW front distribution can be also justified with the dynamics described by sADCP in the second leg. SACW located mainly in the southwest and northeast ubicates the NACW-SACW front crossing the domain in a southwest-northeast direction, slightly changing its distribution and orientation with respect to its description in the previous leg. In the third leg, the shallow filament-shaped intrusion centered at 40 m is not detected. Neither the SACW nor the NACW-SACW front are almost undetectable at 100 m depth. It has been more difficult to relate the field described by the sADCP with that described by hydrography at shallow and deep depths in the last two submesoscale legs possibly due to the low sADCP intensities measured in these legs. Specially in LEG-III, the sADCP velocities do not coincide with the enhancement of the anticyclonic eddy (A1) observed by altimetry neither with the structures described by hydrology.

A continuity is observed in relation to the common structures analyzed and related in the shallow and deep horizontal sections between the first and second legs. The third leg did not have much continuity with the previous leg due to the structures described by salinity, temperature and potential density anomaly changed completely from LEG-II to LEG-III at 10, 40, 70 and 100 m. This made hard to relate the situation analyzed in the third section between 10 and 100 m depth with those previously described in the first and second leg in this highly variable seasonal thermocline zone. However, below 100 m depth, the salinity versus depth equation that determined theoretically the front between NACW and SACW (Burgoa et al., 2021) facilitates the analysis of the hydrological differences (structure and central water masses) between the three sampled legs.

The notable differences observed in the common domain of both submesoscale grids might indicate that the elapsed time between both, approximately two days, might be enough to evolve the hydrological submesoscale features in this area, with the development or decay of thermohaline structures. On the other hand, the opposite sampling courses might also be responsible for some of this variability. Specifically in the common domain, the highest variability is observed from the permanent halocline/thermocline to the shallower waters where the dynamic is more intense and unstable, with abundant processes within the small inertial periods.

Ageostrophic horizontal velocities exhibit a quite random pattern throughout the water column in the three sampled legs. The maximum intensities are obtained at 40 m depth in all the legs, with also some significant intensities between 100 and 300 m, mainly in some specific locations of the first leg where ageostrophy locally exceeds in intensity to the geostrophy increasing the total horizontal current. Taking into account that the currents measured by the sADCP are lower in the two submesoscale legs, the intense geostrophic and ageostrophic horizontal velocities estimated in these two grids need to be highlighted with respect to those estimated

in the mesoscale one (Barceló-Llull et al., 2021). On the other hand, in the first and second legs the geostrophic and ageostrophic horizontal velocities are opposite in direction where the most intense thermohaline and density fronts are detected. This fact is more evident in the first submesoscale grid as the intensities of the geostrophic and ageostrophic currents are higher than in the first mesoscale grid. A clear secondary horizontal circulation normal to the NACW-SACW front is not observed in the first and second legs (Barton, 1987). Even though small alternating cells of upwelling and downwelling due to the ageotrophic and geostrophic deformations are described on the location of the thermohaline front, no significant total vertical velocities are observed over this thermohaline structure because the ageostrophic and geostrophic deformation are opposite cancelling the total kinematic deformation (Pallàs-Sanz, Johnston, and Rudnick, 2010b).

Regarding other findings related to the spatial resolutions, the flow convergence revealed by the sADCP in a time interval shorter than 12 hours is to be pointed out. This convergence was detected within the 9 km that separated the transects H5 and H6 along more than 50 km, and it was not detected in the mesoscale grid or with the altimetry data set. This convergence in the flow might reflect the location of the front between NACW and SACW, which in turn is marked by two large and alternating upwelling and downwelling cells due to the ageostrophic advection.

Submesoscale structures smaller than the deformation radius of 40 km are sampled in all the sampling grids. Despite the resolution of these samplings, most of the submesoscale structures were crossed by the sampling transects. A good example is the intrathermocline eddy crossed during transect L4 in the periphery of the mesoscale anticyclonic eddy, linked to a northward ageostrophic horizontal jet that has an associated vertical dynamic described by a quadrupole of upwelling and downwelling small cells. Additional small isolated structures, as the intrusions defined by strong differences in the salinity field, and to a lesser extent in the temperature, are especially detected within the halocline/thermocline zone (Meunier et al., 2012). The development of these intrusions often associated to the thermohaline front are explained by the interleaving or diapycnal mixing processes (Barton, 1987; Erasmi, Siedler, and Onken, 1998; Martínez-Marrero et al., 2008) which are not well represented in this work as the estimated vertical velocities due to vertical mixing are practically negligible compared to those of other processes. This happens because this version of KPP only takes into account instabilities due to vertical shear and the background of internal wave rupture resulting in non-real values of A_v and K_v (Pallàs-Sanz, Johnston, and Rudnick, 2010a). Therefore the w estimated from the vertical mixing will have greater errors than the other vertical velocities estimated from the processes that employ in situ data (sADCP's and density's fields).

The total vertical velocities estimated in the two grids with the highest sampling resolution (LEG-II and LEG-III) are higher than those of the first leg with the lowest sampling resolution as it also occurs with the geostrophic and ageostrophic horizontal velocities. Specifically, maximum values of $2{\times}10^{-4}$ m s^{-1}, which are more than three times greater than those estimated in the first leg, are reached between 40 and 150 m depth. Furthermore, these values are comparable to those estimated by other authors in uncompensated density fronts (Rudnick, 1996; Pallàs-Sanz, Johnston, and Rudnick, 2010b). However, it has not been possible to carry out a

more extensive and robust analysis considering other sources of vertical velocity such as that due to the wind, which also affects below the MLD, and that associated with the Potential Vorticity conservation (Capet et al., 2008; Pallàs-Sanz, Johnston, and Rudnick, 2010a; Barceló-Llull et al., 2017b) and on the errors associated with each term of the Omega equation (Pallàs-Sanz, Johnston, and Rudnick, 2010b).

Although the largest w is usually that of the ageostrophic deformation, which is practically canceled in most of locations by the w of the geostrophic deformation, the total adiabatic vertical velocity, ignoring the vertical mixing, is also conditioned by the w of the ageostrophic advection, that has a lower value. That is, in all those areas where the ageostrophic deformation is not completely cancelled, the ageostrophic advection is added to it, reaching to the highest total ascending or descending velocities. The total w (the sum of all the w of the adiabatic terms S_{DEFG}, S_{DEFA} and S_{ADV}) of the first leg that describes a vertical velocity dipole, with an upwelling in east and downwelling in west, associated with the large northeastern anticyclonic eddy, and an isolated upwelling cell in southwest, slightly west of the shallow filament-shaped intrusion at 40 m and west of the NACW-SACW front at 150 m depth, fits with the northwest upwelling and the southwest downwelling of the LEG-II domain and with the general downwelling of the LEG-III domain.

In conclusion, the hydrographic and dynamic structure of the deeper horizontal sections (>150 m depth) has more continuity between the different legs (or lasted longer in time) than the mesoscale and submesoscale structure of the shallower horizontal sections (<150 m depth). This is closely related to the fact that horizontal and vertical velocities are maximum between 40 and 100 m and significantly less intense below 150 m. In fact, by the analysis and comparison of the shallow horizontal sections of all the legs is confirmed that the scales of processes above 100 m depth are smaller. Finally, it should be underlined that although the hydrographic and horizontal velocity fields of the last leg do not fit with those described in the two previous legs, the total vertical velocity estimated in the entire water column of the third leg is in accordance with those in LEG-I and LEG-II.

In this work, it is provided an overview of the FLUXES-II cruise with complementary satellite data, that lead to some preliminary findings. Therefore, the scope of this work is to characterize the water masses, the thermohaline front, the mesoscale and submesoscale structures and the dynamic described by the horizontal current fields that is completed by the different sources of w vertical velocities, of a high spatio-temporal resolution survey, that until now seemed difficult to carry out (especially the submesoscale that was a challenge to resolve in situ), in the CVFZ system. The CVFZ is a complex system with multiple processes interacting at a wide range of spatial and temporal scales. Consequently, future studies will be necessary to deepen into these processes themselves and discuss them widely. Particular emphasis will be devoted to the mixing processes that will generate vertical velocities higher than the values of this work. To do it, the in situ mixing coefficients that will be estimated as other authors within the CVFZ will be considered (Martínez-Marrero et al., 2008). These process-oriented studies will resolve and explain a range of scales and will contribute to enhancing our understanding of the meso- and submesoscale features associated to the CVFZ. Important questions

about the frontal instabilities in the dynamical transition between mesoscale and smaller scale structures will probably be created through this path. In addition, it will be appropriate to carry out a more exhaustive study about the double interpolations errors and the uncertainties associated with the sampling procedure (similar to those made by Gomis and Pedder (2005) and Gomis, Pascual, and Pedder (2005) for the Mediterranean Sea).

Part III

Chapter 5

General conclusions and future perspective

5.1 Main conclusions

The huge observational effort made in this thesis with the combination of in situ, remote and modeling data has allowed to study multidisciplinary processes and cover the characterization of the CVFZ from the basin scale to submesoscale increasing significantly its knowledge.

At the basin level, the most intense currents, which are those recorded on the surface and central water levels, are affected by the mesoscale structures related to the Canary Eddy Corridor and the CVFZ. North of the frontal zone, on the subtropical side, the circulation pattern observed in fall, spring and summer is consistent with a southwestward transport described by the Canary Current and Canary Upwelling Current, affected by isolated eddies south of the Canary Islands, and by the North Equatorial Current, more conditioned by the location of the frontal zone and the meso- and submesoscale associated with it. South of the frontal zone, no marked mesoscale is recorded in the tropical domain; however, the vertical location and the angle of the thermohaline front between NACW and SACW with respect to the Mauritanian coast and the position variability of the ITCZ that moves northward in summer, influence the circulation pattern described by the Mauritanian Current and Poleward Under Current.

Leaving aside seasons in which the samplings take place, the entire domain of COCA remains practically to the north of the frontal zone, only affecting to the southernmost circulation. In fact, the most remarkable change in the net mass transport at surface and central waters layers in COCA's domain occurs in the southern transect where in fall the net mass transport is northward with a value around 4 Sv, while in spring it is southward with a value around 5 Sv.

On the other hand, the frontal zone greatly influences the entire circulation pattern in the FLUXES-I's domain, their transects completely surround the thermohaline NACW-SACW front, leaving it enclosed within the domain. This may be one of the reasons that the estimated accumulative mass transports across the FLUXES's transects are significantly lower than in both COCA campaigns. In this case, the accumulated mass transports are reduced or canceled by the abundance of structures associated with the front that influence the transports' estimates. In addition, in COCA's cruises, in which higher intensities are estimated in the accumulated transports per transect, spatial resolution is lower than in the cruise of FLUXES-I. Possibly due to this fact, the mesoscale is not well resolved and the

mass transports are overestimated. Taking into account all the above arguments, away from the coast, at 26°W, higher offshore transport of surface and central waters is observed north of Cape Blanc, than in lower latitudes.

It is unknown how seasonal upwelling affects south of Cape Blanc cause the FLUXES-I cruise was carried out in summer without strong winds. Nevertheless, thanks to some sampling stations carried out next to the coast, it is known that the area closest to the OMZ is quite complex, highly variable and with the circulation perpendicular to the coast, at least in summer, eastward at surface and central waters.

The central water masses show a fairly consistent latitudinal distribution, well differentiated by the thermohaline front that separates the SACW to southeast and the NACW to northwest of it. The predominance of one or the other is greater the further away it is from the front. By contrast, the distribution becomes more complex when the front is close, due to the abundance of different scales processes happen in the area that influence directly the water masses mixing.

One of the most important contributions of this thesis is the proposed methodology that vertically extends the thermohaline front between NACW and SACW beyond 150 m into the water column where both water masses coexist. To do this, the definition of the front given by Zenk, Klein, and Schroder (1991) and the definitions of NACW and SACW proposed by Tomczak (1981) are considered.

The mean salinity fields of GLORYS model allow to give a "synoptic" view of the orientation and shape that the thermohaline NACW-SACW front adopts within the two big domains delimited by the transects sampled during fall 2002, spring 2003 and summer 2017. In all seasons, the sampled front's location coincides with the front location described by GLORYS model. In the case of COCA's autumn and spring cruises, the front is limited to 150 m while it extends to 650-700 m in the summer of FLUXES-I. In this last case, the locations of the front deduced from the distribution of the water masses of the OMP at different depths coincide closely with those described by the salinities of GLORYS (extracted from the proposed methodology) that also show a complex spatial distribution of the thermohaline front with associated intrusions, meanders and eddies and with an orientation that varies with depth.

Regarding the biochemical characteristics of the sampled central water masses, they are very clearly described during summer in the FLUXES-I cruise because the concentrations and distributions of O_2 and dissolved inorganic nutrients coincide with the locations of NACW and SACW. At 300 m, the sampled SACW has O_2 concentrations lower than 60 μmol kg^{-1} and inorganic nutrient concentrations of around 27-30 μmol kg^{-1} for NO_3, 1.5-1.7 μmol kg^{-1} for PO_4, and 7.5-9.9 μmol kg^{-1} for SiO_4H_4. The inorganic nutrients sampled were very limited in both COCA cruises, so instead of them, the outputs of nutrient concentrations of GLORYS-BIO model were used with nitrates, silicates and phosphates values lower than in situ summer ones because the initial conditions used in the model were climatological, specifically those of WOA13. Despite this, the nutrients distributions also coincided with those of NACW and SACW, with lower concentrations in the northwest and higher concentrations in the southeast of the domain. Additionally, DOC is sampled in COCA cruises with higher and more widely distributed concentrations in the water column in fall than in spring. In both cruises, SACW,

located in the southern transect, presents concentrations of DOC 35-40 μmol L^{-1} lower than those found for NACW.

As occurs with the mass transports in the central water levels, inorganic nutrient, O_2 and DOC transports are also conditioned by the CVFZ and particularly by the thermohaline NACW-SACW front. With respect to the lateral transports to the open ocean through COCA domain, the net westward transports of inorganic nutrients and DOC in fall are smaller than in spring at surface and central water levels. In summer, the development of the vertical front between NACW and SACW provides the opportunity to perform the biochemical transport analysis at both sides of the front at these levels. The main difference between both sides is related to the transport of O_2 which is lower on the tropical side due to the proximity of the OMZ.

Below the central waters, the net transport in the south-north direction in the intermediate water layers is intense and northward in fall, while it weakens and reverses southward in spring. However, the net westward mass transport is less intense in fall than in spring at 26°W in these layers. This coincides with the fact that there is a higher contribution of MW in spring and a slightly higher contribution of AAIW in fall.

In summer, as in fall, the predominant circulation pattern is in a south-north direction. Moreover, a net transport towards the coast at 26°W, contrary to that observed at higher latitudes, is estimated. However, the net transport registered in these levels is westward through the transect closest and parallel to the coast. It seems that mesoscale features constitute a main source of variability in the circulation at these water levels in the entire domain. On the other hand, the predominant water mass sampled at these levels is AAIW, even if some isolated MW is observed near Cape Blanc.

In general, taking into account many of the conditioning factors, it could be said that with these studies it has been seen that the domain located slightly north of the CVFZ works as an inorganic nutrient sink in fall 2002, while it works as a source of inorganic nutrients in spring 2003. It is also observed that this domain acts as a source of DOC in that fall, while as a DOC sink in that spring. Regarding to the summer of 2017, the southernmost domain located on the CVFZ acts as an heterotrophic box revealed by the net oxygen consumption and the remineralization of NO_3, PO_4 and SiO_4H_4 below the photic layer.

Finally, the observational in situ effort made with two different spatial resolution and during three successive sampling legs, in FLUXES-II cruise allows to show how dynamically active and complex is the CVFZ, during 18 days of November 2017. For the first time, the ageostrophic and geostrophic horizontal fields and the vertical velocity are exhibited together with the dynamics described by the sADCP to unveil the processes involved in the development of the mesoscale and submesoscale 3-D thermohaline structures (larger and smaller than the deformation radius) sampled by the Seasoar from sea surface to 400 m depth.

According to the behavior of sampled structures, the water column is separated in four domains: the mixed layer waters; the seasonal thermocline with high variability and intense horizontal and vertical velocities between 40 and 100 m depth; the upper central waters with relative high variability and velocities between 100 and 300 m depth; and finally the deeper central waters with few variability and

also with the smallest velocities below 300 m depth. In fact, the structure of the NACW-SACW thermohaline front detected below 100 m depth in all the sampling legs allows to deduce that the variability below 100 m depth is less than that located above 100 m where abundant submesoscale thermohaline structure is detected. However, in some specific zones of the southern area of the first and second leg, the water above 100 m depth has the same physical characteristics as the SACW located below 100 m, where the most intense salinity, temperature and density front is simultaneously described from 100 m to 200 m depth and where the geostrophic and ageostrophic horizontal velocities are in opposite direction. This fact is more evident in the submesoscale grid (of the second leg) due to the geostrophic and ageostrophic currents intensify when the resolution increases.

Regarding other findings related to the spatial resolutions that are not detected in the mesoscale grid, the flow convergence revealed by the data from sADCP reflect the location of the front between NACW and SACW, in which two large and alternating upwelling and downwelling cells are marked due to the ageostrophic advection in the first sobmesoscale grid.

On the other hand, another dynamic structure that significantly influences over all the thermohaline structures sampled in all legs is an anticyclonic mesoscale eddy that is also described by the geostrophy (and therefore is detected by altimetry) that advects intensely the smaller and flatter thermohaline structure above 100 m and to lesser extent the NACW-SACW front below 100 m depth.

Despite the sADCP describes lower current intensities in the two submesoscale legs, the intense geostrophic and ageostrophic horizontal velocities of more than 0.35 m s^{-1} and the large vertical velocities that reach to 2×10^{-4} m s^{-1} need to be highlighted with respect to those estimated in the mesoscale leg.

The estimates of the vertical velocity associated with the vertical mixing by momentum and buoyancy shown in this thesis are at least one order less than the vertical velocities related to geostrophic and ageostrophic deformations and ageostrophic advection. In general in all the sampled legs, the best approximation of the vertical velocity is lower than that expected. This fact may be due to the important reduction of the vertical velocity of the total kinematic deformation that is practically canceled by the subtraction between the ageostrophic and geostrophic deformations' vertical velocities that have practically the same value and with the opposite sign and due to the small values of vertical velocities related to vertical mixing by momentum and buoyancy.

A continuity is observed in relation to the common structures analyzed in all the water column between the first and second sampling legs, during a time-period of 13 days. The third leg did not have much continuity with the previous legs due to the structures changed completely from second to third leg mainly above 100 m depth. In fact, the differences observed in the common domain of both submesoscale grids might indicate that the elapsed time between both, approximately two days, might be enough to the development or decay of the submesoscale thermohaline structures, mainly above 100 m, in the CVFZ.

In contrast, although the hydrographic and horizontal velocities fields of the third leg do not fit with those described in the two previous legs, the total vertical velocity estimated in the entire water column is in accordance with those of the first and second legs, during a period of time of 15 days.

5.2 Future research

In general, this thesis has mainly described and analyzed physical structures and processes from basin scale to submesoscale that occur, originate and evolve in the CVFZ. However, many questions remain to be resolved.

Specifically, it would be necessary to include the diapycnal part that has been omitted in these works in the inverse models to complete these studies. In the future, it would be also made an effort to match the sampling and processing resolution of the ADCP (ship's ADCP or on the rosette) with the hydrological stations' one in order to validate the inverse model velocity outputs with those of the ADCP or to employ them such as the reference level's ones with the aim to reduce errors. Furthermore, instead of estimate generally the mass transports by water levels, it could be done by specific water masses, taking the OMP information and estimating more precise transports.

The circulation patterns conditioned by the location of the thermohaline NACW-SACW front have been studied in spring, fall and summer seasons, but not in winter. In fact, the full seasonal variability cannot be addressed only with in situ observations from those years. Furthermore, it has not been able to deeply analyze the variability of this front or its influence on the main currents in the CVFZ (such as the PUC) and on the annual- and seasonal-mean mass transports, north and south of it, due to the scarce climatological data and the lack of consistency between the transports estimated from in situ data and the outputs of the global reanalysis model GLORYS (particularly in summer of 2017). In addition, it has not been possible to reach to conclusions about the annual and seasonal variability of the transports and the distributions of the different biochemical variables at the basin level.

On the other hand, the importance of the mesoscale in the mean transports has not been deeply analyzed, that is, we do not know what percentage of these transports are due to the mesoscale, independently or dependently of the thermohaline front. Specifically, many doubts have arisen related to the exchange of properties through the thermohaline front and how the mean transports are affected by the generation of eddies and meanders at this frontal system and their later westward propagation.

In future works, the study of smaller scale processes such as mixing and turbulence processes, which are especially key in the exchange of properties through the thermohaline NACW-SACW front, will be addressed with the aim of achieving a more detailed vision and more complete understanding of the CVFZ and the front in itself. Specifically, the vertical velocity values of vertical mixing due to momentum and buoyancy shown in Chapter 4 have associated errors higher than other vertical terms because the assumptions and parameterization used to calculate the mixing coefficients. In order to estimate more adequate and realistic vertical velocities of vertical mixing with lower associated errors, in situ mixing coefficients estimated from the microstructure data collected by the turbulence profiler in that cruise, should be used in the future. In addition, it will be convenient to include the vertical velocity generated by horizontal mixing of momentum, as a new term of the Diabatic Omega equation, to estimate a more adequate value of the total vertical velocity.

The quantity and quality of data from FLUXES-II that have allowed us to

describe the meso- and submesoscale structures associated with the thermohaline NACW-SACW front, will also allow to understand some of these dynamic processes that originate complex structures around the front through a deeper analysis. For this, it will be important to minimize and analyze all the errors made in the work described in Chapter 4. For example, it should be started by using DIVA 3-D interpolation instead of performing the 2-D interpolations of hydrological and dynamic variables, twice. On the other hand, it would also be necessary to complete a more robust analysis of the processes themselves and errors of the vertical velocity estimates. Additionally, it should include other possible sources of vertical velocity (such as the wind)and it should convenient to complete all the obtained information with estimates of possible fluxes and with local and material derivatives of each physical variable. The challenge will be to try to understand the way in which the different processes and structures of the same and/or different scales interact among each other (such as the interaction between the great Cape Blanc filament and the thermohaline front), given that the nature of these processes themshelves and the interaction of the NACW-SACW front with their concomitant mesoscale, submesoscale and small-scale processes are still at the frontiers of our scientific understanding.

Due to the interdisciplinary nature of the presented data, as soon as the physical processes that occur predominantly in the CVFZ will be addressed and understood, it will be possible to begin to describe and analyze how the physical processes of mesoscale, submesoscale and smaller scales, condition the biochemical parameters distributions in those scales. In this way, these results will be able to relate to the transports and distributions observed at the basin level and perhaps it will be possible to understand the function of the thermohaline front and the main mechanisms of exchange of properties through it.

Finally, it should be underlined that it is necessary to continue making observational efforts such as those carried out in these two interdisciplinary projects in order to understand the physical and biochemical processes and their interactions at all levels and especially at mesoscale, submesoscale and smaller scale levels that occur in frontal systems such as the CVFZ where the currently little studied thermohaline front between NACW and SACW is located. In this way, it might be adequately reproduced by models and it will be an opportunity to deeply analyze the physical processes importance on the biochemical processes.

Chapter 6

Resumen en español

6.1 Introducción

Esta tesis contextualizada dentro la disciplina de la Oceanografía Física, pero con algo de carácter multidisciplinar, surge con el fin de completar algunas de las ideas que se han ido estableciendo a lo largo de la historia en torno a la Zona Frontal de Cabo Verde, CVFZ (Zenk, Klein, and Schroder, 1991).

En los años setenta, el margen oriental del Atlántico Norte comienza a investigarse gracias al programa CINECA (Cooperative Investigations of the Northern Part of the Eastern Central Atlantic). Concretamente son dos los descubrimientos que en el año 1974 marcan el comienzo de las investigaciones sobre esta zona frontal. Por un lado, Hughes and Barton (1974) proponen dos patrones de circulación independientes al norte y al sur de Cabo Blanco (aproximadamente en 21°N) y por otro, Fraga (1974) describe un marcado frente entre el Agua Central del Atlántico Norte, NACW, y el Agua Central del Atlántico Sur, SACW (Tomczak, 1981). Unos años más tarde, mientras Barton (1989) confirma el hallazgo del frente mostrando detalladamente su estructura termohalina junto con otras estructuras mesoescalares, Zenk, Klein, and Schroder (1991) introducen el término de Zona Frontal de Cabo Verde en un estudio en el que caracterizan la zona localizada frente a las costas de Cabo Blanco. Precisamente en este último trabajo se propone la localización de la frontera o el límite entre las aguas NACW y SACW en la intersección entre la isohalina 36 y la isóbata de 150 m, siendo éste el criterio de referencia para el frente en la actualidad.

Durante los últimos años se han ido desarrollando algunos estudios en la CVFZ focalizados principalmente en la circulación a escala de cuenca (Zenk, Klein, and Schroder, 1991; Pérez-Rodríguez, Pelegrí, and Marrero-Díaz, 2001; Pastor et al., 2008; Peña-Izquierdo et al., 2012) y en la mezcla y turbulencia de las escalas más pequeñas (Klein and Siedler, 1995; Martínez-Marrero et al., 2008). Sin embargo, para poder completar la caracterización estructural y el conocimiento de su dinámica es necesario aumentar los estudios en la mesoescala y submesoescala con observaciones *in situ*. Actualmente, aún es poco lo que se sabe del frente NACW-SACW y de cómo los distintos procesos de mesoescala y submesoescala que interaccionan entre sí influyen sobre su estructura y disposición afectando a las corrientes oceánicas de la región, y por tanto, repercutiendo en la ventilación de sus aguas, en la distribución de nutrientes inorgánicos, etc.

En general, las regiones frontales suelen estar muy estudiadas porque son áreas

dinámicamente muy activas del océano en donde frecuentemente surgen frentes en densidad u otras variables físicas en un amplio abanico de escalas en los que se dan importantes flujos frontales (Bower and Rossby, 1989; Pastor et al., 2008), procesos de mezcla significativos (Klein and Siedler, 1995; Martínez-Marrero et al., 2008) y movimientos verticales ascendentes y descendentes que facilitan la disponibilidad de nutrientes favoreciendo una alta productividad biológica (Lévy, 2003; Nagai, Tandon, and Rudnick, 2006; McGillicuddy Jr, 2016; Ruiz et al., 2019).

Sin embargo, la CVFZ, por la naturaleza del frente que se genera entre NACW y SACW, que se encuentra cerca de estar completamente compensado en densidad, es decir, los cambios de salinidad compensan los cambios de temperatura en el campo de densidad, no es una zona dinámicamente muy estudiada, al menos, en resolución mesoescalar (y submesoescalar). Asimismo, el estudio y el análisis de estas escalas no es tarea fácil cuando existen abundantes procesos de diferentes escalas que interaccionan entre sí y el esfuerzo observacional que se requiere es tan alto (Pallàs-Sanz, Johnston, and Rudnick, 2010b).

Concretamente en este trabajo, a partir de las mediciones in situ realizadas durante las dos campañas del proyecto COCA (Coastal-Ocean Carbon Exchange in the Canary Region, REN2000-U471-CO2-02-MAR) y las dos campañas del proyecto FLUXES (Carbon Fluxes in a Coastal Upwelling System – Cape Blanc, NW Africa, CTM2015-69392-C3-3-R), se ha querido contribuir al conocimiento de la compleja CVFZ repleta de importante estructura mesoescalar, que se enclava en la convergencia de los giros subtropical y tropical del Atlántico Norte y dentro de la productiva área de afloramiento del noroeste de África.

6.2 Objetivos y estructura

El **objetivo general** de este trabajo de investigación es profundizar en la caracterización de la CVFZ para llegar a alcanzar un mejor entendimiento de los componentes físicos que gobiernan su dinámica, desde la gran escala, en la que se describen los patrones de circulación al norte y al sur de Cabo Blanco influenciados por la mesoescala no resuelta, hasta las escalas en las que se detallan las principales estructuras termohalinas de mesoescala y submesoescala y la dinámica frontal asociada en la que se incluye la circulación ageostrófica secundaria (con sus respectivas componentes horizontal y vertical).

Además, gracias a la excelente base de datos desarrollada con estos dos proyectos (completada con datos de altimetría y salidas de los modelos de reanálisis físico y bioquímico), se va más allá y se pretende describir el comportamiento y la distribución de las distintas masas de agua existentes, así como de otras variables bioquímicas asociadas, como, por ejemplo, los nutrientes inorgánicos. Asimismo, se intentan abordar las incertidumbres en los balances de flujos bioquímicos a gran escala. No obstante, es necesario conocer más profundamente los procesos de mesoescala y menores escalas que influyen en estas estimaciones para poder completarlas y minimizar los errores en sus estimaciones.

Con el fin de tratar de analizar de forma ordenada y organizada lo descrito anteriormente, esta tesis se estructura en tres partes diferenciadas: en la primera parte, se incluye un capítulo introductorio general (**capítulo 1**) con el marco teórico, el

estado del arte, la localización de las estaciones y descripción de las campañas empleadas para recopilar datos y con los objetivos; en la segunda parte, se incluyen tres capítulos centrales (**capítulos 2, 3 y 4**) con tres trabajos independientes en formato de artículo de investigación (dos se encuentran publicados y el tercero está en preparación); y en la tercera parte, se incluyen dos capítulos, uno con las conclusiones y trabajo futuro (**capítulo 5**) y otro, en el que se desarrolla el resumen de la tesis en español (**capítulo 6**).

Concretamente en los capítulos centrales de la segunda parte se abordan independientemente los siguientes **objetivos específicos**:

1. Análisis de los cambios espaciales de la CVFZ detectados en las diferentes estaciones del año, definidos inicialmente por la ubicación del frente NACW-SACW en la cual la isohalina de 36 corta la isóbata de 150 m. Estudio de la influencia de los cambios en los patrones de circulación y en los transportes horizontales de los nutrientes inorgánicos y el Carbono Orgánico Disuelto (DOC) al norte de la CVFZ a escala de cuenca. → en el **capítulo 2**

2. Extensión de la definición del frente NACW-SACW a toda la columna de agua en donde ambas masas de agua centrales coexisten en la CVFZ. Análisis de la influencia del frente (con su nueva definición) sobre las corrientes y sobre la distribución de las masas de agua y su bioquímica (nutrientes inorgánicos y oxígeno disuelto, O_2), al norte y al sur de la CVFZ. → en el **capítulo 3**

3. Descripción de la estructura del frente NACW-SACW y de otras estructuras termohalinas de la CVFZ en resolución mesoescalar y submesoscalar. Análisis de los posibles procesos dinámicos asociados y su relación o vinculación con la circulación horizontal y vertical. → en el **capítulo 4**

Estos objetivos permiten alcanzar unas conclusiones generales aumentando significativamente el conocimiento en torno a la CVFZ.

En el **capítulo 2**, se examinan los patrones de circulación y el impacto de la exportación lateral de nutrientes y materia orgánica al sur de las islas Canarias en frente del noroeste de África, aplicando un modelo inverso a dos conjuntos de datos hidrográficos recopilados en el otoño de 2002 y la primavera de 2003. Estas estimaciones muestran cambios significativos en los patrones de circulación en los niveles centrales desde el otoño a la primavera, particularmente en el límite sur del dominio relacionado con los cambios zonales de la CVFZ. Los transportes hacia el sur en los niveles de superficie y centrales en 26°N son de 5.6±1.9 Sv en otoño y aumentan a 6.7±1.6 Sv en primavera; los transportes hacia el oeste en 26°W son de 6.0±1.8 Sv en otoño y se debilitan a 4.0±1.8 Sv en primavera. En 21°N se observa un cambio importante entre ambas estaciones, con un transporte de masa hacia el norte de 4.4±1.5 Sv en otoño y un transporte hacia el sur de 5.2±1.6 Sv en primavera. En niveles intermedios también se observan diferencias espacio-temporales, destacándose que en otoño se obtiene un transporte neto de masa hacia el norte de 2.0±1.9 Sv en los transectos sur y norte. Por otro lado, esta variabilidad detectada en los patrones de circulación se refleja en los transportes laterales de nutrientes inorgánicos (SiO_2, NO_3, PO_4) y de DOC. De esta ma-

nera, en otoño el área actúa como sumidero de nutrientes inorgánicos y fuente de DOC, mientras que en primavera la situación se invierte, ejerciendo como fuente de nutrientes y sumidero de DOC. En este mismo estudio, se realiza una comparativa entre los flujos de nutrientes obtenidos a partir de las observaciones in situ y los estimados con las salidas de nutrientes del modelo numérico biogeoquímico GLORYS-BIO.

En el **capítulo 3**, se examinan de nuevo los patrones de circulación en un dominio ubicado más al sur, sobre la confluencia de los giros subtropical y tropical del Atlántico Norte durante una campaña realizada en el verano de 2017 en la que se recolectan datos hidrográficos, de oxígeno disuelto (O_2) y de nutrientes inorgánicos hasta 2000 m, a lo largo del perímetro de una caja que encierra la CVFZ y el frente NACW-SACW. Independientemente, se analizan las distribuciones de masas de agua, O_2 y nutrientes inorgánicos y sus respectivos transportes, estimados con un modelo inverso, en los dominios definidos como subtropical y tropical, al norte y al sur del frente. Esto es posible gracias a la metodología propuesta para extender el frente NACW-SACW hasta el límite inferior de aguas centrales. En general, en los niveles de superficie y centrales, se observa un transporte neto hacia el oeste de 3.76 Sv. El transporte neto en niveles intermedios en cambio, es de 3 Sv hacia el norte. Dentro del dominio, se estiman desequilibrios de O_2 y de nutrientes inorgánicos consistentes con un consumo de O_2 y una producción de nutrientes posiblemente debidas a una remineralización de la materia orgánica. A través de los patrones de circulación estimados se deduce que parte de estos nutrientes inorgánicos son transportados al océano interior.

En el **capítulo 4**, se analiza el conjunto de datos in situ de alta resolución recopilados en noviembre del 2017. Estos valiosos datos permiten estudiar la variabilidad espacio-temporal de la CVFZ con dos resoluciones espaciales diferentes y durante tres tramos de muestreo sucesivos en un periodo de tiempo total inferior a un mes. Por primera vez, los campos horizontales de geostrofía y ageostrofía y la velocidad vertical se exhiben junto con la dinámica descrita por el sADCP para revelar los procesos involucrados en el desarrollo de las estructuras termohalinas tridimensionales de mesoescala y submesoescala muestreadas por el Seasoar desde la superficie del mar hasta los 400 m de profundidad en la CVFZ. El frente entre el Agua Central del Atlántico Norte (NACW) y el Agua Central del Atlántico Sur (SACW) detectado en todos los tramos permite deducir que la variabilidad por debajo de los 100 m de profundidad es menor que la situada por encima de los 100 m donde se muestrea abundante estructura termohalina de submesoescala y se estiman las mayores velocidades horizontales y verticales. Sin embargo, el remolino anticiclónico de mesoescala ubicado en el noreste muestreado por el sADCP, con intensidades mayores en el primer tramo y menores en los dos últimos, influye sobre los movimientos advectivos horizontales de las masas de agua y de las estructuras termohalinas asociadas a ellas en toda la columna de agua. Los desplazamientos del frente NACW-SACW se observan especialmente en los lugares donde el frente es muy intenso en salinidad, temperatura y densidad desde los 70 m hasta 200 m de profundidad y simultáneamente las velocidades horizontales geostróficas y ageostróficas tienen direcciones opuestas. Por otro lado, en los dos últimos tramos,

se analiza que las velocidades verticales y las corrientes horizontales geostróficas y ageostróficas aumentan cuando la resolución de muestreo es mayor. Concretamente, en el segundo tramo, donde la malla es de mayor resolución, se mide una importante convergencia de flujo con el sADCP sobre la ubicación del frente NACW-SACW que coincide con la de un dipolo formado por intensos movimientos ascendentes y descendentes asociados a la advección ageostrófica. En general, la mejor aproximación de la velocidad vertical es menor a la esperada en esta zona altamente dinámica y compleja. Este hecho puede deberse por un lado, a que la deformación cinemática total prácticamente se anula por la resta entre las velocidades verticales debidas a las deformaciones geostróficas y geostróficas que tienen valores muy similares y de signo contrario, y, por otro, porque los términos debidos a la mezcla vertical por momento y flotabilidad son especialmente pequeños.

6.3 Conclusiones y trabajo futuro

A nivel de cuenca, las corrientes más intensas, que son las registradas en los niveles de superficie y de aguas centrales, se ven afectadas por las estructuras de mesoescala relacionadas con el Corredor Canario de Remolinos y la CVFZ. Al norte de la zona frontal, en la vertiente subtropical, el patrón de circulación observado en otoño, primavera y verano es consistente con un transporte hacia el suroeste descrito por la Corriente de Canarias y la Corriente de Afloramiento de Canarias, afectadas por remolinos aislados al sur de Canarias, y por la Corriente Ecuatorial del Norte, más condicionada por la ubicación de la zona frontal en sí y la mesoescala y submesoescala asociadas a la misma. Al sur de la zona frontal, no se registra una marcada mesoescala en el dominio tropical; sin embargo, la ubicación vertical y el ángulo del frente termohalino entre NACW y SACW con respecto a la costa de Mauritania y la variabilidad en la posición de la Zona de Convergencia Intertropical, que se desplaza hacia el norte en verano, influyen en el patrón de circulación descrito por la Corriente de Mauritania y la Subcorriente hacia el Polo (Poleward UnderCurrent, PUC).

Sin tener en cuenta las estaciones del año en las que se llevan a cabo las campañas de muestreo, prácticamente todo el dominio de COCA queda al norte de la zona frontal afectando únicamente a la circulación en su área más meridional. De hecho, el cambio más notable en el transporte neto de masa en este dominio ocurre en las capas de superficie y aguas centrales del transecto sur en el cual el transporte de masa es de aproximadamente 4 Sv hacia el norte en otoño, mientras que en primavera se invierte hacia el sur con un valor aproximado de 5 Sv.

El patrón de circulación dentro del dominio de FLUXES-I está completamente influenciado por la CVFZ, debido a que los transectos muestreados bordean la zona frontal, encerrando el frente NACW-SACW dentro. Esta puede ser una de las razones por la que los transportes de masa acumulados estimados a través de estos transectos sean significativamente menores que en las dos campañas de COCA ubicadas al norte. Concretamente en el dominio de FLUXES-I, los transportes de masa acumulados se ven reducidos o anulados por la abundancia de estruc-

tura mesoscalar asociada al frente que influyen sobre sus estimaciones. Asimismo, la resolución espacial de muestreo en las campañas de COCA es menor que en FLUXES-I, por lo que probablemente los transportes de masa puedan estar más sobrestimados por la mesoscala que en FLUXES-I. Teniendo en cuenta los argumentos anteriores, se puede decir que en 26°W, lejos de la costa, existe un mayor transporte hacia mar adentro al norte de Cabo Blanco que en latitudes más bajas, en niveles de superficie y de aguas centrales.

Al sur de Cabo Blanco, se desconoce completamente cómo afecta el afloramiento estacional debido a que la campaña FLUXES-I se realiza en verano sin fuertes vientos. No obstante, gracias a algunas estaciones realizadas próximas a la costa, cercanas a la Zona del Mínimo de Oxígeno, se describe un área bastante compleja, muy variable y con una circulación neta perpendicular y en dirección a la costa que presenta sentidos opuestos en niveles de superficie y aguas centrales, y, en niveles de aguas intermedias.

Las masas de agua centrales muestran una distribución latitudinal bastante consistente, bien diferenciada por el frente termohalino que separa la SACW al sureste y la NACW al noroeste del mismo. El predominio de una u otra es mayor cuanto más alejado se está del frente. Por el contrario, la distribución se vuelve más compleja en la medida que el frente está más cercano, debido a la abundancia de procesos de diferentes escalas que ocurren en la zona y que, a su vez, influyen directamente en la mezcla de las masas de agua.

Una de las contribuciones más importantes de esta tesis es la metodología propuesta por la cual se extiende verticalmente el frente termohalino entre NACW y SACW más allá de 150 m, dentro del rango de la columna de agua en el que coexisten ambas masas de agua. Para desarrollarla, se ha considerado la definición del frente dada por Zenk, Klein, and Schroder (1991) y las definiciones de NACW y SACW propuestas por Tomczak (1981).

Los campos de salinidad media del modelo GLORYS permiten dar una visión "sinóptica" de la orientación y forma que adopta el frente termohalino NACW-SACW dentro de los dos grandes dominios delimitados por los transectos muestreados durante el otoño de 2002, primavera de 2003 y verano de 2017. En todas las campañas oceanográficas, la ubicación del frente muestreado coincide con la ubicación del frente descrita por el modelo GLORYS. En las dos campañas de COCA, realizadas en otoño y primavera, el frente se limita a 150 m mientras que éste se extiende a 650-700 m en el verano de FLUXES-I. En este último caso, las ubicaciones del frente a diferentes profundidades deducidas de las distribuciones de las dos masas de agua centrales dadas por el Método Óptimo Multiparamétrico coinciden estrechamente con las descritas por las salinidades, estimadas con la metodología propuesta y extraídas de GLORYS. Es más, las salinidades que definen el frente termohalino obtenidas del modelo, permiten mostrar su compleja distribución espacial con diferentes orientaciones en función de la profundidad y con abundante estructura mesoescalar asociada (intrusiones, meandros y remolinos).

Las concentraciones y distribuciones del O_2 y de los nutrientes inorgánicos disueltos muestreados coinciden con las ubicaciones y distribuciones de NACW y SACW en la campaña de verano de FLUXES-I. Debido al reducido número de datos in situ recopilados en ambas campañas de COCA, para analizar las distribuciones y estimar los transportes de nutrientes inorgánicos se emplean las concentraciones extraídas del modelo GLORYS-BIO que proporciona valores inferiores a los datos in situ del verano del 2017, posiblemente debido a que las condiciones iniciales utilizadas en el modelo son extraídas de datos climatológicos de WOA13. A pesar de esto, las distribuciones de nutrientes descritas por GLORYS-BIO con concentraciones más bajas en el noroeste y concentraciones más altas en el sureste del dominio, también coinciden con las distribuciones de NACW y SACW. Por otro lado, el *DOC* muestreado en la columna de agua tiene mayores concentraciones y más ampliamente distribuidas en otoño que en primavera. Concretamente, el SACW detectado y ubicado en el transecto sur de ambas campañas COCA presenta concentraciones de *DOC* inferiores a las concentraciones muestreadas dentro del NACW.

Al igual que ocurre con los transportes de masa en los niveles de agua centrales, los transportes de nutrientes inorgánicos, O_2 y *DOC* también están condicionados por la CVFZ y por el frente termohalino NACW-SACW. Con respecto a los transportes laterales hacia mar abierto, los transportes de nutrientes inorgánicos y *DOC* en dirección oeste son menores en otoño que en primavera en los niveles de superficie y aguas centrales dentro del dominio de COCA. En verano, gracias a la extensión vertical del frente entre NACW y SACW, el análisis de los transportes bioquímicos en estos niveles, se realiza en ambos lados del frente independientemente. La principal diferencia entre la zona subtropical, al norte y la zona tropical, al sur, está relacionada con el transporte de O_2 que es menor en el lado más meridional por la cercanía de la Zona del Mínimo de Oxígeno.

Por debajo de las aguas centrales, el transporte neto en las capas de aguas intermedias es intenso y hacia el norte en otoño, mientras que se debilita y se invierte hacia el sur en primavera. Esto coincide con el hecho de que haya una mayor contribución de Agua Mediterránea en primavera y una contribución ligeramente mayor de Agua Antártica Intermedia en otoño. En verano, al igual que en otoño, el patrón de circulación predominante es en dirección sur-norte con un predominio de Agua Antártica Intermedia. Por otro lado, el transporte neto de masa hacia el oeste en los niveles intermedios es menos intenso en otoño que en primavera en 26°W. Sin embargo, en esta misma longitud en verano, se estima un transporte neto en dirección contraria, hacia la costa. Además, en el transecto más cercano a la costa también muestreado en verano, se estima un transporte neto contrario al anterior, hacia el oeste en estos mismos niveles. De esto se deduce que las estructuras mesoscalares constituyen una fuente principal de variabilidad en la circulación en los niveles intermedios dentro del dominio de FLUXES, al menos durante el verano.

En general, teniendo en cuenta muchos de los condicionantes, se podría decir

que el dominio situado ligeramente al norte de la CVFZ funciona como sumidero de nutrientes inorgánicos en el otoño de 2002 y como fuente de nutrientes inorgánicos en la primavera de 2003. Asimismo, se observa que este dominio actúa como fuente de DOC en otoño y de sumidero de DOC en primavera. Con respecto al dominio muestreado más al sur que encierra en sí mismo la CVFZ, actúa como una caja heterótrofa mostrando un consumo neto de oxígeno y una remineralización de NO_3, PO_4 y SiO_4H_4 por debajo de la capa fótica en el verano del 2017.

Por último, el alto esfuerzo observacional in situ realizado durante los 18 días de la campaña de FLUXES-II en noviembre del 2017, permite mostrar cuán dinámicamente activa y compleja es la CVFZ a través de la abundancia de estructura de mesoescala y submesoescala.

Según el comportamiento de las estructuras muestreadas en las resoluciones mesoescalar y submesoscalar, la columna de agua se separa en cuatro dominios: las aguas de la capa de mezcla hasta 40 m de profundidad; la zona de termoclina estacional entre 40 y 100 m; las aguas centrales superiores desde 100 hasta 300 m; y las aguas centrales más profundas de 300 m hacia abajo.

La estructura del frente termohalino NACW-SACW detectado en la columna de agua desde 100 m hacia abajo, permite analizar los cambios del mismo en función de las abundancias y localizaciones de las masas de agua centrales en periodos cortos de tiempo. De este análisis se confirma que la variabilidad por debajo de los 100 m es menor a la de la columna de agua ubicada por encima de los 100 m en dónde existe abundante estructura termohalina de submesoescala (como excepción se muestrea una gran estructura con forma filamentosa de poca salinidad centrada a 40 m) y en dónde se estiman las mayores velocidades horizontales y verticales. Sin embargo, en algunas localizaciones en las que el frente es especialmente intenso en salinidad, temperatura y densidad, y se expande verticalmente desde los 100 hasta los 200 m de profundidad, el agua sobre el lado del frente dónde se ubica el SACW más puro tiene características físicas similares a ésta última con salinidades y temperaturas muy bajas por encima de 100 m. Este hecho, hace que el frente alcance los 70 m de profundidad diferenciando este agua muy poco salina y fría de un agua mucho más salina y cálida. Además, simultaneamente en estas mismas localizaciones donde el frente es intenso, las velocidades horizontales geostróficas y ageostróficas son significativamente altas y tienen direcciones opuestas. En el segundo tramo en el que se aumenta la resolución de muestreo esto último se observa especialmente claro ya que las corrientes horizontales geostróficas y ageostróficas son mayores a las del primer tramo.

En general, tanto las velocidades horizontales como las verticales aumentan cuando la resolución de muestreo aumenta, especialmente en las localizaciones dónde se ubica el frente más intenso que además coincide en ubicación con una importante convergencia de flujo medida por el sADCP y con un dipolo formado por dos celdas de velocidades ascendentes y descendentes intensas que alcanzan valores absolutos máximos de $2{\times}10^{-4}$ m s^{-1} a 40 m de profundidad debidas a la advección ageostrófica.

A partir de 300 m de profundidad, a pesar de que el frente NACW-SACW siga facilitando la diferenciación entre el NACW y el SACW, sus caracteristicas físicas ya no están tan bien diferenciadas como a profundidades más someras, por lo que la variabilidad se reduce significativamente. Además, en esta zona coincide que las velocidades verticales y horizontales son menores a las medidas y estimadas entre 100 y 300 m y mucho menores que las de la termoclina estacional.

Por otro lado, las estructuras dinámicas medidas por el sADCP, principalmente las de mesoescala (que coinciden en gran medida con la geostrofía y por tanto, con lo detectado por altimetría en la superficie), se mantienen coherentes en toda la columna de agua. Durante los pequeños intervalos de tiempo entre una y otra fase, estas estructuras cambian de forma y se desplazan ligeramente influyendo sobre la advección horizontal de las estructuras termohalinas, en mayor medida, con mayores intensidades en las ubicadas por encima de los 100 m y en menor medida, con menores intensidades en el NACW y el SACW y el frente NACW-SACW por debajo de los 100 m.

Cabe destacar que la estimación de la velocidad vertical total en la CVFZ es menor de la esperada. Entre todos los términos que forman la velocidad vertical total, la w debida a la deformación ageostrófica que describe abundantes y pequeñas células alternantes de afloramiento y hundimiento en prácticamente todos los dominios es la que posee los valores más altos. Sin embargo, debido a que la deformación geostrófica también define celdas alternantes contrarias a las anteriores, con velocidades ascendentes y descendentes en las mismas localizaciones y con casi las mismas intensidades pero en sentido contrario, la deformación total queda prácticamente anulada. Este hecho puede ser una de las causas de que la velocidad vertical total sea relativamente pequeña en prácticamente toda la zona. Sin embargo, en aquellas localizaciones en las que la deformación total no se anula por completo, a ésta se le suma la advección ageostrófica resultando un valor significativamente alto de la velocidad vertical total. Un ejemplo de ello es observable sobre el frente NACW-SACW, concretamente en el área de convergencia de flujo detectada por el sADCP en donde también se describe el dipolo de movimientos ascendentes y descendentes (anteriormente descrito).

Sin duda otro de los motivos de que la estimación de la velocidad vertical total sea pequeña en el CVFZ, puede deberse a los bajos valores de w asociados a la mezcla vertical por momento y flotabilidad que poseen al menos un orden menor a las velocidades verticales debidas a ambas deformaciones y a la advección ageostrófica.

En resumen, en esta tesis se han descrito y analizado principalmente procesos y estructuras físicas desde la escala de cuenca hasta la submesoescala que suceden, se originan y evolucionan en la CVFZ. No obstante, nos han quedado muchas preguntas por resolver. Se han estudiado los patrones de circulación condicionados por la localización del frente en las estaciones de primavera, otoño y verano, pero no en invierno. Para completar el estudio de los patrones de circulación con los modelos inversos habría que incluir la parte diapicna e intentar incluir las velocidades del

ADCP como velocidades de referencia, que en estos trabajos se han omitido o no se han tenido en cuenta. Asimismo, debido a la escasez de datos climatológicos en la zona y por la poca coherencia existente entre los transportes estimados a partir de los datos in situ y a partir de las salidas hidrológicas del modelo GLORYS (particularmente para el verano del 2017), no se ha podido analizar profundamente la variabilidad del frente ni la influencia de éste sobre las principales corrientes de la zona (como por ejemplo la PUC) ni sobre los transportes de masa medios anuales y estacionales, al norte y al sur del frente. Debido a esto último, no se han podido alcanzar grandes conclusiones sobre la variabilidad anual y estacional de los transportes y las distribuciones de las distintas variables bioquímicas a nivel de cuenca.

Tampoco se ha analizado profundamente qué peso tiene la mesoescala en los transportes medios, es decir, que porcentaje de estos transportes se debe a la mesoescala, independiente o dependiente del frente termohalino. Concretamente, nos han surgido muchas dudas relacionadas con el intercambio de propiedades a través del frente y de cómo afecta la mesoescala y submesoescala al transporte medio que se dirige costa fuera.

En futuros trabajos, se abordará el estudio de procesos de menor escala como son los procesos de mezcla y turbulencia, que son especialmente claves en el intercambio de propiedades a través del frente NACW-SACW, con el fin de lograr una visión más detallada y un entendimiento más completo del CVFZ. Concretamente, las estimaciones de velocidad vertical por mezcla vertical debido a momento y flotabilidad que se muestran en el capítulo 4 tienen asociado un error mayor, debido a las suposiciones y la parametrización utilizadas para calcular los coeficientes de mezcla, que el que tienen otros términos asociados. En el futuro, para estimar velocidades verticales por mezcla vertical más realistas y con menor error, será conveniente emplear coeficientes de mezcla in situ estimados a partir de los datos de microestructura recopilados por el perfilador de turbulencia en la misma campaña. Asimismo, será conveniente incluir la velocidad vertical generada por mezcla horizontal debida a momento como nuevo término de la ecuación Omega Diabática, con el fin de lograr un valor más adecuado de la velocidad vertical total.

Por otro lado, la cantidad y calidad de los datos de FLUXES-II que han permitido describir las estructuras de mesoescala y submesoescala asociadas al frente termohalino, también permitirán comprender a través de análisis futuros más profundos, algunos de los procesos dinámicos implicados que originan estas complejas estructuras alrededor del frente. Para esto, será importante minimizar y analizar todos los errores cometidos en el trabajo descrito en el capítulo 4. Se deberá comenzar utilizando la interpolación DIVA 3-D en lugar de realizar dos veces las interpolaciones 2-D de variables hidrológicas y dinámicas. Asimismo, es necesario realizar un análisis más robusto de los propios procesos y de los errores en las estimaciones de velocidad vertical. Adicionalmente, se deben analizar e incluir otras posibles fuentes de velocidad vertical (por ejemplo, el viento). También conviene completar toda la información obtenida con estimaciones de posibles flujos a partir del estudio de las derivadas locales y materiales de cada variable física. Dado que

la naturaleza de los procesos de mesoescala, submesoescala y escalas menores en sí mismos que acontecen en la CVFZ y la interacción del frente NACW-SACW con estos procesos colindantes aún se encuentran en las fronteras de nuestra comprensión científica, el reto se centrará en tratar de entender cómo las diferentes estructuras asociadas a procesos de diferentes escalas interactúan entre sí (por ejemplo, la interacción entre el gran filamento del Cabo Blanco y el frente termohalino).

Debido a la naturaleza interdisciplinaria de los datos presentados, tan pronto como todos los procesos físicos predominantes en la CVFZ se alcancen a comprender, se podrá comenzar a analizar cómo estos procesos de mesoescala, submesoescala y escalas más pequeñas condicionan las distribuciones de los parámetros bioquímicos en dichas escalas. De esta forma, estos resultados podrán relacionarse con los transportes y distribuciones observados a nivel de cuenca y quizás sea posible comprender la función del frente termohalino y los principales mecanismos de intercambio de propiedades a través del mismo.

Finalmente, cabe subrayar que es necesario seguir realizando esfuerzos observacionales como los que se llevan a cabo en estos dos proyectos interdisciplinares para comprender los procesos físicos y bioquímicos y sus interacciones en todos los niveles, especialmente en los niveles de mesoescala, submesoescala y menores escalas, que acontecen en sistemas frontales como la CVFZ. De esta forma, la complejidad de los procesos frontales y sus interacciones podrán ser adecuadamente reproducidos por modelos físicos y se podrá realmente comenzar a estudiar su influencia e importancia sobre los procesos bioquímicos.

Acknowledgements (Agradecimientos)

Ángel y Francis, en primer lugar me gustaría daros las gracias por la oportunidad que me habéis dado de formarme junto a vosotros; me siento muy afortunada de haber tenido unos guías tan sumamente humanos y que, día tras día, no hayáis perdido la paciencia conmigo. Gracias por saber llevar mis nervios, por tranquilizarme y por hacer el esfuerzo de buscar las palabras más adecuadas en cada momento. Además de transmitirme vuestros conocimientos, hemos podido hablar y discutir sobre un amplio abanico de temas y curiosidades que, relacionados o no relacionados con la ciencia, también me han enriquecido.

Ángel, valoro muchísimo el gran esfuerzo que realizas compaginando familia con todo tipo de gestiones, clases, tutorización y dirección de trabajos a estudiantes... Gracias por intentar sacar siempre tiempo (donde no había) para reunirnos y ayudarme con todo tipo de consultas.

Francis, muchísimas gracias por ser como eres y sobre todo por motivarme e incentivarme siempre en aprender cosas nuevas. Gracias por tu dedicación y por tu persistente supervisión de conceptos, código, inglés... Gracias por prestarme el modelo inverso, por hacer lo complicado sencillo y por estar siempre al pie de cañon con todas las revisiones de papers y no papers ¡eres grande!

Enric, no tengo palabras para agradecerte todo lo que ha supuesto que me acogieses en CICESE, ha estat tot un honor. Muchísimas gracias por ser tan generoso y por facilitarme la vida en México compartiendo mucho de tu tiempo, dentro y fuera del cubo. Ha sido un verdadero placer conocer esa mente tan motivada (que tienes) y de que me hayas introducido en el mundo de los procesos mesoscalares y submesoscalares. Gracias por enseñarme nociones y facilitarme código sobre cómo interpolar de forma óptima, aplicar el método iterativo de Rudnick para geostrofía, estimar velocidades verticales con la Ecuación Ω...

A todas y cada una de las personas que han formado parte de FLUXES, gracias por hacerlo posible. Me gustaría agradecer a los que se embarcaron (tripulación del Sarmiento, estudiantes, científicos, UTM, otros técnicos), a los se quedaron en Tierra durante y a todos los que siguen trabajando en resultados y publicaciones para que poco a poco vayan saliendo adelante. En especial, me gustaría agradecer a dos personas que he tenido el gran placer de conocer en alta mar: Bieito, no sé sinceramente como sería una campaña sin ti...jaja, siempre pendiente de todo y de todos, gracias por acordarte de mí, ayudarme y mandarme ánimos! y Luís, gracias por el esfuerzo de venir desde Chile, tu predisposición, actitud y compañerismo primordiales en la segunda campaña.

Por otro lado, me gustaría dar las gracias al team OFYGA, en especial a Ángeles y Borja, por estar siempre pendientes y cuidar de todos nosotros. También he de agradecer el apoyo recibido por parte del Departamento de Física, en especial, de Antonio M., Diana G. y Carmen G., con los que he podido compartir tiempo en el mar, en la facultad y fuera de ella. Gracias a todos por vuestros consejos, ánimos y humor.

Simón y Ananda, muchísimas gracias por contar conmigo y darme la oportunidad de retomar la oceanografía física. Aunque fuese breve el tiempo que permanecí en IMEDEA, estuve muy a gusto y creo que realmente me sirvió como calentamiento y de empujón para comenzar la tesis. Gràcis!

Estoy muy agradecida con todas las personas que forman, o han formado, la gran familia del CICESE. Muchísimas gracias por la enorme hospitalidad recibida en ambas estancias, por el cariño y por hacerme sentir como en casa, les extraño! Gracias por hacer que mi tiempo en Ensenada estuviese lleno de experiencias intensas en las que además de trabajar hemos podido cotorrear entre chelas, pláticar durante los asados, jugar al ping-pong, surfear,... Sheila, gracias por tus sinceras y tan sabias palabras. Javi, gracias por darme tranquilidad, optimismo y apoyo en todo momento. Lucía (Lucy in the sky with diamonds...), gracias por hacer tan fácil esta amistad, gracias por esos chidos momentos compartidos a remojo, entre infusiones de ginger, paseando al Porto,...

Agradecer a la resistencia de chicas CCM en la isla (Melissa y Lourdes), que encuentren siempre un hueco para quedar, hablar de recuerdos de los tiempos en la uni, ponernos melancólicas y/o reírnos con temas salados mientras desconectamos de nuestros agobios. No me olvido tampoco de ti Tebita, que siempre que vuelves a casa haces por vernos y ponernos al día.

Jacobi y Blin, gracias por acogerme en Salinetas con una mano delante y otra detrás cuando llegue de Mallorca. Gracias por ayudarme en la primera fase de doctorado complicada para mí. Gracias por esa época en la que ibamos todos juntos al agua o a cualquier lugar como si volviésemos en el tiempo atrás y estuviésemos de nuevo en Santander. Muchísimas gracias por ser mi ohana norteña en Canarias y sí, os debo una comida!

Ernes, gracias por estar presente en momentos como la oral del Ocean Science en San Diego y por encima de todos, en Asturias cuando pasó lo de Ama. Agradezco que no hayas perdido tu curioso humor en USA o en tu vuelta a Donosti de dónde siempre recibo ánimos acompañados de chistes o memes aptos sólo para nosotros.

Sarita, muchísimas gracias por apoyarme incondicionalmente estuvieses en Sope, Lancaster, Boston y/o Barcelona. Gracias por escucharme y entenderme. Gracias por nuestras largas y motivadas conversaciones llenas de reflexiones. Gracias por mostrarme la vida llena de matices y ser el ejemplo a seguir.

Me gustaría agradecer a Beuca y Juanin, al Núcleo B (Gerez eta Joe), a Corxeto y a mis ñoñostiarras (Ainhoa y Leire), que me hayan arropado en momentos clave y que hayan hecho que la distancia, entre el mar Cantábrico, Península y las aguas canarias, sea chiquitita de alguna manera.

También me gustaría tener unas palabras para los compis del máster de profesorado que han sido super comprensivos y me han echado siempre un cable con los trabajos grupales en los últimos meses.

Tío Richard, creo que no ha habido nadie de la familia que me haya preguntado más por cómo iba con la tesis que tú, que si cuándo la terminaba, defendía... ¡aquí la tienes! Gracias por ser un pilar de los Gregorios también en este periodo.

Antton, muchísimas gracias por querer formar parte del "pitxi-team". Siempre te agradeceré lo mucho que me has acompañado, cuidado, mimado, aguantado y hecho reír a carcajadas incluso en momentos complicados de este camino (para ambos ¿no?). Gracias por creer en mí y tener infinita paciencia, respeto e interés por este trabajo ¡Ya deberías de tener convalidado el grado de Ciencias del Mar!

Gardotza ta Aita, bihotz-bihotzez, eskerrik asko. Son casi cinco años que Ama nos dejó cuando estaba comenzando la tesis... creo que ella estaría pero que muy orgullosa de todos nosotros, ¡de los tres! Muchísimas gracias por estar siempre siempre ahí. Sin vosotros, ¡esto no hubiese sido posible!

Bibliography

Aguiar, Eva et al. (2020). "Multi-platform model assessment in the Western Mediterranean Sea: impact of downscaling on the surface circulation and mesoscale activity". In: *Ocean Dynamics* 70.2, pp. 273–288.

Aken, Hendrik M van, Gereon Budeus, and Michael Hähnel (1995). "The anatomy of the Arctic frontal zone in the Greenland Sea". In: *Journal of Geophysical Research: Oceans* 100.C8, pp. 15999–16014.

Alonso-González, I. J. et al. (2009). "Lateral POC transport and consumption in surface and deep waters of the Canary Current region: A box model study". In: *Global Biogeochemical Cycles* 23.2, pp. 1–12. ISSN: 08866236. DOI: 10.1029/2008GB003185.

Álvarez, Marta and Xosé Antón Álvarez-Salgado (2009). "Chemical tracer transport in the eastern boundary current system of the North Atlantic". In: *Ciencias Marinas* 35.2, pp. 123–139.

Álvarez-Salgado, X. A. and J. Arístegui (2015). *Oceanographic and biological features in the Canary Current Large Marine Ecosystem, Chapter 4.3, Organic matter dynamics in the Canary Current*. Vol. 115. ISBN: IOC Annual Report Series No. 8 UNESCO 2002.

Álvarez-Salgado, X. A. et al. (2007). "Contribution of upwelling filaments to offshore carbon export in the subtropical Northeast Atlantic Ocean". In: *Limnology and Oceanography* 52.3, pp. 1287–1292. ISSN: 00243590. DOI: 10.4319/lo.2007.52.3.1287.

Anderson, Laurence A and Jorge L Sarmiento (1994). "Redfield ratios of remineralization determined by nutrient data analysis". In: *Global biogeochemical cycles* 8.1, pp. 65–80.

Appen, Wilken-Jon von et al. (2020). "High-resolution physical–biogeochemical structure of a filament and an eddy of upwelled water off northwest Africa". In: *Ocean Science* 16.1, pp. 253–270.

Arístegui, J et al. (1994). "Island-induced eddies in the Canary Islands". In: *Deep Sea Research Part I: Oceanographic Research Papers* 41.10, pp. 1509–1525.

Arístegui, Javier et al. (2009). "Sub-regional ecosystem variability in the Canary Current upwelling". In: *Progress in Oceanography* 83.1-4, pp. 33–48.

Auger, Pierre-Amaël et al. (2016). "What drives the spatial variability of primary productivity and matter fluxes in the north-west African upwelling system? A modelling approach". In: *Biogeosciences* 13.23, pp. 6419–6440.

Azam, Farooq (1998). "Microbial control of oceanic carbon flux: the plot thickens". In: *Science* 280.5364, pp. 694–696.

Barceló-Llull, Bàrbara et al. (2017a). "Anatomy of a subtropical intrathermocline eddy". In: *Deep Sea Research Part I: Oceanographic Research Papers* 124, pp. 126–139.

Barceló-Llull, Bàrbara et al. (2017b). "Ageostrophic Secondary Circulation in a Subtropical Intrathermocline Eddy". In: *Journal of Physical Oceanography* 47.5, pp. 1107–1123. ISSN: 0022-3670. DOI: 10.1175/JPO-D-16-0235.1. URL: http://journals.ametsoc.org/doi/10.1175/JPO-D-16-0235.1.

Barceló-Llull, Bàrbara et al. (2021). "Fine-Scale Ocean Currents Derived From in situ Observations in Anticipation of the Upcoming SWOT Altimetric Mission". In: *Frontiers in Marine Science*, p. 1070.

Barth, Alexander et al. (2010). "A web interface for griding arbitrarily distributed in situ data based on Data-Interpolating Variational Analysis (DIVA)". In: *Advances in Geosciences* 28.28, pp. 29–37.

Barth, John A, Timothy J Cowles, and Stephen D Pierce (2001). "Mesoscale physical and bio-optical structure of the Antarctic Polar Front near 170 W during austral spring". In: *Journal of Geophysical Research: Oceans* 106.C7, pp. 13879–13902.

Barton, E. D. et al. (1998). "The transition zone of the Canary Current upwelling region". In: *Progress in Oceanography* 41.4, pp. 455–504. ISSN: 00796611. DOI: 10.1016/S0079-6611(98)00023-8.

Barton, ED (1987). "Meanders, eddies and intrusions in the thermohaline front off Northwest Africa". In: *Oceanologica acta* 10.3, pp. 267–283.

— (1989). *The poleward undercurrent on the eastern boundary of the subtropical North Atlantic*. Springer, pp. 82–95.

Barton, Eric D, Adriana Huyer, and Robert L Smith (1977). "Temporal variation observed in the hydrographic regime near Cabo Corveiro in the northwest African upwelling region, February to April 1974". In: *Deep Sea Research* 24.1, pp. 7–23.

Benazzouz, Aïssa et al. (2014a). "An improved coastal upwelling index from sea surface temperature using satellite-based approach–The case of the Canary Current upwelling system". In: *Continental Shelf Research* 81, pp. 38–54.

Benazzouz, Aïssa et al. (2014b). "On the temporal memory of coastal upwelling off NW Africa". In: *Journal of Geophysical Research C: Oceans* 119.9, pp. 6356–6380. ISSN: 21699291. DOI: 10.1002/2013JC009559.

Bentamy, Abderrahim and Denis Croize Fillon (2012). "Gridded surface wind fields from Metop/ASCAT measurements". In: *International journal of remote sensing* 33.6, pp. 1729–1754.

Bonino, Giulia et al. (2021). "Drivers and impact of the seasonal variability of the organic carbon offshore transport in the Canary upwelling system". In: *Biogeosciences* 18.8, pp. 2429–2448.

Bower, Amy S and T Rossby (1989). "Evidence of cross-frontal exchange processes in the Gulf Stream based on isopycnal RAFOS float data". In: *Journal of Physical Oceanography* 19.9, pp. 1177–1190.

Brandt, Peter et al. (2015). "On the role of circulation and mixing in the ventilation of oxygen minimum zones with a focus on the eastern tropical North Atlantic". In: *Biogeosciences* 12.2, pp. 489–512.

Brasseur, P et al. (1996). "Seasonal temperature and salinity fields in the Mediterranean Sea: Climatological analyses of a historical data set". In: *Deep Sea Research Part I: Oceanographic Research Papers* 43.2, pp. 159–192.

Broecker, WS (1974). "NO, a conservative-mass tracer, Earth Planet". In: *Sci. Letters* 23, pp. 100–107.

Buongiorno Nardelli, Bruno (2020). "A multi-year time series of observation-based 3D horizontal and vertical quasi-geostrophic global ocean currents". In: *Earth System Science Data* 12.3, pp. 1711–1723.

Burgoa, N. et al. (2020). "Mass, nutrients and dissolved organic carbon (DOC) lateral transports off northwest Africa during fall 2002 and spring 2003". In: *Ocean Science* 16.2, pp. 483–511. DOI: 10.5194/os-16-483-2020. URL: https://os.copernicus.org/articles/16/483/2020/.

Burgoa, Nadia et al. (2021). "Cape Verde Frontal Zone in summer 2017: lateral transports of mass, dissolved oxygen and inorganic nutrients". In: *Ocean Science* 17.3, pp. 769–788. DOI: 10.5194/os-17-769-2021.

Candela, Julio (2001). *International Geophysics, Chapter 5.7, Mediterranean water and global circulation*. Vol. 77. Elsevier, pp. 419–429.

Capet, Xavier et al. (2008). "Mesoscale to submesoscale transition in the California Current System. Part II: Frontal processes". In: *Journal of Physical Oceanography* 38.1, pp. 44–64.

Carr, Mary Elena and Edward J. Kearns (2003). "Production regimes in four Eastern Boundary Current systems". In: *Deep-Sea Research Part II: Topical Studies in Oceanography* 50.22-26, pp. 3199–3221. ISSN: 09670645. DOI: 10.1016/j.dsr2.2003.07.015.

Castellanos, Paola et al. (2015). "Response of the surface tropical Atlantic Ocean to wind forcing". In: *Progress in Oceanography* 134, pp. 271–292.

Chelton, Dudley (October 2001). *Report of the high-resolution ocean topography science working group meeting*. Technical Report Reference 2001-4, Citeseer: College of Oceanic and Atmospheric Sciences, Oregon State University, Corvallis, Oregon, p. 224.

Chelton, Dudley B et al. (1998). "Geographical variability of the first baroclinic Rossby radius of deformation". In: *Journal of Physical Oceanography* 28.3, pp. 433–460.

Chu, Peter C and Wang Guihua (2003). "Seasonal variability of thermohaline front in the central South China Sea". In: *Journal of oceanography* 59.1, pp. 65–78.

Colling, Angela (2001). *Ocean circulation, Chapter 3.4, Divergences and convergences*. Vol. 3. Butterworth-Heinemann in association with the Open University. ISBN: 0-7506-5278-0.

Comas-Rodríguez, I et al. (2011). "The Azores Current System from a meridional section at 24.5 W". In: *Journal of Geophysical Research: Oceans* 116.C9.

Copin-Montegut, Claire and Gérard Copin-Montegut (1983). "Stoichiometry of carbon, nitrogen, and phosphorus in marine particulate matter". In: *Deep Sea Research Part A. Oceanographic Research Papers* 30.1, pp. 31–46.

Cushman-Roisin, Benoit and Jean-Marie Beckers (2011). *Introduction to geophysical fluid dynamics: physical and numerical aspects, Chapter 1.4, Scales of motions*. Academic press.

D'asaro, Eric et al. (2011). "Enhanced turbulence and energy dissipation at ocean fronts". In: *Science* 332.6027, pp. 318–322.

de Boyer Montégut, Clément et al. (2004). "Mixed layer depth over the global ocean: An examination of profile data and a profile-based climatology". In: *Journal of Geophysical Research C: Oceans* 109.12, pp. 1–20. ISSN: 01480227. DOI: 10.1029/2004JC002378.

Del Giorgio, Paul A and Carlos M Duarte (2002). "Respiration in the open ocean". In: *Nature* 420.6914, p. 379.

Dewey, Richard K and James N Moum (1990). "Enhancement of fronts by vertical mixing". In: *Journal of Geophysical Research: Oceans* 95.C6, pp. 9433–9445.

Dilmahamod, Ahmad Fehmi et al. (2021). "Generation mechanisms of mesoscale eddies in the Mauritanian Upwelling Region". In: *Journal of Physical Oceanography*.

Ekman, Vagn Walfrid (1923). *Über Horizontalzirkulation bei winderzeugten Meeresströmungen*. R. Friedländer & Sohn.

Emery, W. J. (2008). "Water Types and Water Masses". In: *Encyclopedia of Ocean Sciences: Second Edition*, pp. 291–299. DOI: 10.1016/B978-012374473-9.00108-9.

Emery, W. J. and J. Meincke (1986). "Global water masses: summary and review". In: *Oceanologica Acta* 9.4, pp. 383–391. ISSN: 03991784.

Emery, William J (2001). "Water types and water masses". In: *Encyclopedia of ocean sciences* 6, pp. 3179–3187.

Erasmi, Wolfgang, Gerold Siedler, and Reiner Onken (1998). "Energy conversion in the cape verde frontal zone". In: *Journal of Geophysical Research: Oceans* 103.C10, pp. 21469–21479.

Estrada-Allis, SN et al. (2019). "Vertical Velocity Dynamics and Mixing in an Anticyclone near the Canary Islands". In: *Journal of Physical Oceanography* 49.2, pp. 431–451.

Falkowski, Paul G, Richard T Barber, and Victor Smetacek (1998). "Biogeochemical controls and feedbacks on ocean primary production". In: *Science* 281.5374, pp. 200–206.

Fedorov, Konstantin Nikolaevich (1986). *The physical nature and structure of oceanic fronts*. Springer-Verlag New York Inc., New York, NY.

Fernández-Castro, Bieito, Beatriz Mouriño-Carballido, and Xosé Antón Álvarez-Salgado (2018). "Non-redfieldian mesopelagic nutrient remineralization in the eastern North Atlantic subtropical gyre". In: *Progress in Oceanography* 171, pp. 136–153.

— (2019). "Non-redfieldian mesopelagic nutrient remineralization in the eastern North Atlantic subtropical gyre". In: *Progress in Oceanography* 171, pp. 136–153.

Ferrari, Raffaele and Daniel L Rudnick (2000). "Thermohaline variability in the upper ocean". In: *Journal of Geophysical Research: Oceans* 105.C7, pp. 16857–16883.

Fiekas, Volker et al. (1992). "A view of the Canary Basin thermocline circulation in winter". In: *Journal of Geophysical Research* 97.C8, pp. 12495–12510. ISSN: 01480227. DOI: 10.1029/92JC01095.

Firing, Eric (1995). "Processing ADCP data with the CODAS software system version 3.1". In: *Joint Institute for Marine and Atmospheric Research, University of Hawaii & National Oceanographic Data Center.*

Fraga, Fernando (1974). "Distribution des masses d'eau dans l'upwelling de Mauritanie". In:

Fu, Yao, Johannes Karstensen, and Peter Brandt (2018). "Atlantic Meridional Overturning Circulation at 14.5 N in 1989 and 2013 and 24.5 N in 1992 and 2015: volume, heat, and freshwater transports". In: *Ocean Science* 14.4, pp. 589–616. ISSN: 1812-0792. DOI: 10.5194/os-14-589-2018. URL: https://www.ocean-sci.net/14/589/2018/.

Gabric, Albert J. et al. (1993). "Offshore export of shelf production in the Cape Blanc (Mauritania) giant filament as derived from coastal zone color scanner imagery". In: *Journal of Geophysical Research: Oceans* 98.C3, pp. 4697–4712.

Ganachaud, Alaxandre (2003a). "Error budget of inverse box models: The North Atlantic". In: *Journal of Atmospheric and Oceanic Technology* 20.11, pp. 1641–1655. ISSN: 07390572.

Ganachaud, Alexandre (2003b). "Large-scale mass transports, water mass formation, and diffusivities estimated from World Ocean Circulation Experiment (WOCE) hydrographic data". In: *Journal of Geophysical Research* 108.C7, p. 3213. ISSN: 0148-0227. DOI: 10.1029/2002JC001565. URL: http://doi.wiley.com/10.1029/2002JC001565.

Ganachaud, Alexandre and Carl Wunsch (2002). "Large-scale ocean heat and freshwater transports during the world ocean circulation experiment". In: *Journal of Climate* 16.4, pp. 696–705. ISSN: 08948755.

Ganachaud, Alexandre Similien (1999). "Large Scale Oceanic Circulation and Fluxes of Freshwater, Heat, Nutrients and Oxygen". PhD thesis. Massachusetts Institute of Technology and Woods Hole Oceanographic Institution. DOI: 10.1575/1912/4130.

Garabato, Alberto C Naveira et al. (2001). "Mesoscale subduction at the Antarctic Polar Front driven by baroclinic instability". In: *Journal of Physical Oceanography* 31.8, pp. 2087–2107.

Garcia, H. E. et al. (2014a). "World Ocean Atlas 2013, Volume 3: Dissolved Oxygen, Apparent Oxygen Utilization, and Oxygen Saturation". In: *NOAA Atlas NESDIS* 75, p. 27.

— (2014b). "World Ocean Atlas 2013, Volume 4: Dissolved Inorganic Nutrients (phosphate, nitrate, silicate)". In: *NOAA Atlas NESDIS* 76, p. 25.

García-Muñoz, Mercedes et al. (2004). "Distribution and transport of organic matter along a filament-eddy system in the Canaries - NW Africa coastal transition zone region". In: *Progress in Oceanography* 62.2-4, pp. 115–129. ISSN: 00796611. DOI: 10.1016/j.pocean.2004.07.005.

García-Muñoz, Mercedes et al. (2005). "Exchange of carbon by an upwelling filament off Cape Ghir (NW Africa)". In: *Journal of Marine Systems* 54.1-4 SPEC. ISS. Pp. 83–95. ISSN: 09247963. DOI: 10.1016/j.jmarsys.2004.07.005.

Garric, G and L Parent (2018). *Product user manual for global ocean reanalysis products GLOBAL-REANALYSIS-PHY-001-025.*

Gill, Adrian E (2016). *Atmosphere—ocean dynamics.* Elsevier.

Giordani, Hervé, Guy Caniaux, and Louis Prieur (2005). "A simplified 3D oceanic model assimilating geostrophic currents: Application to the POMME experiment". In: *Journal of physical oceanography* 35.5, pp. 628–644.

Giordani, Hervé and Serge Planton (2000). "Modeling and analysis of ageostrophic circulation over the Azores oceanic front during the SEMAPHORE experiment". In: *Monthly weather review* 128.7, pp. 2270–2287.

Giordani, Hervé, Louis Prieur, and Guy Caniaux (2006). "Advanced insights into sources of vertical velocity in the ocean". In: *Ocean Dynamics* 56.5, pp. 513–524.

Gomis, Damià, Ananda Pascual, and Mike A Pedder (2005). "Errors in dynamical fields inferred from oceanographic cruise data: Part II. The impact of the lack of synopticity". In: *Journal of Marine Systems* 56.3-4, pp. 334–351.

Gomis, Damià and Mike A Pedder (2005). "Errors in dynamical fields inferred from oceanographic cruise data: Part I. The impact of observation errors and the sampling distribution". In: *Journal of Marine Systems* 56.3-4, pp. 317–333.

Gomis, Damià, Simón Ruiz, and Mike A Pedder (2001). "Diagnostic analysis of the 3D ageostrophic circulation from a multivariate spatial interpolation of CTD and ADCP data". In: *Deep Sea Research Part I: Oceanographic Research Papers* 48.1, pp. 269–295.

Gould, WJ (1985). "Physical oceanography of the Azores Front". In: *Progress in Oceanography* 14, pp. 167–190.

Grasshoff, K., M. Ehrhardt, and K. Kremling (1999). "Determination of nutrients". In: *Methods of Seawater Analysis*, 159–228.

Hagen, Eberhard (1985). "A meandering intermediate front North-West off Cape Verde islands". In: *Oceanogr. Trop* 20, pp. 71–83.

— (2001). "Northwest African upwelling scenario". In: *Oceanologica Acta* 24.December 1999, pp. 113–128. ISSN: 03991784. DOI: 10.1016/S0399-1784(00)01110-5.

Halkin, D, H. T. Rossby, and T Rossby (1985). "Structure and Transport of the Gulf Stream at 73 N". In: *Journal of Physical Oceanography* 15, pp. 1439–1452.

Hansell, Dennis A (2002). "DOC in the global ocean carbon cycle". In: *Biogeochemistry of marine dissolved organic matter*.

— (2013). "Recalcitrant dissolved organic carbon fractions". In: *Annual review of marine science* 5, pp. 421–445.

Hansell, Dennis A et al. (2009). "Dissolved organic matter in the ocean: A controversy stimulates new insights". In: *Oceanography* 22.4, pp. 202–211.

Hansen, H P. and F. Koroleff (1999). *Determination of nutrients, Chapter 10, Methods of Seawater Analysis*. Wiley-VCH Verlag GmbH, pp. 159–228. ISBN: 9783527295890. DOI: 10.1002/9783527613984.

Haynes, R., E. D. Barton, and I. Pilling (1993). "Development, persistence, and variability of upwelling filaments off the Atlantic coast of the Iberian Peninsula". In: *Journal of Geophysical Research* 98.C12, p. 22681. ISSN: 0148-0227. DOI: 10.1029/93JC02016. URL: http://doi.wiley.com/10.1029/93JC02016.

Hempel, G. (1982). "The Canary Current:Studies of an Upwelling System, A Symposium held in Las Palmas, 11-14 April 1978". In: *Secretariat of the International Council for the Exploration of the Sea* 180. ISSN: 0074-4336.

Hernández-Guerra, Alonso et al. (1993). "Phytoplankton pigment patterns in the Canary Islands area as determined using Coastal Zone Colour Scanner data". In: *International Journal of Remote Sensing* 14.7, pp. 1431–1437.

Hernández-Guerra, Alonso et al. (2005). "Canary Current and North Equatorial Current from an inverse box model". In: *Journal of Geophysical Research: Oceans* 110.12, pp. 1–16. ISSN: 21699291. DOI: 10.1029/2005JC003032.

Hernández-Guerra, Alonso et al. (2017). "Recirculation of the Canary Current in fall 2014". In: *Journal of Marine Systems* 174, pp. 25–39. ISSN: 09247963. DOI: 10.1016/j.jmarsys.2017.04.002.

Hernández-León, S. et al. (2019). "Carbon export through zooplankton active flux in the Canary Current". In: *Journal of Marine Systems* 189.July 2018, pp. 12–21. ISSN: 09247963. DOI: 10.1016/j.jmarsys.2018.09.002. URL: https://doi.org/10.1016/j.jmarsys.2018.09.002.

Horii, Takanori et al. (2011). "Intraseasonal vertical velocity variation caused by the equatorial wave in the central equatorial Indian Ocean". In: *Journal of Geophysical Research: Oceans* 116.C9.

Hosegood, PJ et al. (2017). "Nutrient pumping by submesoscale circulations in the mauritanian upwelling system". In: *Progress in Oceanography* 159, pp. 223–236.

Hoskins, BJ, I Draghici, and HC Davies (1978). "A new look at the ω-equation". In: *Quarterly Journal of the Royal Meteorological Society* 104.439, pp. 31–38.

Hoskins, Brian J (1982). "The mathematical theory of frontogenesis". In: *Annual review of fluid mechanics* 14.1, pp. 131–151.

Hughes, P. and E. D. Barton (1974). "Stratification and water mass structure in the upwelling area off northwest Africa in April/May 1969". In: *Deep-Sea Research and Oceanographic Abstracts* 21.8. ISSN: 00117471. DOI: 10.1016/0011-7471(74)90046-1.

IOC, SCOR, and IAPSO (2010). "IAPSO, 2010: The International Thermodynamic Equation of Seawater—2010: Calculation and use of thermodynamic properties". In: *Intergovernmental Oceanographic Commission, Manuals and Guides* 56, p. 220.

Jackett, D. R. and T. J. McDougall (1997). "A Neutral Density Variable for the World's Oceans". In: *Journal of Physical Oceanography* 27.2, pp. 237–263. ISSN: 0022-3670.

Karstensen, Johannes, Lothar Stramma, and Martin Visbeck (2008). "Oxygen minimum zones in the eastern tropical Atlantic and Pacific oceans". In: *Progress in Oceanography* 77.4, pp. 331–350.

Karstensen, Johannes and Matthias Tomczak (1998). "Age determination of mixed water masses using CFC and oxygen data". In: *Journal of Geophysical Research: Oceans* 103.C9, pp. 18599–18609.

Kawase, M and Jorge Louis Sarmiento (1985). "Nutrients in the Atlantic thermocline". In: *Journal of Geophysical Research: Oceans* 90.C5, pp. 8961–8979.

Klein, Birgit and Gerold Siedler (1989). "On the origin of the Azores Current". In: *Journal of Geophysical Research: Oceans* 94.C5, pp. 6159–6168.

— (1995). "Isopycnal and diapycnal mixing at the Cape Verde Frontal Zone". In: *Journal of physical oceanography* 25.8, pp. 1771–1787.

Klein, Birgit and Matthias Tomczak (1994). "Identification of diapycnal mixing through optimum multiparameter analysis: 2. Evidence for unidirectional diapycnal mixing in the front between North and South Atlantic Central Water". In: *Journal of Geophysical Research: Oceans* 99.C12, pp. 25275–25280.

Käse, R. et al. (1986). "A Quasi-Synoptic Survey of the Thermocline Circulation and Water Mass Distribution Within the Canary Basin". In: *Journal of Geophysical Research: Oceans* 91.6, pp. 9739–9748.

Käse, R. H. and G Siedler (1982). "Meandering of the subtropical front south-east of the Azores". English. In: *Nature* 300.5889, pp. 245–246.

Kuzmina, Natalia (2016). "Generation of large-scale intrusions at baroclinic fronts: an analytical consideration with a reference to the Arctic Ocean". In: *Ocean Science* 12.6, pp. 1269–1277.

Kuzmina, NP (2000). "On the parameterization of interleaving and turbulent mixing using CTD data from the Azores Frontal Zone". In: *Journal of marine systems* 23.4, pp. 285–302.

LaCasce, Joseph H and Amala Mahadevan (2006). "Estimating subsurface horizontal and vertical velocities from sea-surface temperature". In: *Journal of Marine Research* 64.5, pp. 695–721.

Large, William G, James C McWilliams, and Scott C Doney (1994). "Oceanic vertical mixing: A review and a model with a nonlocal boundary layer parameterization". In: *Reviews of geophysics* 32.4, pp. 363–403.

Lázaro, Clara et al. (2005). "Seasonal and interannual variability of surface circulation in the Cape Verde region from 8 years of merged T/P and ERS-2 altimeter data". In: *Remote Sensing of Environment* 98.1, pp. 45–62. ISSN: 00344257. DOI: 10.1016/j.rse.2005.06.005.

Lévy, Marina (2003). "Mesoscale variability of phytoplankton and of new production: Impact of the large-scale nutrient distribution". In: *Journal of Geophysical Research: Oceans* 108.C11.

Lima, Ivan D, Donald B Olson, and Scott C Doney (2002). "Biological response to frontal dynamics and mesoscale variability in oligotrophic environments: Biological production and community structure". In: *Journal of Geophysical Research: Oceans* 107.C8, pp. 25–1.

Locarnini, R. A. et al. (2013). "World Ocean Atlas 2013, Volume 1: Temperature". In: *NOAA Atlas NESDIS* 73, p. 44.

Locarnini, R. A. et al. (2018). "World Ocean Atlas 2018, Volume 1: Temperature". In: *NOAA Atlas NESDIS* 81, p. 52.

Lønborg, Christian and Xosé Antón Álvarez-Salgado (2014). "Tracing dissolved organic matter cycling in the eastern boundary of the temperate North Atlantic using absorption and fluorescence spectroscopy". In: *Deep Sea Research Part I: Oceanographic Research Papers* 85, pp. 35–46.

Lovecchio, Elisa, Nicolas Gruber, and Matthias Münnich (2018). "Mesoscale contribution to the long-range offshore transport of organic carbon from the Canary Upwelling System to the open North Atlantic". In: *Biogeosciences* 15.16, pp. 5061–5091.

Lovecchio, Elisa et al. (2017). "On the long-range offshore transport of organic carbon from the Canary Upwelling System to the open North Atlantic". In: *Biogeosciences* 14.13, pp. 3337–3369.

Luyten, JR, Joseph Pedlosky, and Henry Stommel (1983). "The ventilated thermocline". In: *Journal of Physical Oceanography* 13.2, pp. 292–309.

Macdonald, Alison M. (1998). "The global ocean circulation: A hydrographic estimate and regional analysis". In: *Progress in Oceanography* 41.3, pp. 281–382. ISSN: 00796611. DOI: 10.1016/S0079-6611(98)00020-2.

Machín, F. (2003). "Variabilidad espacio temporal de la Corriente de Canarias, del afloramiento costero al noroeste de África y de los intercambios atmósfera-océano de calor y agua dulce". Spanish. PhD thesis. Universidad de Las Palmas de Gran Canaria. ISBN: 9788469106778.

Machín, F., A. Hernández-Guerra, and J. L. Pelegrí (2006). "Mass fluxes in the Canary Basin". In: *Progress in Oceanography* 70.2-4, pp. 416–447. ISSN: 00796611. DOI: 10.1016/j.pocean.2006.03.019.

Machín, Francisco and Josep Lluís Pelegrí (2009). "Northward penetration of Antarctic intermediate water off Northwest Africa". In: *Journal of Physical Oceanography* 39.3, pp. 512–535.

Machín, Francisco et al. (2010). "Seasonal Flow Reversals of Intermediate Waters in the Canary Current System East of the Canary Islands". In: *Journal of Physical Oceanography* 40.8, pp. 1902–1909. ISSN: 0022-3670. DOI: 10.1175/2010JPO4320.1. URL: http://journals.ametsoc.org/doi/abs/10.1175/2010JPO4320.1.

Mahadevan, Amala (2016). "The Impact of Submesoscale Physics on Primary Productivity of Plankton". In: *Annual review of marine science* 8, pp. 161–84. ISSN: 1941-0611. DOI: 10.1146/annurev-marine-010814-015912. URL: http://www.ncbi.nlm.nih.gov/pubmed/26394203.

Mahadevan, Amala and David Archer (2000). "Modeling the impact of fronts and mesoscale circulation on the nutrient supply and biogeochemistry of the upper ocean". In: *Journal of Geophysical Research: Oceans* 105.C1, pp. 1209–1225.

Mahadevan, Amala and Amit Tandon (2006). "An analysis of mechanisms for submesoscale vertical motion at ocean fronts". In: *Ocean Modelling* 14.3-4, pp. 241–256.

Martel, Françoise and Carl Wunsch (1993). "The North Atlantic Circulation in the Early 1980s-An Estimate from Inversion of a Finite-Difference Model". In: *Journal of Physical Oceanography* 23.5, pp. 898–924. ISSN: 0022-3670.

Martínez-Marrero, A. et al. (2008). "Distribution of water masses and diapycnal mixing in the Cape Verde Frontal Zone". In: *Geophysical Research Letters* 35.7, pp. 0–4. ISSN: 00948276. DOI: 10.1029/2008GL033229.

Mason, Evan et al. (2011). "Seasonal variability of the Canary Current: A numerical study". In: *Journal of Geophysical Research: Oceans* 116.C6.

Matear, RJ and AC Hirst (2003). "Long-term changes in dissolved oxygen concentrations in the ocean caused by protracted global warming". In: *Global Biogeochemical Cycles* 17.4.

MATLAB (2018). *version R2018b*. Natick, Massachusetts: The MathWorks Inc. URL: https://www.mathworks.com/products/matlab.html.

— (2019). *version R2019b*. Natick, Massachusetts: The MathWorks Inc. URL: https://www.mathworks.com/products/matlab.html.

McDougall, TJ et al. (2012). "A global algorithm for estimating Absolute Salinity." In: *Ocean Science* 8.6.

McDougall, Trevor J and Paul M Barker (2011). "Getting started with TEOS-10 and the Gibbs Seawater (GSW) oceanographic toolbox". In: *SCOR/IAPSO WG* 127, pp. 1–28.

McDougall, Trevor J et al. (2003). "Accurate and computationally efficient algorithms for potential temperature and density of seawater". In: *Journal of Atmospheric and Oceanic Technology* 20.5, pp. 730–741.

McDowell, Scott E. and H. Thomas Rossby (1978). "Mediterranean water: An intense mesoscale eddy off the Bahamas". In: *Science* 202.4372, pp. 1085–1087.

McGillicuddy, DJ et al. (1998). "Influence of mesoscale eddies on new production in the Sargasso Sea". In: *Nature* 394.6690, pp. 263–266.

McGillicuddy Jr, Dennis J (2016). "Mechanisms of physical-biological-biogeochemical interaction at the oceanic mesoscale". In: *Annual Review of Marine Science* 8, pp. 125–159.

McWilliams, James C (2021). "Oceanic frontogenesis". In: *Annual review of marine science* 13, pp. 227–253.

Meunier, Thomas et al. (2012). "Upwelling filaments off Cap Blanc: Interaction of the NW African upwelling current and the Cape Verde frontal zone eddy field?" In: *Journal of Geophysical Research: Oceans* 117.C8.

Mittelstaedt, E, D Pillsbury, and RL Smith (1975). "Flow patterns in the Northwest African upwelling area". In: *Deutsche Hydrografische Zeitschrift* 28.4, pp. 145–167.

Mittelstaedt, Ekkehard (1983). "The upwelling area off Northwest Africa—a description of phenomena related to coastal upwelling". In: *Progress in Oceanography* 12.3, pp. 307–331.

— (1991). "The ocean boundary along the northwest African coast: Circulation and oceanographic properties at the sea surface". In: *Progress in Oceanography* 26.4, pp. 307–355. ISSN: 0079-6611. DOI: https://doi.org/10.1016/0079-6611(91)90011-A.

Nagai, Takeyoshi, A Tandon, and Daniel L Rudnick (2006). "Two-dimensional ageostrophic secondary circulation at ocean fronts due to vertical mixing and large-scale deformation". In: *Journal of Geophysical Research: Oceans* 111.C9.

Onken, Reiner and Birgit Klein (1991). "A model of baroclinic instability and waves between the ventilated gyre and the shadow zone of the North Atlantic Ocean". In: *Journal of physical oceanography* 21.1, pp. 53–67.

Paillet, Jérôme and Herlé Mercier (1997). "An inverse model of the eastern North Atlantic general circulation and thermocline ventilation". In: *Deep-Sea Research Part I: Oceanographic Research Papers* 44.8, pp. 1293–1328. ISSN: 09670637. DOI: 10.1016/S0967-0637(97)00019-8.

Pallàs-Sanz, E., T. M S Johnston, and D. L. Rudnick (2010a). "Frontal dynamics in a California Current System shallow front: 1. Frontal processes and tracer structure". In: *Journal of Geophysical Research: Oceans* 115.12. ISSN: 21699291. DOI: 10.1029/2009JC006032.

— (2010b). "Frontal dynamics in a California Current System shallow front: 2. Mesoscale vertical velocity". In: *Journal of Geophysical Research: Oceans* 115.12. ISSN: 21699291. DOI: 10.1029/2010JC006474.

Pascual, Ananda et al. (2017). "A multiplatform experiment to unravel meso-and submesoscale processes in an intense front (AlborEx)". In: *Frontiers in Marine Science* 4, p. 39.

Pastor, M. V. et al. (2013). "Physical drivers of interannual chlorophyll variability in the eastern subtropical North Atlantic". In: *Journal of Geophysical Research: Oceans* 118.8, pp. 3871–3886. ISSN: 21699291. DOI: 10.1002/jgrc.20254.

Pastor, María V., Pedro Vélez-Belchí, and A. Hernández-Guerra (2015). *Oceanographic and biological features in the Canary Current Large Marine Ecosystem, Chapter 3.2, Water masses in the Canary Current large marine ecosystem*. Vol. 115. ISBN: IOC Annual Report Series No. 8 UNESCO 2002.

Pastor, Maria V et al. (2008). "Water and nutrient fluxes off Northwest Africa". In: *Continental Shelf Research* 28.7, pp. 915–936.

Pastor, María V. et al. (2012). "Meridional changes in water mass distributions off NW Africa during November 2007/2008". In: *Ciencias Marinas* 38.1B, pp. 223–244.

Pelegrí, J. L., A. Marrero-Díaz, and A. W. Ratsimandresy (2006). "Nutrient irrigation of the North Atlantic". In: *Progress in Oceanography* 70.2-4, pp. 366–406. ISSN: 00796611. DOI: 10.1016/j.pocean.2006.03.018.

Pelegrí, J. L. et al. (2005). "Coupling between the open ocean and the coastal upwelling region off northwest Africa: Water recirculation and offshore pumping of organic matter". In: *Journal of Marine Systems* 54.1-4 SPEC. ISS. Pp. 3–37. ISSN: 09247963. DOI: 10.1016/j.jmarsys.2004.07.003.

Pelegrí, Josep L. and A. Benazzouz (2015a). *Oceanographic and biological features in the Canary Current Large Marine Ecosystem, Chapter 3.4, Coastal Upwelling off north-west Africa*. Vol. 115. ISBN: IOC Annual Report Series No. 8 UNESCO 2002.

— (2015b). *Oceanographic and biological features in the Canary Current Large Marine Ecosystem, Chapter 4.1, Inorganic nutrients and dissolved oxygen in the Canary Current large marine ecosystem*. Vol. 115. ISBN: IOC Annual Report Series No. 8 UNESCO 2002.

Pelegrí, Josep L. and Jesús Peña-Izquierdo (2015). *Oceanographic and biological features in the Canary Current Large Marine Ecosystem, Chapter 3.3, Eastern Boundary currents off northwest Africa*. Vol. 115. ISBN: IOC Annual Report Series No. 8 UNESCO 2002.

Pelegrí, Josep L et al. (2017). *Deep-Sea Ecosystems Off Mauritania, Chapter 3, Oceanography of the Cape Verde Basin and Mauritanian Slope Waters*. Springer, pp. 119–153.

Peña-Izquierdo, Jesús et al. (2012). "The continental slope current system between Cape Verde and the Canary Islands". In: *Scientia Marina* 76.S1, pp. 65–78. ISSN: 1886-8134. DOI: 10.3989/scimar.03607.18C.

Peña-Izquierdo, Jesús et al. (2015). "Water mass pathways to the North Atlantic oxygen minimum zone". In: *Journal of Geophysical Research: Oceans* 120.5, pp. 3350–3372.

Pérez, Fiz F. et al. (2001). "Mixing analysis of nutrients, oxygen and inorganic carbon in the Canary Islands region". In: *Journal of Marine Systems* 28.3-4, pp. 183–201. ISSN: 09247963. DOI: 10.1016/S0924-7963(01)00003-3.

Pérez-Hernández, M. Dolores et al. (2013). "The source of the Canary current in fall 2009". In: *Journal of Geophysical Research: Oceans* 118.6, pp. 2874–2891. ISSN: 21699291. DOI: 10.1002/jgrc.20227.

Pérez-Rodríguez, P, J L Pelegrí, and A Marrero-Díaz (2001). "Dynamical characteristics of the Cape Verde frontal zone". In: *Scientia Marina* 65.S1, pp. 241–250. ISSN: 0214-8358. DOI: 10.3989/scimar.2001.65s1241.

Pietri, Alice et al. (2021). "Skills and Limitations of the Adiabatic Omega Equation: How Effective Is It to Retrieve Oceanic Vertical Circulation at Mesoscale and Submesoscale?" In: *Journal of Physical Oceanography* 51.3, pp. 931–954.

Pollard, Raymond (1986). "Frontal surveys with a towed profiling conductivitytemperaturedepth measurement package (SeaSoar)". In: *Nature* 323.6087, pp. 433–435.

Pollard, Raymond T and Lloyd A Regier (1992). "Vorticity and vertical circulation at an ocean front". In: *Journal of Physical Oceanography* 22.6, pp. 609–625.

Poole, Robert and Matthias Tomczak (1999). "Optimum multiparameter analysis of the water mass structure in the Atlantic Ocean thermocline". In: *Deep Sea Research Part I: Oceanographic Research Papers* 46.11, pp. 1895–1921.

Powers, Jordan G et al. (2017). "The weather research and forecasting model: Overview, system efforts, and future directions". In: *Bulletin of the American Meteorological Society* 98.8, pp. 1717–1737.

Roden, Gunnar I (1975). "On North Pacific temperature, salinity, sound velocity and density fronts and their relation to the wind and energy flux fields". In: *Journal of Physical Oceanography* 5.4, pp. 557–571.

— (1977). "Oceanic subarctic fronts of the central Pacific: Structure of and response to atmospheric forcing". In: *Journal of Physical Oceanography* 7.6, pp. 761–778.

— (1980). "On the subtropical frontal zone north of Hawaii during winter". In: *Journal of Physical Oceanography* 10.3, pp. 342–362.

— (1984). "Mesoscale oceanic fronts of the North Pacific". In: *Annales geophysicae*. Vol. 2, pp. 399–410.

— (1986). "Thermohaline fronts and baroclinic flow in the Argentine Basin during the austral spring of 1984". In: *Journal of Geophysical Research: Oceans* 91.C4, pp. 5075–5093.

— (1989). "The vertical thermohaline structure in the Argentine Basin". In: *Journal of Geophysical Research: Oceans* 94.C1, pp. 877–896.

Rodriguez, Jaime et al. (2001). "Mesoscale vertical motion and the size structure of phytoplankton in the ocean". In: *Nature* 410.6826, pp. 360–363.

Roquet, Fabien et al. (2015). "Accurate polynomial expressions for the density and specific volume of seawater using the TEOS-10 standard". In: *Ocean Modelling* 90, pp. 29–43.

Rudnick, Daniel L (1996). "Intensive surveys of the Azores Front: 2. Inferring the geostrophic and vertical velocity fields". In: *Journal of Geophysical Research: Oceans* 101.C7, pp. 16291–16303.

Rudnick, Daniel L and James R Luyten (1996). "Intensive surveys of the Azores Front: 1. Tracers and dynamics". In: *Journal of Geophysical Research: Oceans* 101.C1, pp. 923–939.

Ruiz, S. et al. (2014). "Geostrophic and ageostrophic circulation of a shallow anticyclonic eddy off Cape Bojador". English. In: *Journal of Geophysical Research: Oceans* 119.2, pp. 1257–1270.

Ruiz, Simón et al. (2009). "Vertical motion in the upper ocean from glider and altimetry data". In: *Geophysical Research Letters* 36.14.

Ruiz, Simón et al. (2019). "Effects of oceanic mesoscale and submesoscale frontal processes on the vertical transport of phytoplankton". In: *Journal of Geophysical Research: Oceans* 124.8, pp. 5999–6014.

Sangrà, P. et al. (2007). "On the nature of oceanic eddies shed by the Island of Gran Canaria". In: *Deep-Sea Research Part I: Oceanographic Research Papers* 54.5, pp. 687–709. ISSN: 09670637. DOI: 10.1016/j.dsr.2007.02.004.

Sangrà, Pablo et al. (2005). "Life history of an anticyclonic eddy". In: *Journal of Geophysical Research: Oceans* 110.C3.

Sangrà, Pablo et al. (2009). "The Canary Eddy Corridor: A major pathway for long-lived eddies in the subtropical North Atlantic". In: *Deep-Sea Research Part I: Oceanographic Research Papers* 56.12, pp. 2100–2114. ISSN: 09670637. DOI: 10.1016/j.dsr.2009.08.008.

Santana-Falcón, Yeray et al. (2017). "Organic carbon budget for the eastern boundary of the North Atlantic subtropical gyre: Major role of DOC in mesopelagic respiration". In: *Scientific Reports* 7.1, pp. 1–12. ISSN: 20452322. DOI: 10.1038/s41598-017-10974-y.

Schlitzer, Reiner (2019). *Ocean Data View*. Version 5.1.7. URL: http://odv.awi.de..

Schmitt, Raymond W (1994). "Double diffusion in oceanography". In: *Annual Review of Fluid Mechanics* 26.1, pp. 255–285.

Shaffer, Gary (1996). "Biogeochemical cycling in the global ocean: 2. New production, Redfield ratios, and remineralization in the organic pump". In: *Journal of Geophysical Research: Oceans* 101.C2, pp. 3723–3745.

Shcherbina, Andrey Y et al. (2009). "Characterizing thermohaline intrusions in the North Pacific subtropical frontal zone". In: *Journal of physical oceanography* 39.11, pp. 2735–2756.

Siedler, Gerold et al. (1992). "Seasonal changes in the tropical Atlantic circulation: Observation and simulation of the Guinea Dome". In: *Journal of Geophysical Research: Oceans* 97.C1, pp. 703–715.

Smith, Walter H. F. and David T. Sandwell (1997). "Global Sea Floor Topography from Satellite Altimetry and Ship Depth Soundings". In: *Science* 277.5334, pp. 1956–1962. DOI: 10.1126/science.277.5334.1956. eprint: http://science.sciencemag.org/content/277/5334/1956.full.pdf. URL: http://science.sciencemag.org/content/277/5334/1956.

Soufflet, Yves et al. (2016). "On effective resolution in ocean models". In: *Ocean Modelling* 98, pp. 36–50.

Spall, Michael A (1997). "Baroclinic jets in confluent flow". In: *Journal of physical oceanography* 27.6, pp. 1054–1071.

Stern, Melvin E (1960). "The "salt-fountain" and thermohaline convection". In: *Tellus* 12.2, pp. 172–175.

Stramma, Lothar (1984). "Geostrophic transport in the warm water sphere of the eastern subtropical North Atlantic". In: *Journal of Marine Research* 42.3, pp. 537–558. ISSN: 00222402. DOI: 10.1357/002224084788506022.

Stramma, Lothar and Gerold Siedler (1988). "Seasonal changes in the North Atlantic subtropical gyre". In: *Journal of Geophysical Research: Oceans* 93.C7, pp. 8111–8118. ISSN: 0148-0227. DOI: 10.1029/JC093iC07p08111.

Stramma, Lothar et al. (2008). "Oxygen minimum zone in the North Atlantic south and east of the Cape Verde Islands". In: *Journal of Geophysical Research: Oceans* 113.4, pp. 1–15. ISSN: 21699291. DOI: 10.1029/2007JC004369.

Thomas, Catherine, Gustave Cauwet, and Jean-François Minster (1995). "Dissolved organic carbon in the equatorial Atlantic Ocean". In: *Marine Chemistry* 49.2-3, pp. 155–169.

Thomas, Leif N (2008). "Formation of intrathermocline eddies at ocean fronts by wind-driven destruction of potential vorticity". In: *Dynamics of Atmospheres and Oceans* 45.3-4, pp. 252–273.

Thomas, Leif N, Amit Tandon, and Amala Mahadevan (2008). "Submesoscale processes and dynamics". In: *Ocean modeling in an Eddying Regime* 177, pp. 17–38.

Thomsen, Soeren et al. (2019). "Remote and local drivers of oxygen and nitrate variability in the shallow oxygen minimum zone off Mauritania in June 2014". In: *Biogeosciences* 16.5, pp. 979–998.

Tintoré, Joaquín et al. (1991). "Mesoscale dynamics and vertical motion in the Alboran Sea". In: *Journal of Physical Oceanography* 21.6, pp. 811–823.
Tippins, Duncan and Matthias Tomczak (2003). "Meridional Turner angles and density compensation in the upper ocean". In: *Ocean Dynamics* 53.4, pp. 332–342.
Tomczak, Matthias (1979). "The CINECA experience". In: *Marine Policy* 3.1, pp. 59–65. ISSN: 0308-597X. DOI: https://doi.org/10.1016/0308-597X(79)90040-X.
Tomczak, Matthias and J. Stuart Godfrey (2003). *Regional oceanography, an introduction*. Ed. by 2003 Delhi Daya Publishing House. 2nd edition. Elsevier. ISBN: 9788170353065.
Tomczak Jr, Matthias (1981). "An analysis of mixing in the frontal zone of South and North Atlantic Central Water off North-West Africa". In: *Progress in Oceanography* 10.3, pp. 173–192. ISSN: 00796611. DOI: 10.1016/0079-6611(81)90011-2.
Troupin, Charles et al. (2010). "High-resolution climatology of the northeast Atlantic using Data-Interpolating Variational Analysis (DIVA)". In: *Journal of Geophysical Research: Oceans* 115.C8.
Troupin, Charles et al. (2012). "Generation of analysis and consistent error fields using the Data Interpolating Variational Analysis (DIVA)". In: *Ocean Modelling* 52, pp. 90–101.
Turner, JS0312 (1974). "Double-diffusive phenomena". In: *Annual Review of Fluid Mechanics* 6.1, pp. 37–54.
UNESCO (1985). "The international system of units (SI) in oceanography". In: *Technical Paper in Marine Science* 45, pp. 1–124.
Valiente, S et al. (2022). "Dissolved and suspended organic matter dynamics in the Cape Verde Frontal Zone (NW Africa)". In: *Progress in Oceanography* 201, p. 102727.
Van Aken, Hendrik M (2000). "The hydrography of the mid-latitude northeast Atlantic Ocean: I: The deep water masses". In: *Deep Sea Research Part I: Oceanographic Research Papers* 47.5, pp. 757–788.
Vélez-Belchí, P et al. (2021). "The Canary Intermediate Poleward Undercurrent: Not Another Poleward Undercurrent in an Eastern Boundary Upwelling System". In: *Journal of Physical Oceanography* 51.9, pp. 2973–2990.
Viúdez, Álvaro, Joaquín Tintoré, and Robert L Haney (1996). "About the nature of the generalized omega equation". In: *Journal of the atmospheric sciences* 53.5, pp. 787–795.
Voituriez, Bruno and Rémy Chuchla (1978). "Influence of the Southern Atlantic Central Water on the distribution of salinity and oxygen in the northeast tropical Atlantic Ocean". In: *Deep-Sea Res* 25, pp. 107–117.
Volkov, Denis L, Tong Lee, and Lee-Lueng Fu (2008). "Eddy-induced meridional heat transport in the ocean". In: *Geophysical Research Letters* 35.20.
Wanninkhof, Rik (2014). "Relationship between wind speed and gas exchange over the ocean revisited". In: *Limnology and Oceanography: Methods* 12.6, pp. 351–362.
Williams, Richard G and Michael J Follows (2003). "Physical transport of nutrients and the maintenance of biological production". In: *Ocean biogeochemistry*. Springer, pp. 19–51.
Wunsch, Carl (1978). "North Atlantic general circulation west of 50°W determined by inverse methods". English. In: *Reviews of Geophysics* 16.4, pp. 583–620.
— (1996). *The ocean circulation inverse problem*. English. Cambridge;New York; Cambridge University Press. ISBN: 9780521480901;0521480906;
Yu, Xiaolong et al. (2019). "An annual cycle of submesoscale vertical flow and restratification in the upper ocean". In: *Journal of Physical Oceanography* 49.6, pp. 1439–1461.
Zenk, Walter, Birgit Klein, and Michael Schroder (1991). "Cape Verde Frontal Zone". In: *Deep Sea Research Part A. Oceanographic Research Papers* 38, S505–S530. ISSN: 01980149. DOI: 10.1016/S0198-0149(12)80022-7.
Zhang, Zhengguang, Wei Wang, and Bo Qiu (2014). "Oceanic mass transport by mesoscale eddies". In: *Science* 345.6194, pp. 322–324.
Zweng, M. M. et al. (2013). "World Ocean Atlas 2013, Volume 2: Salinity". In: *NOAA Atlas NESDIS* 74, p. 39.
Zweng, M. M. et al. (2018). "World Ocean Atlas 2018, Volume 2: Salinity". In: *NOAA Atlas NESDIS* 82, p. 50.